# Emplacement of the 2.44 Ga ultramafic layered Kemi Intrusion, Finland: PGE, geochemical and Sm-Nd isotopic implications

A THESIS SUBMITTED IN FULFILMENT OF THE REQUIREMENTS
FOR THE DEGREE OF

MASTER OF SCIENCE

OF

RHODES UNIVERSITY

By

Sean Aaron Linkermann

January 2010

## Abstract

Europe's largest chrome deposit is hosted by the 2.44 Ga Kemi ultramafic layered intrusion. The lower half of the intrusion consists of peridotites, pyroxenites and chromitite layers while the upper half consists of websterites, gabbronorites and leucogabbros. The mafic minerals of the lower and upper parts of the intrusion are altered to serpentine, chlorite, talc, amphiboles and carbonates. However, the original mineralogy is still preserved in the middle part of the intrusion. Earlier work on the Kemi intrusion concentrated mainly on the economically important chromitite layers and suggested that these layers were formed through contamination of a single pulse of primitive magma by underlying Archaean basement crustal material.

The broad variations of the major element concentrations reflect variations in the mode of the Kemi rocks. The petrology, which shows olivine- and orthopyroxene-dominated rocks in the lower portion of the intrusion to plagioclase- and clinopyroxene-dominated rocks in the upper portion, shows a gross consistency with a fractional crystallization process. The incompatible elements are relatively enriched in the lower portion of the intrusion which is not consistent with a broad fractional crystallization process. These variations suggest that the ultramafic portion of the Kemi Intrusion is relatively enriched in trapped liquid compared to the mafic portion.

$\varepsilon^{2.44}_{Nd}$ values ranges from +4 (consistent with depleted mantle source) to -10 (indicating a contribution from Archaean crust). The lower peridotites, pyroxenites and websterites have $\varepsilon^{2.44}_{Nd}$ values ranging between depleted mantle signatures and -2, whereas the gabbroic cumulates have $\varepsilon^{2.44}_{Nd}$ values which cover a range from around -5 to -10. Nd isotopic variation in the lower part of the profile is punctuated by distinct spikes to lower $\varepsilon^{2.44}_{Nd}$ corresponding to the chromitite horizons. Both the lower and upper portions of the Kemi Intrusion show enrichment of $LREE_{C1}$ relative to $HREE_{C1}$. The $LREE_{C1}$ enriched values start to increase markedly from about the 1000 meter mark and continue to increase in value towards the roof of the intrusion.

The main enrichment of PGE (ΣPPGE = 55 to 148 ppb) occurs approximately 90 to 160 m above the basal contact, beginning within and

continuing above the main chromitite ore horizon. The mantle-normalized PGE abundances of the main chromitite horizon and the peridotites and pyroxenites below it show enrichment of $IPGE_{PM}$ (Os + Ir + Ru) relative to $PPGE_{PM}$ (Rh + Pd + Pt). In contrast, the overlying rocks are characterised by enrichment of $PPGE_{PM}$ relative to $IPGE_{PM}$. These PGE-patterns suggest the influence of two distinct controlling processes above and below the main chromitite reef.

The isotopic data are consistent with the initial introduction of multiple pulses of depleted mantle-derived magma crystallising olivine and pyroxene. Before the parent magma was fed into the Kemi magma chamber, it underwent crustal contamination and assimilation in a staging chamber within the lower crust. Some of these pulses were “critically crustally contaminated”, inducing chromite saturation and precipitation. The modelling also predicts minor in-situ contamination of the parent magma in the Kemi chamber with its wall and roof rocks. Above the main chromitite layer (about 160 m above the basal contact), the chromite content decreases and the $PPGE_{PM}/IPGE_{PM}$ values increase which is consistent with scavenging of the IPGE into the lowermost layers and/or evolving magma compositions. Above 1000 m, the isotopic and REE data indicate a new magma pulse which has also been extensively contaminated in the staging magma chamber before emplacement into the Kemi magma chamber. The contamination in the staging magma chamber increased which is reflected in a progressively larger crustal component towards the top of the Kemi Intrusion.

## Dedication

This thesis is dedicated to the memory of Professor Tuomo Alapieti. A giant in the exploration and scientific studies of the Fennoscandian layered intrusions, he will be sorely missed. Thank you for all your help and advice.

## Acknowledgements

My thanks and appreciation to the following people:

The Finnish Academy of Sciences for their funding contribution towards this project;

Risto Kaukonen, of Oulu University, for the organisation of my field trip to Oulu and Kemi and for his support during my stay in Oulu and work at Oulu University;

Outokumpu Chrome Oy, Kemi mine, for allowing me to sample their bore-hole core collections;

Timo Huhtelin, mine geologist of the Kemi mine, for all his support and help during my visit to the Kemi mine and translation of finish bore-hole logs;

John Hepple and his staff (Caster, Chris and Bongani) for the preparation of the thin sections. A special thanks to John for his continued support and patience during my sample preparation;

Ashley Goddard, special thanks for her support and help in the registration and administration side of my project;

Shireen Govender and Petrus Le Roux, of the Geology Department UCT, for their help during the preparation and analysis of my isotope samples;

Prof. Julian 'Goonie' Marsh, special thanks for your invaluable input and positive critiques which improved the quality of my thesis;

Unnamed examiners for their time and patience;

And finally, Dr Steve Prevec, my supervisor. Without his continued help and support this thesis would never have been completed. His knowledge and guidance gave me the confidence to attempt this scientific study. Thank you.

## Table of Contents

## List of Figures

## List of Tables

# 1 Introduction

Early Paleoproterozoic layered intrusions, 2.44 Ga years in age, are found over a vast area of the northern Fennoscandian Shield. These intrusions are distributed over three countries: Sweden, Finland and Russia (Figure 1). The layered intrusions that occur in Finland are found in two different areas (e.g. Alapieti *et al*., 1990). The first group is called the Tornio – Näränkävaara belt. It forms a discontinuous belt extending eastwards from the northern edge of the Gulf of Bothnia. This belt comprises the Tornio, Kemi and Penikat Intrusions in the west and the Portimo and Koillismaa layered igneous complexes in the east. The second group contains the Koitelainen and Akanvaara Intrusions and its satellite bodies and is located in northern Finnish Lapland (Figure 1). These intrusions are located stratigraphically within late Archaean granitoids or at the contact between these granitoids and overlying Paleoproterozoic volcanic and sedimentary rocks.

A number of different igneous processes have been proposed to explain the genesis of the 2.44 Ga Fennoscandian and other layered intrusions. Some authors believe that since the layered intrusions are connected in space and time with dyke swarms and large volumes of extrusive rocks the intrusions are related to mantle plume activity (e.g. Heaman, 1997; Puchtel *et al*., 1997). Other authors argued that the magmas are derived from a depleted mantle source, with a large component of crustal contamination occurring during emplacement (Alapieti *et al*., 1990; Saini-Eidukat *et al*., 1997; Hanski *et al*., 2001).

A recent hypothesis proposed to explain the relative homogeneity of $\varepsilon_{Nd}$ values found in the 2.44 Ga Fennoscandian layered intrusions is that contamination of the parent magma may have occurred before the final emplacement of the intrusions (e.g. Hanski *et al*., 2001), in a staging magma chamber located in the lower crust or at the crust-mantle boundary (e.g. McCandless *et al*., 1999). The Fennoscandian intrusions were all fed with this contaminated parent magma via a plumbing system of dykes that was connected to the lower, temporary magma chamber (Ernst and Buchan, 1997; Elliot and Fleming, 2000). Iljina and Hanski (2005) took this idea one step further and proposed that the western and central intrusions of the Tornio – Näränkävaara belt were fed with two kinds of genetically

and isotopically similar parental magmas, one with relatively higher Cr content (> 1 000 ppm) and the other with a lower Cr content (< 600 ppm).

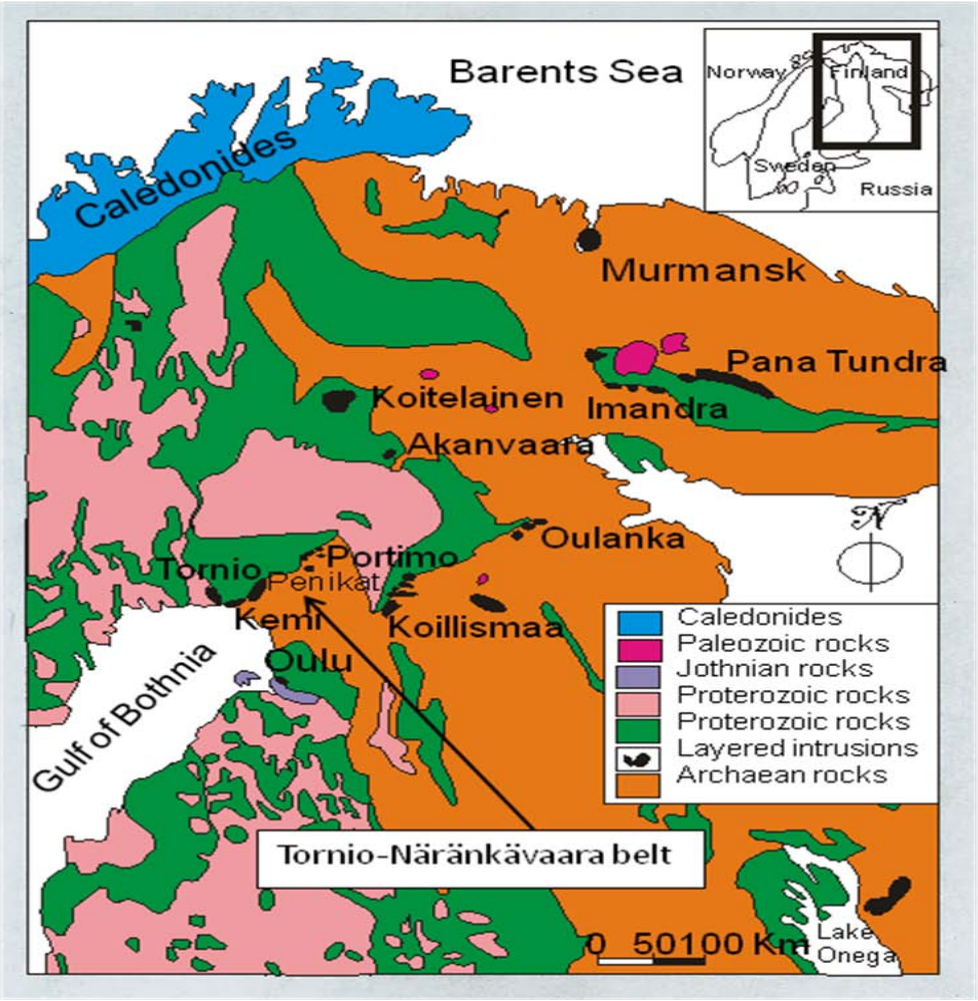


**Figure 1:** Generalized geological map of the north eastern part of the Fennoscandian Shield showing the locations of the most important 2.44 Ga aged layered intrusions. Modified after Alapieti *et al*. (1990) and Alapieti (2005).

Two of the most important economic deposits found in the Fennoscandian layered intrusions are chromitite layers and reef-type PGE mineralized zones (Alapieti *et al*., 1990). The current popular explanation for the formation of chromitite layers involves mixing of compositionally and genetically different magmas forcing the resultant magma composition into the primary stability field of chromite (e.g. Irvine, 1975; Lambert *et al*., 1994; Eales and Cawthorn, 1996). There are multiple variations to this model; ranging from evolved and primitive magmas of the same source (e.g. Naldrett *et al*., 1990) to depleted magma being contaminated with enriched felsic country rocks (Irvine, 1975). There are two main

explanations for the formation of reef-type PGE enriched zones. The first involves the collection of PGE from the melt by sulphide droplets that settle on the crystal pile to form the PGE reefs (Barnes and Maier, 2002). The second explanation is that the PGE are collected by a rising intercumulus liquid rich in volatiles and precipitated at a reaction front during compaction of the crystal pile (Boudreau and McCallum, 1989 and 1992).

The origin of the PGE mineralization in chromitite layers remains controversial, partly because many chromitites are sulphide-poor and thus a link between PGE concentration and magmatic sulphides is less evident (Maier, 2005). One idea is that the PGE in the chromitites were originally concentrated by magmatic sulphides but the sulphur was removed from the melt leaving the PGE behind as platinum-group minerals trapped in the chromites. Another idea is that some of the PGE in the chromitites (notably the IPGE (Os, Ir and Ru) and Rh) could have been concentrated by means of solid solution in the chromite (Peach and Mathez, 1996; Righter *et al*., 2004).

In this study, the focus is on the Kemi Intrusion, a layered intrusion found in the western part of the Tornio – Näränkävaara belt. The Kemi Intrusion is significant as it is the only Fennoscandian layered intrusion that presently hosts a commercially viable mine. The Kemi Intrusion has previously been described by Alapieti *et al*. (1989). Based on petrographical, mineralogical and geochemical investigations they concluded that the parent magma of the Kemi Intrusion evolved via an assimilation – fractional crystallization (AFC) process. The various chromitite layers that occur within the Kemi Intrusion formed as a direct result of felsic contamination of the parent magma.

The aim of this study is to conduct a geochemical study covering a profile across the intrusion, focusing on the major, minor and trace element concentrations. This can be used to determine if the Kemi magma evolved via an AFC process or if other igneous processes are required to explain the genesis of the Kemi Intrusion. The Nd isotopic compositions will be determined to investigate possible magmatic mantle sources and the role of the Archaean country rock as contaminants. The Nd isotopic data will also prove useful for comparing the genetic relationship and origin of the Kemi Intrusion with the other Fennoscandian layered intrusions. For the first time the PGE concentrations across the Kemi Intrusion will be determined. These results will be compared with other PGE results from

Fennoscandian and other layered intrusions to help outline possible ore genesis models.

# 2 Geological setting

## 2.1 General overview of the Fennoscandian Shield

### 2.1.1 Precambrian supra-crustal rocks of Finland

The Precambrian supra-crustal rocks of Finland are divided into four main groups. The oldest group consists of late Archaean greenstones and schists. This is followed by late Archaean or early Paleoproterozoic continental and epi/pericontinental metasediments and metavolcanics of eastern and northern Finland, which are known as the Karelian Supergroup. The next group consists of early Proterozoic schists and metavolcanics of southern and central Finland, known as the Svecofennian Supergroup. The youngest group contains middle to late Proterozoic continental sandstones and shales which are known as the Jotnia Supergroup (Laajoki, 1986; Vogel *et al*., 1998). The 2.44 Ga Fennoscandian layered intrusions are located within the late Archaean granitoids or at the contact between the Archaean granitoids and the Karelian sediments and volcanics (Alapieti *et al*., 1990). It is possible that rocks from the late Archaean granitoids or the Karelian Supergroup could be the source of contamination for the layered intrusions.

### 2.1.2 Late Archaean greenstones and schists

The Archaean rocks in the Fennoscandian Shield include two different cratons, the Karelian craton in the south-west (Finland) and the Kola craton in north-east (Russia). The Kalerian craton can be divided into the Belomorian mobile belt and three complexes: Central Kalerian, Iisalmi and Pudasjärvi. There are two different groups of granitoids found in the Kalerian craton based on age. The eastern and western part of the craton yield Neoarchaean (2.8 Ga) and Mesoarchaean (3.1 Ga) aged rocks while the centre of Kalerian craton has granitoids 3.1 Ga years in age (Laajoki, 1986; Sorjonen-Ward and Luukonen, 2005; Weihed *et al*., 2005).

### 2.1.3 The Karelian Supergroup

The Karelian sediments show similar characteristics to sediments formed from Atlantic-type rifted continental margins. The Karelian

Supergroup comprises of four unconformity-bounded groups (e.g., Simonen, 1980; Vogel *et al*., 1998). The oldest group is the Sumi Group which consists of basal conglomerates, arkoses and metasediments intercalated with various volcanic and volcanoclastic rocks which lie unconformably on the Archaean basement. The Sumi Group represents the rifting stage of an Atlantic-type rifted continental margin (Laajoki, 1986; Vogel *et al*., 1998; Weihed *et al*., 2005).

The weathered sediments of the first cycle were transported and redeposited by fluvial processes to form the quartz-pebble conglomerates and the metapsammites of the second Karelian group (called the Sariola Group). This cycle represents the narrow sea/inland basin stage of an Atlantic-type rifted continental margin (Laajoki, 1986; Vogel *et al*., 1998).

The Sariola Group is overlain unconformably by the Jatulian Group, a thick (1-3 km) sequence of quartzite, dolomite, metapelite and other rocks representing a typical Precambrian quartz arenite-carbonate association (Vogel *et al*., 1998). The Jatulian Group represented the open sea stage of an Atlantic-type rifted continental margin and is considered as the product of an epi- or pericontinental sea (Laajoki, 1986).

The Jatulian Group is overlain unconformably by the Kalevian Group, which consists mostly of turbiditic metasediments (Vogel *et al*., 1998). The Kalevian Group begins with a conglomerate whose clasts consist mainly of quartzites, metavolcanics, etc. The conglomerate grades via a turbiditic quartzite into either grade-bedded phylites or mica schists, depending on the degree of metamorphism. These rocks represent the ‘flysch’ stage and may be derived from the Svecofennides (e.g., Simonen 1980), or may represent pericontinental turbidites (Laajoki, 1986).

### 2.1.4 2.44 Ga Fennoscandian ultramafic layered intrusions

Early Proterozoic layered intrusions are scattered throughout the Fennoscandian Shield. The outcrops of these intrusions vary greatly in size, ranging from one square kilometre to several hundred square kilometres (Alapieti *et al*., 1990). Numerous age determinations have been carried out on these intrusions. Many different dating methods have been used, including U-Pb zircon, Pb-Pb whole rock, and Sm-Nd methods. These have together yielded a fairly coherent set of ages, the mean being 2440 Ma (e.g., Patchet *et al*., 1981; Alapieti, 1982).

The intrusions have undergone a complex history of deformation and metamorphism associated with the Jatulian (2200-2100 Ma), Kalerian (2000-1900 Ma) and Svecofennian (1900-1800 Ma) orogenic events (Laajoki, 1986 and Alapieti *et al*., 1990). These events affected the intrusions in different ways. Those located in the eastern parts are generally less metamorphosed than those in the west. Thus the original magmatic minerals of the intrusions in the western part have been altered to varying extents, with the replacement of olivine by serpentine, the pyroxenes by uralites and plagioclase by chlorite and the epidote minerals. However, cumulus textures are generally fairly well preserved as pseudomorphs even in the completely metamorphosed intrusions. Thus the cumulus stratigraphy of the intrusions can generally be determined (Alapieti *et al*., 1990).

Most of the intrusions are emplaced within the late Archaean granitoids or at the contact between these and the overlying Proterozoic supracrustal rocks (the Karelian Formations), the lowermost layer of which is commonly represented by polymictic conglomerates. During the tectonic events mentioned above, many of the intrusions were broken up to form a number of tilted blocks. In many cases the present hanging wall rocks are younger than the underlying intrusions. This indicates that the original roof and commonly also the uppermost cumulates have been destroyed by erosion before the deposition of the overlying supra-crustal sequence (Alapieti *et al*., 1990).

The intrusions in Finland are concentrated principally in two areas. The first group forms a discontinuous belt (the Tornio-Näränkävaara intrusion belt) which crosses northern Finland. This belt features the Tornio, Kemi and Penikat intrusions and the scattered Portimo and Koillismaa layered igneous complexes. The second group comprises the Koitelainen and Akanvaara Intrusions and associated satellite bodies in central Finnish Lapland (Alapieti *et al*., 1990).

Examples of all the ore types (as summarized by Alapieti and Lahtinen, 2002) characteristic of layered intrusions are encountered in the Finnish intrusions. Chromitite layers of varying thickness and grade are found in the Tornio, Kemi, and Penikat intrusions. The Akanvaara, Koitelainen, Portimo and the Koillismaa Complex are characterized by platinum-group element (PGE)-bearing base metal sulphide deposits in their basal zones. Mineralized zones enriched in PGE are also encountered

in layered series' in the Penikat intrusion and the Portimo Complex. Vanadium-bearing Fe-Ti oxide deposits are found in the Koillismaa intrusions (Alapieti *et al*., 1990).

The emplacement of these layered intrusions in the Fennoscandian Shield was part of world-wide igneous activity indicated by the occurrence of large layered intrusions of similar age in other cratons. The Jimberlana Intrusion in the Yilgarn Block in Australia (2420 ± 30 Ma; McClay and Campbell, 1976) and the Great Dyke in the Zimbabwe Craton (2579 ± 7 Ma; Mukasa *et al*., 1998) are examples of these large layered intrusions of broadly similar ages in other cratons (Alapieti *et al*., 1990).

### 2.1.5 Classification of the 2.44 Ga Fennoscandian intrusions

Alapieti and Lahtinen (2002) broadly divided the 2.44 Ga Fennoscandian Intrusions into three lithological categories:

(1) ultramafic-mafic complexes

(2) mafic intrusions, and

(3) intermediate 'megacyclic' intrusions.

The layered series of the ultramafic-mafic type has a thick ultramafic lower part overlain by anorthositic and gabbroic rocks, as seen in the Bushveld and Stillwater Intrusions. The Tornio, Kemi, Näränkävaara and Kivakka intrusions represent this type. The layered series of the mafic type has thin or absent ultramafic lower sections relative to a thick gabbro-anorthosite sequence above. This type includes the Koillismaa Complex. The layered series of the intermediate megacyclic type of intrusion is composed of distinct megacyclic units (MCU) which themselves have ultramafic lower parts and gabbroic and anorthositic upper portions. The megacyclic units differ in composition within the intrusions, the upper MCUs usually being distinctly poorer in magnesium and chromium than the lower ones. Examples of this type are the Penikat and Portimo Complex (Alapieti and Lahtinen, 2002).

The intrusions of the Tornio-Näränkävaara belt either belong to group1 ultramafic-mafic complexes or group 3 intermediate MCU complexes. Iljina and Hanski (2005) took this sub-division of the Tornio-Näränkävaara belt intrusions one step further. They concluded that these intrusions were fed with two kinds of parental magma. The first magma was a more primitive, chromium-rich magma while the second magma was a less primitive, chromium-poor magma. Some of the intrusions were only fed

with the first, chromium-rich magma (e.g., Tornio) or the second, chromium-poor magma (Suhanko Body, Portimo Intrusion) whereas other intrusions (e.g., Penikat) were fed with both, first the more primitive, chromium-rich magma and then the less primitive, chromium-poor magma. The intrusions that belong to the group 1 ultramafic-mafic complexes evolved from the primitive, chromium-rich magma while the intrusions that are group 3 intermediate MCU complexes evolved from the evolved, chromium-poor magma (with the exception of the Penikat Intrusion).

### 2.1.6 PGE mineralization styles of the Fennoscandian intrusions

According to Maier (2005) the PGE deposits found world-wide can be sub-divided into seven broad groupings based on their genetic models and stratigraphic location with their intrusion:

(1) PGE-enriched intervals along the base or the sidewall of intrusions, often hosted by variably-texture of gabbronoritic rocks (e.g., the Platreef of the Bushveld Complex).

(2) PGE-mineralized intervals within ultramafic silicate cumulates in the lower portions of the intrusions. In some cases (e.g., Kapalagulu) this can be relatively close to the basal contact (50–200 m), whereas in other examples (e.g., Main Sulphide Zone of the Great Dyke) the reef occurs at the top of the ultramafic zone, some 2300 m above the base of the intrusion.

(3) PGE-enriched chromitites (e.g., UG2 of the Bushveld).

(4) PGE-enriched layers associated with layered mafic–ultramafic cumulates in the central portions of intrusions (e.g., Merensky Reef of the Bushveld Complex, J-M reef of the Stillwater Complex).

(5) PGE-enriched intervals in the upper, gabbroic–dioritic, often magnetite-rich, portions of intrusions (e.g., Stella and Skaergaard).

(6) Occurrences related to late magmatic and/or hydrothermal fluids (e.g., Lac des Iles).

(7) PGE as by-products in some magmatic Ni–Cu sulphide occurrences.

The PGE mineralization of the 2.44 Ga Fennoscandian layered intrusions falls under the first five groups of the Maier (2005) classification scheme which suggests a number of varied ore genesis processes were at work during the evolution of these deposits. The PGE mineralization of the 2.44 Ga Fennoscandian layered intrusions can be divided into six

categories (Table 1) based on host mineral associations and stratigraphic location in the intrusions (Alapieti and Lahtinen, 2002).

**Table 1:** PGE mineralization styles in 2.44 Ga Fennoscandian layered intrusions (after Alapieti and Lahtinen, 2002)

| Style | Mineralization | Setting | Examples |
|---|---|---|---|
| **1** | Disseminated and massive base metal and PGE sulphide deposits | Marginal facies of intrusions (but apparently not basal breccias), associated with silicic contamination | Suhanko Block of Portimo; western Koillismaa |
| **2** | PGE offset minerlization | Offset mineralization (foorwall-hosted shoots) | Narkaus Intrusion (Portimo Complex) |
| **3** | Base metal and PGE sulphide-bearing reefs | Reefs within the layered series (Merensky-type) | AP, PV reefs of Penikat Intrusion; SK, RK, reefs of Portimo Complex |
| **4** | Sulphide-poor PGE reefs | Reefs within the layered series, often with disseminated chromite or with chlorite schists | SJ reefof Penikat Intrusion |
| **5** | Disseminated base-metal sulphide-PGE deposits | Associated with microgabbronorites within the layered series | Western Koillismaa Complex; Oulanka Complex |
| **6** | PGE enrichments associated with upper chromitites | Associated with "upper chromitites" that occur at unusually high stratigraphic levels | Koitelainen and Akavaara Intrusions |

## 2.2 The Kemi Intrusion

### 2.2.1 Shape and stratigraphy of the Kemi Intrusion

The description of the stratigraphy, mineral chemistry and geochemistry of the Kemi Intrusion that follows is taken from Alapieti *et al*. (1989) and (1990). The Kemi intrusion may be considered the most historically significant of the early Proterozoic Fennoscandian layered intrusions because it hosts the only mine, namely the Kemi chrome mine. The intrusion strikes north-eastward along the boundary between the Archaean granites and the Svecokarelidic Peräpohja schist belt. The U-Pb zircon data yielded an age of 2430 $\pm$ 4 Ma (Perttunen and Vaasjoki, 2001) and the Pb-Pb data for whole rocks defined an age of 2.44 $\pm$ 0.16 Ga (Manhes *et al*., 1980).

The present surface section of the intrusion is lenticular in shape, some 15 km long and 0.2 to 2 km wide (Figure 2). The lenticular shape is interpreted

as representing the cross-section of an originally funnel-shaped intrusion which was tilted by tectonic movements during the Svecokarelian orogeny to form a body dipping about 70° northwest. Geophysical interpretations suggest that it extends downwards for at least 2 km. The individual cumulate layers, laterally extensive throughout the intrusion, are thickest in the middle part of the intrusion and become thinner towards the edges. Inclined underground tunnelling has recently proved that the magmatic conduit which fed the magma chamber was located just below this thickening of the cumulate layers.

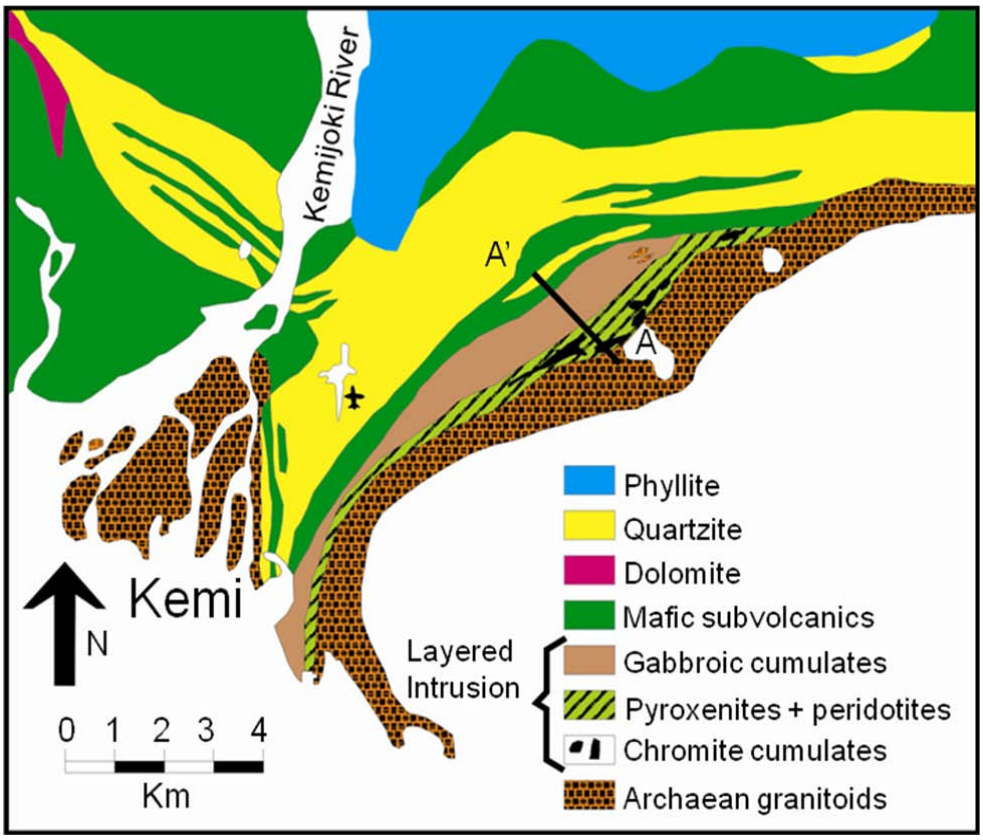


**Figure 2:** Generalized geological map of the Kemi Intrusion, showing the location of the drilling profile A-A' from where the samples were collected. After Alapieti *et al*. (1989).

The generalized geology of the Kemi area, including the Kemi Intrusion, is shown in Figure 2. The footwall of the intrusion consists of late Archaean granitoids. The hanging wall rocks are, locally, younger mafic volcanics, subvolcanic sills 2150 Ma in age, or a polymictic conglomerate (basal unit of the Karelian Formations), also younger than the intrusion. This indicates that the present upper contact is erosional, implying that the

original roof rocks and the uppermost cumulates of the layered series may have been removed by erosion.

The Kemi Intrusion underwent lower amphibolite facies metamorphism during the Svecokarelian orogeny. The original magmatic silicates have been completely altered to secondary minerals in the lower and upper parts of the intrusion, but in the middle part they have been preserved and are fresh. Many chromites throughout the intrusion have nevertheless preserved their original composition in their cores, even though the silicates of the same rock have been completely altered.

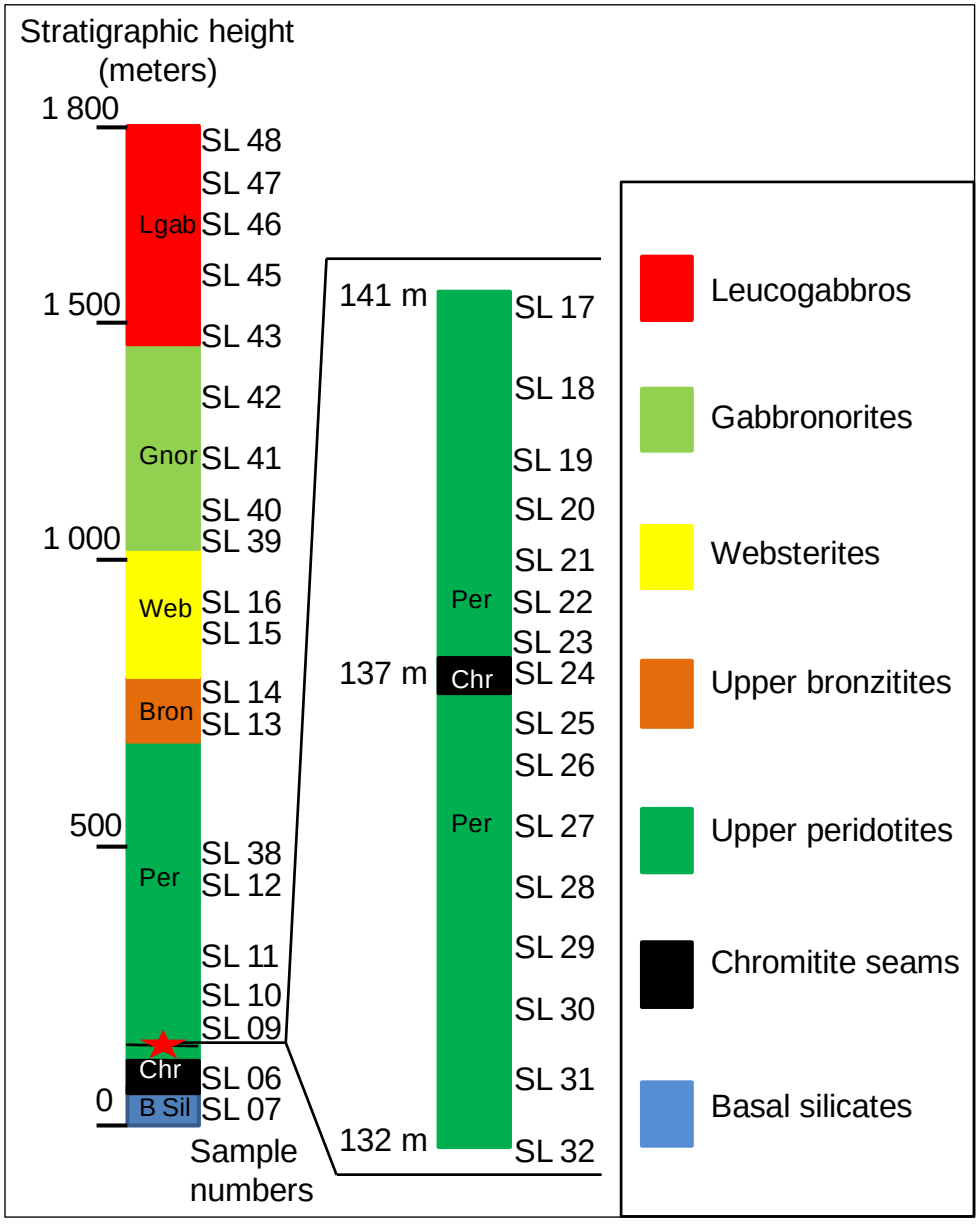


**Figure 3:** The stratigraphic sequence of the Kemi Intrusion with major rock types (Table 2) and sample locations (Tables 4 and 5).The res star represents the stratigraphic position of the small chromitite layer. After Alapieti *et al*. (1989).

The stratigraphic sequences of the Kemi Intrusion are shown in Figure 3. A complex basal contact (i.e., a marginal zone), as is typical of the other layered intrusions in northern Finland, has not been observed in the Kemi Intrusion. Either no such series formed at all or else it was obliterated by magmatic erosion. Instead, a fine-grained ultramafic marginal rock about 10 cm thick, which has preserved its original texture, occurs in contact with the basement granitoids. The contact of the fine-grained marginal rock with the underlying granitoids is irregular, showing pronounced interaction with the basement. As a result sialic xenoliths of many types are common in this marginal rock. The silicate minerals in this fine-grained ultramafic rock are completely recrystallised but the chromite has been preserved and occurs as euhedral phenocrysts about 0.5 mm in diameter.

The lowermost portion of the intrusion is composed of a markedly altered sequence 50 to 100 m thick. The lower part of this zone consists of a bronzite-chromite cumulate (refer to Table 2 for the description of the rock- type nomenclature) and the upper part consists of an olivine-chromite ± bronzite cumulate, with 0.5 – 1.5 m chromitite interlayers.

**Table 2:** Rock-type nomenclature used in this study (after Alapieti *et al*., 1989). The term bronzitite is used in this study (instead of the IUGS recommended term orthopyroxenite) to describe rocks that consist of predominantly orthopyroxene cumulates because the Kemi chrome mine still uses the outdated term.

| Conventional Rock Name | Cumulus mineral assemblage |
|---|---|
| **Bronzitite** | Orthopyroxene (bronzite) with minor olivine and chrome spinel |
| **Peridotite** | Olivine and orthopyroxene (bronzite) with minor chrome spinel |
| **Chromitite** | Chrome spinel with minor olivine |
| **Websterite** | Clinopyroxene (augite) and orthopyroxene (bronzite) |
| **Gabbronorite** | Plagioclase and clinopyroxene (augite) with minor orthopyroxene (bronzite) |
| **Leucogabbro** | Plagioclase with minor clinopyroxene (augite) |

This lowermost sequence is followed by the main chromitite layer. The main chromitite layer extends across the whole length of the intrusion

and varies in thickness from a few millimetres at the margins to about 90 meters locally in the centre of the intrusion. The silicate cumulates are also thickest in the middle part. The main chromitite layer is composed of two parts with a more silicate-rich rock between them. The cumulate minerals in this more silicate-rich layer are chromite and olivine, and the intercumulus minerals are poikilitic bronzite and to a lesser extent augite.

The main chromitite layer is overlain by 550 m of peridotitic cumulates with olivine, chromite and occasional bronzite as the cumulus phase. About 15 chromite-rich interlayers, varying in thickness from 5 cm to 2.5 m in the centre of the intrusion, are located in the peridotitic sequence. The uppermost interlayer being about 370 m above the main sequence.

Bronzite re-appears as the dominant cumulus mineral from about 700 m upwards with olivine and chromite as the other cumulus phases. This is the upper bronzitite layer. A further 100 m above, augite becomes the main cumulus mineral alongside bronzite while olivine and chromite disappears. This rock forms the websterite layer.

At about 1000 m above the base, plagioclase reached cumulus phase status alongside augite and bronzite. This rather monotonous plagioclase $\pm$ pyroxene cumulate (the gabbronorite and leucogabbro layers) continues upwards for 800 m to the contact with the hanging wall.

Alapieti *et al*. (1989) concluded that the Kemi Intrusion represents a simple fractionated suite from ultramafic peridotites and bronzitites to gabbroic and anorthositic cumulates. They concluded that in-situ contamination and assimilation of Archaean country rock in the magma chamber led to the formation of the various chromitite layers found in the Kemi Intrusion.

### 2.2.2 Minerals and mineral chemistry of the Kemi Intrusion

Silicates:

Olivine is a typical cumulus mineral of ultramafic rocks. It has been completely altered in the lowermost cumulates. The olivines analyzed showed a constant composition of $Fo_{82}$ – $Fo_{83}$ (Alapieti *et al.,* 1989). Ca-poor pyroxene or bronzite (with a fairly constant composition of $En_{83}$) is present as a cumulus phase throughout the lower portion of the intrusion. It occurs typically in the form of large oikocrysts. The $Cr_2O_3$ content of the orthopyroxenes is quite high; the mean value is 0.51 wt. %. Ca-rich pyroxene is represented by augite in the Kemi Intrusion. It is found as an

intercumulus mineral in the lower half of the intrusion but becomes a cumulus mineral in the websterites and gabbronorites. Like the orthopyroxenes, it has high chromium content, the mean being about 1 wt. %.

Plagioclase occurs as an intercumulus phase in the peridotitic cumulates, with an anorthite content of $An_{65}$. It first appears as a cumulus mineral about 1 000 m above the basal contact of the intrusion coinciding with the start of the gabbro layers. Here the plagioclase abundance increases sharply and its anorthite content rises to $An_{82}$ where it persists as the predominant cumulus phase until the hanging wall contact.

Oxides:

Chromite is by far the most prominent Cr-Fe-Ti oxide in the Kemi Intrusion, occurring as a cumulus mineral in the lower part of the intrusion. The chromite grains in the silicate-rich rocks are altered at the rims with aluminium and magnesium content decreasing from the core of the grain outward. The chromium content remains fairly constant and the nickel content increases towards the rim, as the altering chromite probably absorbed nickel from the surrounding mafic silicates.

The Cr content of the chromite grains in the chromite-rich layers below the main chromitite layer and in the main chromitite layer itself is fairly constant, whereas the Cr content of the chromites decreases in the chromite-rich layers above the main chromitite layer. The highest Cr contents are found in the main chromitite layer. The Al, Fe, Ti and vanadium concentrations all increase from the main chromitite layer upwards.

The chromite grains are in many places characterized by spherical silicate inclusions, 5 to 100 µm in diameter. The most common, and usually the largest, inclusions are composed of mafic silicates similar to those in the surroundings of the chromite grains. However, there are significant amounts of felsic inclusions that are completely different in composition to the surrounding mafic cumulates. The most common felsic inclusions are albite-bearing inclusions.

Sulphides:

The sulphides occur as weakly, disseminated phases in the Kemi Intrusion, being most abundant in the silicate-rich rock in the middle part of

the main chromitite layer and the peridotites immediately above the main chromitite layer. The sulphide assemblage is pyrrhotite-pentlandite-chalcopyrite.

Platinum-group minerals (PGM) are quite common in the chromitite layers (Alapieti *et al*., 1989). They are mostly represented by Os, Ir, Ru and Rh alloys, sulphides (especially laurite) and sulpharsenides. Only a few Pt and Pd minerals are found. The primary PGM (such as laurite, osmiridium and osarsite) occur as euhedral to subhedral inclusions in the chromites and the secondary PGM (irarsite, osmiridum and osarsite) form anhedral grains in the gangue minerals (Kojonen *et al*., 2005).

### 2.2.3 Geochemistry of the Kemi Intrusion

The emergence of plagioclase as a cumulus phase divides the Kemi intrusion into an upper and a lower portion. The lower portion or zone will be referred to as the ultramafic zone and the upper portion the mafic zone. This contact between the ultramafic and mafic portion is reflected in the variation of the major element concentrations across the Kemi Intrusion. As expected, the $Al_2O_3$ content shows a steep increase above the contact between the pyroxenitic and gabbroic cumulates. The MgO content remains relatively constant up to the top of the peridotites, above which they decline steadily toward the roof of the intrusion. A sharp rise in CaO content is seen where augite becomes a cumulus mineral in the websterites, after which CaO content decreases toward the roof of the intrusion. $Na_2O$ concentrations increase steadily throughout the intrusion and the highest $K_2O$ content is found in the leucogabbros of the upper part of the intrusion.

The nickel content is constant, about 0.1 wt percent in the lower part of the intrusion. Ni content begins to decrease in the upper part of the peridotites (where there is a decrease in modal percentage of olivine), continuing towards the roof of the intrusion. One of the small chromite-rich layers above the main chromitite layer contains high La and Ce concentrations of 130 and 300 ppm, respectively. The highest Pd, Pt and Rh concentrations recorded in the Kemi intrusion (50, 180 and 120 ppb respectively) from Alapieti *et al*. (1989) are found immediately above this small chromite-rich layer.

The chromium content is unusually high throughout the intrusion. The chromite-rich layers generally contain 20 wt percent Cr. The Cr content

of the peridotites and bronzitites is relatively constant, varying between 0.2 and 0.6 wt percent. Only in the lower part of the gabbroic cumulates does the Cr content fall below 0.1wt percent.

PGE data from the Kemi Intrusion (Alapieti and Huhtelin, 2005) show that the main chromitite layer is $IPGE_{PM}$ enriched relative to the $PPGE_{PM}$ values. However, the silicates immediately above the main chromitite layer are $PPGE_{PM}$ enriched. The PGE data of Alapieti and Huhtelin (2005) is not representative of the entire Kemi Intrusion as the few samples that were analyzed for their PGE content were taken only from the main chromitite layer and surrounding silicates. There remains an incomplete PGE profile from the basal silicates to the upper-most gabbros.

### 2.2.4 The main chromitite layer

The main chromitite layer parallels the basal contact zone of the intrusion and is found throughout the length of the complex. This layer varies in thickness from a few millimetres at the margins to about 90 meters in the centre of the intrusion. Alapieti *et al*. (1989) divided the main chromitite layer into three different units. The informal names of these units, from bottom to top, are the main unit, the altered unit and the uppermost unit.

The thickness of the main unit (the lowest unit of the main chromitite layer) averages 40 m. The upper contact of the unit against the altered unit is stratigraphically 100 to 150 m above the basal contact of the complex. Several strike-slip faults have displaced the upper contact of the main unit with respect to the basal contact of the intrusion.

The altered unit overlies the main unit. It contains intensely altered ultramafic silicate rock with abundant thin chromite layers. This silicate rock type was pyroxenite but now consists of talc and carbonates. Some of the inter-layered chromite layers can be traced for several tens of meters but most of the layers extend for only a few meters. Innumerable small faults cut the layering and make it difficult to trace individual layers.

Sparse chromitite layers occur in the well-preserved peridotitic cumulate above the intensely altered ultramafic rock. This is the uppermost unit of the main chromitite layer.

The aim of this study does not require the division of the main chromitite layer into three units. It will create unnecessary and confusing

nomenclature. For the purpose of this study the three units of Alapieti *et al*. (1989) will considered as one layer: the main chromitite layer.

# 3 Methodology

## 3.1 Sample collection strategy

The Kemi Intrusion is currently being mined for its chromite deposits. The mining activity ruled out any sampling from the intrusion itself due to safety reasons. Sampling was restricted to the bore-hole core collections of the Kemi Mine and Oulu University. The nine bore-holes (Table A1) that were used for sampling cover the complete stratigraphic sequence of the intrusion and the drilling profile A-A' in Figure 2 show the profile along which the bore-holes are located. The drilling profile A-A' is located roughly in the middle of the intrusion where the cumulate layers are thickest. This places the drilling profile near the feeder of the intrusion.

Samples were collected at intervals of roughly 100 meters from the basal contact through to the top of the intrusion. The sampling interval was varied to avoid alteration and to ensure that every major lithostratigraphic rock unit of the intrusion was sampled. In all, twenty-four samples were collected. Samples SL-04 through to SL-16 and SL-38 encompassed the ultramafic portion of the intrusion (from the basal silicates to the websterites) and samples SL-39 to SL-48 are from the mafic portion (Figure 3).

A small chromitite layer was identified in the upper peridotites (located 47 meters above the main chromitite layer sample SL-06). Figure 3 summarizes the location of the samples taken from the small chromitite layer and surrounding peridotites. The spacing of the samples ranged from 0.2 meters to 1 meter.

Three additional samples (Samples SL-01 to SL-03) from the basement granites (below the basal contact of the Kemi Intrusion) were collected to study possible country rocks contaminants.

## 3.2 Sample preparation

Appendix B records the details of the standard techniques outlined below.

### 3.2.1 Crushing and milling of samples into powders

The core samples were crushed into powder via three stages, each stage reducing the particle size of the powders. The samples were first crushed with an Osborn-Massco jaw crusher, placed in a Herzog swing-mill and finally powdered in a Fritsch agate mill. In-between the milling of each sample the mills and crusher were cleaned with water and quartz to prevent contamination.

### 3.2.2 Fusion disks preparation and manufacture

The fusion disks were used to determine the major element concentrations of the samples. Appendix B records the relevant masses of the samples used and any other added compounds used in the standard fusion disk preparation technique of Norrish and Hutton (1969).

### 3.2.3 Powder pellets manufacture

The powder pellets were used to determine some of the minor and trace element concentrations of the samples. The sample was encased in boric acid crystals within a hollow, metal tube. The sample was pressed into a powder pellet using a hydraulic press.

### 3.2.4 Dissolution process: Stellenbosch University ICP-MS

The samples and standards were dissolved in an acidic solution of HF and $HNO_3$ and left to dry out on a heating plate. The dissolution and drying of the dried samples with $HNO_3$ was repeated twice. The dried samples were dissolved a fourth time with $HNO_3$ and decanted into centrifuge tubes to be analyzed by ICP-MS.

Six duplicate analyses were completed for three random samples (SL-11, SL-16 and SL-48, Tables D6 and D7).

### 3.2.5 Dissolution process: University of Cape Town MC-ICP-MS

The samples were dissolved in an acidic solution of HF and $HNO_3$ and left to dry out on a heating plate as preparative step prior to the separation of Nd from the matrix by ion exchange column chemistry using resin. The dissolution and drying of the dried samples with HCl was repeated twice. The dried samples were dissolved a fourth time with HCl and decanted into centrifuge tubes. The samples were centrifuged twice.

### 3.2.6 Column chemistry: Cation exchange process (University of Cape Town MC-ICP-MS)

The primary columns are used first to collect the REE (Rare Earth Element) fraction out of the sample and the REE fraction is stored in Teflon beakers. The samples are left to dry out on a heating plate and then are dissolved with HCl. The secondary columns are used to collect Neodymium, Nd, out of the REE fraction. The samples are left to dry out on a heating plate and were then dissolved with $HNO_3$.

### 3.2.7 Platinum group elements: Quebec University ICP-MS

Due to financial restrictions not all the samples were analyzed for their PGE concentrations. Twenty samples were analyzed for its PGE, sulphur, nickel and copper concentrations (see Table C9 for which samples was chosen). The samples chosen were representative of all lithostratigraphic rock units found in the Kemi Intrusion. About half the samples (eight) are from the profile across the small chromitite layer and the surrounding peridotites (There was not enough powdered material from the small chromitite layer for this procedure, so only the peridotites surrounding the small layer were analyzed).

Five grams from each sample was placed in a glass bottle, labelled and sent to Quebec University to be analyzed by ICP-MS.

# 4 Petrography and description of the Kemi Intrusion

## 4.1 Country rock granites

The floor rocks to the Kemi Intrusion consist of Archaean granites. The granites are phaneritic, holocrystalline and hypidiomorphic equigranular. The dominant phase is K-feldspar which is coarse-grained (2 – 5 mm) and subhedral in shape. Medium-grained, subhedral quartz (0.1 – 2 mm) is also abundant. Some grains show deformation features (undulose extinction, grain boundary-migration and sub-grain rotation). There are also some recrystallised euhedral quartz grains which occur in small veins. Coarse-grained plagioclase (~ 3 mm) is present and some of the grains show hydrothermal alteration features (sericite is present). Biotite is present as anhedral to subhedral grains and is fine-grained (0.1 to 1 mm) in size.

## 4.2 Kemi Intrusion

### 4.2.1 Basal bronzitites and peridotites

The lowest unit of the intrusion is composed of bronzitites and peridotites. They are heavily altered and deformed (Figure 4c) but the cumulate textures are still visible (Figure 4a). These rocks are holocrystalline, phaneritic, coarse-grained (2 - 5 mm), equigranular and are meso- to adcumulates. The dominant phase is orthopyroxene; it is present in excess of 65% modal abundance in the bronzitites. The orthopyroxene grains show a bastite texture, which indicates hydrous alteration (Wicks and Whittaker, 1977). They are subhedral in shape, and show exsolution lamellae of clinopyroxene (Figure 4a and 4c). The intercumulus material consists of a rim of chlorite (fibrous and pale green in colour), epidote and/or clinozoite (granular and anomalous blue or yellow interference colours) with a core of amorphous material (anomalous brown interference colours and dark grey to black in cross polarized light). The amorphous core is not always present. The intercumulus material present (25% modal abundance) is interpreted as saussuritized plagioclase (Figure 4d). The The rest of the rock consists of euhedral medium-grained (0.1 – 1 mm) chromite grains. The grains only occur in the intercumulus material, not as inclusions in the cumulate grains. This suggests that the orthopyroxene grains crystallized first followed by the plagioclase and the chromite (Figure 4a and 4c).

### 4.2.2 Main chromitite layer

The main economic chromitite layer (Figure 5) lies above the basal bronzitites and peridotites. It consists of 90% chromite (modal abundance) with the rest composed of serpentine and chlorite (Figure 5). The rock is phaneritic, holocrystalline and inequigranular (medium-grained, subhedral silicate phases of 0.5 – 3mm in size with finer-grained, euhedral chromite grains of 0.1 – 1mm in size). The main silicate phase has been totally altered to serpentine and chlorite, but it was probably a mixture of orthopyroxene (Alapieti *et al*., 1989) and olivine (the mesh texture is clearly visible). There are a few chromite grains in the silicate phases. This suggests that the chromite grains crystallized first followed by the silicate phases which incorporated some of the chromite grains as inclusions.

### 4.2.3 Upper peridotites

The chromitite layer is overlain by a 550 meter thick sequence of peridotites with a number of thin (5 cm to 2.5 meters) chromitite interlayers. Thin-sections SL-08 through to SL-13 and SL-17 through to SL-32 (the detailed profile across a small chromitite layer) are from this sequence. Most of the samples have been altered but SL-12 and -13 (Figures 6g, j, k and l) still have some original material preserved. These rocks are phaneritic, holocrystalline and are meso- to adcumulates. The dominant phase is olivine (estimated at around 60% modal abundance) and occurs as euhedral, coarse-grained (2 – 5 mm) crystals with abundant irregular fractures (Figure 6a and 6b). Most of the olivines have been completely altered to serpentine (Figure 6d). The dominant type of serpentine present is lizardite (Wicks and Whittaker, 1977; Wicks *et al*. 1977). The altered olivine shows a mesh texture (Figure 6c). It consists of a collection of irregular polygonal cells. Each cell has a central core of relict olivine or serpentine (depending on degree of alteration) and each central core is surrounded by a rim of serpentine (sometimes fibrous). These serpentine mesh rims follow the original irregular cracks of the grain or the grain boundaries. Orthopyroxene is also present but not as a prominent cumulus phase (25% modal abundance). The orthopyroxene grains are sub- to euhedral and 3 – 6 mm in size. The orthopyroxene grains are not as altered as the olivines but some grains do show a bastitic texture (Figure 6e and 6f).

The intercumulus material is saussuritized plagioclase. It appears the same as the intercumulus material in the basal bronzitites. The chlorite -epidote rim is only present when olivine borders the intercumulus material. When orthopyroxene borders the intercumulus material, there is no chloritic rim, and only the amorphous brown material is present (Figure 6g and 6h).

There are two opaque phases present. The larger (~ 0.1 – 0.5 mm) euhedral grains are chromite. The chromites only occur in the orthopyroxene grains and surround the olivine crystals (which suggest that the olivine crystallized first) (Figures 6a, b and i). Magnetite grains (anhedral, fine-grained, < 0.1 mm) are associated with the serpentinisation of olivine. Magnetite occurs as veinlets concentrated in the serpentine mesh rims or as cross-cutting lenses (of the mesh rims) which can be seen in Figure 6j.

A number of the olivine and orthopyroxene grains have reaction rims. When bordering the plagioclase, olivine showed a thin double rim of amphibole. The outer rim consists of granular subhedral amphibole (not always present) and the inner rim of very fine grained fibrous amphibole (Figure 6k). Both rims are less than 0.1 mm in width. Occasionally, large laths (> 0.1 mm) of amphibole are present in the rims (possible recrystallised grains of the inner rim?). When olivine borders orthopyroxene there is only an inner rim of very fine grained amphibole, or no rim at all (Figure 6l). There are no rims between the orthopyroxene grains. Olivine crystallized first with chromite, followed by interstitial orthopyroxene and lastly plagioclase.

### 4.2.4 Upper bronzitites

On top of the upper peridotite sequence is a bronzitite (SL-14) layer. This bronzitite is similar to the basal bronzitites. However, the upper bronzitite contains more orthopyroxene (75% modal abundance), less plagioclase (10% modal abundance) and minor olivine (5% modal abundance). The orthopyroxenes are generally coarser-grained; ranging from 3 – 7 mm in size as opposed to 2 – 5 mm in the lower meta-bronzitites. The olivines are anhedral and coarse-grained (1 – 4mm). The olivine has been almost totally replaced by serpentine and magnetite and only the cores of the olivine grains are preserved. Some of the grains have incomplete amphibole rims (Figure 7). The intercumulus material is saussuritized plagioclase, of broadly similar appearance as that in the peridotites (i.e., the chlorite-epidote rim is only present when olivine borders the intercumulus material).

### 4.2.5 Websterites

Overlaying the upper bronzitite layer is a websterite sequence (SL-15 and SL-16). These rocks are phaneritic, holocrystalline, equigranular and are meso- to adcumulates. The dominant phase is clinopyroxene, present in 60% modal abundance. The clinopyroxene are coarse-grained (2 – 5 mm) and are subhedral to euhedral in shape. Some of the clinopyroxene grains appear zoned; the core includes exsolution lamellae while the rim does not (Figure 8a, 8b and 8c). The other main phase is orthopyroxene (present in 25% modal abundance). The orthopyroxene grains are relatively coarse-grained (> 5 mm). The orthopyroxene grains

are sub- to anhedral and exsolution lamellae are present. The clinopyroxene grains show a bastitic texture, where they have been altered to serpentine. Some of the clinopyroxene grains show rims like the olivines in upper peridotites (Figures 6k and 8c). The larger anhedral orthopyroxene grains appear to surround the smaller clinopyroxene grains and some of the orthopyroxene crystals appear to have been recrystallised. The intercumulus material appears to be saussuritized plagioclase (Figure 8d). It consists of fine-grained (~ 0.1 mm) epidote and clinozoite. There are no chromite grains.

### 4.2.6 Gabbronorites and leucogabbros

Samples of these rocks were too small to allow powders for analyses and thin-sections to be made. However, petrographic descriptions of the gabbroic units can be found in Alapieti *et al*. (1989) and are briefly summarized in the following: At about 1 000 meters above the basal contact of the intrusion, overlying the websterite sequence, plagioclase reached cumulus status phase alongside augite. This rather monotonous plagioclase $\pm$ pyroxene cumulate (the gabbronorite and leucogabbro layers) continues upwards for 800 m to the contact with the hanging wall. In the upper part of this sequence the Ca-rich pyroxene occurs as the intercumulus phase, marking the transition from the gabbronorites to the leucogabbros.

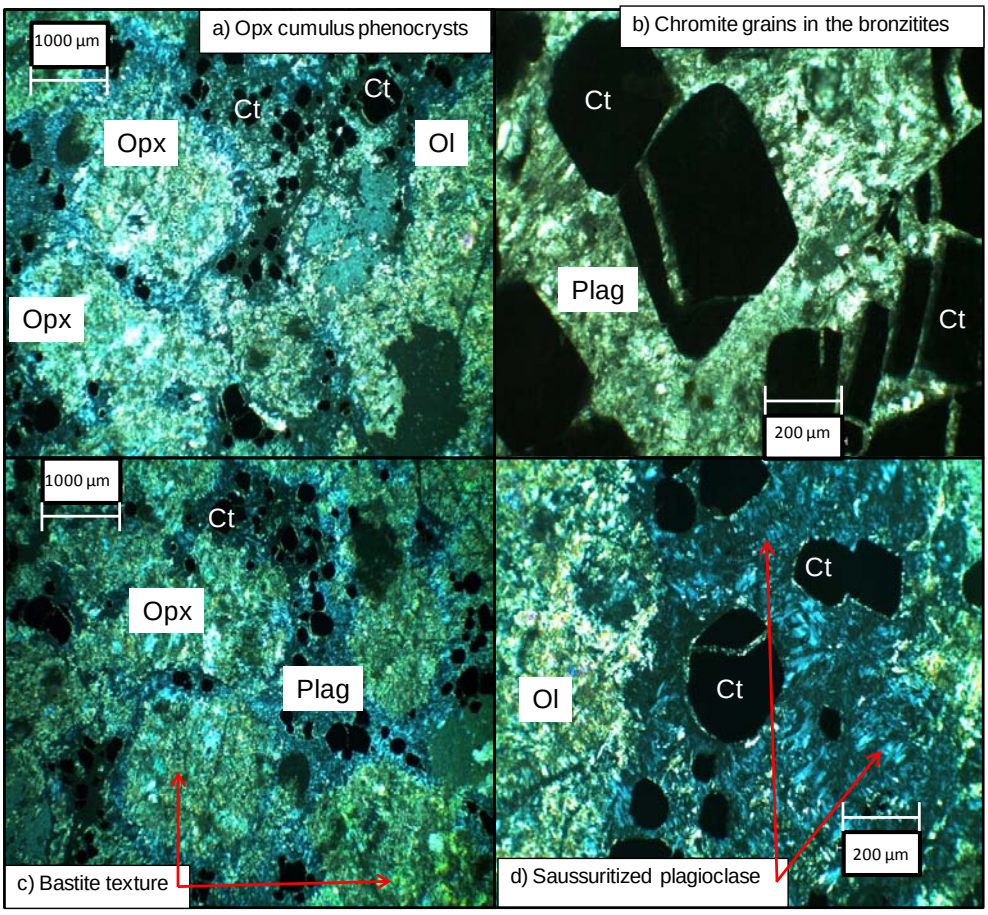


**Figure 4:** The Basal silicates: a) SL-07 taken at 2.5x magnification under cross-polar light (XPL) showing the cumulus orthopyroxene (Opx) and olivine (Ol) phenocrysts in the bronzitites. Also note the chromite (Ct) grains surrounding the cumulus orthopyroxene and olivine phenocrysts; b) SL-05 taken at 10x magnification under XPL showing the chromitite grains in the bronzitites; c) SL-07 taken at 2.5x magnification under XPL showing the bastite texture in the orthopyroxene phenocrysts and d) SL-07 taken at 10x magnification under XPL showing the saussuritized intercumulus plagioclase (Plag).

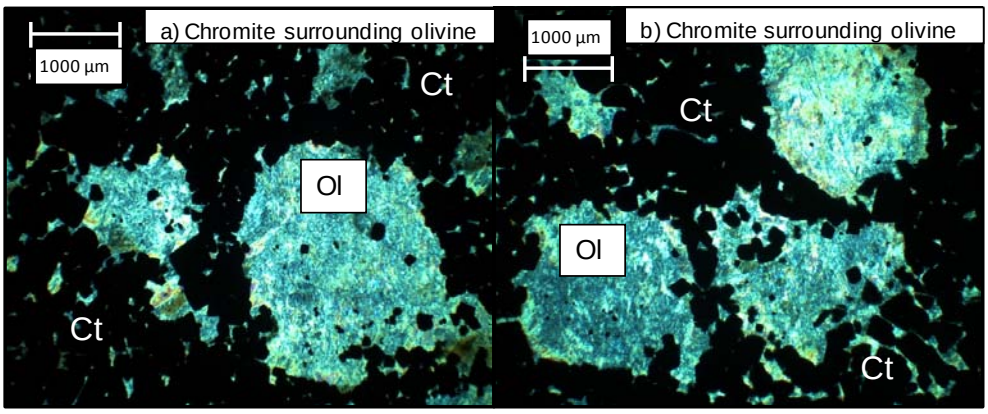


**Figure 5:** Main chromitite layer: a) SL-06a and b) SL-06b taken at 2.5x magnification under XPL showing the chromitite grains surrounding the olivine phenocrysts (note the mesh structures).

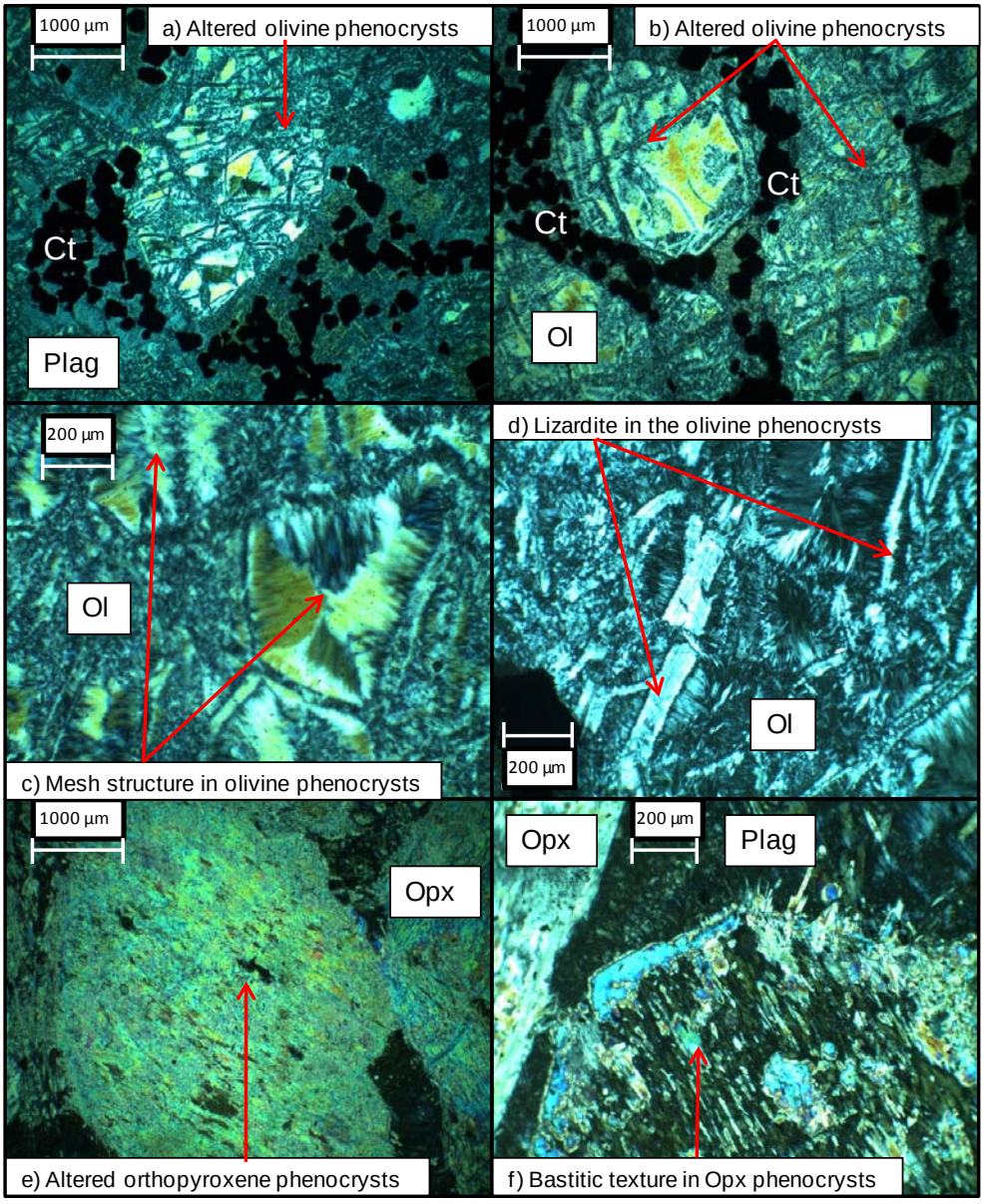


**Figure 6:** Upper peridotites: a) SL-08 taken at 2.5x magnification under XPL showing the altered olivines with abundant irregular cracks; b) SL-08 taken at 2.5x magnification under XPL showing the altered olivine surrounded by small chromitite crystals; c) SL-08 taken at 10x magnification under XPL showing the mesh structure in the altered olivines; d) SL-08 taken at 10x magnification under XPL showing lizardite; e) SL-09 taken at 2.5x magnification under XPL showing the altered orthopyroxene phenocrysts and f) SL-09 taken at 10x magnification under XPL showing the bastitic texture in the altered orthopyroxene phenocrysts.

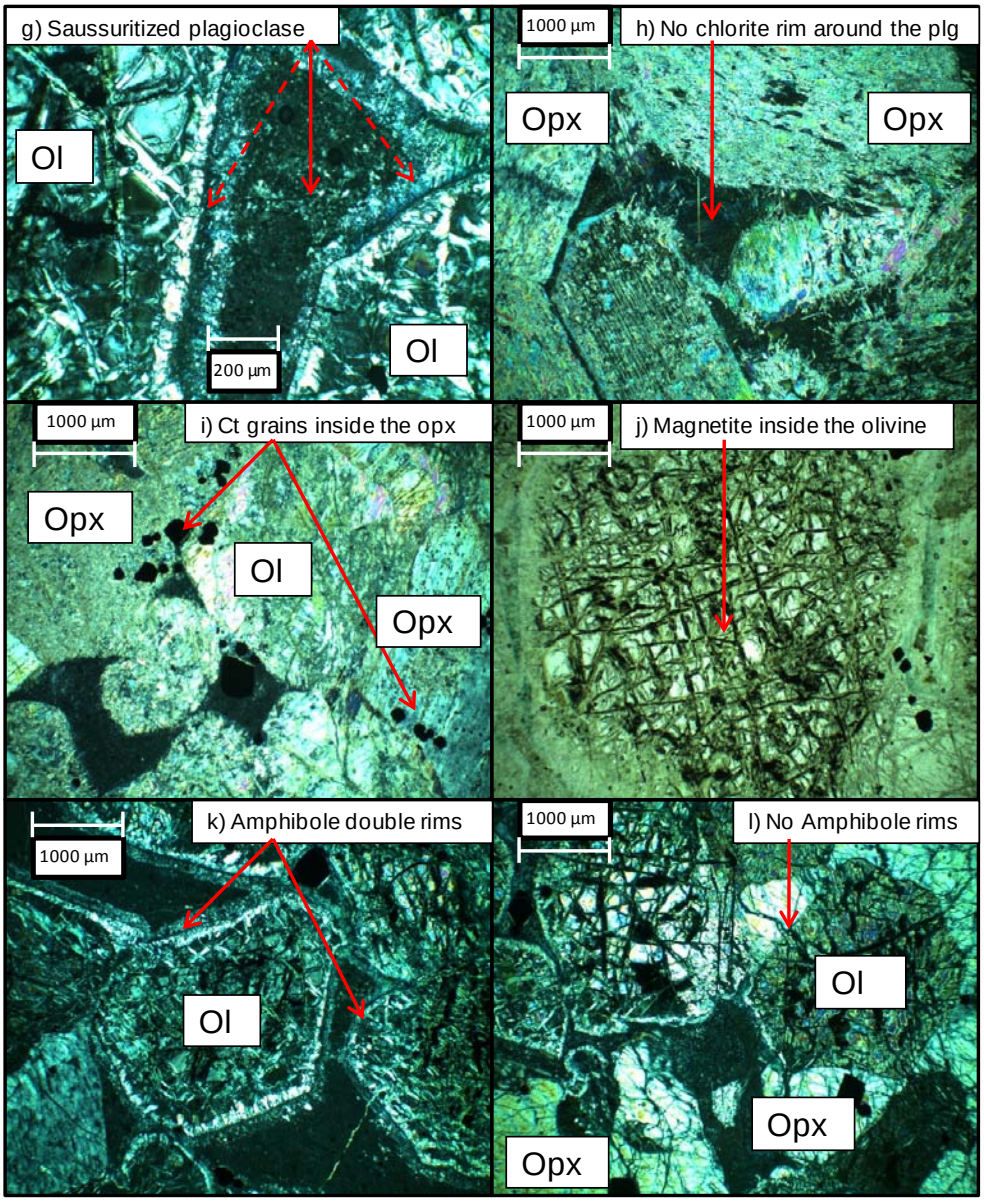


**Figure 6 continued:** Upper peridotites: g) SL-12 taken at 10x magnification under XPL showing the saussuritized intercumulus plagioclase with chlorite – epidote rim (dashed arrows); h) SL-09 taken at 2.5x magnification under XPL showing the saussuritized intercumulus plagioclase without chlorite – epidote rim and cumulus orthopyroxene phenocrysts; i) SL-10 taken at 2.5x magnification under XPL showing the chromitite grains occurring in the orthopyroxene phenocrysts but not the olivines; j) SL-12 taken at 2.5x magnification under plain polar light (PPL) showing the alteration product magnetite occurring as veinlets concentrated around the cracks in the olivines; k) SL-12 taken at 2.5x magnification under XPL showing the double amphibole rim surrounding the olivines and l) SL-12 taken at 2.5x magnification under XPL showing the lack of double amphibole rims surrounding the orthopyroxenes.

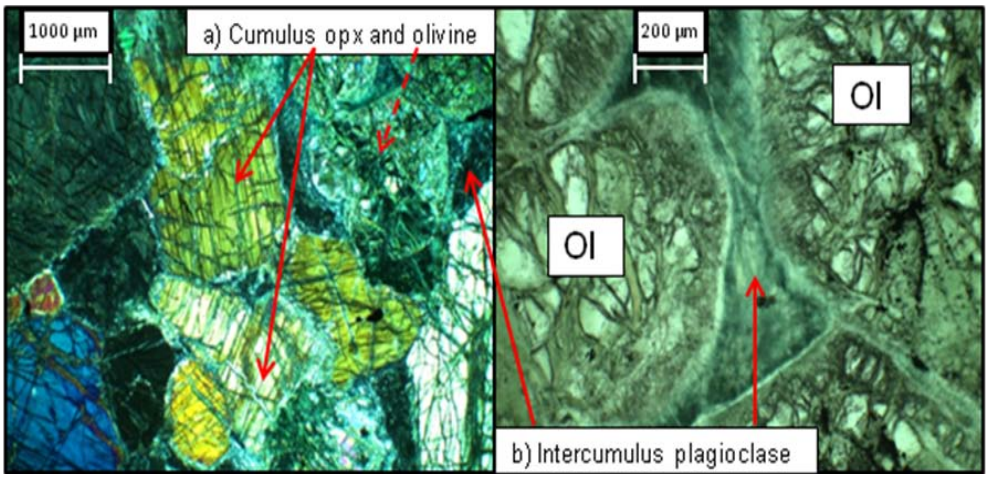


**Figure 7:** Upper bronzitites: a) SL-13 taken at 2.5x magnification under XPL showing cumulus orthopyroxene and olivine phenocrysts (totally altered to serpentine, dashed arrow) and the saussuritized intercumulus plagioclase and b) SL-13 taken at 10x magnification under PPL showing the olivine phenocrysts and saussuritized intercumulus plagioclase.

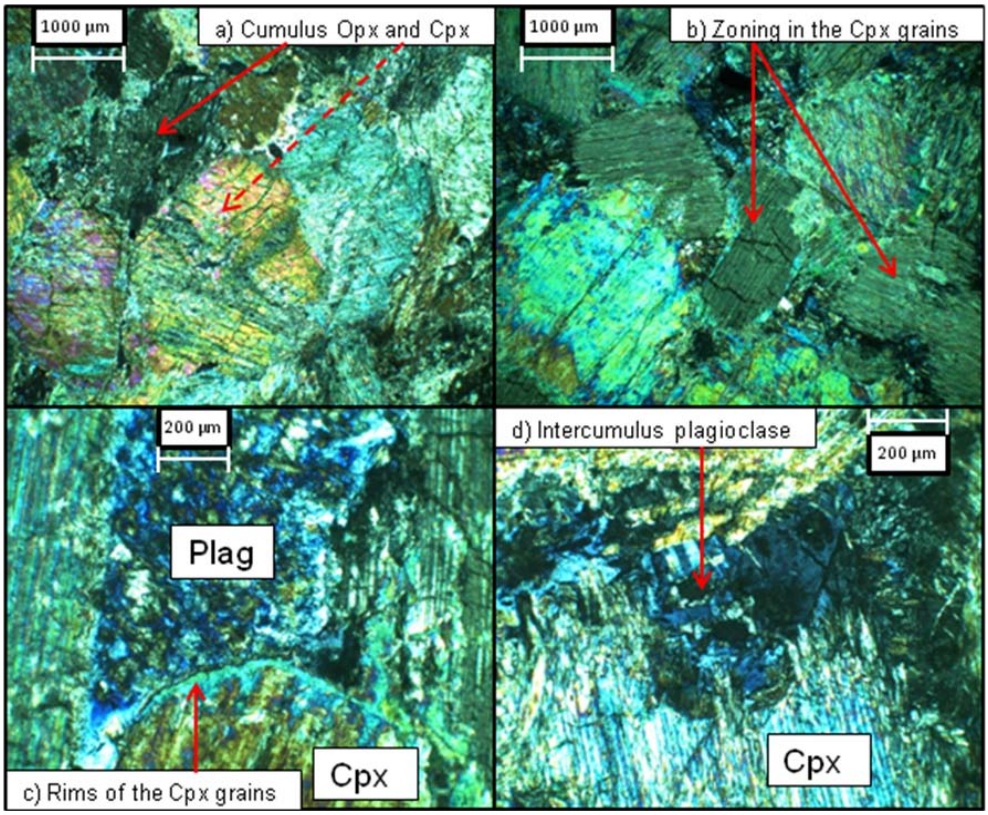


**Figure 8:** Websterites: a) SL-15 taken at 2.5x magnification under XPL showing the cumulus ortho- and clinopyroxene (cpx, dashed arrows); b) SL-16a taken at 2.5x magnification under XPL showing the exsolution lamellae in the clinopyroxene cores; c) SL-16a taken at 10x magnification under XPL showing the rims of the clinopyroxene grains and d) SL-15 taken at 10x magnification under XPL showing the saussuritized intercumulus plagioclase. The relict albite twinning structure is still visible.

# 5 Results

The full analytical results for the Kemi samples are tabulated in Appendix C. Table 3 summarize the key data from the Kemi Intrusion (the small chromitite and the surrounding peridotites have been left out). The uncertainties, errors and the results for the blanks, standards and duplicate sample values are recorded in Appendix D.

The major element analyses are shown in Table C1. Of the forty-three XRF analyses, twenty have acceptable totals between 98.5 and 101.5. The remaining XRF analyses are split into two groups. Eleven analyses (chromitites and peridotites) have totals ranging from 54 to 98, well below the acceptable range. The second group consists of twelve analyses (peridotites and gabbros) with totals ranging from 101.8 to 103. The low totals of the chromitite and peridotite samples can be explained by two factors. The analytical procedure of the XRF spectrometer cannot determine the $Cr_2O_3$ concentrations of the samples at such high concentrations. They contain as much as 4 % Cr (Table C6) or 6 weight percentage (wt %) $Cr_2O_3$. Secondly, not all the chromites were dissolved in the flux during the preparation of the fusion disks (the disks contained small black chromite grains). Since the missing chromium was taken into account in the correction procedure the major element results of the samples with low totals are deemed valid (Marsh, pers. comm.). The high totals of the second group of analyses (peridotites and gabbros) are due to the flux absorbing moisture from the air during the preparation of the fusion disks. Taking this into account the major element results from these samples are acceptable (Marsh, pers. comm.).

The major element analyses were normalized due to the high loss of ignition (LOI) values (Table C2). They were recalculated on a LOI-, $H_2O$-, $Cr_2O_3$- and NiO-free (the set-up of the XRF spectrometer did not allow it to detect the NiO content of the fusion disks) basis. Whole rock major element contents (Table C6) was obtained using an ICP-AES at Stellenbosch University. The set-up of the ICP-AES detector did allow it to detect the Cr content (ppm) of the samples. The major element data was recalculated again with the Cr content (converted to $Cr_2O_3$ weight percentage) but there was a negligible difference in values between the two sets of normalized major element results. The LOI-, $H_2O$-, $Cr_2O_3$- and NiO-free recalculated results are the basis for all the figures that show major element results.

**Table 3:** Key whole rock geochemical data from the Kemi Intrusion. The small chromitite and the surrounding peridotites have been left out. * indicate values below the detection limits. See Appendix C for full results.

| Sample | Rock-type | MgO (wt %) | CaO (wt %) | Cr (ppm) | Cu (ppm) | S (ppm) | Ir (ppb) | Ru (ppb) | Rh (ppb) | Pt (ppb) | Pd (ppb) | $\varepsilon^{2.44}$Nd | $La/Sm_{C1}$ | Zr (ppm) |
|---|---|---|---|---|---|---|---|---|---|---|---|---|---|---|
| SL 04 | Bronzitite | 24.56 | 4.56 | 25323 | - | - | - | - | - | - | - | - | 3.40 | 10.7 |
| SL 05 | Bronzitite | 31.32 | 5.41 | 32366 | * | * | 7.6 | 34.8 | 4.6 | 11.6 | 11.7 | -1.6 | 2.94 | 20.0 |
| SL 07 | Bronzitite | 36.17 | 1.48 | 18942 | * | * | 9.9 | 51.7 | 4.4 | 2 | 2.5 | -1.5 | 2.29 | 5.1 |
| SL 06 | Chromitite | 35.52 | 0.04 | 24597 | * | 60 | 94.1 | 162.9 | 11.9 | 9.5 | 33.4 | -7.2 | 1.53 | 2.3 |
| SL 08 | Peridotite | 33.88 | 1.68 | 28871 | - | - | - | - | - | - | - | - | 2.75 | 5.1 |
| SL 09 | Peridotite | 23.77 | 9.66 | 2159 | 26.4 | 33 | 3.8 | 0.7 | 15.2 | 106.8 | 25.9 | -1.8 | 2.56 | 33.0 |
| SL 10 | Peridotite | 28.47 | 5.71 | 4831 | - | - | - | - | - | - | - | - | 1.77 | 5.3 |
| SL 11 | Peridotite | 30.75 | 4.32 | 2684 | 17.4 | 294 | 0.7 | 0.8 | 1.5 | 6 | 26.3 | - | 2.13 | 4.1 |
| SL 12 | Peridotite | 32.51 | 3.72 | 4077 | - | - | - | - | - | - | - | - | 1.62 | 6.4 |
| SL 38 | Peridotite | 32.87 | 2.36 | 955 | 20.5 | 164 | 1.7 | 1 | 2.3 | 6.2 | 3.3 | -8 | 1.60 | 6.8 |
| SL 13 | Bronzitite | 29.08 | 4.06 | 2782 | - | - | - | - | - | - | - | - | 1.80 | 3.2 |
| SL 14 | Bronzitite | 28.83 | 4.88 | 3627 | 31.9 | 92 | 1.4 | 0.5 | 2.9 | 14 | 8.3 | -1.2 | 2.60 | 16.7 |
| SL 15 | Websterite | 18.90 | 14.11 | 4013 | - | - | - | - | - | - | - | - | 2.50 | 13.3 |
| SL 16 | Websterite | 18.82 | 15.53 | 4171 | 20.9 | 28 | 0.9 | 0.2 | 2.1 | 15.9 | 11.2 | -1 | 1.13 | 9.3 |
| SL 39 | Gabbronorite | 13.88 | 15.56 | 1972 | 14.4 | 46 | 0.5 | 0.2 | 1.2 | 3.6 | 3.8 | -8.8 | 1.57 | 4.3 |
| SL 40 | Gabbronorite | 14.44 | 9.55 | 1307 | - | - | - | - | - | - | - | - | 1.85 | 8.5 |
| SL 41 | Gabbronorite | 14.67 | 12.26 | 842 | - | - | - | - | - | - | - | - | 1.86 | 6.6 |
| SL 42 | Gabbronorite | 12.18 | 14.93 | 1003 | 10.4 | 53 | 0.3 | 0.1 | 0.6 | 4.5 | 2.8 | -7.7 | 1.48 | 6.4 |
| SL 43 | Leucogabbro | 7.00 | 13.90 | 159 | - | - | - | - | - | - | - | - | 2.17 | 3.4 |
| SL 44 | Leucogabbro | 13.73 | 8.37 | 23 | - | - | - | - | - | - | - | - | 1.49 | 3.7 |
| SL 45 | Leucogabbro | 10.15 | 15.82 | 422 | 27.4 | 232 | 0.3 | 0.2 | 0.5 | 1.6 | 2.7 | - | 1.46 | 3.5 |
| SL 46 | Leucogabbro | 1.52 | 15.83 | 53 | - | - | - | - | - | - | - | -5.3 | 2.19 | 6.8 |
| SL 47 | Leucogabbro | 8.71 | 8.41 | 691 | 161.2 | 244 | 0.2 | 0.2 | 0.2 | 5.6 | 2 | -10.1 | 2.63 | 16.0 |
| SL 48 | Leucogabbro | 11.45 | 12.17 | 958 | - | - | - | - | - | - | - | - | 1.77 | 9.0 |

The minor and trace element analyses are shown in Table C3 while Table D2 shows the minor and trace element analyses of various standards. The analyses of the standards show negligible differences to their recommended contents.

The rare earth element analyses are shown in Table C5 while Table D3 shows the rare earth element analyses of the standard BHVO2. The analyses of the standard show negligible differences to their recommended contents. Three samples (a peridotite, websterite and a leucogabbro) were analysed in triplicate (Tables D6 and D7). Table D8 these results which show minor differences between the various Sm and Nd results.

Table C7 lists the $^{143}Nd/^{144}Nd$ isotopic analyses from the selected samples. The constants used to calculate the $\varepsilon_{Nd}$ are shown in Table B5. The $^{147}Sm/^{144}Nd$ ratios were calculated from the Sm and Nd concentrations of the samples and the natural abundance of $^{147}Sm$ in Sm and $^{144}Nd$ in Nd. Given the error built in from the ICP-MS Nd and Sm concentration data, plus the fact that separate sample aliquots were used for elemental concentrations and for isotope ratios, the error introduced by not using the measured isotopic compositions should fall within the overall uncertainty. To calculate the error values for the $\varepsilon_{Nd}$ (Appendix D) the errors on the Nd and Sm were first calculated based on six duplicate analyse (Table D8). The errors for the $^{143}Nd/^{144}Nd$ ratios were based on the duplicate isotopic analyses on standard Jndi 1 (Table D9). The error values for the $\varepsilon_{Nd}$ (Table D10) are an acceptable 0.8 epsilon unit on average (Figure 41). The only sample that had a large $\varepsilon_{Nd}$ error is that of the main chromitite layer sample (SL-06).

Table C9 shows the PGE analyses and Table D11 shows the PGE analyses of the standards BB-235 and AMIS-0005. The PGE results of the standards were within an acceptable range of their recommended contents. Samples SL-11 and -14 through to -47 have osmium concentrations that are below the detection limits (0.31 ppm). For these samples the osmium concentrations were assumed to be at most 0.31 ppm for the sake of the primitive mantle-normalized PGE diagrams.

The errors were deemed acceptable for most of the results and are not discussed further. In the instances where the errors are of significance they are discussed in the relevant sections that follow.

Appendix A describes the technique used to calculate the stratigraphic height of each sample above or below the basal contact of the

Kemi Intrusion. Tables 4 and 5 summarize the stratigraphic height of the samples.

**Table 4:** A summary of the rock-types and stratigraphic height (strat height) of the samples above (or below) the basal contact of the Kemi Intrusion. The samples from the small chromitite layer and surrounding peridotites are excluded.

| Sample | Rock - type | Strat height | Sample | Rock - type | Strat height |
|---|---|---|---|---|---|
| **SL 01** | Granite | -66.06 | **SL 14** | Bronzitite | 790.85 |
| **SL 02** | Granite | -47.84 | **SL 15** | Websterite | 906 |
| **SL 03** | Granite | -21.82 | **SL 16** | Websterite | 959.67 |
| **SL 04** | Bronzitite | 6.00 | **SL 39** | Gabbronorite | 1020.24 |
| **SL 05** | Bronzitite | 9.08 | **SL 40** | Gabbronorite | 1117.85 |
| **SL 07** | Bronzitite | 51.13 | **SL 41** | Gabbronorite | 1223.51 |
| **SL 06** | Chromitite | 90.01 | **SL 42** | Gabbronorite | 1317.95 |
| **SL 08** | Peridotite | 161.55 | **SL 43** | Leucogabbro | 1399.15 |
| **SL 09** | Peridotite | 157.24 | **SL 44** | Leucogabbro | 1464.63 |
| **SL 10** | Peridotite | 244.31 | **SL 45** | Leucogabbro | 1555.13 |
| **SL 11** | Peridotite | 343.79 | **SL 46** | Leucogabbro | 1646.76 |
| **SL 12** | Peridotite | 445.68 | **SL 47** | Leucogabbro | 1761.69 |
| **SL 38** | Peridotite | 488.61 | **SL 48** | Leucogabbro | 1849.9 |
| **SL 13** | Bronzitite | 691.65 | | | |

**Table 5:** A summary of the rock-types and stratigraphic height (strat height) of the samples from the small chromitite layer and the surrounding peridotites of the Kemi Intrusion.

| Sample | Rock - type | Strat height |
|---|---|---|
| **SL 17** | Peridotite | 140.36 |
| **SL 18** | Peridotite | 139.77 |
| **SL 19** | Peridotite | 139.1 |
| **SL 20** | Peridotite | 138.45 |
| **SL 21** | Peridotite | 137.84 |
| **SL 22** | Peridotite | 137.44 |
| **SL 23** | Peridotite | 137.2 |
| **SL 24** | Chromitite | 137.01 |
| **SL 25** | Peridotite | 136.28 |
| **SL 26** | Peridotite | 135.85 |
| **SL 27** | Peridotite | 135.19 |
| **SL 28** | Peridotite | 134.61 |
| **SL 29** | Peridotite | 133.96 |
| **SL 30** | Peridotite | 133.35 |
| **SL 31** | Peridotite | 132.7 |
| **SL 32** | Peridotite | 131.93 |

## 5.1 Major element concentrations

The major element analyses are shown in Tables C1 and C2. The variations in the major element concentrations plotted against the stratigraphic height are shown in Figure 9. The $SiO_2$ contents show a constant range throughout the intrusion (ranging from 46 to 55 weight percentage, wt %), with the exception of the main chromitite horizon (21 wt %) and the surrounding silicates (low 40's wt %). FeO and MgO show similar trends. Elevated FeO and MgO occur at the base of the intrusion (above 6 wt % for FeO and 18 wt % for MgO) while the gabbroic rocks contains relatively lower FeO and MgO contents (below 6 wt % for FeO and 15 wt % for MgO). The $TiO_2$ and MnO contents show roughly similar trends to the FeO and MgO trends. Rocks with elevated $TiO_2$ and MnO occur at the base of the intrusion. The CaO and $Al_2O_3$ wt % trends are opposite to the FeO and MgO trends with a few minor differences. The websterites have elevated CaO (15 wt % CaO) and the gabbroic rocks have prominent CaO and $Al_2O_3$ (8 wt % CaO and over 13 wt % $Al_2O_3$).

Some of the major oxide data for the rocks together with appropriate mineral compositions taken from the literature are plotted in Figure 10. A decrease in MgO corresponds to an increase in $SiO_2$, $Al_2O_3$ and CaO. The FeO vs CaO and $SiO_2$ plots (Figure 11) show a similar trend of decreasing MgO and corresponding increases in CaO and $SiO_2$. The FeO vs $Al_2O_3$ plot suggests two trends: the ultramafic rocks exhibit a decrease in FeO at constant $Al_2O_3$ while the gabbroic rocks show an increase in $Al_2O_3$ and decreasing FeO. The $Al_2O_3$ vs CaO plot (Figure 11) shows two sub-groups. The bronzitites, peridotites and chromitites have relatively low $Al_2O_3$ and CaO (both lower than 10 wt %). The second group are the websterites and gabbros with relatively high $Al_2O_3$ and CaO (both are higher than 10 wt %).

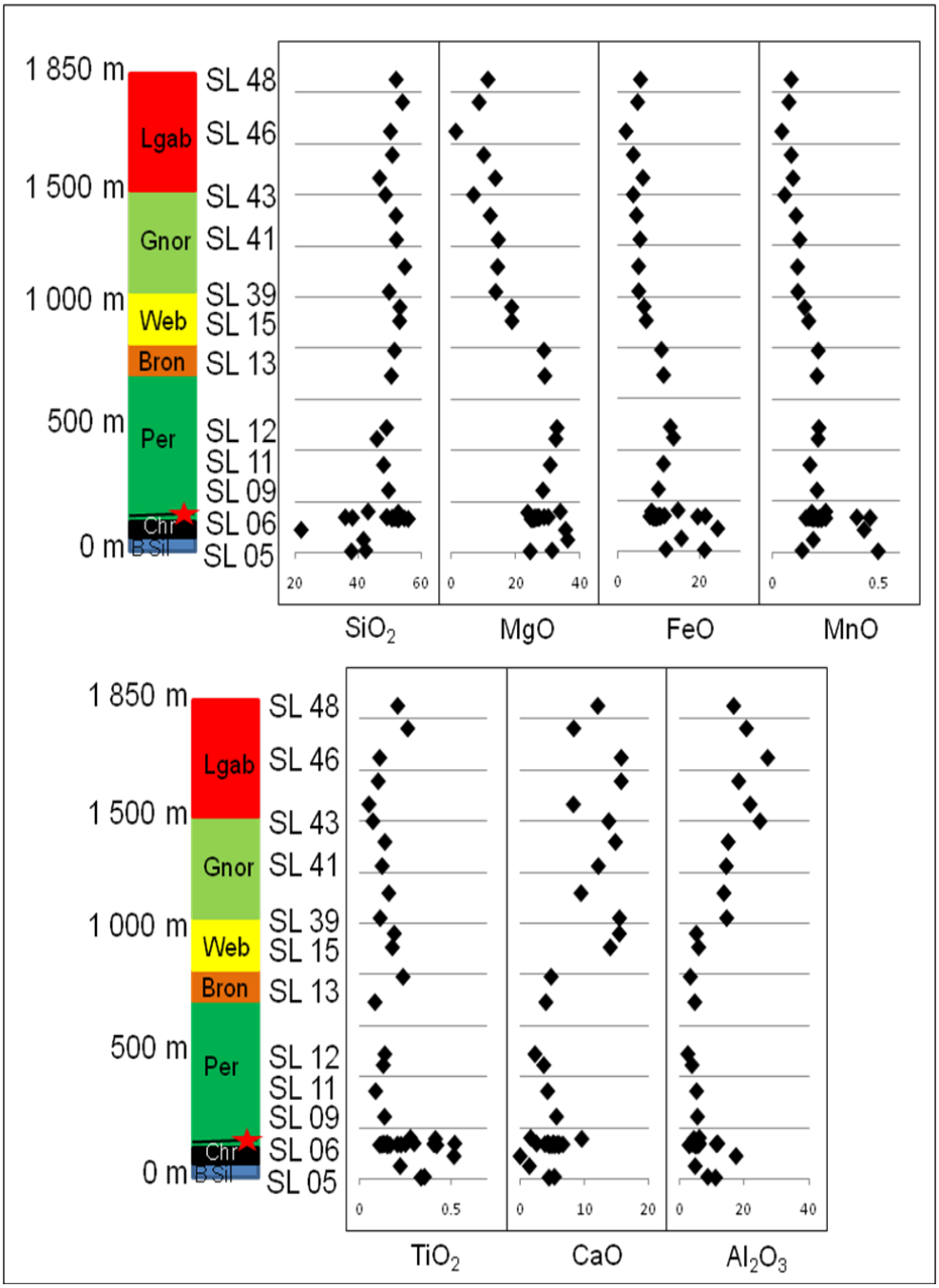


**Figure 9:** Variations of the major elements in weight percentages (wt %) with stratigraphic height in the Kemi Intrusion. The red star represents the stratigraphic position of the small chromitite layer and the surrounding peridotites.

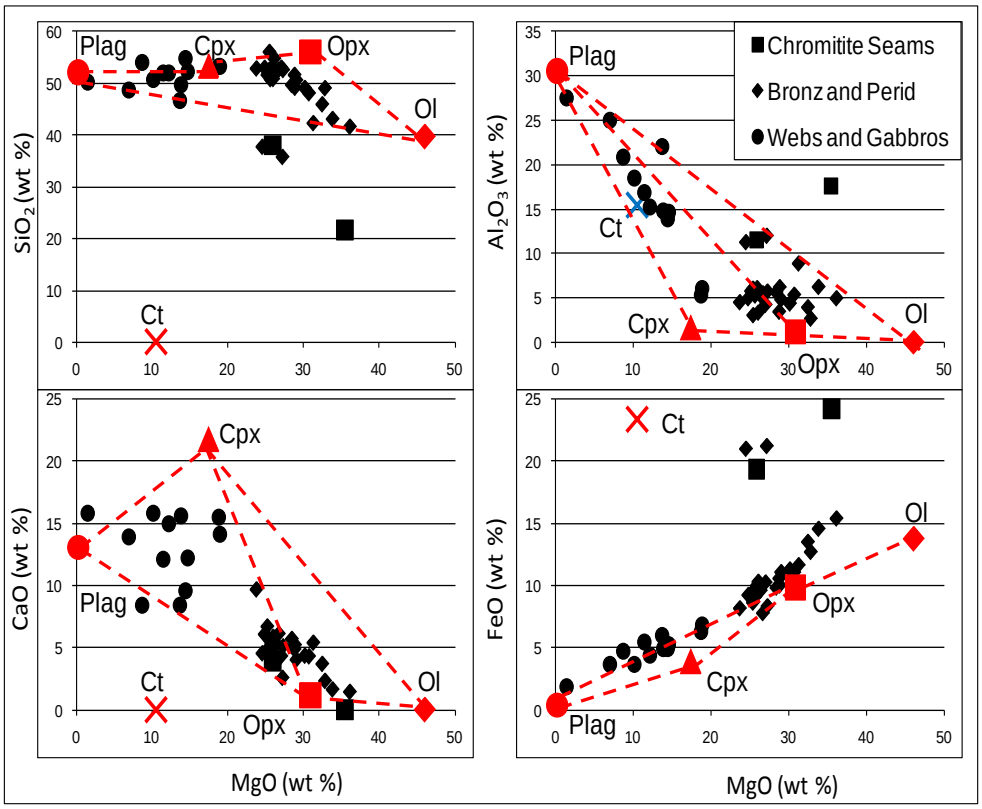


**Figure 10:** Variation diagram of MgO versus $SiO_2$, $Al_2O_3$, CaO and FeO. Also plotted are the average major element concentrations of olivine (Ol), orthopyroxene (Opx), clinopyroxene (Cpx) and plagioclase (Plag) from the Lower Zone, Critical Zone (Teigler, 1990) and Main Zone (Mitchell, 1986) of the Bushveld Complex and a weighted chromites average (Ct) from the various chromitite layers of the Kemi Intrusion (Alapieti *et al.*, 1989). Bronz - bronzitites, Perid – peridotites and Webs – websterites.

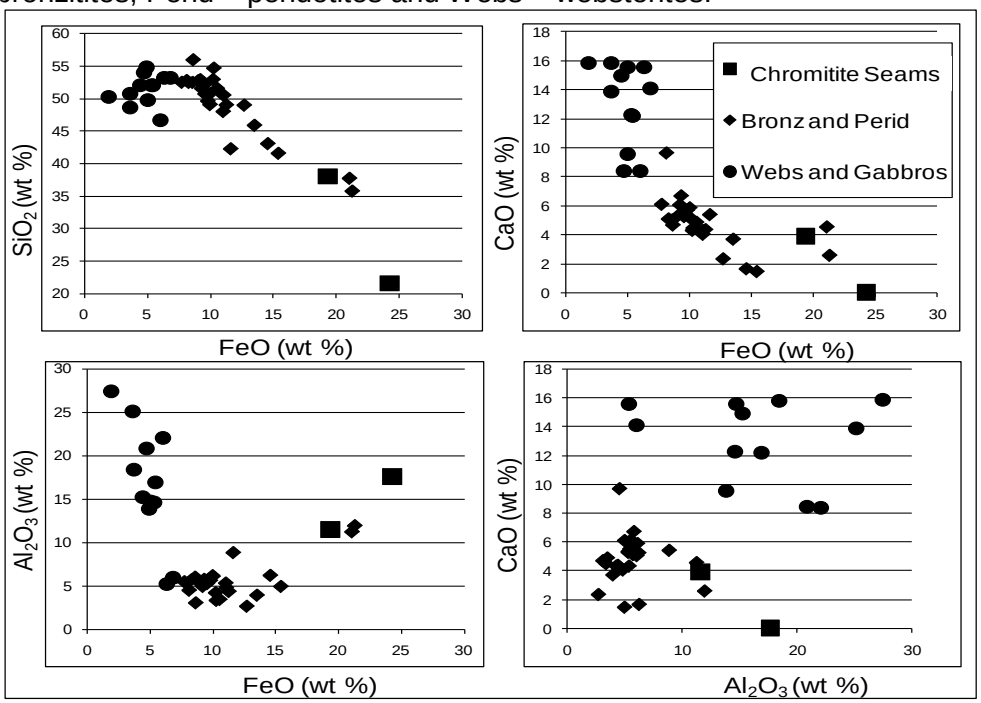


**Figure 11:** Variation diagram of FeO versus $SiO_2$, $Al_2O_3$, CaO, and $Al_2O_3$ versus CaO.

## 5.2 Minor and trace element concentrations

### 5.2.1 Incompatible elements

The incompatible element results are shown in Table C3. The binary variation diagrams of Zr, Nb and Y versus MgO (Figure 12) show that the majority of the ultramafic rocks and the mafic rocks have similar incompatible element contents (2 to 20 ppm Zr, 0.1 to 1.6 ppm Nd and 0.5 to 6 ppm Y). These concentrations are very low for mafic rocks and are a clear indication that these rocks are meso- to adcumulates. The exception to this trend is a small number of upper peridotites which have slightly higher concentrations of these elements which suggests that these rocks have retained some of their residual liquid.

The primitive mantle normalized incompatible element profiles (Figure 13) show different trends for the ultramafic and mafic rocks. The bronzitites and peridotites have fractionated trends that decrease from Rb to Yb, with negative Nb anomalies. The websterites lack the negative Nb anomalies but do have positive Eu anomalies. The gabbros show a decrease from Rb to Yb, except for strong positive Sr and Eu anomalies.

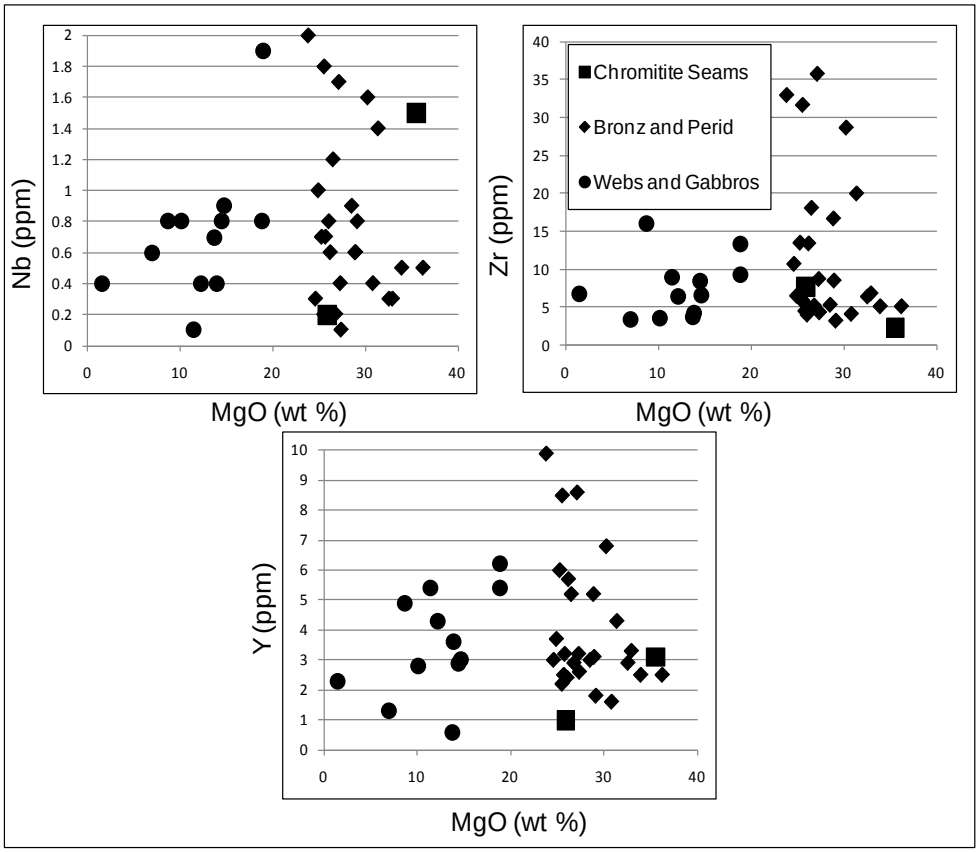


**Figure 12:** Variation diagram of Zr, Nb and Y versus MgO.

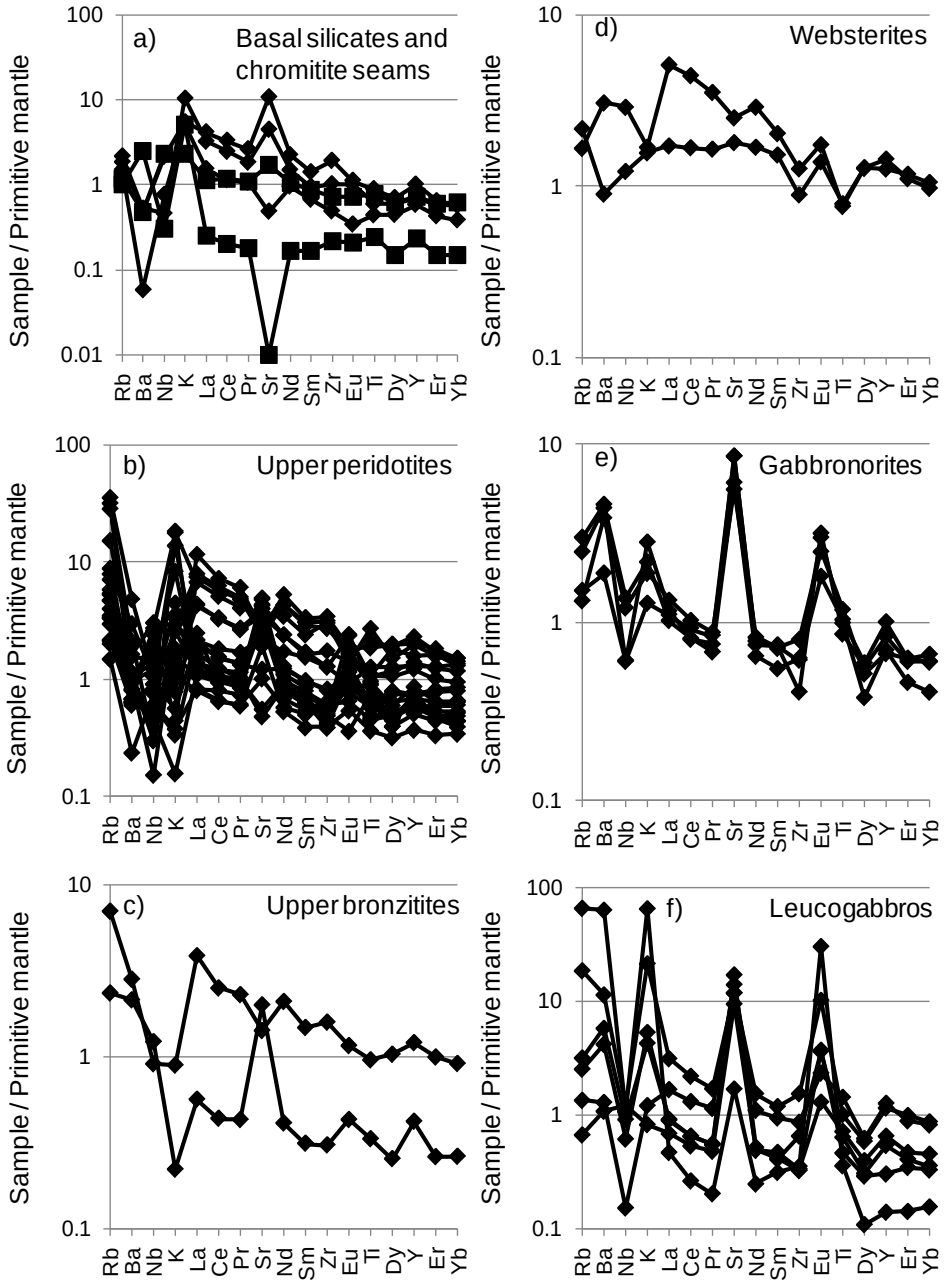


**Figure 13:** Primitive mantle-normalized incompatible element diagrams for (a) the basal silicates (diamonds) and chromitite layers (squares), (b) the upper peridotites, (c) the upper bronzitites, (d) the websterites, (e) the gabbronorites, and (f) the leucogabbros. Normalizing values from McDonough and Sun (1995); see Table C4.

### 5.2.2 Rare earth elements

Results of the REE analyses are shown in Table C5. The chondrite-normalized REE profiles (Figure 14) of the ultramafic and mafic rocks are LREE-enriched. The bronzitites and peridotites have negative slopes from La to Yb ($La/Yb_{C1}$ ratios range from 2 to 7). The ultramafic rocks show positive and negative Eu anomalies. The websterites do not show Eu

anomalies. The gabbros have lower $La/Sm_{C1}$ ratios than the ultramafic rocks ($La/Yb_{C1}$ ratios range from 1 to 4) and they show strong positive Eu anomalies.

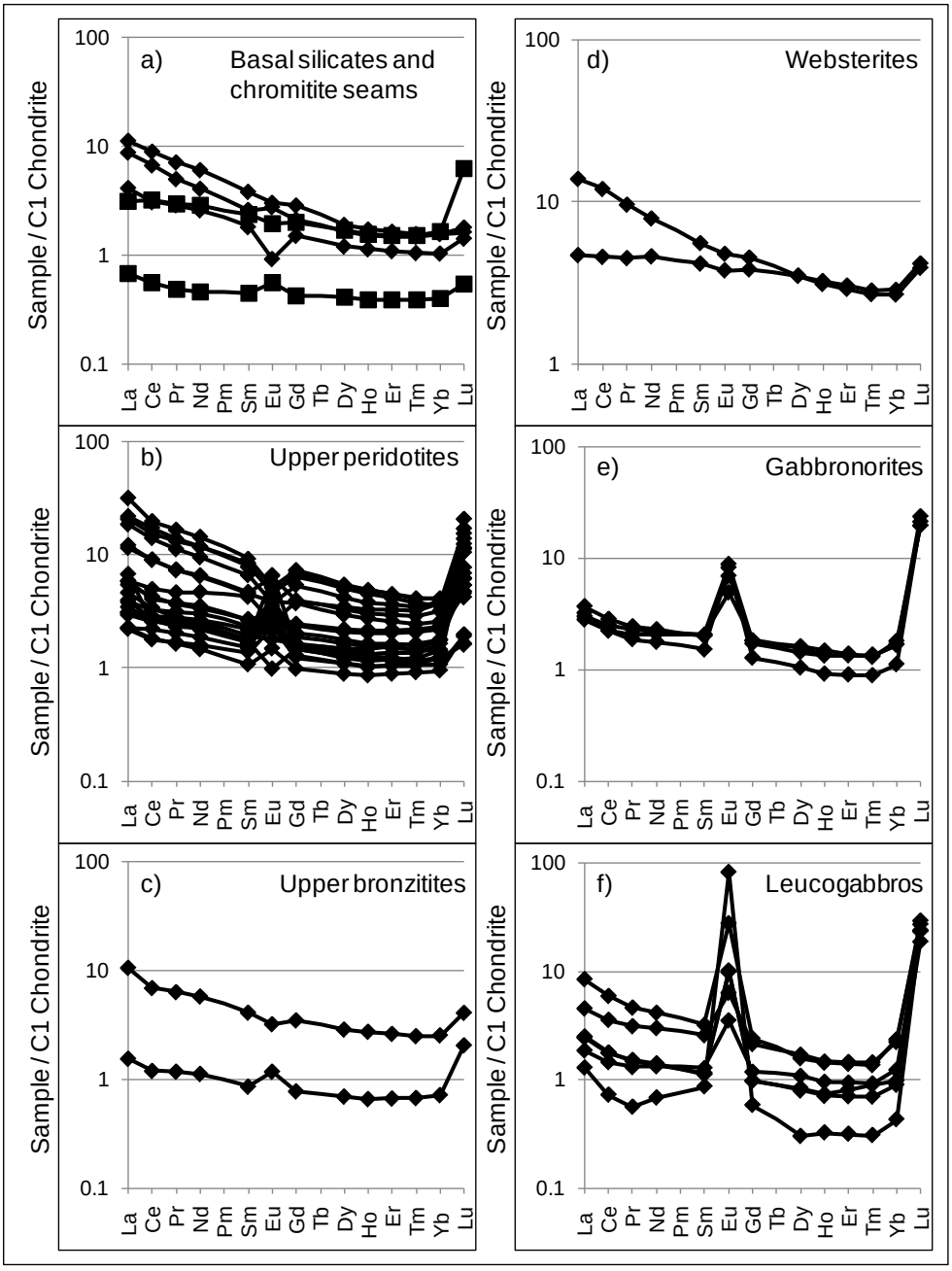


**Figure 14:** C1 chondrite-normalized rare earth element diagrams for (a) the basal silicates (diamonds) and chromitite layers (squares), (b) the upper peridotites, (c) the upper bronzitites, (d) the websterites, (e) the gabbronorites, and (f) the leucogabbros. Normalizing values from McDonough and Sun (1995).

All the REE profiles show enriched $Lu_{C1}$ values and the mafic rocks (gabbronorites and leucogabbros) show enriched $Gd_{C1}$ and $Er_{C1}$ values. Enriched $Lu_{C1}$, $Gd_{C1}$ and $Er_{C1}$ values are not found in the literature

concerning other 2.44 to 2.5 Ga Fennoscandian layered intrusion (e.g. Hanski *et al*., 2001; Iljina and Hanski, 2005). These anomalies are believed to be analytical artefacts. To calculate the Eu* values for the Eu anomalies the $Gd_{C1}$ values were not used but a weighted average of the $Sm_{C1}$ and $Dy_{C1}$ values was used (Table F2).

Figure 15 shows certain REE concentrations and $(La/Yb)_{C1}$, $(La/Sm)_{C1}$ and $(Dy/Yb)_{C1}$ ratios plotted against the stratigraphic height of the intrusion. The concentrations in the REE do not systematically increase with an increase in stratigraphic height. The ultramafic and mafic rocks show similar REE contents (majority of samples show less than 2 ppm for individual REE). However, some of the highest concentrations of REE (e.g., in excess of 4 ppm for La and Nd respectively) can be found in the lower portion of the upper peridotite assemblage. The upper bronzitites and websterites also show slightly elevated concentrations (e.g., in excess of 2 ppm for La and Nd respectively). In Figure 15 the REE ratios ($La/Yb_{C1}$, $La/Sm_{C1}$ and $Dy/Yb_{C1}$) show the same trend as the REE concentrations, both the ultramafic and mafic rocks have similar values. Again the lower portion of the upper peridotites and sections of the upper bronzitites and websterites have slightly higher values of the ratios.

### 5.3 Nd isotopic compositions

Only whole-rock Nd isotopic ratios were obtained from the samples of this study. The calculated initial $\varepsilon_{Nd}$ values at 2.44 Ga (Table C8) are plotted against the stratigraphic height in Figure 16a. The majority of the samples from the lower portion of the intrusion (the peridotites and bronzitites) have values ranging from depleted (+4) to slightly enriched (-2). The two chromitite layers and one peridotite sample have the lowest $\varepsilon_{Nd}$ in the ultramafic portion of the intrusion (ranging from –4 to –8). The samples from the mafic portion of the intrusion have enriched $\varepsilon_{Nd}$ ranging from –5 to –10. Figure 16b shows the $\varepsilon_{Nd}$ plotted against the stratigraphic height of the small chromitite layer. The lowest $\varepsilon_{Nd}$ is found in the chromitite ($\varepsilon_{Nd}$ = -4) and progressively less higher $\varepsilon_{Nd}$ occur in the peridotites distally located relative to the chromitite.

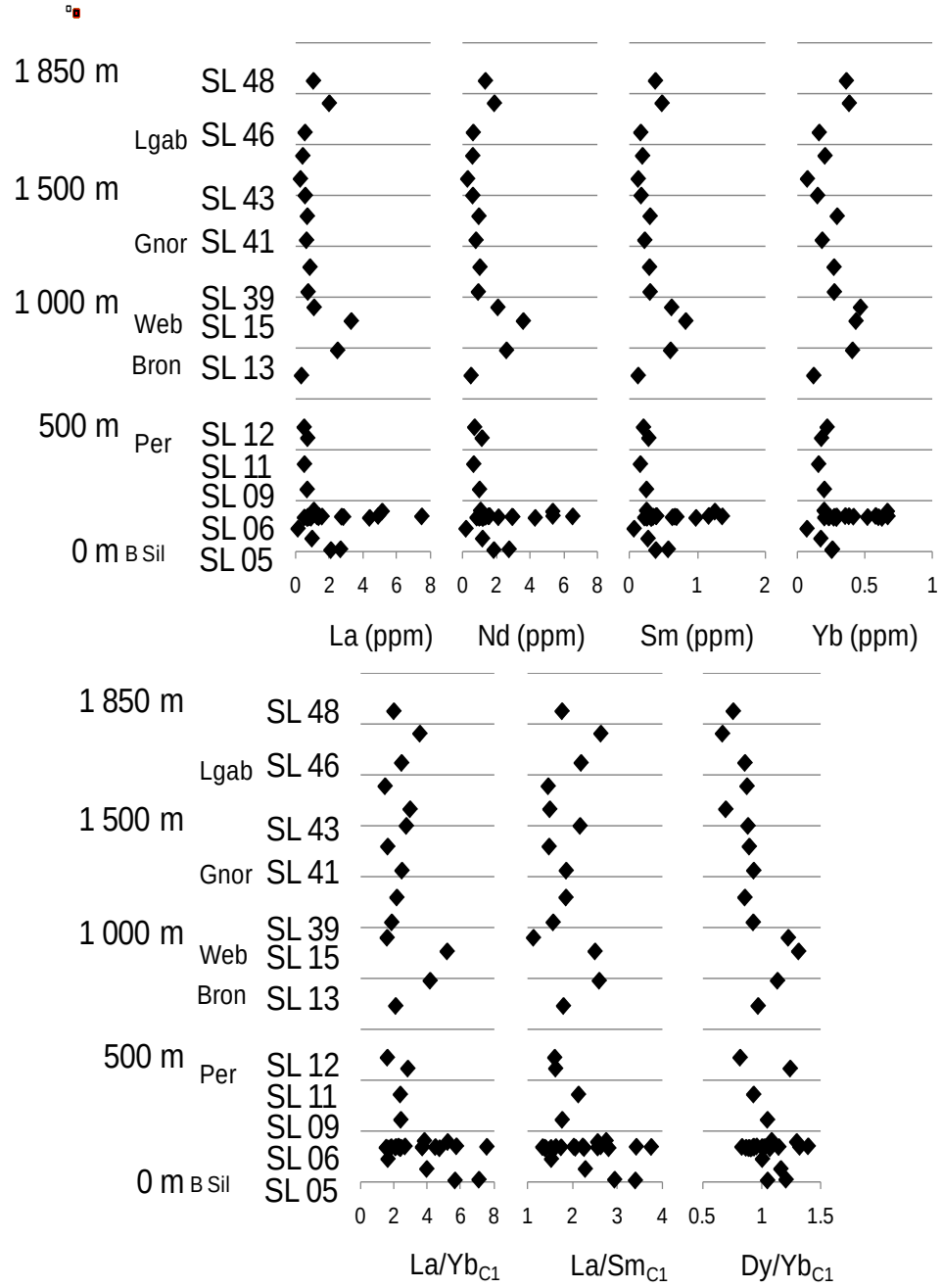


**Figure 15:** Plot of the certain REE concentrations and La/Yb$_{C1}$, La/Sm$_{C1}$ and Dy/Yb$_{C1}$ ratios versus the stratigraphic height. The red star represents the stratigraphic position of the small chromitite layer and the surrounding peridotites.

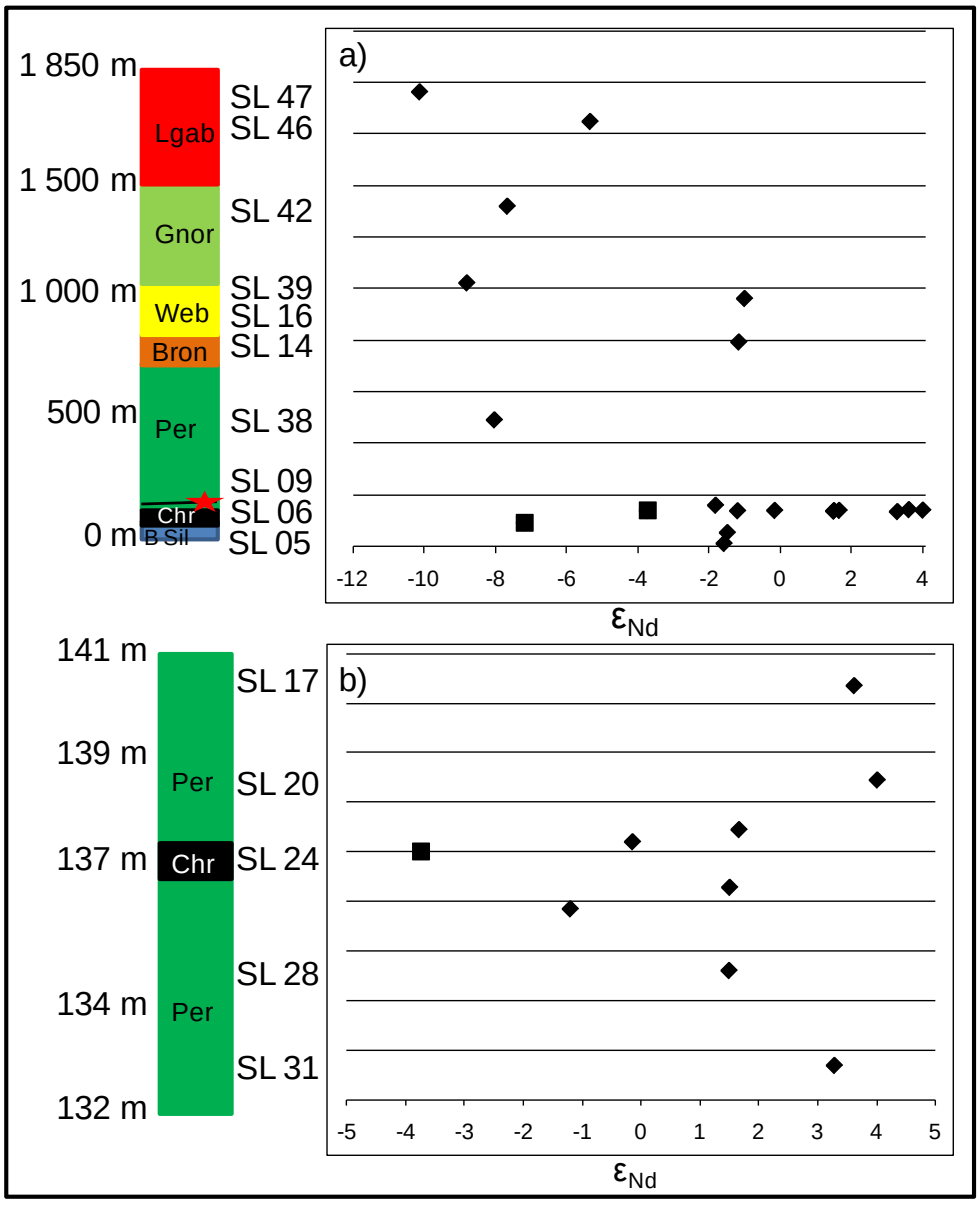


**Figure 16:** (a) Plot of the $\varepsilon_{Nd}$ versus stratigraphic height, (b) plot of the $\varepsilon_{Nd}$ across the small chromitite layer above the main chromitite layer. Diamonds represent silicate cumulates and squares chromitite samples. The red star represents the stratigraphic position of the small chromitite layer and the surrounding peridotites.

### 5.4 PGE concentrations

Concentrations of PGE are shown in Table C9. The variations in PGE, S, Cr and Cu concentration versus stratigraphic height (Figure 17) all show the same general trend. The two lowest rock units (the basal silicates and the main chromitite layer) have the highest PGE and Cr concentrations (ranging from 10 to 100 ppb for individual PGE and over 10 000 ppm for Cr). These concentrations steadily decrease with height towards the top of

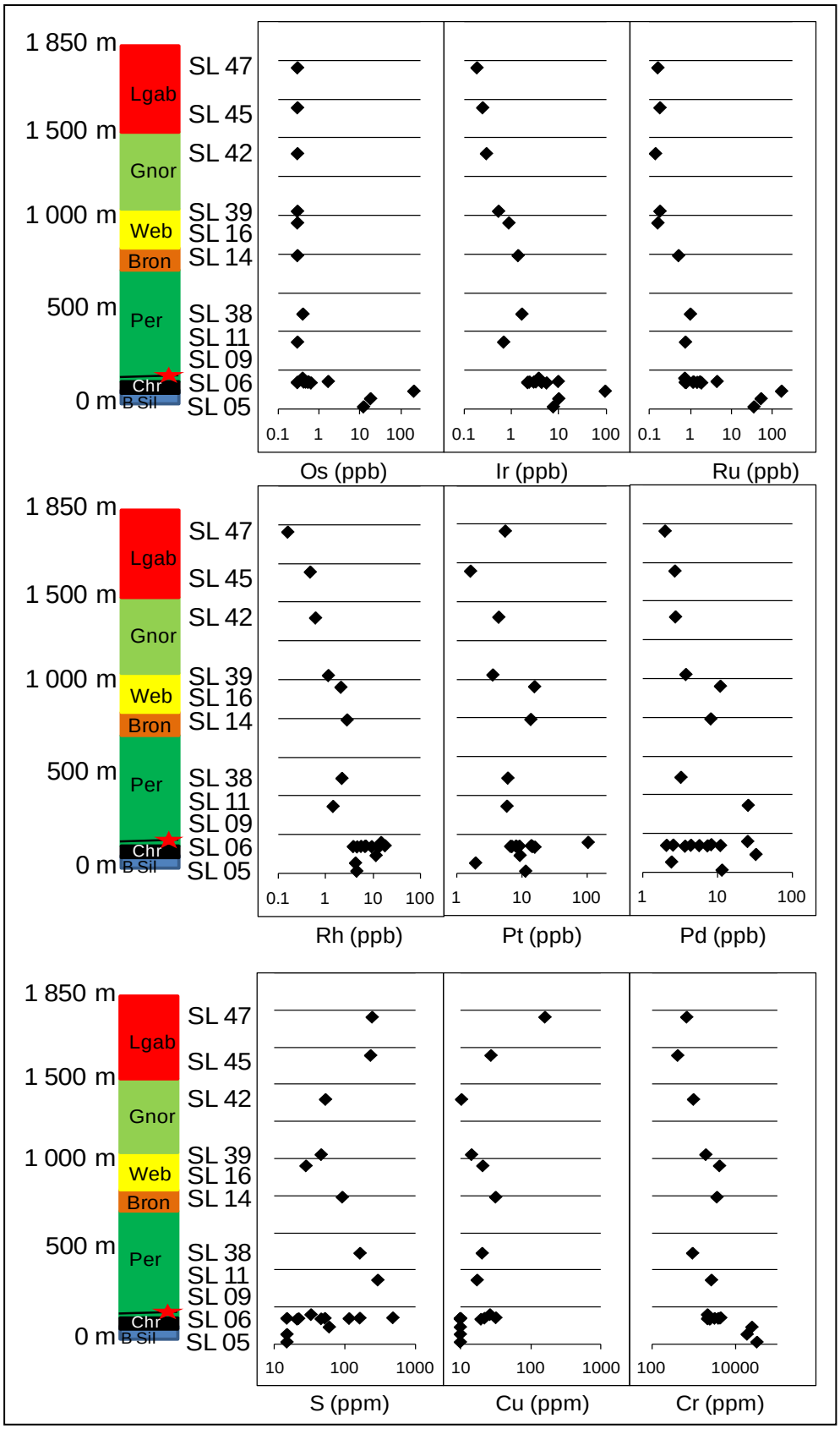


**Figure 17:** Variations of the individual PGE, S, Cu and Cr contents versus the stratigraphic height. The red star represents the stratigraphic position of the small chromitite layer and the surrounding peridotites.

the intrusion with the lowest concentrations (between 0.1 and 1 ppb for individual PGE and roughly 100 ppm for Cr) occurring in gabbros. The S and Cu contents are lowest in the basal silicates and main chromitite layer and show a broad increase towards the gabbros, although several peridotites show relatively high S and Cu contents.

Figure 18a shows the IPGE (Ir, Os and Ru), PPGE (Pt, Pd and Rh) and the total PGE concentrations versus the stratigraphic height. There is a general decrease in total PGE content from the basal peridotites (ΣPGE = 83 to 88 ppb) to the uppermost leucogabbros of the intrusion (ΣPGE = 5 to 8 ppb). However, there are two zones of relative enrichment for the PGE; the first zone (ΣPGE = 153 to 515 ppb) occurs approximately 90 to 160 m above the basal contact, beginning within and continuing above the main chromitite ore horizon. A second enrichment zone occurs about 1000 m above the basal contact (ΣPGE = 27 to 30 ppb). Figure 18a also shows a reversal between the IPGE and PPGE concentrations. In the lowest part of the intrusion (the basal silicates and the main chromitite layer) the ΣIPGE are higher than the ΣPPGE, but for the rest of the intrusion (from the upper peridotites to the gabbros) the ΣPPGE are higher than the ΣIPGE.

Figure 18b shows the variations in the ΣIPGE, ΣPPGE and ΣPGE abundances across the small chromitite layer. The peridotite samples furthest from the small chromitite layer show the highest total PGE concentrations, at over 40 ppb. The peridotite samples immediately above and below the small chromitite layer have the lowest total PGE concentrations, under 30 ppb. The same trend is identified in the ΣIPGE and ΣPPGE concentrations.

Figure 19 shows several binary variation diagrams of ΣPGE versus sulphur and other chalcophile elements. The ΣPGE, Cu and Ni show no discernable trends with S (Figure 19a). Several samples (either peridotites or gabbros) with similar ΣPGE, Cu or Ni contents show a range in S contents from roughly 50 ppm to over 500 ppm. However ΣIPGE are positively correlated with Cr.

Plots of Pt and Pd versus Cu, Pt versus Pd and Pd versus Ir (Figure 19b) show no discernable trends. Pt and Ru are positively correlated with Ir.

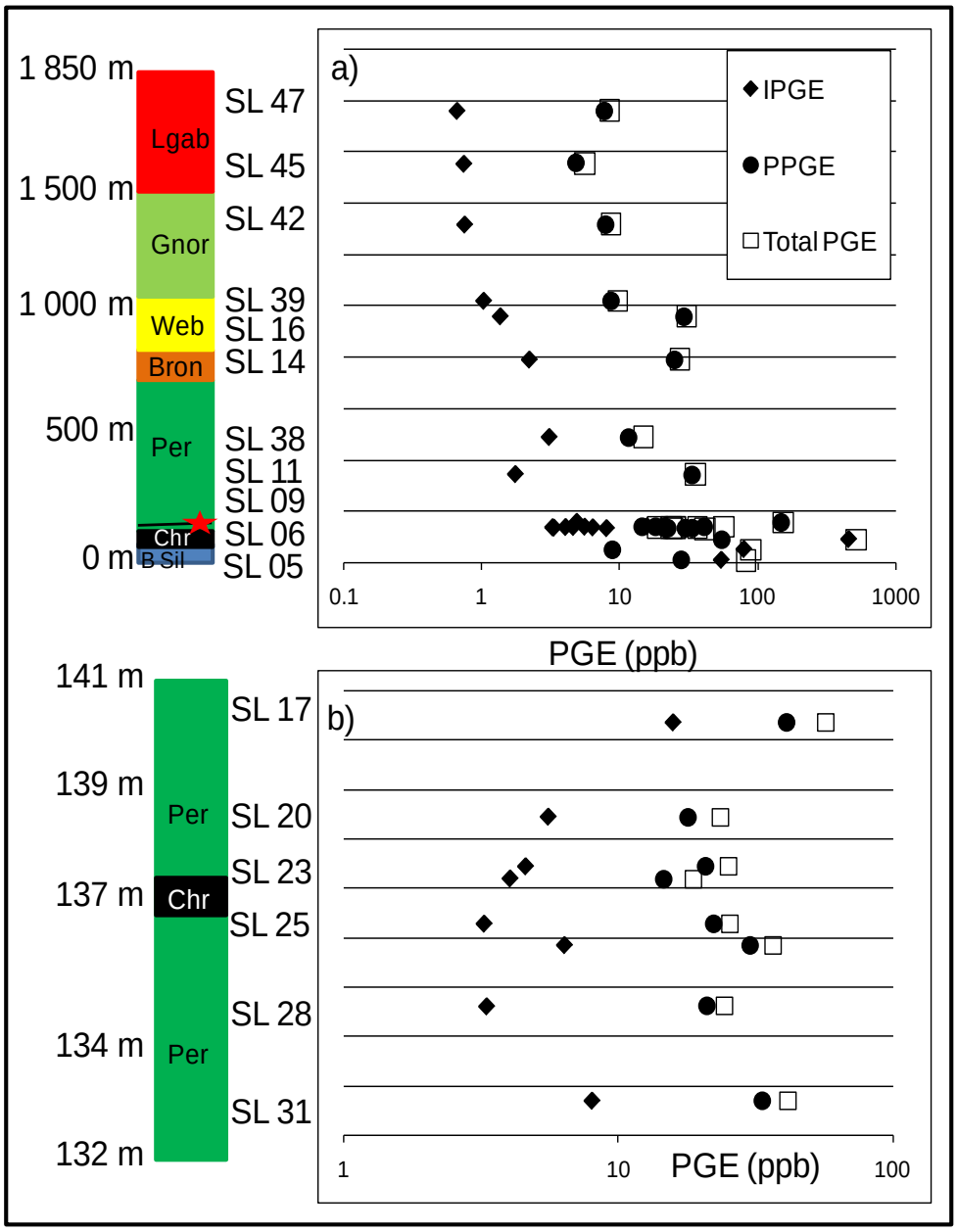


**Figure 18:** Variations in the IPGE (Ir, Os and Ru), PPGE (Pt, Pd and Rh) and the total PGE concentrations versus (a) stratigraphic height, (b) stratigraphic height across the small chromitite layer.

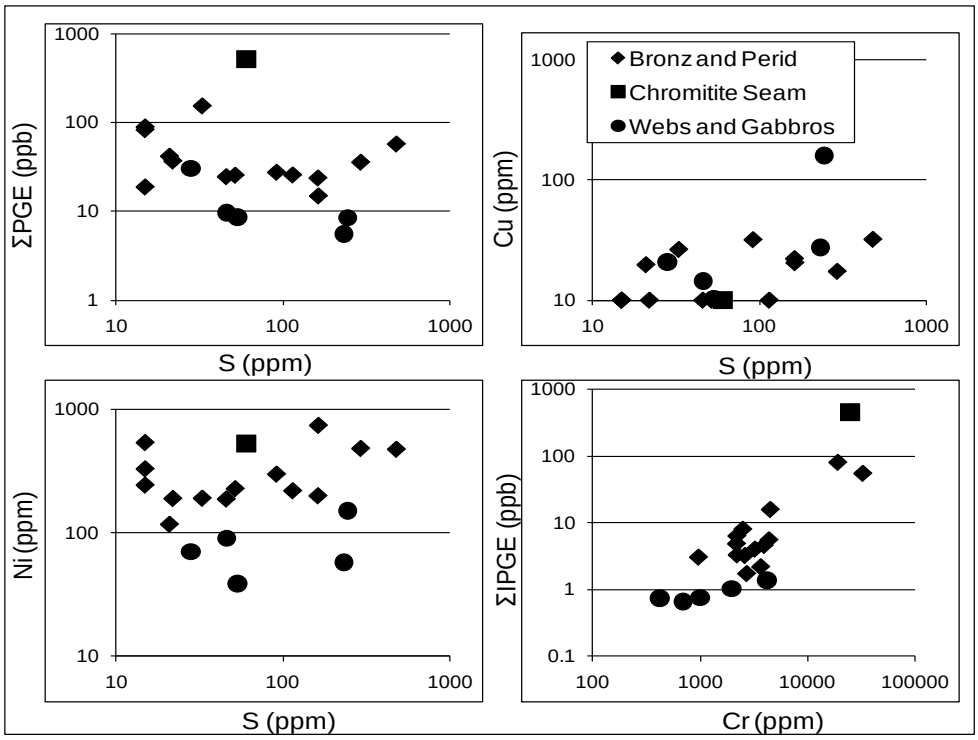


**Figure 19a:** Variation diagram of ΣPGE, Cu and Ni versus S and ΣIPGE versus Cr.

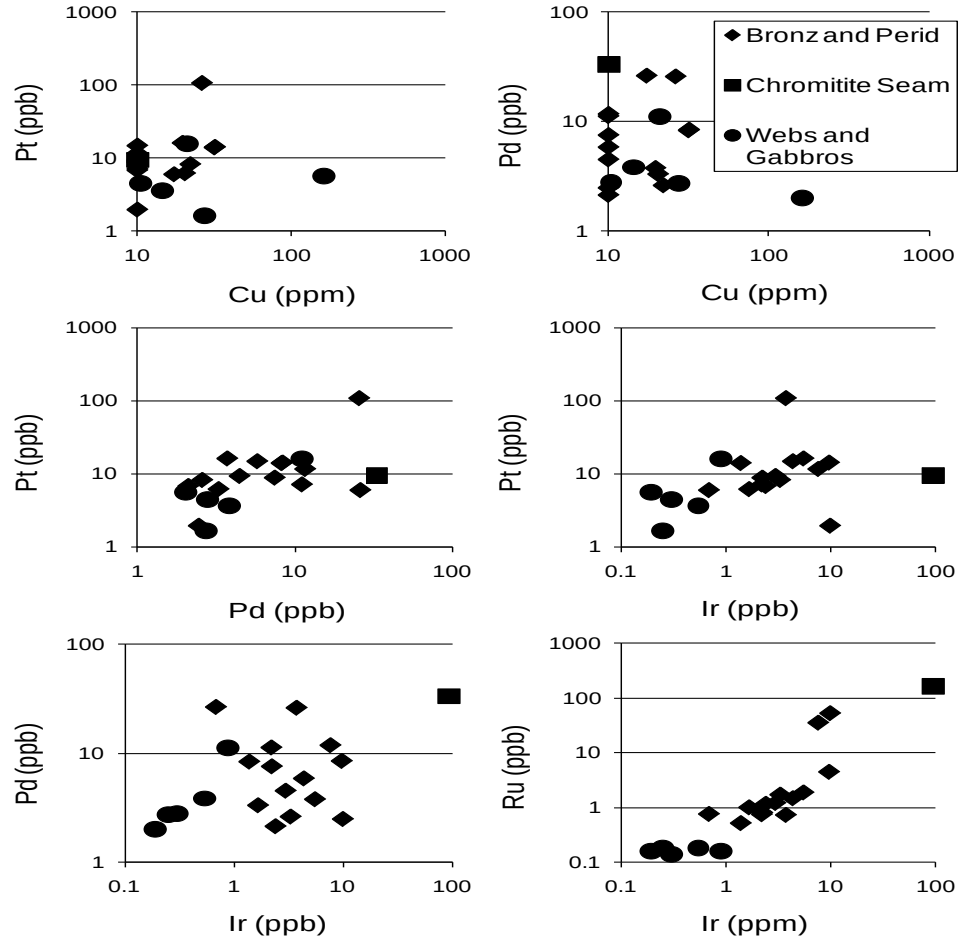


**Figure 19b:** Variation diagram of Pt and Pd Vs Cu, Pt Vs Pd and Pt, Pd and Ru Vs Ir.

The PGE / sulphur ratios (Figure 20) increase with height to the base of the websterites and then decrease with height to the top of the intrusion.

The highest ΣIPGE / sulphur ratios are found in the main chromitite layer whereas the highest ΣPPGE / sulphur ratios are found in the upper peridotites immediately above the main chromitite layer (best seen in Figure 21a). The ΣPGE / sulphur ratios show a subtle reversal at the small chromitite layer (Figure 21b).

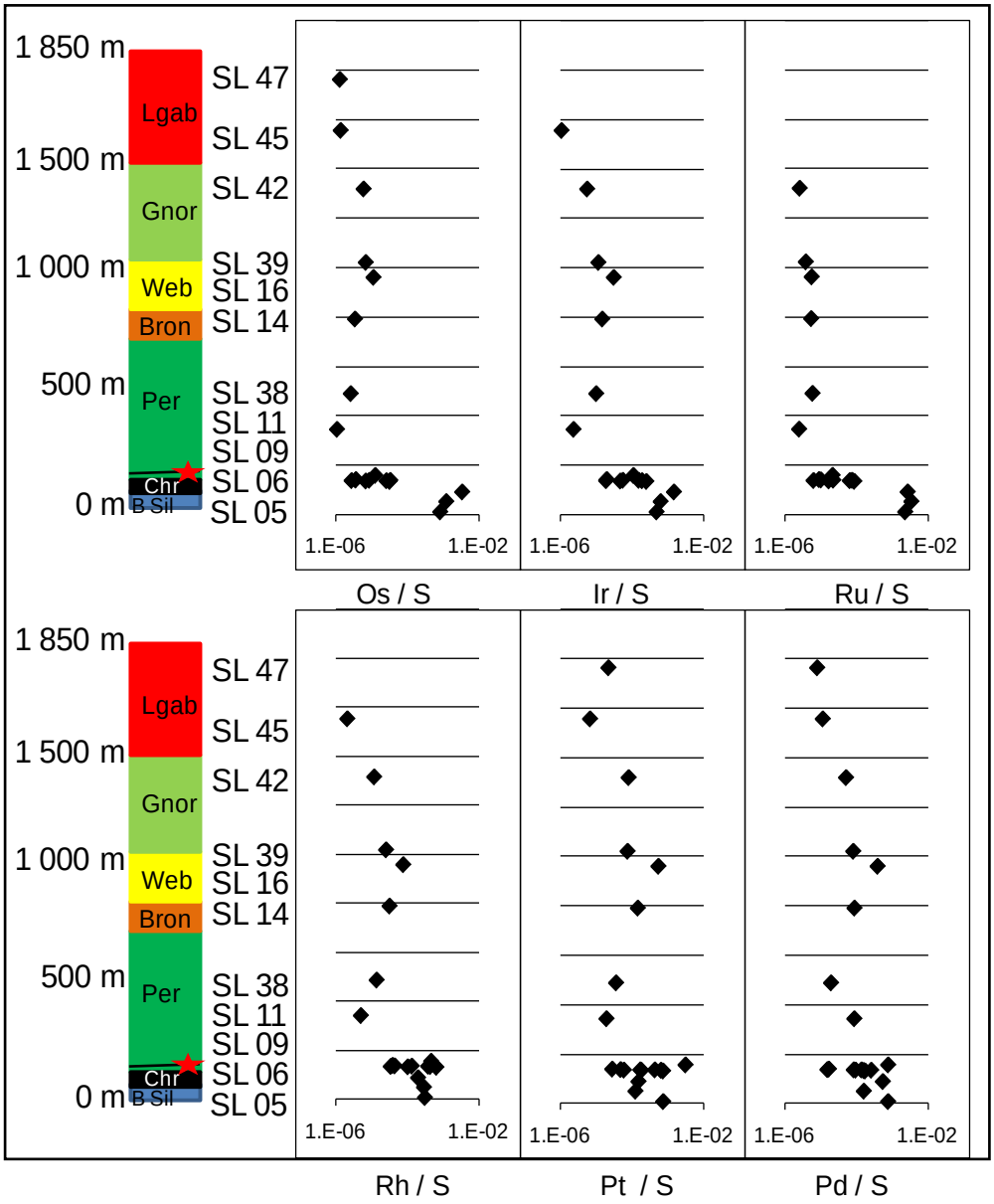


**Figure 20:** Variations for PGE / sulphur ratios versus stratigraphic height.

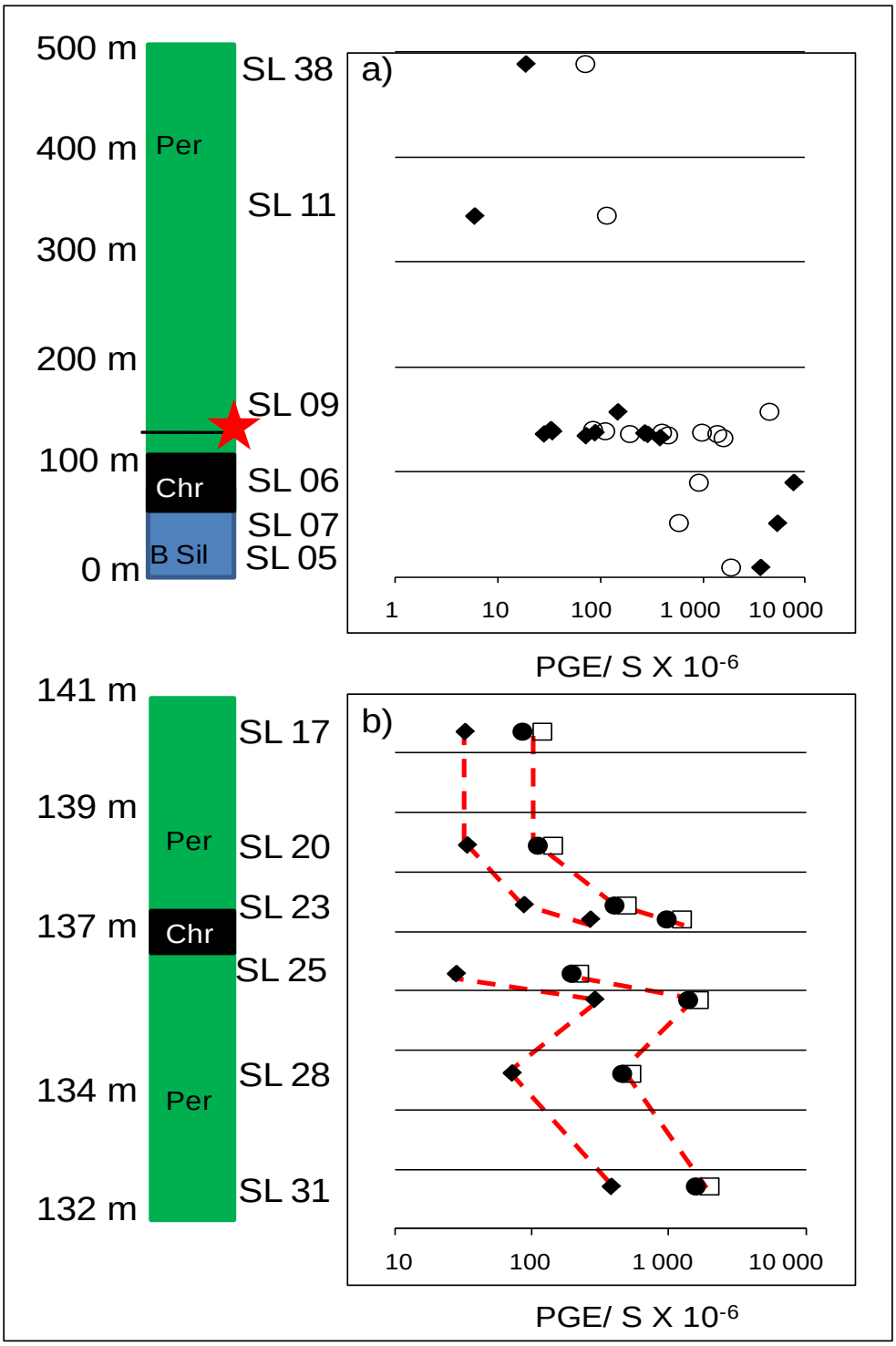


**Figure 21:** Variations for ΣIPGE- and ΣPPGE / sulphur in (a) the lowest 600 meters of the intrusion and (b) across the small chromitite layer above the main chromitite layer.

The mantle-normalized PGE abundances (Figure 22) of the main chromitite horizon and the peridotites and pyroxenites below it, (Figure 22a) show enrichment of $IPGE_{PM}$ (values of 1 to 100) relative to $PPGE_{PM}$ (0.1 to 10). In contrast, the overlying rocks (Figure 22b - f) are characterised by

enrichment of $PPGE_{PM}$ (0.1 to 10) relative to $IPGE_{PM}$ (0.01 to 1). The PGE data from Alapieti and Huhtelin (2005) are consistent with these results.

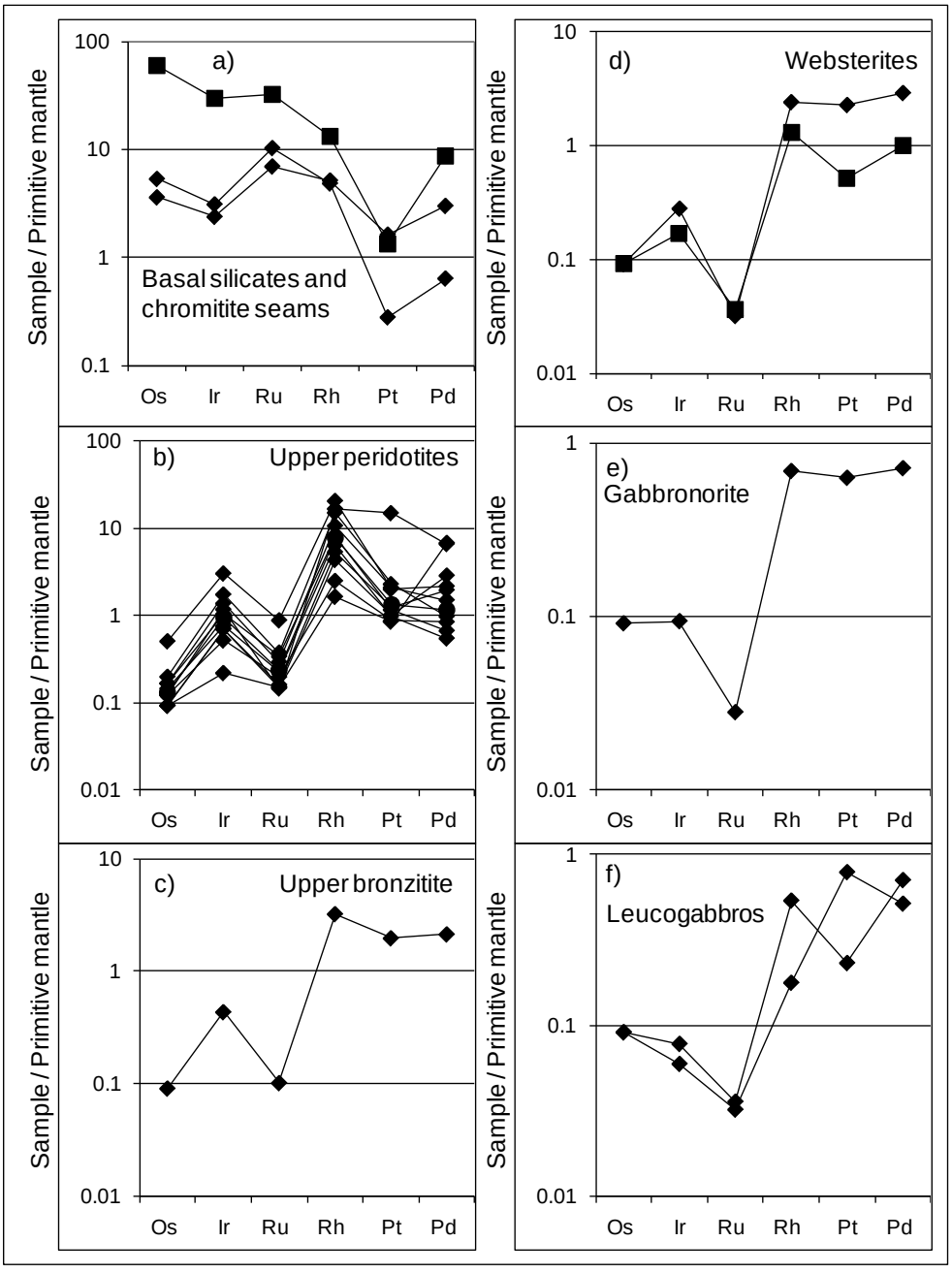


**Figure 22:** Primitive mantle-normalized PGE diagrams for (a) the basal silicates (diamonds) and chromitite layers (squares), (b) the upper peridotites, (c) the upper bronzitites, (d) the websterites, (e) the gabbronorites, and (f) the leucogabbros. Normalizing values after McDonough and Sun (1995).

# 6 Discussion

## 6.1 Correlation of major and minor element geochemistry data with the petrography of the Kemi Intrusion

### 6.1.1 Major element data

Variations of MgO, FeO, MnO and $TiO_2$ correspond well with the modal abundances of the main rock forming minerals in the intrusion.

The MgO versus FeO and $SiO_2$ plots (Figure 10) show the affect that the chromite cumulates have on the composition of the lower portion of the intrusion. The lower silicate cumulates are dominated by olivine and orthopyroxene but the presence of significant modal chromite (Figures 4 and 6) pulls the composition of the rocks away from the olivine – orthopyroxene tie-line towards the chromite average composition. In the upper portion of the intrusion there are no chromite cumulates and chromite crystallization had no effect on the composition of the websterites through to the leucogabbros.

In plots of MgO vs $Al_2O_3$ and MgO vs CaO (Figure 10) the consistency between the mineralogy and major oxide composition is illustrated. The composition of the websterites and gabbros (dominated by orthopyroxene, clinopyroxene and plagioclase) is consistent with their plotting within the orthopyroxene-clinopyroxene-plagioclase triangle in Figure 10.

Figures 10 and 11 show a compositional gap between the ultramafic and mafic rocks. A similar gap is a feature of the Bushveld Complex (e.g., Teigler, 1990). A possible explanation for this compositional gap is crystal settling. The olivine and orthopyroxene crystals would have settled and accumulated at the base of the magma chamber. The fractionated CaO and $Al_2O_3$-enriched magma would then be the source for the mafic rocks and would produce the compositional gap between the ultramafic and mafic rocks. The two trends observed in the FeO vs $Al_2O_3$ plot (Figure 11) can be explained by the involvement of chromite in the ultramafic rocks and the absence of cumulus chromite associated with the mafic rocks. This interpretation is consistent with those of Alapieti *et al*. (1989).

### 6.1.2 Minor and trace element data

The incompatible trace element abundances in a cumulate rock reflect the proportion of trapped intercumulus liquid. Variations in immobile HFSE abundances between adjacent samples probably reflect different proportions of trapped liquid (Henderson, 1975). Figure 12 shows the abundances of some incompatible elements versus the whole rock MgO and Figure 15 certain REE concentrations and $La/Yb_{C1}$, $La/Sm_{C1}$ and $Dy/Yb_{C1}$ ratios versus stratigraphic height. One would expect the gabbros, which crystallized after the ultramafic cumulates to contain a higher proportion of trapped liquid, and hence higher incompatible elements abundances than the underlying ultramafic rocks, but this is not the case. The majority of ultramafic rocks have similar incompatible element abundances to the gabbros and in fact the highest incompatible element abundances occur in several of the ultramafic peridotites. This is similar to the Bushveld Complex, where the ultramafic rocks have higher incompatible element abundances than the mafic rocks (e.g., Teigler, 1990; Maier, 1991). This trend has not been fully explained but some authors (e.g., Barnes and Maier, 2002; Wilson and Chunnett, 2006) propose that late stage processes such as compaction and deformation of the crystal mush could have affected the ratio of cumulates to trapped liquid. On the evidence of incompatible trace elements the ultramafic rocks of the Kemi Intrusion contain more trapped liquid than the mafic rocks and this may suggest that some of the ultramafic rocks underwent less compaction and expulsion of the trapped liquid than the mafic rocks.

The mantle-normalized incompatible element profiles (Figure 13) show that most rocks of the Kemi Intrusion have negative Nb anomalies and the gabbros have positive Sr and Eu anomalies (the Nb anomalies should be treated with caution as Nb is flanked by the mobile elements Ba and K in Figure 13). Negative Nb anomalies are commonly interpreted to indicate crustal contamination or the presence of a crustal component in the mantle source (e.g., Wilson, 1989; Rollinson, 1993), suggesting that a crustal component played a role in the evolution of the Kemi Intrusion. Eu anomalies can occur because Eu occurs in two valence states: $Eu^{2+}$ and $Eu^{3+}$. The ionic radii of $Eu^{2+}$ and $Sr^{2+}$ are similar to $Ca^{2+}$ and therefore can substitute for the Ca in minerals such as plagioclase (Goldschmidt, 1937). Accumulation of plagioclase relative to liquid will cause relative enrichment of $Eu^{2+}$ and $Sr^{2+}$ in the cumulate rocks and create positive Eu anomalies

(e.g., Hanson, 1980; Taylor, 1982; Hess, 1989; Blundy and Wood, 2003). Positive Eu anomalies can also be generated by the expulsion of trapped liquid from plagioclase-bearing rocks.

Figure 23 shows the variation in the Eu/Eu* ratios versus stratigraphic height. Values above 1 represent positive Eu and values below 1 represent negative Eu. The lower portion of the intrusion has Eu/Eu* values mostly around unity with the chromitites being the only exception. The upper portion of the intrusion has positive Eu/Eu* ratios. The positive Sr and Eu anomalies observed from the Kemi gabbros are consistent with the presence of cumulus plagioclase and the reduced abundance of trapped liquid in the gabbros.

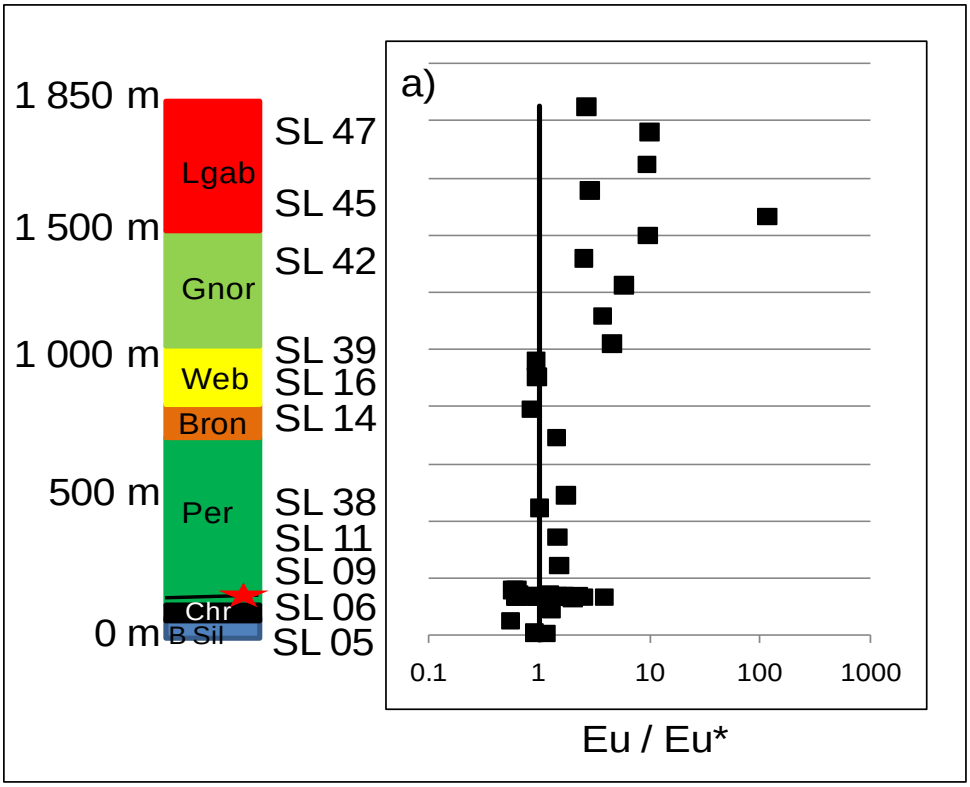


**Figure 23:** Plot of the Eu / Eu* anomalies versus stratigraphic height.

The overall upward variations in major element abundances and modal mineralogy may be consistent with a fractional crystallization model (such as proposed by Alapieti *et al*., 1989) but the petrogenetic model for the Kemi Intrusion needs to be refined to take into account several new sets of data obtained from this study. The sections below present a refined petrogenetic model based on these new data.

## 6.2 Constraints on the magma source

### 6.2.1 Major element data

Based on mineralogy and chemical composition of cumulates from various Fennoscandian layered intrusions, it has been concluded that the 2.44 to 2.5 Ga intrusions of the Tornio-Näränkävaara belt were fed by two types of parental magma (Iljina and Hanski, 2005) (Figure 24). The first magma was a more primitive, Cr-rich magma while the second magma was a less primitive, Cr-poor magma. Not all the intrusions of the Tornio-Näränkävaara belt were generated from both types of magma. The Tornio Intrusion, for example, was generated from the higher-Cr magma while the Suhanko and Konttijärvi blocks of the Portimo Intrusion were generated from the lower-Cr magma. Other intrusions (such as the Penikat Intrusion or the Narkaus block of the Portimo Intrusion) experienced influx of both magma types, first the higher-Cr magma and then the lower-Cr magma.

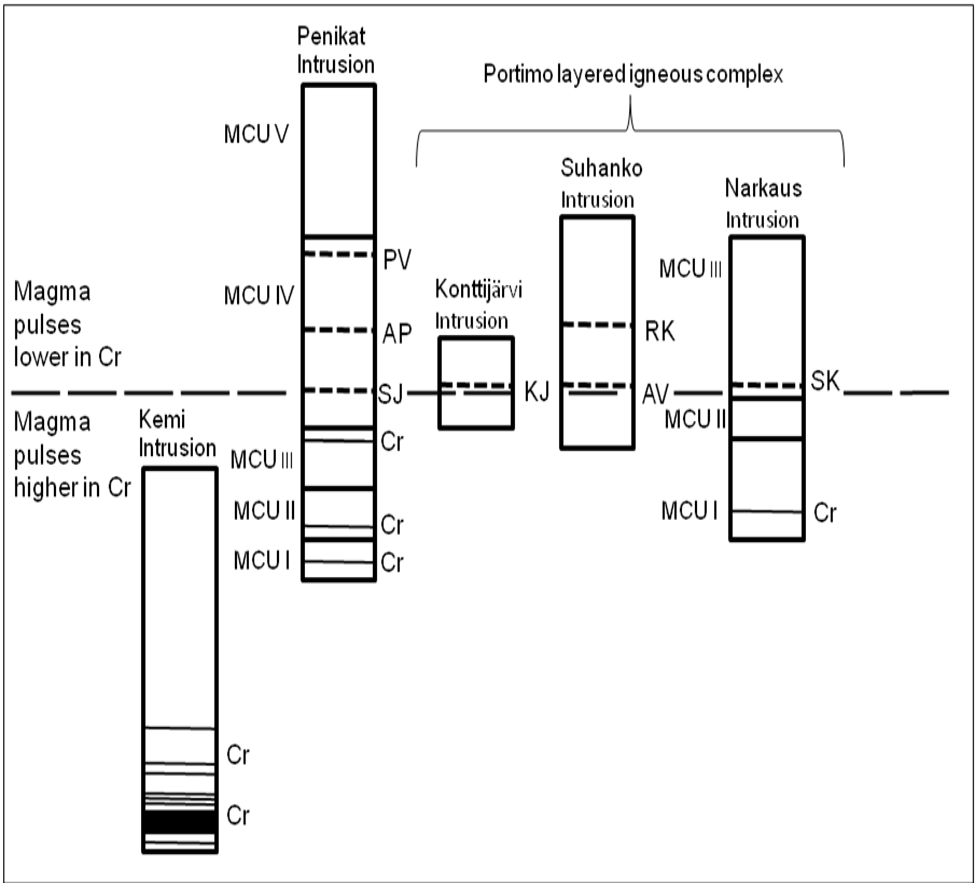


**Figure 24:** Simplified stratigraphic columns of some of the layered intrusions in the Tornio- Näränkävaara belt and their correlation based on different magma types. Also shown are occurrences of some of the principal PGE reefs and deposits (SJ – Sompujärvi, AP- Ala-Penikka, PV – Paasivaara, KJ – Konttijärvi, AV – Ahmavaara, RK – Rytikangas, SK – Siika-Kämä) and chromitite layers (Cr). MCU – megacyclic unit. Modified after Iljina and Hanski (2005).

Figure 25 compares the compositions of the mafic and ultramafic rocks from the Kemi Intrusion with those of other Fennoscandian layered intrusions and related dykes. Cumulates derived from the primitive, higher-Cr magma are represented by two possible feeder dykes and the weighted average of the lowest mega-cyclic unit (Penikat MCU I) of the Penikat Intrusion. The less primitive, lower-Cr magma is represented by the weighted averages of the fourth MCU of Penikat (Penikat MCU IV), third MCU of the Narkaus block from the Portimo Intrusion (Port Nas MCU III) and the Suhanko block (Port Suh) of the Portimo Intrusion (Iljina and Hanski, 2005).

Alapieti (1996) identified a possible feeder dyke for the Kemi Intrusion. His data and those from Alapieti *et al*. (1990) for the Loljunmaa Dyke (LJ Dyke) from the Penikat Intrusion are also included in Figure 25. If the gabbroic cumulates are derived exclusively from a residual liquid with an initial compositions similar to that of the two dykes, then the composition of a parent magma (as represented by these two dykes) should plot in between the ultramafic cumulates and the products of their residual liquids in Figure 25. This is the case. The composition of the Kemi feeder dyke (and that of the LJ dyke) broadly plots in between the ultramafic cumulates and the gabbros. In some of the variation diagrams (e.g., $SiO_2$ – MgO plot) the composition of the "parent" magma (as represented by these two dykes) overlaps that of the more Mg-rich gabbros. This can be accounted for with the tentative conclusion that the "parent" magma fractionated to form the ultramafic cumulates and the gabbros were derived from the residual liquid but some of the gabbros acquired cumulate pyroxene which accounted for the higher $SiO_2$ concentrations.

The weighted average of all the Kemi samples (KA, Alapieti *et al*., 1989) plots nearest the rocks derived from the primitive, Cr-rich parent magma (the two dykes and Penikat MCU I). The pyroxenes of the Kemi Intrusion are characterized by a high Cr content (orthopyroxenes contain 0.5 wt. % and the clinopyroxenes a range of 0.8 to 1.2 wt. %, Alapieti *et al*., 1989). Based on the major element data (Figure 25) it appears that the magma that fed the Kemi chamber could have been the primitive, Cr-rich magma of Iljina and Hanski (2005). The major element data also suggest that the Kemi Feeder dyke and the LJ dyke were of similar composition which would indicate that Penikat MCU I and the Kemi Intrusion were fed by a compositionally similar magma.

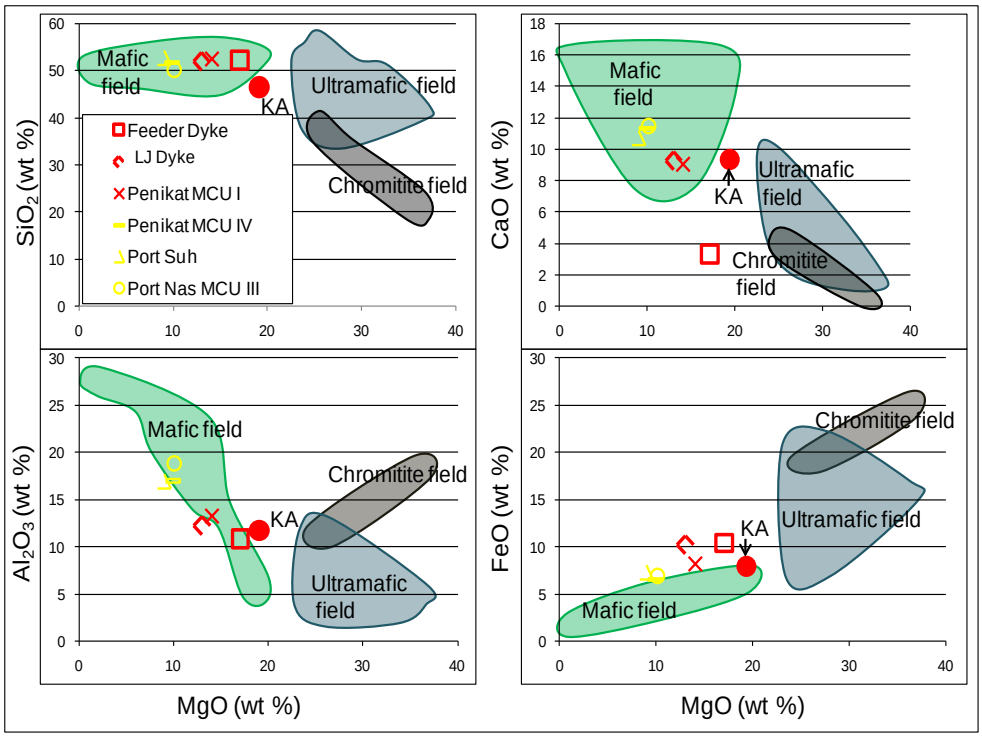


**Figure 25:** Variation diagram of MgO in wt % versus $SiO_2$, $Al_2O_3$, CaO and FeO in wt % of the samples from the Kemi Intrusion (Chromitite layers represented by black field, bronzitites and peridotites represented by blue ultramafic field, websterites and gabbros represented by green mafic field). Plotted as well are the weighted average of all the Kemi samples (KA, Alapieti *et al*., 1989); the Loljunmaa dyke (LJ dyke) from the Penikat Intrusion (Alapieti *et al*., 1990); the 'feeder' dyke of the Kemi Intrusion (Alapieti and Huhtelin, 2005); average of the lowest (MCU I) and fourth mega-cyclic unit (MCU IV) of Penikat; average of the Suhanko Body, Portimo (Port Suh) and the third MCU of the Narkaus Body (Port Nas MCU III), Portimo (Alapieti *et al*., 1990).

### 6.2.2 Incompatible element and REE

Literature on the 2.44 to 2.5 Ga Fennoscandian layered intrusions has suggested that the parent magmas of these intrusions were derived from mantle plume activity with associated contamination and assimilation of crustal material (e.g., Puchtel *et al*., 1997; Saini-Eidukat *et al*., 1997; Hanski *et al*., 2001; Iljina and Hanski, 2005).

It has been shown that if a depleted mantle-derived magma is contaminated with continental crust; the resultant REE patterns will show relative LREE enrichment (e.g., Puchtel *et al*., 1997). This is a feature of the Kemi rocks (Figures 14 and 15) and many rocks also have negative Nb anomalies (Figure 13). This would suggest a possible crustal component to the parent magma of the Kemi Intrusion.

The LREE-enriched nature and negative Nb anomalies of the Kemi Intrusion is characteristic of the other 2.44 Ga Fennoscandian intrusions

(e.g., Saini-Eidukat *et al*., 1997; Anderson and Thalhammer, 1998; Hanski *et al*., 2001). This agreement in incompatible element data suggests that the parental magmas of the Fennoscandian layered intrusions might have been derived from the same source. Based on the isotopic data from the Koitelainen and Akanvaara Intrusions, Hanski *et al*. (2001) favours this model of shared parental magma, and Iljina and Hanski (2005) showed that the primitive, Cr-rich parent magma was LREE-enriched. This would suggest that the parent magma of the Kemi Intrusion could have been similar to that of the other Fennoscandian layered intrusions, in particular the primitive, Cr-rich magma proposed by Iljina and Hanski (2005).

### 6.2.3 Nd isotope data

Previous work on other 2.44 to 2.5 Ga Fennoscandian layered intrusions has shown that their $\varepsilon_{Nd}$ values fall within a narrow range around -2 (Huhma *et al*., 1990; Tolstikhin *et al*., 1992; Balashov *et al*., 1993; Amelin and Semenov, 1996; Saini-Eidukat *et al*., 1997; Turchenko *et al*., 1998; Anderson and Thalhammer, 1998; Glebovitsky *et al*., 2001; Hanski *et al*., 2001; Lauri *et al*., 2006). Based on Nd isotopic compositions, some of these authors (e.g., Puchtel *et al*., 1997, Saini-Eidukat *et al*., 1997; Hanski *et al*., 2001; Lauri *et al*., 2006) have suggested that the parental magma of the Fennoscandian layered intrusions was an ultramafic melt derived from the depleted mantle that underwent crustal contamination.

The majority of the samples from the ultramafic portion of the Kemi Intrusion range between $\varepsilon_{Nd}$ of +4 to -2 (Figure 16). The negative $\varepsilon_{Nd}$ values are in broad agreement with the Nd isotopic composition of rocks of other Fennoscandian intrusions. Positive $\varepsilon_{Nd}$ are notable because the presence of depleted mantle signatures is extremely rare in the Palaeoproterozoic. Conversely, the main and small chromitite layer samples, and one upper peridotite sample, show $\varepsilon_{Nd}$ as low as -8, suggestive of localized contamination events. The samples from the mafic portion of the Kemi Intrusion show $\varepsilon_{Nd}$ ranging from -5 to -10. This suggests that these rocks crystallized from magma with a significant crustal component.

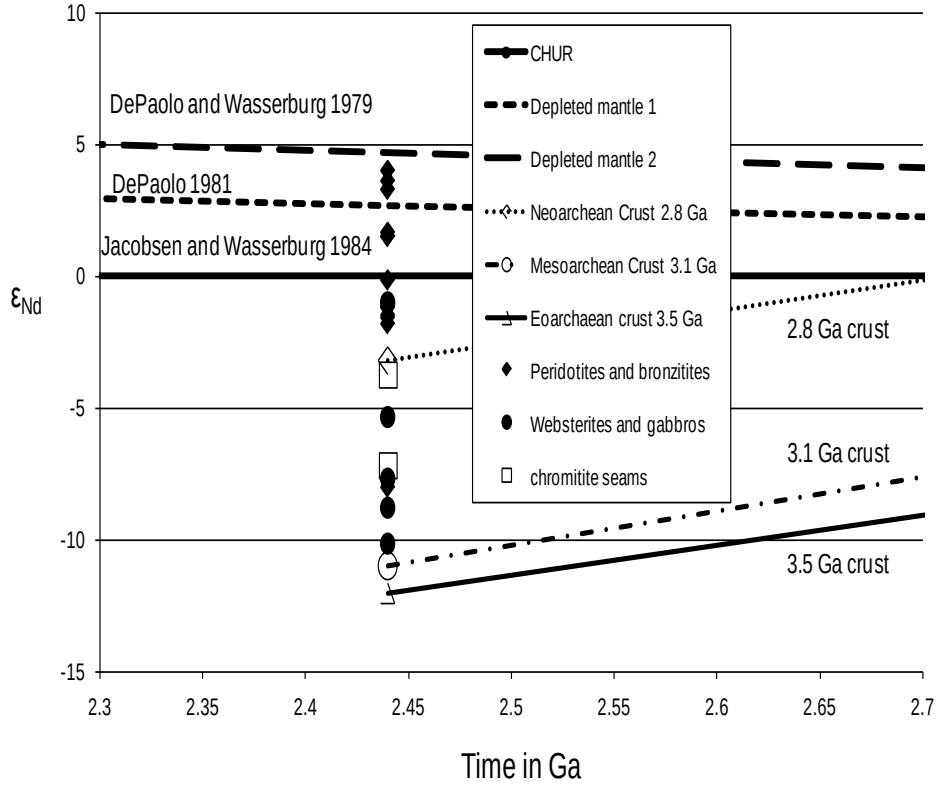


**Figure 26:** Possible magma reservoirs and country rock contaminants plotted against the $\varepsilon_{Nd}$ values from the Kemi Intrusion. Depleted mantle 1 from DePaolo (1981a); Depleted mantle 2 from DePaolo and Wasserburg (1979); CHUR mantle from Jacobsen and Wasserburg (1984); Neoarchaean crust from Hanski *et al.* (2001); Mesoarchaean crust from Hanski *et al*. (2001) and Jahn *et al.* (1984). Theoretical Eoarchaean crust with a minimum age of 3.5 Ga.

The isotopic data from the intrusion was used to constrain possible magma sources and crustal contaminants for the Kemi magmas (Figure 26). The first magma source is derived from a chondritic reservoir (CHUR). The second and third sources are derived from depleted mantle reservoirs. The DePaolo (1981a) Nd-isotope evolution model would produce a parent magma with an $\varepsilon_{Nd}$ of +2.6 which would appear to be consistent with the majority of the Kemi peridotites and bronzitites. However, there are 3 peridotites that have $\varepsilon_{Nd}$ of over +3. In order to explain these high $\varepsilon_{Nd}$ the DePaolo and Wasserburg (1979) Nd-isotope evolution model is also considered (this would produce a parent magma with $\varepsilon_{Nd}$ of +4.7).

The Fennoscandian layered intrusions were emplaced within late Archaean granitoids or at the contact between these and the overlying Proterozoic supracrustal rocks (Alapieti *et al*., 1990). These Archaean crustal rocks belong to the Karelian domain and range in age from the

Mesoarchaean (3.1 Ga) to the Neoarchaean (2.8 Ga) (Sorjonen-Ward and Luukonen, 2005). The eastern Fennoscandian intrusions (such as the Akanvaara and Koitelainen intrusions) were intruded into Mesoarchaean country rocks (Hanski *et al.*, 2001). The western intrusions (such as Kemi and Penikat) were intruded into Neoarchaean country rocks (Sorjonen-Ward and Luukonen, 2005). Both are considered as possible contaminants. Some of the gabbro samples have $\varepsilon_{Nd}$ that is similar to that of Mesoarchaean crustal rocks. This would imply either an enriched source for the gabbros or contamination by large amounts of 3.1 Ga crust. To account for this a third possible Archaean crustal contaminant needs to be considered for the Kemi Intrusion, i.e., Eoarchaean crust (minimum age to be discussed in Chapter 6.3, to follow).

There is disagreement over the Nd isotopic composition and Nd content of the parent magmas of the Fennoscandian layered intrusions. Saini-Eidukat *et al*. (1997) proposed that a siliceous high-magnesium basalt (SHMB) with an $\varepsilon_{Nd}$ of -3 and a Nd concentration of 7 ppm was the parent magma. Puchtel *et al*. (1997) favoured a parental komatiitic magma but with an $\varepsilon_{Nd}$ of -2 and a Nd concentration of 10 ppm. Iljina and Hanski (2005) favoured a parent magma with a composition similar to that of the Loljunmaa, Portimo and Viianki dykes and a Nd concentration of 10 ppm. Lauri *et al*. (2006) also favoured komatiite parent magma with an $\varepsilon_{Nd}$ of +2.6 and a Nd concentration of 2 ppm.

Four different parent magmas were therefore considered as possible candidates for the Kemi magmas for modelling purposes (see section 6.3). The first two are a komatiite and basalt magma with a delpeted $\varepsilon_{Nd}$ of +5. The komatiite has a Nd concentration of 2 ppm and a $La/Yb_{C1}$ ratio of 3.4, while the basalt has 10 ppm Nd and a $La/Yb_{C1}$ of 5.75. The komatiite composition is based on a typical peridotite from Sigurdsson (2000) and komatiites from Putchel *et al*. (1997), and the basalt composition derives from the Loljunmaa, Portimo and Viianki dykes (Iljina and Hanski, 2005). The same komatiite and basalt magmas described above are then also modelled but with an $\varepsilon_{Nd}$ of 0. It is unlikely that a magma with “near chondritic” Nd isotopic values could be the source of the Kemi Intrusion as a number of the peridotites have positive $\varepsilon_{Nd}$ values (in the range of +3) but a magma derived from a chondritic reservoir is included in the modelling to investigate if such a reservoir could have been the source of some of the Kemi magmas.

Two different contaminants were initially chosen to model the possible effect of contamination on the parent magmas (section 6.3). Both were allocated a composition (Nd concentration of 14 ppm and $La/Yb_{C1}$ of 78) that is the same as that of the granitic country rocks to the Kemi Intrusion (Tables 5 and C5; samples SL-01 through to SL-03). One was assigned a Mesoarchaean age (*ca.* 3.1 Ga, corresponding to the oldest known local Fennoscandian crust) with $\varepsilon_{Nd}^{2.44}$ of -11 (Jahn *et al*., 1984; Hanski *et al*., 2001) and the other a Neoarchaean age (*ca.* 2.8 Ga, corresponding to known local crust) with $\varepsilon_{Nd}^{2.44}$ of -3.2 (Hanski *et al*., 2001).

## 6.3 Geochemical modelling

Figure 27 shows the effect of the different contaminants on the komatiite and basaltic magmas (see Appendix E for the starting parameters used and the results of the mixing calculations). $\varepsilon_{Nd}$ versus $La/Yb_{C1}$ and $La/Sm_{C1}$ were modelled because the Nd-isotopic signature and $La/Yb_{C1}$ and $La/Sm_{C1}$ ratios of the cumulate rocks should be consistent with that of the magma from which they have crystallized. Rocks with an $\varepsilon_{Nd}$ of 0 or lower could have been derived from magmas with “near chondritic” Nd isotopic values but the peridotites with $\varepsilon_{Nd}$ above +1 cannot be derived from these “near chondritic” magmas. Thus, in attributing the Kemi sequence to one parent magma type, the two “near chondritic” magmas must be discarded as candidates for the Kemi parental magma.

The ultramafic rocks appear to contain either a Mesoarchaean or a Neoarchaean crustal component or both. These crustal components are interpreted as upper Archaean crust because the Fennoscandian intrusions were emplaced within these Archaean granitoids. Contamination of magmas with $\varepsilon_{Nd}$ of +5 by between 1 % and 25 % of Mesoarchaean (3.1 Ga) crust would explain the $\varepsilon_{Nd}$ (+4 to -2) and $La/Yb_{C1}$ range (2 to nearly 7) of the peridotites and bronzitites but a larger amount of contamination (2 to 80 %) with the Neoarchaean (2.8 Ga) crust is required to produce rocks with the same $\varepsilon_{Nd}$ and $La/Yb_{C1}$ range. The mafic rocks and the chromitite layers appear to contain a significant Mesoarchaean component (20 to as much as 80 %, depending on the parent magma composition). The mafic rocks and chromitites have lower $\varepsilon_{Nd}$ than the Neoarchaean crust and thus contamination of the magma with Neoarchaean crust cannot account for the $\varepsilon_{Nd}$ of the gabbros and chromitites.

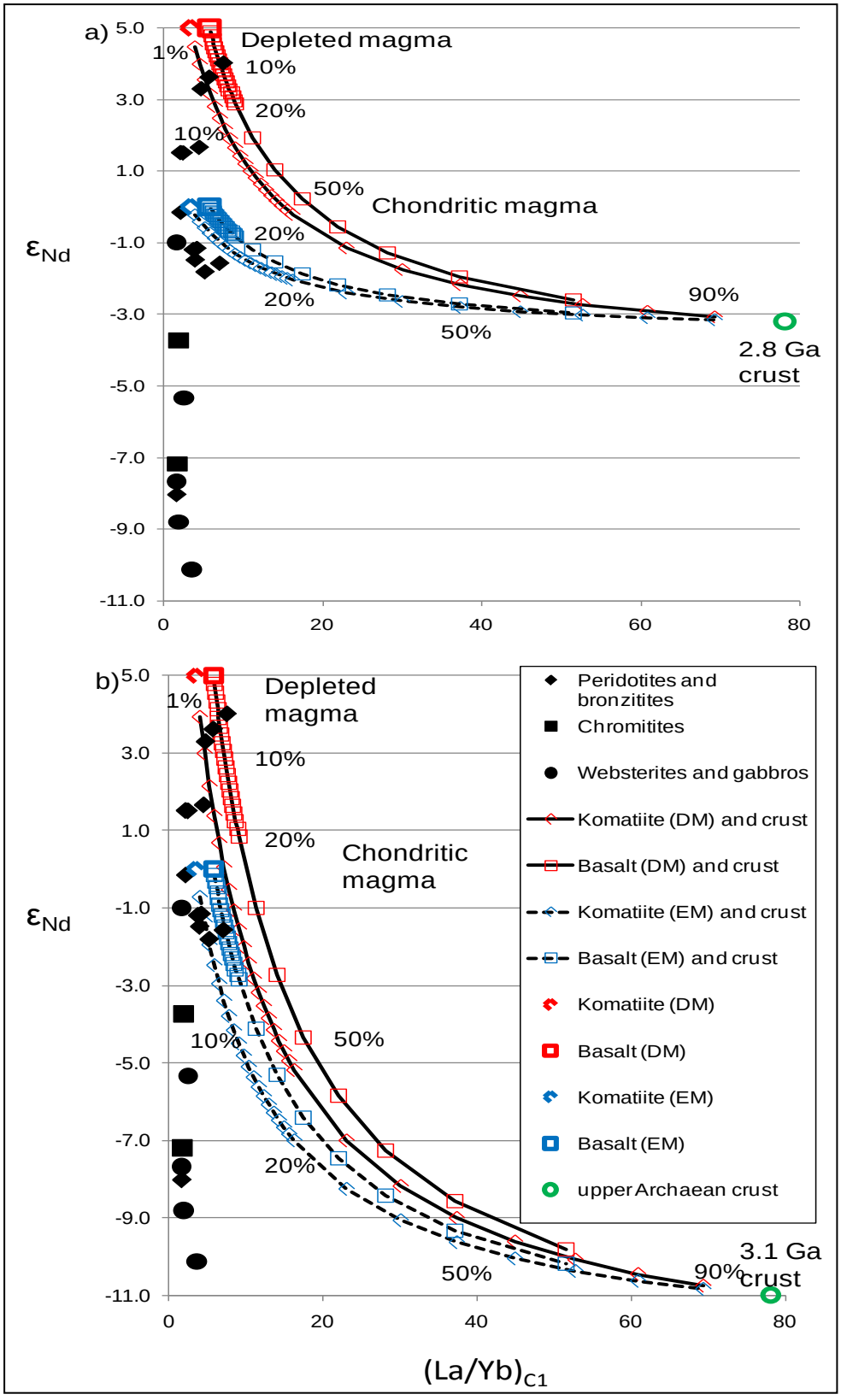


**Figure 27:** $La/Yb_{C1}$ versus isotopic composition, demonstrating mixing of a) Neoarchaean crust (2.8 Ga) and b) Mesoarchaean crust (3.1 Ga) with magmas with $\varepsilon_{Nd}$ of both 0 and +5. The mixing lines are graduated every 10 % of added crust, except below 20 % where every percent is shown. DM – komatiite and basaltic magmas with $\varepsilon_{Nd}$ of +5. EM – komatiite and basaltic magmas with $\varepsilon_{Nd}$ of 0.

Taylor (1980) and DePaolo (1981b) explained that the proportion of country rock that is assimilated to cumulates crystallized depends on the heat capacity of the country rock and the enthalpy of fusion of the crystallizing cumulates (Table E9). For example, assuming an initial temperature of 150$^{o}$C for the country rock, heating 1 gram of Archaean country rock by 1000$^{o}$C would require 330 calories of energy. The average enthalpy of fusion (weighted average of all the individual mineral fusion values) for the Kemi Intrusion was 191 calories of energy released per 1 gram of crystallized cumulate. Therefore 1.7 grams of cumulate is required to crystallize to provide enough energy to assimilate 1 gram of country rock. A more realistic ratio would be 3 grams of cumulate to 1 gram of country rock assimilated due to the energy loss assumptions outlined in Taylor (1980). This proportion of 3 grams of cumulates to 1 gram of country rock limits the amount of Archaean country rock that the Kemi magmas could have assimilated, in this case roughly 30 %. The high amounts of contamination with Neoarchaean and Mesoarchaean crust predicted in Figure 27 (30 to 80 %) are unrealistic.

A series of Archaean crustal contaminants (from 3.2 to 4 Ga) were modelled using the composition of the bulk Archaean crust from Taylor and McLennan (1995) and the Nd isotopic signature of the Mesoarchaean rocks (the $\varepsilon_{Nd}$ were re-adjusted for the older ages). Assuming a maximum of 30 % crustal contamination the youngest possible Archaean crustal contaminant would have to be 3.7 Ga in age (Eoarchaean-aged crust). The 3.7 Ga aged crust would have a theoretical $\varepsilon_{Nd}^{2.44}$ of -15, Nd concentration of 16 ppm and $La/Yb_{C1}$ of 4.6. The theoretical Archaean crust is interpreted as lower Archaean crust because no Eoarchaean nor Paleoarchaean granitoids have yet been identified in the Fennoscandian Shield.

Figure 28 shows the effect of contamination on the komatiite and basaltic magmas with $\varepsilon_{Nd}$ of +5 by Eoarchaean crustal material. A wide range of contamination (3 to 25 %) of the basaltic magma by Eoarchaean crust could produce the $\varepsilon_{Nd}$ range (+4 to -2) of the peridotites and bronzitites. A larger amount of contamination (30 to 65 %) of the basaltic magma is required to produce $\varepsilon_{Nd}$ range of the mafic rocks and chromitite layers, which would require that the Kemi magma did not have the same Nd composition and $La/Yb_{C1}$ ratio to that of the Loljunmaa, Portimo and Viianki dykes. The komatiite magma only requires a maximum of 30 %

contamination by Eoarchaean crust to produce the $\varepsilon_{Nd}$ range of the Kemi rocks (+4 to -10).

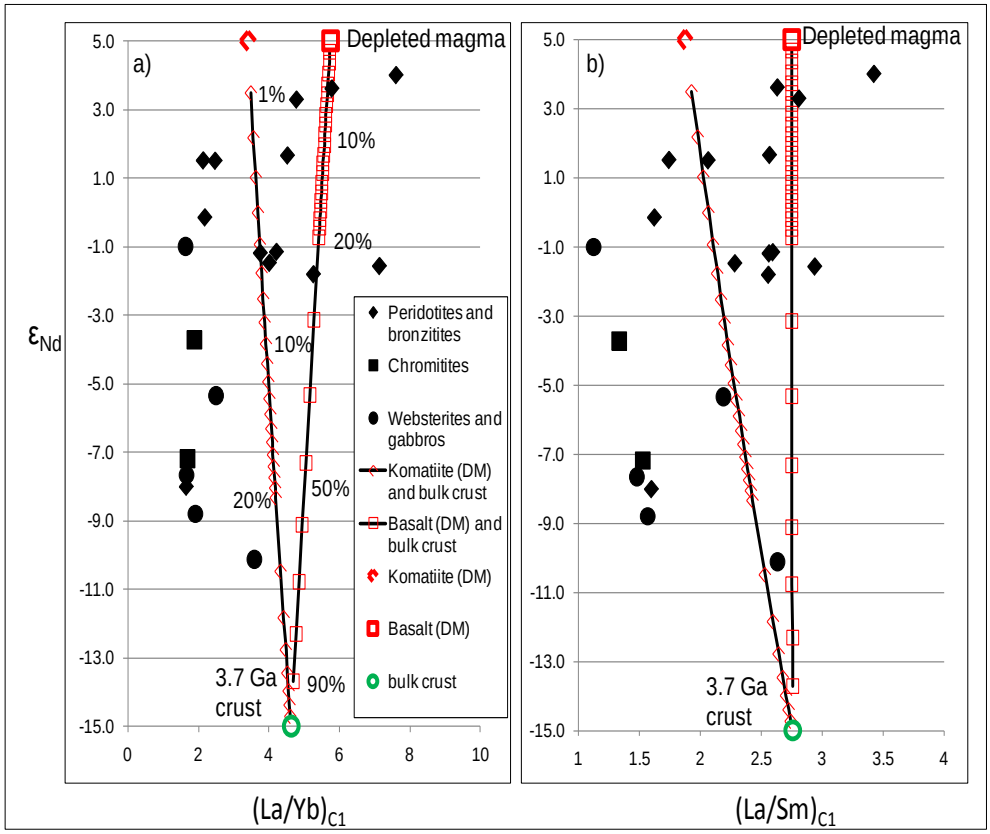


**Figure 28:** a) $La/Yb_{C1}$ and b) $La/Sm_{C1}$ versus isotopic composition, demonstrating mixing of the Eoarchaean crust with magmas with $\varepsilon_{Nd}$ of +5. The mixing lines are graduated every 10 % of added crust, except below 20 % where every percent is shown.

Figure 28 shows that a range of contaminants are required. For most of the rocks with negative $\varepsilon_{Nd}$ a contaminant with low $La/Yb_{C1}$ and $La/Sm_{C1}$ ratios (4 and 2.5 respectively) is required. In contrast, rocks with positive $\varepsilon_{Nd}$ require a contaminant with high $La/Yb_{C1}$ and $La/Sm_{C1}$ ratios (8 and 3.5 respectively).

Figure 29 shows the effect of contamination on the komatiite magma with $\varepsilon_{Nd}$ of +5 by both lower, older crustal material (it's $La/Yb_{C1}$ and $La/Sm_{C1}$ ratios, 4.6 and 2.7 respectively, are lower than that of the Neoarchaean crustal material) and upper crustal material (Neoarchaean crust was chosen because the age of the Kemi granitic country rock is 2.8 Ga). The group of peridotites with relatively high $La/Yb_{C1}$ and $La/Sm_{C1}$ ratios (over 5 and 3.5 respectively) and elevated $\varepsilon_{Nd}$ (over +3) could crystallize from the komatiite magma that has undergone 1 to 4 %

contamination by upper crustal material. The remaining Kemi ultramafic rocks appear to be derived from 1 to 7 % contamination by lower crustal material. The mafic rocks and chromitite layers require 8 to 20 % contamination by the older crustal material.

**Summary of modelling results**

Various authors (e.g., Saini-Eidukat *et al*., 1997; Hanski *et al*., 2001; Iljina and Hanski, 2005, Lauri *et al*., 2006) propose that the mantle-derived magma experienced felsic contamination and accompanying crystal fractionation in a staging magma chamber in the lower crust prior to emplacement in the upper crust. The apparent isotopic and REE pattern homogeneity of the Fennoscandian intrusions could be explained if all the intrusions were fed from the staging chamber in the lower crust.

Modelling in the current study indicate that the parent magma did not have a "near chondritic" source but had an elevated positive $\varepsilon_{Nd}$ signature with a relatively low Nd concentration and $La/Yb_{C1}$ and $La/Sm_{C1}$ ratios. The contamination of the parent magma was not restricted to one contaminant alone. The ultramafic rocks show a contribution from both the upper and lower Archaean crust, one Eoarchaean and the other Meso- to Neoarchaean in age. The mafic rocks and the chromitite layers were derived from a magma that underwent contamination in the lower crust only. Three possibilities arise from these modelling results.

**Staging chamber located in the lower crust**

One possible interpretation is that the original Kemi magma (and that of the other Fennoscandian intrusions) was derived from a $\varepsilon_{Nd}$-depleted source and pooled in a staging magma chamber in the lower crust. There the magma underwent contamination by lower crustal material. The amount of contamination ranged from 1 to 30 % (depending on the age of the lower crust Eoarchaean granitoids). The resultant magma was fed to the different layered intrusions.

**Metasomatised mantle**

Some of the peridotites with positive $\varepsilon_{Nd}$ (indicative of a depleted source) and relative high $La/Yb_{C1}$ and $La/Sm_{C1}$ ratios (indicative of an enriched source) cannot be explained by the lower crustal contamination of

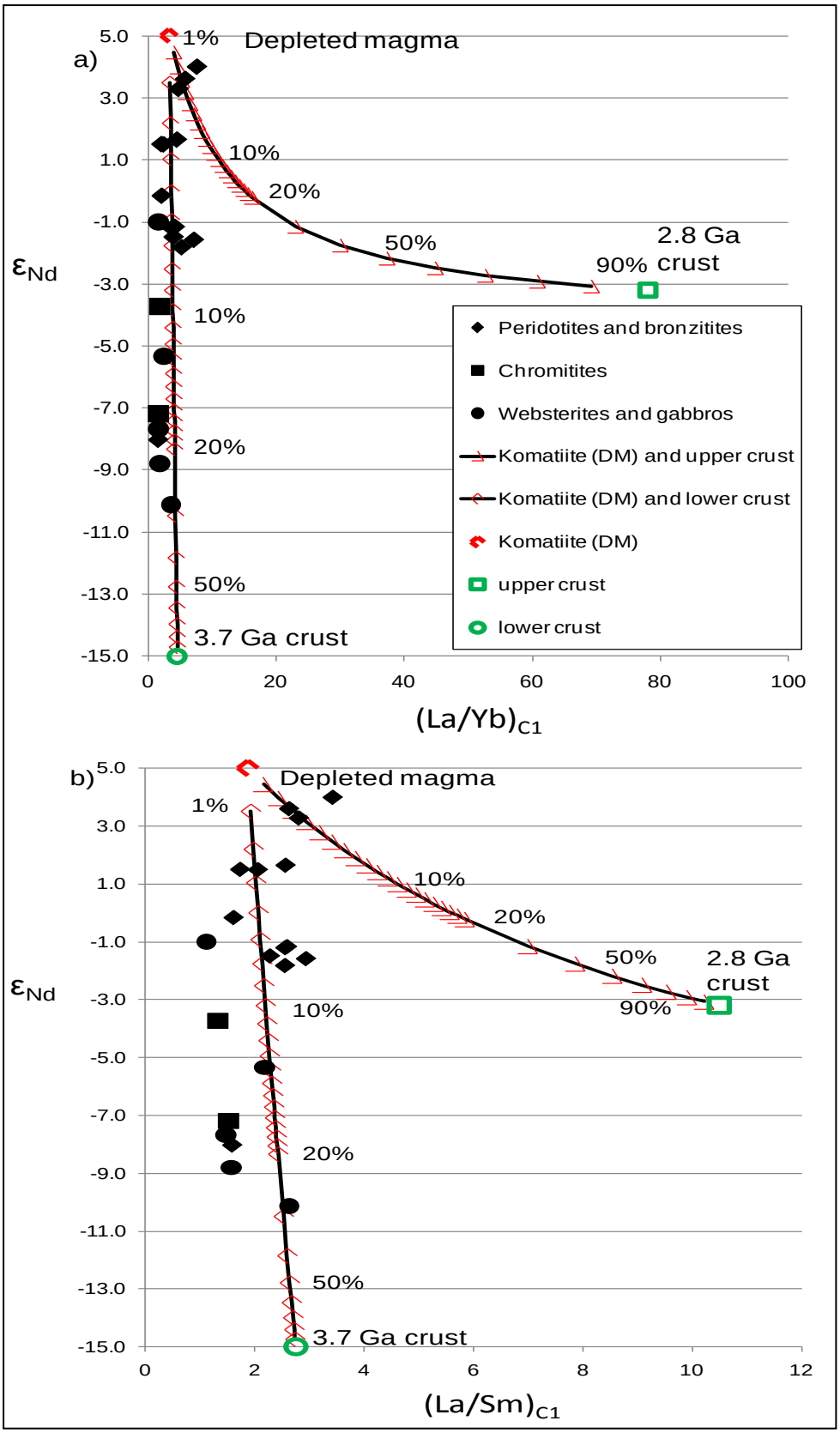


**Figure 29:** (a) $La/Yb_{C1}$ and (b) $La/Sm_{C1}$ versus isotopic composition, demonstrating mixing of upper and lower Archaean crusts with a magma with $\varepsilon_{Nd}$ of +5. The mixing lines are graduated every 10 % of added crust, except below 20 % where every percent is shown. The symbols are the same as in Figures 27 and 28.

a mantle-derived magma. One explanation could be a magma derived from an enriched mantle (e.g., metasomatised sub-continental lithospheric mantle, or SCLM) with the enrichment occurring shortly before melting (Maier, pers. comm. 2010).

**In-situ contamination in the upper crust**

In Figure 14 some of the upper peridotites have the highest $La/Sm_{C1}$ ratios. Figure 30a shows the REE patterns of three Archaean granite country rock samples from the Kemi area. The 2.8 Ga granites have $La/Sm_{C1}$ ratios of 5 to 20, similar to ratios of 3 to 4 displayed by the peridotites. Figure 29 shows that contamination of the magma with Archaean upper crustal material (2.8 Ga in age) could produce the peridotites with the observed $\varepsilon_{Nd}$ and $La/Sm_{C1}$ ratios.

This indicates that additional in-situ contamination of the magma (derived from the staging chamber in the lower crust) in the upper crust could have occurred. The modelling results of this study show (Figures 28 and 29) that the mafic rocks only experienced contamination by lower crustal rocks. It appears that the upper portion of the intrusion (the websterites and gabbros) experienced no additional in-situ contamination by upper crustal rocks. This in-situ contamination is initially significant but progressively diminishes as crystal growth on the walls of the chamber armour the magma against further contamination.

## 6.4 Origin of the Kemi Intrusion

### 6.4.1 Previous and existing models of chromitite formation

An important feature contributing to the understanding of the evolution of the Kemi intrusion is the main chromitite layer, because the presence of a 60 meter thick chromitite layer in a layered intrusion the size of Kemi is unusual. A simple one-stage fractional crystallization model for the Kemi Intrusion does not explain the formation of the main chromitite layer or the location of the PGE mineralized zones in the intrusion.

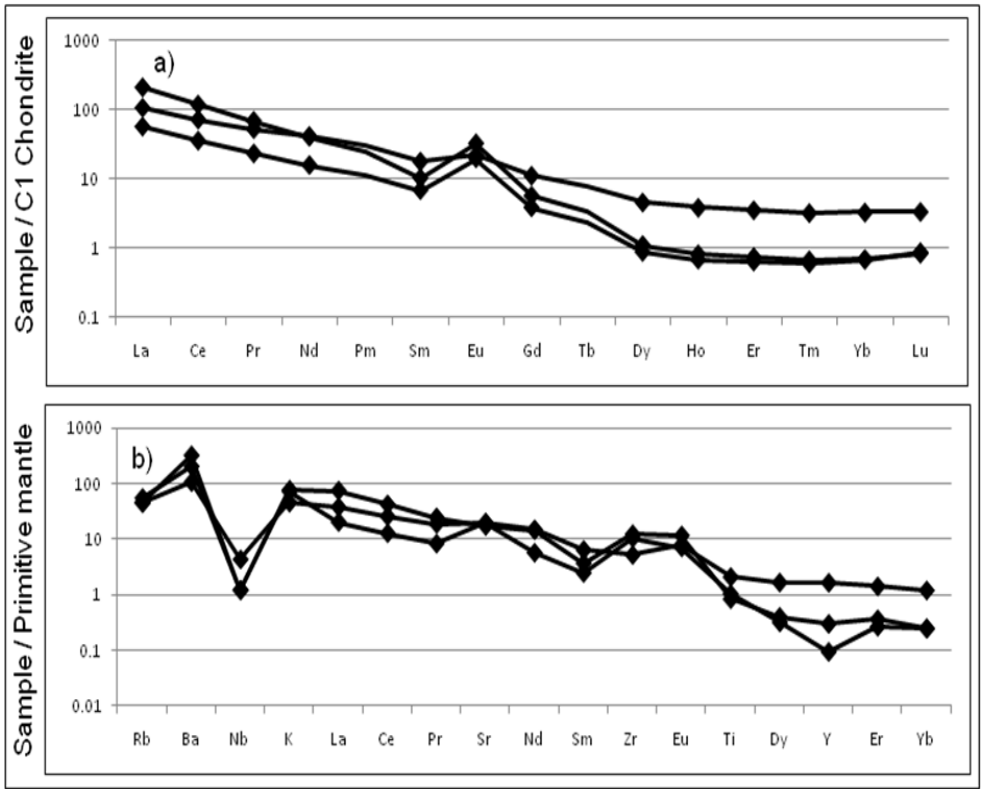


**Figure 30:** (a) C1 chondrite-normalized rare earth element diagrams patterns and, (b) Primitive mantle-normalized incompatible element patterns for the 2.8 Ga Archaean granites from the Kemi area. Normalizing values after McDonough and Sun (1995).

Several models have been proposed for the formation of stratiform chromitite layers in layered intrusions. McDonald (1965) suggested that such layers form by separation of a chromite-rich immiscible liquid from a silicate melt. In contrast, Jackson (1966) claimed that existence of a chromitite-rich immiscible liquid in a basic magma is unlikely. Based on the experimental work of Levin *et al*. (1964), Jackson (1966) showed that chromium – silicate immiscibility occurs only at high temperatures (around 1700$^{o}$C) in simple systems. Another model is that the crystallization of spinel was influenced by variations in the oxygen fugacity (Campbell and Desborough, 1969; Ulmer, 1969; Murck and Campbell, 1986). It has been shown that an increase in oxygen fugacity of the melt promotes the crystallization of spinel instead of silicates (e.g., Kennedy, 1955; Osborn, 1959). Experiments conducted by Hill and Roeder (1974) suggest that crystallization of spinel, as a result of oxygen fugacity change, will result in chromitites with decreased $Al_2O_3$ content and Cr/Fe ratios.

A third proposal is that a change in pressure in the chamber could drive the composition of the magma into the stability field of chromite

(Cameron, 1980; Lipin, 1993). An increase in pressure would also increase the stability of pyroxene relative to plagioclase (which would be consistent with the association of chromitite and cumulus orthopyroxene in the upper peridotites), as opposed to a change in oxygen fugacity which has little effect on the relative stability of pyroxene and plagioclase (Hill and Roeder, 1974). Cawthorn (2005) argued that magma replenishment and venting may cause the required magnitudes of pressure changes within the magma chamber, but this has been questioned by Mondal and Mathez (2007).

### 6.4.2 Magma – mixing models for chromitite formation

Much of the literature suggests that a magma-mixing model best explains the formation of the chromitite layers in layered intrusions (e.g., Irvine, 1975; von Gruenewaldt and Merkle, 1995; Eales and Cawthorn, 1996). The magma-mixing model involves altering the composition of a magma with cotectic proportions of olivine-chromite until it resides in the chromite-only field (in Ol-$SiO_2$-Cr space). This can be done in three ways:

**Model 1: Mixing of differentiated and primitive magma**

This model involves the mixing of injections of primitive magma (P in Figure 31) with an evolved magma already resident in the chamber (E in Figure 31) (Irvine, 1977). The hybrid magma (PE) now lies in the chromite field. It will then crystallize chromite alone which will drive the composition of the liquid back to the olivine-chromite cotectic at point Y, thus producing a chromitite layer. Naldrett *et al*. (1990) suggested that such a process was responsible for the formation of chromitite layers in the Bushveld Lower Zone and the Stillwater Complex.

**Model 2: Mixing of A- and U-type magmas**

The second model involves the mixing between two magmas of different lineages with one parent magma having ultramafic characteristics (U-type magma) and the other having anorthositic traits (A-type magma; Sharpe and Irvine, 1983; Irvine and Sharpe, 1986). Irvine and Shape (1986) showed that chromite would be the sole liquidus phase over almost the whole intermediate composition region of a U-type and A-type mixture. This phase equilibrium relationship arises because, in the resultant liquid, the liquidi of the silicate minerals are depressed in an eutectic-like fashion, whereas the chromite liquidus rises slightly from a straight line between its

crystallization temperatures in the end-member melts. This type of magma mixing has been proposed for the genesis of Bushveld Complex chromitites (e.g., von Gruenewaldt and Merkle, 1995).

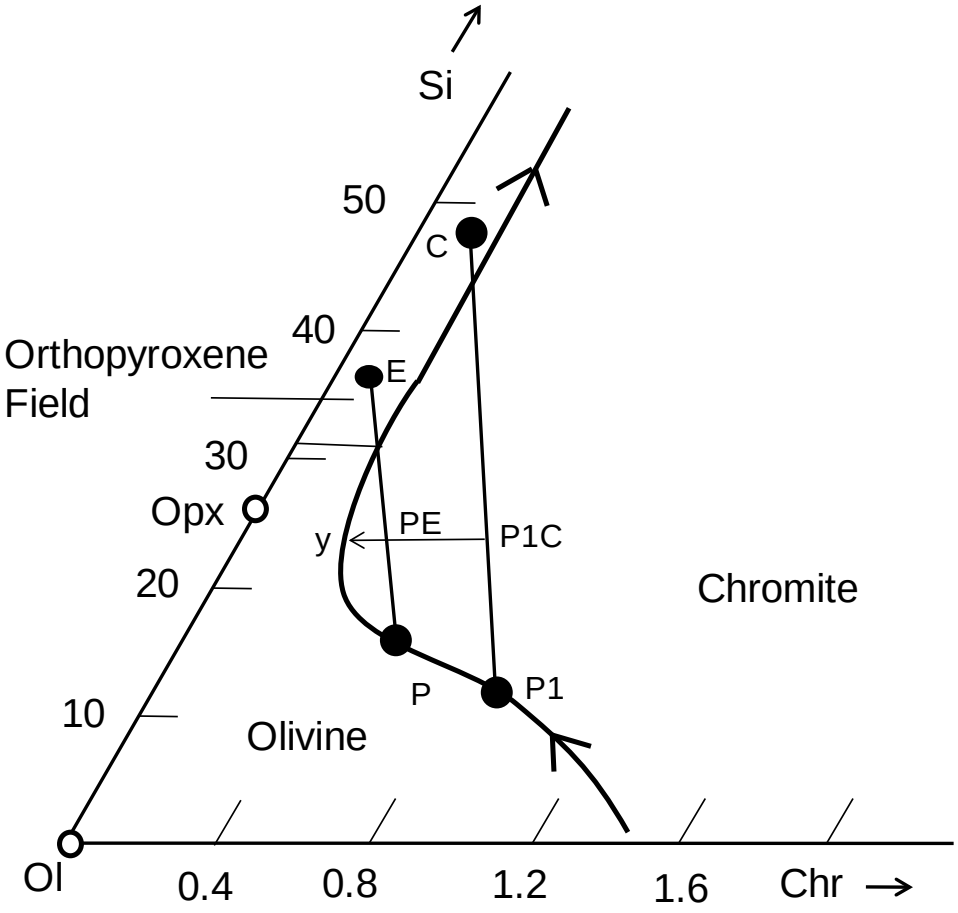


**Figure 31:** Schematic phase diagram of the olivine-chromite-quartz (Ol-Opx-Si) illustrating the consequence of mixing primitive magma (P) with a well fractionated variant (E) and the addition of silica-rich matreial (C) to a a primitive magma (P1). After Irvine (1977) and Naldrett *et al*. (1990).

**Model 3: Crustal contamination**

The third magma mixing model involves the contamination of continuous inputs of parental magma with felsic melt derived from the country rocks (Irvine, 1975). In Figure 31, the parent magma (P1) is sitting on the olivine-chromite cotectic. The magma is contaminated by silica-rich material (C in Figure 31) and the composition of the resultant magma (P1C) now lies in the chromite field. It will crystallize chromite alone which will drive the composition of the liquid back to the olivine-chromite cotectic at point Y, resulting in the formation of a chromitite layer. Campbell and

Turner (1986) used this mechanism as an explanation for the B chromitite layer in the Stillwater Complex.

Variations of the third model have been proposed. One such idea would include in situ contamination of the main magma chamber which is continuously replenished by repeated magma injections (e.g., Schoenberg *et al*., 1999). Another idea involves contamination of the magma in a staging chamber, possibly at the mantle-crust boundary, followed by additional in situ contamination in the final magma chamber (e.g., McCandless *et al*., 1999).

**The Kemi Intrusion**

A sequence of rocks formed via Model 1 would show no isotopic variation (mixing of magmas from the same source) but sequences formed by Models 2 and 3 would show isotopic variation (mixing of magmas from difference sources). The isotopic variations displayed by the rocks of the Kemi Intrusion (Figure 16) therefore eliminate Model 1 but Models 2 and 3 may be relevant for the formation of the chromitite layers.

Rocks crystallized via Model 2 may show the association of the chromitite layers with cumulates derived from distinct lineages (e.g., the J-M Reef of the Stillwater Complex occurs in an anorthosite → peridotite → troctolite rock sequence, Irvine and Sharpe, 1983; the MG and UG chromitites of the Bushveld Complex occur in anorthosite → chromitite → pyroxenite → norite cyclic sequences, Hatton and von Gruenewaldt, 1987). Such diversity of rock types associated with chromitites is best explained by blending of two magmas of different compositions (Barnes and Naldrett, 1986; Lambert *et al*., 1994). The rock sequence of the ultramafic portion of the Kemi Intrusion (lower peridotites + bronzitites → main chromitite layer → upper peridotites→ upper bronzitites) shows cumulates derived from one type of magma only, an ultramafic magma (or the mixing of two types of ultramafic magma: an olivine-crystallising magma and an orthopyroxene-crystallising magma, as seen in Figure 31). This casts doubt on Model 2 being responsible for the formation of the main chromitite layer.

The presence of granitic xenoliths in the rocks of the Kemi Intrusion suggests that the Kemi magmas underwent crustal contamination by granitic country rocks. The alkali rich silicate inclusions found in the chromite grains (Alapieti *et al*., 1989) suggest that a contamination event of the Kemi magma lead to chromite precipitation. The modelling results

(section 6.3) indicate that contamination of the Kemi magma by Eoarchaean basement may have created the chromitites. This all supports Model 3.

### 6.4.3 Proposed model for the evolution of the Kemi Intrusion and the main chromitite layer

Alapieti *et al*. (1989) suggested that contamination of the parental magma by continental crust is the most plausible model for formation of the chromitite layers of the Kemi intrusion. This is broadly consistent with the results of this study, although the contamination of the primitive parent magma resulting in the formation of the chromitite layers must have involved Eoarchaean basement, rather than local country rock.

Any model for the origin of the Kemi Intrusion should consider the following, the first five of which are from Alapieti *et al*. (1989):

1 - The Kemi intrusion forms a sill-like intrusion in which no distinct mega-cyclic units are observed such as those found in other layered intrusions in the Fennoscandian Shield.

2 - The contact between the intrusion and the basement gneiss is irregular, showing pronounced interaction between the intrusion and the gneiss.

3 - The basal bronzitites and peridotites and the main chromitite layer have the following cumulate sequence: orthopyroxene + chromite → olivine + chromite + orthopyroxene → chromite.

4 - The chromite grains in the chromite-rich layers contain silicate inclusions which are rich in alkalis and silica.

5 - Granitic (country rock) xenoliths occur in the rocks of the Kemi Intrusion with some of the xenoliths occurring as high as 200 meters above the main chromitite layer.

6 - $\varepsilon_{Nd}$ of the rocks of the intrusion have a range from depleted mantle (*ca*. +4) to enriched crustal ( – 10) values.

The following sequence of events (four stages) have been proposed by Alapieti *et al*. (1989) to explain the formation of the main chromitite layer:

**Stage one**

The evolution of the Kemi intrusion was initiated by the entry of the first pulse of magma into the chamber (point a, Figure 32a). Modelling in the current study suggests that the initial magma had $\varepsilon_{Nd}$ as high as +5 but that this magma underwent contamination in a staging chamber in the lower crust (section 6.3) and perhaps simultaneously at the level of emplacement. The first magma pulse probably caused melting of the felsic wall-rocks. This early contamination event (dashed line, Figure 32a) was responsible for the movement of the magma composition from the olivine field to the orthopyroxene field (point b, Figure 32a) where orthopyroxene crystallization started. As a result the lowermost cumulates at the base of the intrusion are bronzititic in composition. Evidence for the contamination of the first pulse of magma are the negative $\varepsilon_{Nd}$ of these bronzitites ($\varepsilon_{Nd}$ of –2, Figure 16) and the presence of granitoid clasts associated with some of the ultramafic Kemi rocks. The two stratigraphically lowest samples (SL-04 and SL-05) have $La/Sm_{C1}$ ratios over 3 (Figure 15), the highest values observed in the intrusion. The elevated $La/Sm_{C1}$ ratios are best explained by contamination. Once crystallization began a chilled margin at the floor and roof of the chamber would have formed, discouraging further contamination.

A chromite-bearing dyke beneath the thickest part of the Kemi Intrusion has been proposed as a feeder conduit for the intrusion (Alapieti, 1996). Iljina and Hanski (2005) believed that the composition of this dyke provides evidence that the parental magma was saturated in chromite and carried suspended chromite grains into the magma chamber. Three bronzitites from the basal zone (section 4.2.1) contain chromite grains interstitial to the orthopyroxene (Figure 4) suggesting the crystallization sequence orthopyroxene → chromite + minor plagioclase. This sequence is not consistent with the proposed chromite-saturated parent magma for the intrusion. Therefore the model of Alapieti *et al*. (1989) needs modification such that the first stage of chromite crystallization occurred after the magma had entered the magma chamber, also suggesting that the chromite need not have been carried in suspension into the chamber (unless it was also carrying suspended orthopyroxene). The crystallization of orthopyroxene would drive the composition of the contaminated magma towards the orthopyroxene-chromite cotectic (point c, Figure 32a). Here

both orthopyroxene and chromitite would have crystallized out of the magma to form the lowermost bronzitite layer.

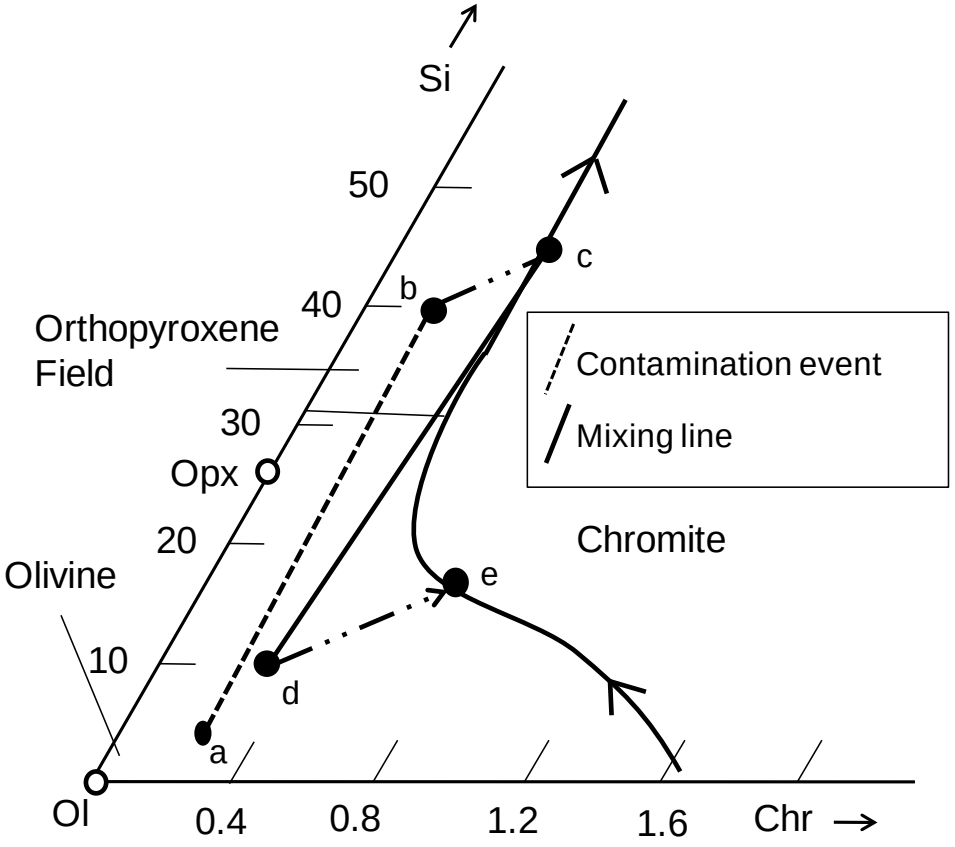


**Figure 32a:** Schematic phase diagram of the olivine-chromite-quartz (Ol-Chr-Si) and illustrating the consequence of mixing primitive mafic magma with enriched felsic country rocks during the first two stages as outlined it the text. After Irvine (1975) and Alapieti *et al.* (1989).

**Stage two**

Entry of a fresh magma pulse (with the same composition as point a in Figure 32a) into the chamber commenced the second stage. The fresh magma mixed with the contaminated magma (solid mixing line in Figure 32a) and moved the composition of the liquid into the olivine field (point d, Figure 32a) where further crystallization resulted in olivine cumulates. Olivine crystallization drove the composition of the magma towards the olivine-chromite cotectic (point e, Figure 32a), whereupon it crystallized olivine and chromite. This resulted in the deposition of the olivine + chromite cumulate above the orthopyroxene + chromite cumulate.

**Stage three**

Entry of a third pulse of fresh magma (with a composition PC in Figure 32b) into the chamber commenced the third stage. The current study (section 6.3) suggests that this third pulse of magma was a contaminated melt. This is inconsistent with the Alapieti *et al.* (1989) model which proposed that the third pulse of magma consisted of a primitive melt.

The contaminated magma mixed with the magma in the chamber (point e, Figure 32b) moving the composition of the liquid into the chromite field (point f, Figure 32b), where sole chromite crystallization resulted in the formation of the main chromitite layer. Evidence for this proposed contamination is found in the form of small alkali-rich silicate inclusions in chromite grains, described by Alapieti *et al*. (1989). It is also possible that such inclusions could also have originated through metamorphism of the chromite grains (which the intrusion has undergone) as described by Evans and Frost (1975) and Barnes (2000). The high negative $\varepsilon_{Nd}$ (– 8) of the main chromitite layer is evidence that the chromites crystallized from a magma with a significant crustal component.

During the accumulation of the main chromitite the composition of the liquid reverted to the cotectic (point g, Figure 32b) which resulted in olivine and chromite crystallizing in cotectic proportions. The petrography of the upper bronzitites (Figure 6) shows that the olivine and chromite are euhedral while the orthopyroxene is sub-euhedral to anhedral. This suggests that olivine and chromite preceded crystallization of orthopyroxene. Orthopyroxene grains may also enclose chromite, a feature which is consistent with this crystallization sequence.

**Stage four**

The presence of thin chromitite layers above the main chromitite layer suggests that the liquid composition shifted back to the primary field of chromite periodically (point h, Figure 32b). These shifts may have resulted from continued mixing of the resident magma with small pulses of contaminated magma (contaminated in the staging chamber with lower crustal material). The variation in $\varepsilon_{Nd}$ with height is evidence for continued minor contamination of the resident magma.

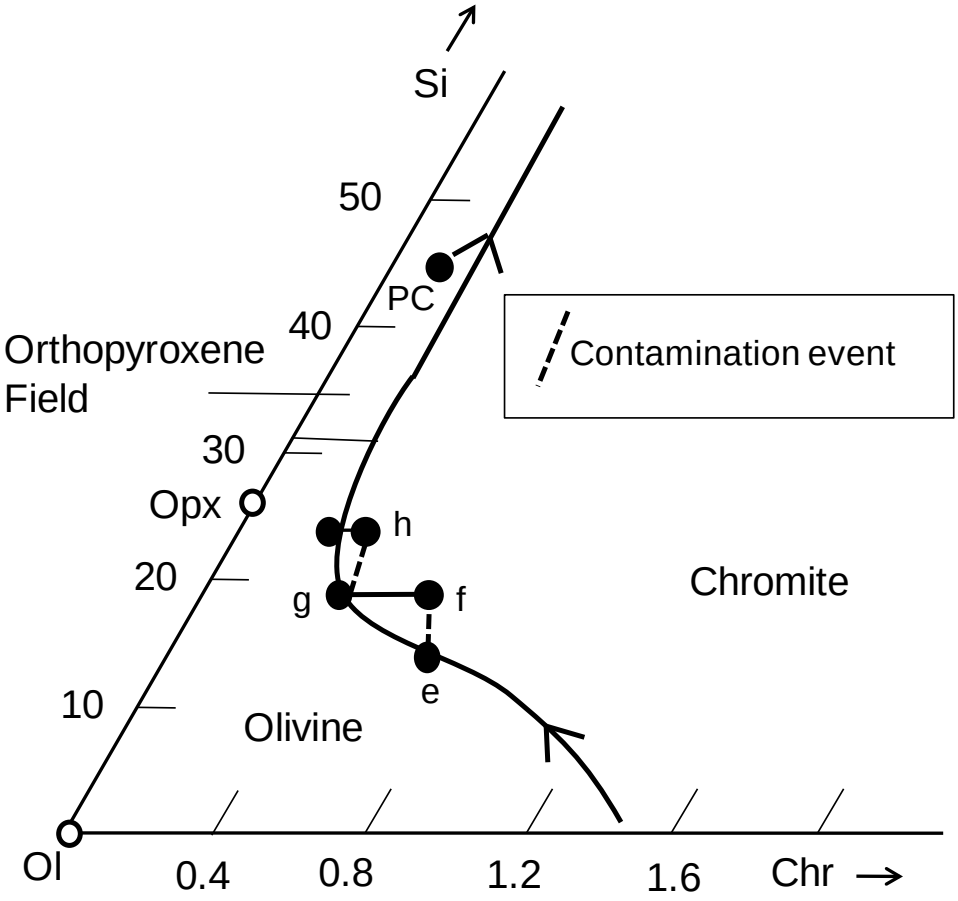


**Figure 32b:** Schematic phase diagram of the olivine-chromite-quartz (Ol-Chr-Si) and illustrating the consequence of mixing primitive mafic magma with enriched felsic country rocks during the third and fourth stages as outlined it the text. After Irvine (1975) and Alapieti *et al.* (1989).

**Stage five**

In the current study the Nd isotopic results (Figure 16) and the contamination modelling (section 6.3) suggest that addition of another stage to the model of Alapieti *et al.* (1989) is required to explain the evolution of the rock types above the upper peridotites. The continued crystallization of olivine would have moved the composition of the resident magma into the pyroxene and plagioclase fields and crystallized the overlying bronzitite and websterite layers (Figures 7 and 8) some 700 to 1 000 meters above the basal contact.

The contact between the lower ultramafic and upper mafic zone of the intrusion is roughly 1 000 meters above the basal contact. The mafic zone is characterized by gabbronorite and leucogabbro with cumulus plagioclase. The transition from ultramafic cumulates to mafic cumulates

can be explained by the continued fractional crystallization of the evolved magma. The low $\varepsilon_{Nd}$ in this zone (ranging from – 5 to – 10) suggests that the magmas from which these rocks crystallized were contaminated by 3.7 Ga old lower crustal material (Section 6.3). This indicates that there were increasing proportions of contamination occurring in a staging chamber hosted by 3.7 Ga rocks in the lower crust and that in-situ contamination in the Kemi chamber may have ceased (possibly all the unstable wall-rocks and roof-rocks had already fallen into the magma pool or maybe the magma was not as turbulent now to cause wall-rocks to become dislodged?).

## 6.5 Origin of the PGE-enriched zones

### 6.5.1 Models for the formation of PGE ores

There are two main competing models for the origin of PGE stratiform deposits. The traditional model (e.g., Campbell *et al*., 1983, Naldrett *et al*., 1990) involves mixing of two different magmas leading to the creation of an immiscible sulphide liquid in the silicate melt. Settling of the denser immiscible sulphide liquid through the magma allows the sulphide liquid to scavenge the PGE from the silicate melt. The PGE-enriched sulphide liquid accumulates in stratiform layers on the cumulate crystal pile.

The more recent model involves the interaction of a volatile-rich fluid, which has exsolved from the interstitial liquid within the cumulate pile, with cumulates and residual melt in the magma chamber (e.g., Barnes and Campbell, 1988; Boudreau and McCallum, 1989; 1992). These authors propose that a chlorine-rich fluid migrates upwards through the cumulate pile and scavenges any sulphur and PGE present in the cumulates. When the upward-migrating fluid meets the stratigraphically higher, hotter intercumulus melt, which is not yet fluid saturated, it dissolves in the melt. This adds both sulphur and PGE to the silicate melt resulting in sulphide precipitation.

#### 6.5.1.1 Fluid-transport model

The key test for the involvement of volatile-rich fluids in the PGE mineralization of the Kemi Intrusion would be the Pd/Ir and Pt/Ir ratios. PGE deposits of hydrothermal origin (e.g., the Lac des Iles Complex) have extremely high Pd/Ir and Pt/Ir ratios (in excess of 250) due to the mobility of PPGE relative to IPGE (e.g., Brügmann *et al*., 1989; Lavigne and Michaud,

2001). The majority of the Pd/Ir and Pt/Ir ratios from the Kemi Intrusion (Figure 35) are in the range of 10 to 20.

Textural evidence for the role of late magmatic fluids includes the association of apatite, graphite and pegmatitic textures with the ore zones (e.g., Barnes and Campbell, 1988). The low Pd/Ir and Pt/Ir ratios, lack of pegmatitic textures and the lack of apatite, graphite and significant sulphide horizons provide no support for the involvement of hydrothermal volatile-rich fluids in PGE enrichment of the Kemi Intrusion.

#### 6.5.1.2 Magma-mixing model

As with the chromitites there are three models on the mixing theme that could produce an immiscible sulphide liquid in the silicate melt:

**Model 1: Mixing of differentiated and primitive magma**

The mixing of two batches of the same magma at different stages of fractionation (points A and B, Figure 33) can stimulate sulphide segregation from the silicate melt (e.g., Haughton *et al.,* 1974; Li *et al*., 2001). Naldrett *et al*. (1990) supported this model because it seemed to offer an explanation for the enrichment of sulphide and PGE in some relatively differentiated Bushveld chromitites (Figure 33). However, recent studies (Barnes *et al*., 2009) have shown that the Bushveld magmas are so strongly sulphur undersaturated that the whole concept of sulphide saturation being caused by mixing of two batches of the same magma has to be treated with caution.

If this model were to apply to the Kemi Intrusion all rocks would have uniform Nd isotopic compositions, which they do not (Figure 16).

**Model 2: Mixing of magmas of different lineages**

It has been suggested that the mixing of two sulphur undersaturated magmas of different lineages could initiate sulphur saturation (e.g., Naldrett and von Gruenewaldt, 1989; Li *et al*., 2001).

**Model 3: Crustal contamination**

Sulphur saturation can be achieved by the contamination of the magma with siliceous country rocks (e.g., Irvine, 1975).

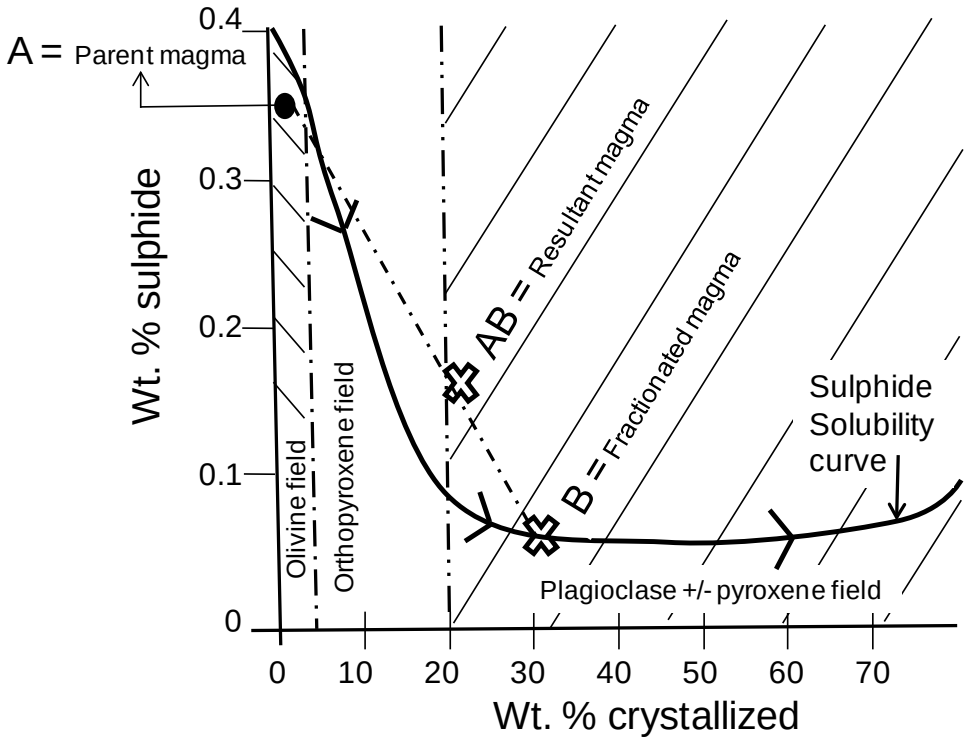


**Figure 33:** Schematic diagram showing the relationship between the concave shaped sulphur solubility curve and a fractionating magma. From Naldrett and von Gruenewaldt (1989).

The isotopic heterogeneity of the Kemi rocks is consistent with both of these models accounting for PGE enrichment in the Kemi Intrusion. However, the low sulphur abundances of the relatively PGE-enriched Kemi rocks (Table C9) are inconsistent with Models 2 and 3. Merkle (1992) showed that post-magmatic modification of PGE-enriched chromites could result in a significant loss of sulphur from the chromites which could explain how a sequence of rocks derived from Models 2 or 3 could have low sulphur abundances.

The lack of discernable trends in the variations of PGE, Cu and Ni with sulphur (Figure 19a) suggests that chalcophile element variations were not controlled by sulphide. The low sulphur abundances combined with the uniformly low copper contents (Table C9) and relatively low PGE contents of the Kemi rocks suggests that the magma may have never attained sulphur saturation throughout the evolution of the Kemi Intrusion. This is unusual because the formation of the massive main chromitite layer should have led to a significant reduction in the iron content and decreased sulphur solubility of the magma. This all suggests that sulphur was not the

main controlling agent responsible for the enrichment of PGE in the Kemi rocks and other potential agents need to be considered for that role.

### 6.5.2 Models of enrichment of PGE in chromitites

The close association of the main chromitite layer and the main PGE enrichment zone (Figure 17) would suggest that the origin of the main chromitite layer is linked to that of PGE enrichment. The origin of PGE mineralization in chromitites remains controversial, partly because many chromitites are sulphur-poor and thus a link between PGE concentration and magmatic sulphides is less evident (e.g., Maier, 2005). Four major models have been distinguished:

**Model 1: Flux-melting and percolation of a fluid-rich intercumulus liquid**

Nicholson and Mathez (1991) suggested that the Merensky chromitite stringers crystallized from a liquid that formed in response to flux-melting of a norite–pyroxenite by percolation of a fluid-rich intercumulus liquid ascending through the semi-consolidated cumulate pile. If the protocumulates contained small amounts of disseminated sulphides it is conceivable that these were concentrated during flux melting to form the reef.

**Model 2: PGM in solid solution in chromites**

Some of the PGE in the chromitites (notably the IPGE and Rh) could have been concentrated by means of solid solution into the chromite from the magma (Peach and Mathez, 1996; Righter *et al*., 2004).

Possible empirical evidence in support of this model is the well-defined positive correlation between the IPGE and Cr in some mafic–ultramafic intrusions, notably the Fiskanaesset Complex of Greenland (Morgan *et al*., 1976), and the Thole sills of South Africa which are associated with the Usushwana Complex (Maier and Passaportis, 2004).

**Model 3: PGE originally concentrated by magmatic sulphides followed by desulphidation**

Super-saturation in both sulphide and chromite could have been triggered by contamination, or precipitation of chromite (in response to contamination; Irvine (1975)) could have triggered sulphide supersaturation

(e.g., Naldrett and von Gruenewaldt, 1989). As sulphur is bonded to $Fe^{2+}$ in the magma, crystallization of Fe-rich minerals, notably chromite and magnetite, causes a decrease in sulphur solubility. The lack of sulphides in some chromitites and magnetite layers is thus puzzling (e.g., Hulbert and von Gruenewaldt, 1982; Maier *et al*., 2003). The lack of sulphides in the chromitite layers suggests that some sulphur was lost during crystallization and cooling of the rocks (Naldrett and Lehmann, 1988). Desulphidation may partially occur during interaction of the sulphide with chromite (Naldrett and Lehmann, 1988; Mathez, 1999), according to the reaction:

$4/3\ Fe_2O_3$ (chromite) + $1/3\ FeS = Fe_3O_4$ (chromite) + $1/6\ S_2$

Sulphur loss could have caused the fugacity of sulphur to drop sufficiently in the sulphide liquid, resulting in the crystallization of IPGE-rich platinum-group minerals (PGM) such as laurite from the sulphide liquid (Barnes and Maier, 2002); or the formation of residual monosulphide solid solution (mss) enriched in IPGE and a Pd- and Pt-rich sulphide liquid (e.g., Maier and Barnes 1999; Peregoedova *et al*., 2004). The mss could exsolve IPGE-rich PGM which is retained by the chromitites; and the Pt- and Pd-rich sulphide melt could have been filter pressed during compaction, which would crystallize above the chromitites (Maier and Barnes, 1999; Barnes and Maier, 2002).

**Model 4: Crystallization of chromite may lead to localized reducing environment**

Mungall (2002) and Finnigan and Brenan (2004) presented experimental evidence that crystallization of chromite may lead to localized reducing environment of the silicate melt surrounding the chromite promoting nucleation and crystallization of PGE alloys. The latter may be enclosed by the crystallizing chromite. However, it remains to be determined whether the PGE can diffuse fast enough to the crystal surfaces of the platinum-group minerals (PGM) to permit the crystals to grow to their observed sizes.

### 6.5.3 Application of models to the Kemi Intrusion

**Model 1: Flux-melting and percolation of a fluid-rich intercumulus liquid**

Model 1 seems unlikely as the various chromitite layers that occur in the Kemi Intrusion are massive in nature and can be traced across the

entire length of the intrusion. They do not occur as stringers and thus Model 1 does not apply. Model 1 also requires the flux-melting of a norite-pyroxenite but there are no norite rocks above or below the main chromitite layer.

**Model 2: PGM in solid solution in chromites**

The sulphur-poor nature of many chromitites and the relatively rare association of chromite-hosted laurite with other PGE or BMS have lead some authors (e.g., Hiemstra, 1979; Scoon and Teigler, 1994; Peach and Mathez, 1996; Righter *et al*., 2004) to propose that the laurite or IPGE-enriched PGM crystallized directly out of the silicate liquid and was subsequently enclosed by the crystallizing chromites as opposed to crystallizing out of a segregated sulphide-liquid. Tredoux *et al*. (1985) explained that the PGE would need to form atomic clusters in the silicate magma in order to crystallize directly out of the melt. These clusters would essentially pre-concentrate the PGE. Theoretically, the heavier PGE (Os, Ir and Pt) should have a higher chance of forming clusters than the lighter PGE (Ru, Rh and Pd) and thus the chromitite layers would be dominated by Os, Ir and Pt. The majority of the PGM described from the Kemi rocks are laurites and IPGE-enriched PGM (Kojonen *et al*., 2005) and the lack of significant modal proportions of BMS suggest that this model may be a valid explanation for the PGE-enrichment of the Kemi rocks.

A weakness of this model is that it requires the magma to become saturated in PGM when the PGE are only present at ppb concentrations (e.g., Mathez, 1999) as is evident in the Kemi Intrusion. Secondly, PGE clustering have not been experimentally proved and their existence is strongly questioned (e.g., Mathez, 1999). Also, the main chromitite seam is Os-, Ir- and Ru-enriched but is relatively depleted in Pt. Thirdly, physical inclusions of PGM in the chromites could also account for the high IPGE observed in the chromites of the Kemi Intrusion (Kojonen *et al*., 2005). Lastly the literature has no reports of chromites with PGE in solid solution.

**Model 3: PGE originally concentrated by magmatic sulphides**

**Main chromitite layer**

A feature of the lower, larger PGE enriched zone is the reversal between the ΣIPGE and ΣPPGE concentrations which occurs between the main chromitite layer and the overlying upper peridotites (Figures 18 and

22). Von Gruenewaldt *et al*. (1989) showed that low (Pt + Pd)/IPGE and Pd/Ir ratios indicate that both chromite and sulphide played a role in concentrating the PGE while high values favour sulphide as the controlling agent. The low (Pt + Pd)/IPGE and Pd/Ir ratios (less than 1 for both) of the basal silicates and the main chromitite layer (Figures 34 and 35) indicate that chromite and sulphide was crystallizing out of the melt together and they both may have been responsible for concentrating PGE during the formation of these rocks.

The upper peridotites sampled above the main chromitite layer have higher (Pt + Pd)/IPGE and Pd/Ir ratios (over 2, Figures 34 and 35) and higher ΣPPGE concentrations (over 100 ppm, Figure 18) than the basal samples. This would suggest that there is an increase in the amount of sulphide separating from the melt and a decrease in the amount of chromite separating which lead to a relative enrichment of ΣPPGE in these rocks. The highest (Pt + Pd)/IPGE and Pd/Ir values are found in the upper, mafic portion of the intrusion which suggest that sulphides alone are separating from the melt during the crystallization of the mafic rocks. Strangely, the Pd/Ir ratios are very low when compared to gabbroic cumulates of other layered intrusions, e.g. the Bushveld Complex (e.g., Maier and Barnes, 2010).

The enrichment of IPGE relative to PPGE in chromite-bearing rocks has been observed by several authors (e.g., Crocket, 1981; Barnes *et al.*, 1988). This is demonstrated in Figure 19a. The IPGE is positively correlated with the Cr which suggests that the IPGE was partitioned into the chromite grains. The chromite grains in the Kemi Intrusion contain IPGE- and Rh-PGM inclusions, most notably laurite (Kojonen *et al.,* 2005). A possible explanation for all these observations is that the IPGE are fractionated from the sulphide melt into the crystallizing chromitites as IPGE-dominated PGM inclusions (e.g. laurite). The remaining melt is relatively enriched in PPGE (Maier and Barnes, 1999).

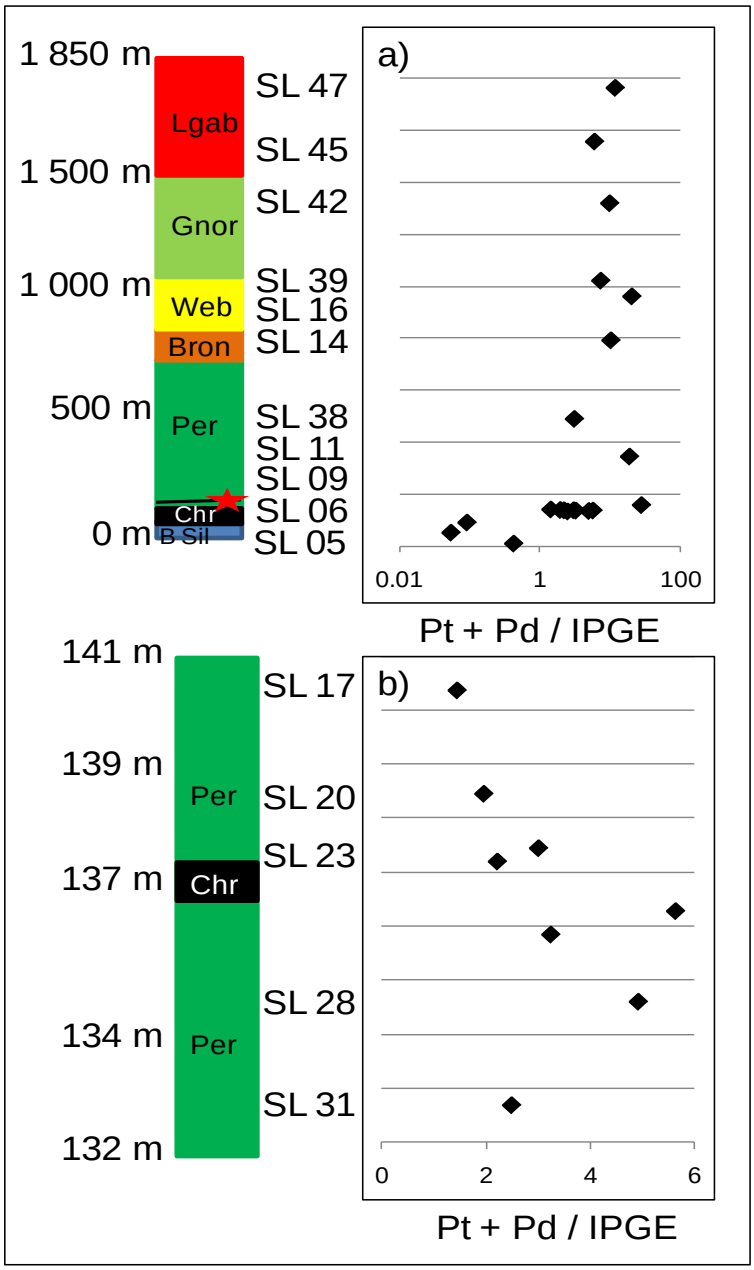


**Figure 34:** Variations in the Pt + Pd / IPGE abundances versus the stratigraphic height across (a) the entire intrusion, and (b) the small chromitite layer above the main chromitite layer.

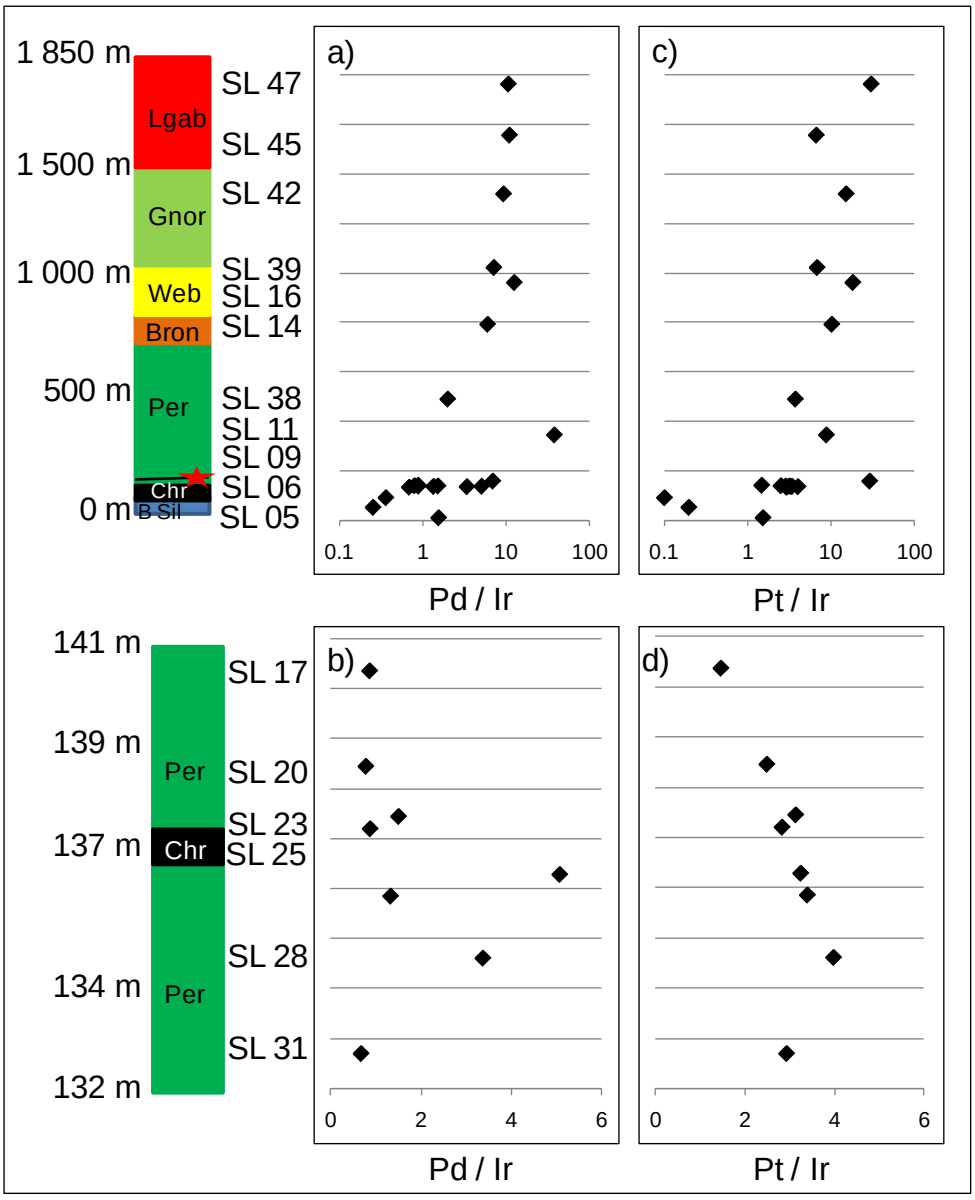


**Figure 35:** Variations in the Pd / Ir and Pt / Ir ratios versus the stratigraphic height across (a and c respectively) the entire intrusion and (b and d respectively) the small chromitite layer above the main chromitite layer.

**The small chromitite layer above the main chromitite layer**

The variations of total PGE abundances across the small chromitite layer (Figure 18b) and the (Pt + Pd)/IPGE and Pd/Ir ratios (Figures 34b and 35b) clearly show the enrichment of PPGE relative to IPGE in the upper peridotite samples. This is consistent with the prediction of Model 3 that the magma that crystallized the rocks immediately overlying the main chromitite layer would be PPGE-enriched.

There are no systematic changes in the PGE abundances, Pd/Ir and PGE/S ratios between the peridotites above and below the small

chromitite layer. This homogeneity provides little insight into the role chromite may have had in influencing the behaviour and distribution of PGE during the formation of the small chromitite layer.

A subtle reversal above the small chromitite layer is visible in the PGE/S plot (Figure 21b). The ratio shows a steady decrease with height above the small chromitite layer. This is due to the increase in sulphur abundance of the peridotites above the small chromitite seam (the PGE contents are broadly constant). This could be due to the break-down of the desulphidation reaction of Naldrett and Lehmann (1988) because the peridotites above the small chromitite layer do not contain enough chromite grains for this reaction to occur. Hence the systematic increase in sulphur content.

More detailed sampling of the small chromitite layer and the surrounding peridotites is required to reduce the uncertainty surrounding the influence the small chromitite layer may have had on the behaviour and distribution of PGE in these rocks.

**The second PGE-enriched zone**

The second zone of PGE enrichment is characterized by relatively high PGE concentrations and high PGE / sulphur ratios (Figures 18a and 20). The PGE enrichment occurs immediately below the ultramafic-mafic contact of the intrusion (the 30 ppb ΣPGE content of the upper bronzitites and websterites is nearly double that of the underlying peridotite and overlying gabbroic cumulates). The high (Pt + Pd)/IPGE and Pd/Ir ratios (both about 10, Figures 34 and 35) and the lack of chromite in this second zone of enrichment suggest that sulphur alone was the controlling agent for the PGE mineralization, which is inconsistent with Model 3. This PGE enrichment zone occurs immediately below the first appearance of cumulus plagioclase in the Kemi Intrusion, and is thus somewhat analogous to the Main Sulphide Zone of the Great Dyke or the main PGE reef in the Munni Munni Intrusion of Australia.

More detailed sampling of the second PGE-enriched zone is required to provide a clearer insight into the evolution of this PGE-enriched zone.

**Problems with model 3**

The model of an original sulphide control of the PGE in the chromitites and the subsequent loss of Pd- and Pt-enriched sulphide liquid is supported by the observation that PGM in the chromitites are often associated with base metal sulphides (BMS) (e.g., McLaren and De Villiers, 1982; von Gruenewaldt *et al*., 1986; Talkington and Lipin, 1986; Li *et al*., 2004). BMS were not observed in this study (section 4) and they are rare in Kemi rocks (Alapieti *et al*., 1989). The low sulphur abundances (Table C9) casts doubt on wether the Kemi magma ever attained temporary sulphur saturation as described in model 3.

The low sulphur and copper contents (50 to 300 ppm and 10 to 30 ppm respectively, Figure 17) suggests that the Kemi magma was sulphur undersaturated. If the Kemi magma is assumed to have 1000 ppm sulphur and 100 ppm copper (typical of basalts) then the sulphur undersaturated cumulates should have sulphur and copper contents in the range of 100 to 300 ppm and 10 to 30 ppm respectively, which is in agreement with the data from this study. The highest PGE contents in terrestrial basalts are 25 ppb each for Pt and Pd which would result in cumulates with 3 to 8 ppb each for Pt and Pd. The cumulates show Pt and Pd contents far above this range which would suggest that there is a small amount of cumulus PGE in these cumulates.

During compaction of the chromite crystal pile, the fractionated PPGE-rich sulphide liquid would be pushed up and out of the cumulates into the silicate liquid above (Barnes and Maier, 2002). However, it has been questioned if the heavier, denser sulphide liquids (e.g., Merkle and McKenzie, 2002) could be pushed upwards due to the large difference in density between a sulphide and silica liquid.

Based on the geochemical and PGE data there is still uncertainty on whether model 2 or 3 can provide satisfactory explanations for the PGE-enrichment of the main chromitite layer.

**Model 4: Crystallization of chromite may lead to localized reducing environment**

The results of this study cannot confirm whether Model 4 is applicable so this model remains a possibility, but without any evidence for or against it.

### 6.5.4 PGE-enriched zones: comparison of the Kemi Intrusion with those of other intrusions

The PGE profile obtained in this study is similar to that of Kojonen *et al*. (2005) which shows enrichment of IPGE relative to PPGE in the main chromitite seam. Three representative mantle-normalized PGE profiles (one of the main chromitite layer, one of the peridotite immediately overlying the main chromitite layer and one of a websterite) from the Kemi Intrusion were compared to other PGE-reefs from other layered intrusions (Figures 36 and 37). The PGE profiles of the peridotite and the websterite are similar to those of the Merensky Reef, J-M Reef and the sulphide reefs from the Penikat and Portimo Intrusions which are depleted in IPGE relative to PPGE. The Merensky Reef and the peridotite and websterite show a flat or slightly negative slope from Rh to Pd whereas all the other reefs show a strong positive slope from Rh to Pd. The PGE profile of the main chromitite layer of the Kemi Intrusion is enriched in IPGE relative to PPGE and has a negative slope from Rh to Pd.

Figure 37 shows the Kemi main chromitite layer compared to several UG chromitite layers and the Merensky Reef and one chromitite layer from the Penikat Intrusion. The shape of the profile of the Kemi chromitite layer is different to that of the other chromitite layers. The Bushveld layers and the Penikat layer all show a positive slope from Os to Pd with enriched PPGE relative to IPGE. The Kemi layer exhibits a negative slope from Os to Pd with enriched IPGE relative to PPGE. A possible explanation for this difference could be the stratigraphic locations of those chromitites within their respective intrusions. The main Kemi chromitite layer is the lowermost chromitite layer in the intrusion while the Merensky Reef and UG chromitites occur stratigraphically above the Lower and Middle Group chromitites within the Bushveld Complex. The Pt and Pd abundances and the PPGE/IPGE ratios of the LG chromitites are higher than those of the UG chromitites. The IPGE were likely concentrated into the chromite grains of the LG and MG chromitites, probably as grains of laurite and alloys. The bulk of the Pt, Pd along with lesser proportions of the other PGE were concentrated into the sulphide liquid that would eventually crystallize out the Merensky and UG chromitites (e.g., Scoon and Teigler, 1994; Naldrett *et al*., 2009).

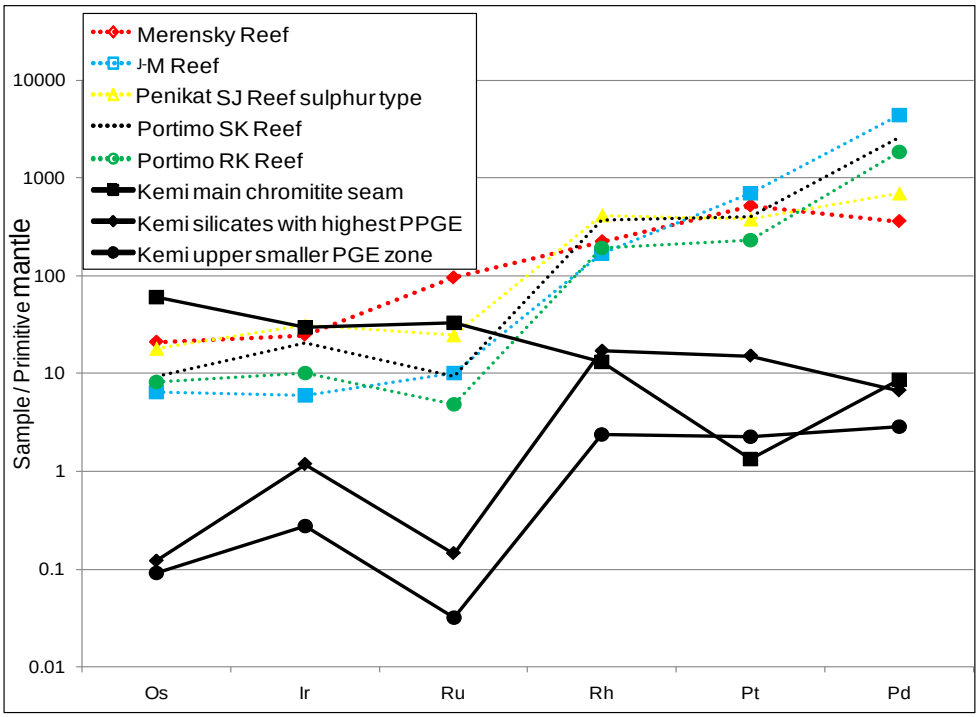


**Figure 36:** Comparison of the primitive mantle-normalized PGE profile of the PGE-enriched zones of the Kemi Intrusion with those of other intrusions. Merensky Reef from Barnes and Maier (2002); J-M Reef from Barnes *et al*. (1985); Penikat from Halkoaho *et al*. (1989), (1990); Halkoaho (1993); Portimo from Iljina (1994).

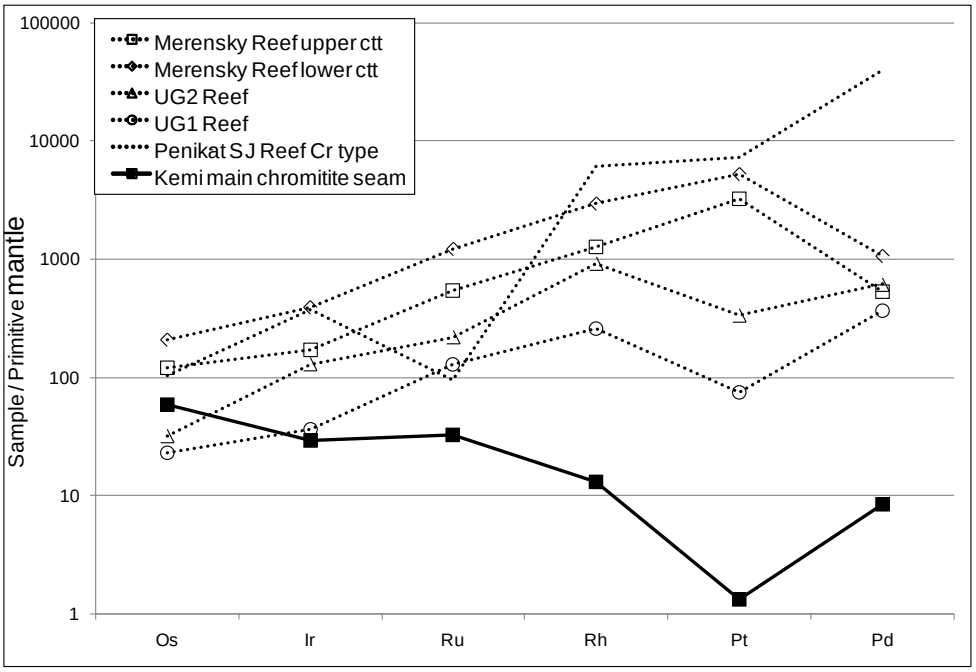


**Figure 37:** Comparison of primitive mantle-normalized PGE values from various PGE-enriched chromitite reefs with the main chromitite reef of the Kemi Intrusion. Merensky Reef from Barnes and Maier (2002); the UG reefs from von Gruenewaldt and Merkle (1995); and the Penikat S-J Reef Cr type from Halkoaho *et al*. (1989), (1990); Halkoaho (1993).

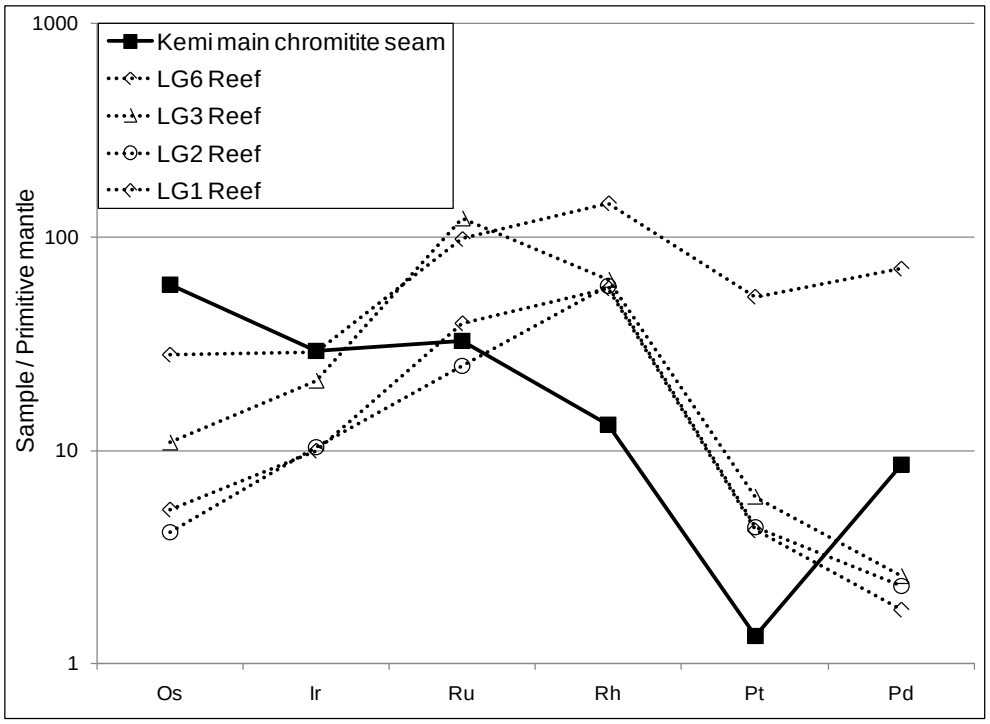


**Figure 38:** Comparison of primitive mantle-normalized PGE values from various Lower Group chromitite reefs of the Bushveld Complex with the main chromitite reef of the Kemi Intrusion. The LG reefs are from von Gruenewaldt and Merkle (1995).

Figure 38 shows the Kemi main chromitite layer plotted against some of the LG chromitite layers. The LG chromitites are IPGE enriched relative to the PPGE with a positive slope from Os to Rh and a negative slope from Rh to Pd, which is similar to the profile of the main chromitite layer. This is consistent with the IPGE-enriched nature of the stratigraphically lower chromitites and the PPGE-enriched nature of the stratigraphically higher chromitites within an intrusion. The Kemi main chromitite layer is analogous to the IPGE-enriched LG chromitites in terms of its stratigraphic location while the same principle applies to that of the other Fennoscandian reefs which are PGE-enriched and the PPGE-enriched Merensky Reef.

## 7 Conclusions

The Palaeoproterozoic (*ca. 2.5* - 2.4 Ga) layered intrusions that are scattered throughout the north eastern part of the Fennoscandian Shield (in Finland, Sweden and Russia) contain significant economic deposits such as chromitite layers and PGE deposits. Of all the 2.44 Ga layered

intrusions only one to date is host to a commercially viable mine. The Kemi Intrusion, located near the town of Kemi in northern Finland, is currently being mined for its chromitite deposits. The Kemi Intrusion is located stratigraphically at the contact between Neoarchaean granitoids (2.8 Ga in age) and the overlying Proterozoic sequence of volcanic and sedimentary rocks.

As noted in previous studies conducted on the Kemi Intrusion (e.g., Alapieti *et al*., 1989), the variations in major element concentrations with stratigraphic height of the intrusion correspond well with the petrology of the intrusion. The parent magma would have first started crystallizing olivine and orthopyroxene cumulates forming the peridotites and bronzitites, followed by the pyroxene cumulates of the websterites and finally the plagioclase cumulates of the gabbronorites and leucogabbros.

There is strong evidence that the intrusions of the Tornio-Näränkävaara belt were fed with two types of parental magma; a primitive, Cr-rich magma and a less primitive, Cr-poor magma. Based on the major element data it appears that the magma from which the Kemi Intrusion crystallized could have been the primitive, Cr-rich magma.

The trace and incompatible element concentrations do not systematically increase with increase in stratigraphic height of the intrusion, as is expected. The highest trace and incompatible element concentrations occur in some of the peridotites. This suggests that a small group of peridotites contain a higher proportion of trapped liquid than the rest of the intrusion.

The ultramafic portion of the intrusion shows a range in $\varepsilon_{Nd}$ from depleted (+4) to slightly enriched (-2). The slightly enriched $\varepsilon_{Nd}$ are typical of 2.44 Ga layered intrusions. The depleted $\varepsilon_{Nd}$ values are notable because the presence of depleted mantle signatures is extremely rare in the Palaeoproterozoic. The two chromitite layers sampled in the lower portion of the intrusion show negative $\varepsilon_{Nd}$ (-4 to -8) and the mafic portion of the intrusion show negative $\varepsilon_{Nd}$ (-5 to -10) as well. These negative $\varepsilon_{Nd}$ indicate the presence of crustal material in the evolution of these rocks.

The isotopic data require the Kemi parent magma was derived from a depleted mantle source instead of a “near chondritic” source. The modelling results indicate that the lower, ultramafic portion possibly underwent contamination from both upper crustal material (3.1 Ga to 2.8

Ga in age) and lower crustal material (at least 3.7 Ga in age) and the mafic portion lower crustal material only.

This combination of upper and lower crustal contaminants indicates that the Kemi magma first underwent contamination in a staging chamber within the lower crust. This is consistent with the prevailing models of emplacement for the Fennoscandian intrusions (e.g., Saini-Eidukat *et al*., 1997; Hanski *et al*., 2001; Iljina and Hanski, 2005; Lauri *et al*., 2006). The magma experienced felsic contamination and accompanying crystal fractionation in a staging magma chamber in the lower crust prior to emplacement of the magma into the upper crust. Additional in-situ contamination of the magma by the upper crust may have occurred as well.

The main PGE-enriched zone of the Kemi Intrusion occurs in the main chromitite layer and the peridotites immediately above the main chromitite layer. The basal silicates and the main chromitite layer are IPGE-enriched while the rest of the intrusion is PPGE-enriched.

The preferred model for the formation of the main PGE-enriched zone is that the original concentration of PGE occurred via sulphide scavenging. The contamination event that led to the formation of the main chromitite layer also caused temporary sulphur saturation in the magma. The reaction between the chromites and sulphides caused sulphur-undersaturation in the sulphide liquid. Due to the low levels of sulphur the PGE crystallized out of the sulphide liquid as PGM. The PGM scavenged the IPGE from the sulphide liquid and thus enriched the sulphide liquid in PPGE. The IPGE-dominant PGMs would be enclosed in the crystallizing chromite grains. Hence the main chromitite layer is IPGE-enriched. The peridotites immediately above the main chromitite layer would crystallize from the PPGE-enriched liquid. This would explain the decoupling of the IPGE from the PPGE seen in the Kemi Intrusion.

## Reference List


Alapieti, T.T., 1982. The Koillismaa layered igneous complex, Finland – its structure, mineralogy and geochemistry, with emphasize on the distribution of chromium. *Geological survey of Finland bulletin* **319**, 116.

Alapieti, T.T., Kujanaa, J., Lahtinen, J.J., and Papunen, H., 1989. The Kemi stratiform chromitite deposit, northern Finland. *Economic Geology* **84**, 1057 – 1077.

Alapieti, T.T., Filen, B.A., Lahtinen, J.J., Lavrov, M.M., Smolkin, N.F., and Voitsekhovsky, S.N., 1990. Early proterozoic layered intrusions in the northeastern part of the Fennoscandian Shield. *Mineralogy and Petrology* **42**, 1 -22.

Alapieti, T.T., 1996. The Kemi and Penikat layered intrusions. IGCP Project 336, Field conference on layered mafic complexes and related ore deposits of Northern Finland. *In*: *Guide to the pre-symposium field trip in Finland, August 9, **1996***. Espoo, Geological survey of Finland.

Alapieti, T.T., and Lahtinen, J.J., 2002. Platinum group element mineralization in layered intrusions of northern Finland and the Kola Peninsula, Russia. *The geology, geochemistry, mineralogy and mineral beneficiation of PGE.* 507 – 546.

Alapieti, T.T., 2005. Early Palaeoproterozoic (2.5 – 2.4 Ga) Tornio-Näränkävaara layered intrusion belt and related chrome and platinum-group element mineralization, northern Finland. *In*: Alapieti, T.T., and Kärki, A.J., Eds. *10th International Platinum Symposium. Guide to the post-symposium field trip,* pp. 7.

Alapieti, T.T., and Huhtelin, T.A., 2005. The Kemi intrusion and associated chromitite deposit. *In*: Alapieti, T.T., and Kärki, A.J., Eds. *10th International Platinum Symposium. Guide to the post-symposium field trip,* pp. 26.

Amelin, Yu V., and Semenov, V.S., 1996. Nd and Sr isotope geochemistry of mafic layered intrusions in the eastern Baltic Shield: Implications for the sources and contamination of Paleoproterozoic continental mafic magmas. *Contribution to Mineralogy and Petrology,* **124**, 255–272.

Anderson, J.C.Ø., and Thalhammer, O.A.R., 1998. The Mount General'skaya layered intrusion: evidence for an enriched mantle reservoir beneath the Pechenga area, Kola Peninsula, Russia. 8th International Platinum Symposium, 28 June-3 July, 1998, *Abstracts. Geol. Soc. S. Afr. and S. Afr. Inst. Min. Metall., Symp. Series* **S18**, 13–15.

Balashov, Y.A., Bayanova, T.B., and Mitrofanov, F.P., 1993. Isotope data on the age and genesis of layered basic-ultrabasic intrusions in the Kola Peninsula and northern Karelia, northeastern Baltic Shield. *Precambrian Research* **64**, 197–205.

Barnes, S.-J., and Naldrett, A.J., and Gorton, M.P., 1985, The origin of the fractionation of platinum-group elements in terrestrial magmas. *Chemical Geology* **53**, 303 – 323.

Barnes, S.-J., Boyd, R., Korneliussen, A., Nilsson, L.-P., Often, M., Pedersen, R.B., and Robins, B., 1988. The use of mantle normalization and metal ratios in discriminating between the effects of partial melting, crystal fractionation and sulphide segregation on platinum-group elements, gold, nickel and copper: examples from Norway. *In*: Prichard, H.M., Potts, P.J., Bowles, J.F.W., and Cribb, S.J., Eds. *Geo-Platinum 87.* Amsterdam, Elsevier, pp. 113 – 347.

Barnes, S.-J., and Maier, W.D., 2002. Platinum-group elements and microstructures of normal Merensky Reef from Impala Platinum Mines, Bushveld Complex. *Journal of Petrology* **43**, 103 - 128.

Barnes, S.-J., Savard, D., Bèdard, L.P., and Maier, W.D., 2009. Selenium and sulphur concentrations in the Bushveld Complex of South Africa and implications for formation of the platinum-group element deposits. *Mineralium Deposita* **44**, 647 – 663.

Barnes, S.J., and Naldrett, A.J., 1986. Geochemistry of the J-M Reef of the Stillwater Complex, Minneapolis Adit area. II. Silicate mineral chemistry and petrogenesis. *Journal of Petrology* **27**, 791 – 825.

Barnes S.J., and Campbell, I.H., 1988. Role of late magmatic fluids in Merensky-type platinum deposits: a discussion. *Geology* **16**, 488 – 491.

Barnes, S.J., 2000. Chromite in komatiites, II. Modification during greenschist to mid-amphibolite facies metamorphism. *Journal of Petrology* **41**, 387 – 409.

Blundy, J., and Wood, B., 2003. Partitioning of trace elements between crystals and melts. *Earth and Planetary Science Letters* **210**, 383 – 397.

Boudreau, A.E., and McCallum, I.S., 1989. Investigations of the Stillwater Complex: Part V. Apatites as indicators of evolving fluid compositions. *Contributions to Mineralogy and Petrology* **102**, 138 - 153.

Boudreau, A.E., and McCallum, I.S., 1992. Concentration of platinum-group elements by magmatic fluids in layered intrusions. *Economic Geology* **87**, 1830 – 1848.

Brügmann, G.E., Naldrett, A.J., and Macdonald, A.J., 1989. Magma mixing and constitution zone refining in the Lac des Iles Complex, Ontario; genesis of platinum-group element mineralization. *Economic Geology* **84**, 1557 – 1573.

Cameron, E.N., 1980. Evolution of the lower critical zone, central sector, eastern Bushveld Complex, and its chromitite deposits. *Economic Geology* **75**, 845 – 871.

Campbell, I.H., and Desborough, G.A., 1969. Occurrence and characteristics of chromite deposits – Eastern Bushveld Complex. *Economic Geology* **4**, 23 – 40.

Campbell, H., Naldrett, A.J. and Barnes, S.J., 1983. A model for the origin of the platinum-rich sulphide horizons in the Bushveld and Stillwater Complexes. *Journal of Petrology* **24**, 133 - 165.

Campbell, H., and Turner, J.S., 1986. The role of convection in the formation of platinum and chromite deposits in layered intrusions. *Mineralogical Association of Canada Short Course Handbook* **12**, 236 – 278.

Cawthorn, R.G., 2002. The role of magma mixing in the genesis of PGE mineralization in the Bushveld Complex: thermodynamic calculations and new interpretations – discussion. *Economic Geology* **97**, 663 – 666.

Cawthorn, R.G., 2005. Pressure fluctuations and the formation of the PGE-rich Merensky and chromitite reefs, Bushveld Complex. *Mineralium Deposita* **40**, 231 – 235.

Crocket, J.H., 1981. Geochemistry of the platinum-group minerals. *Canadian Institute of Mineralogy and Metallurgy Special Issue* **23**, 47 – 64.

DePaolo, D.J., 1981a. Neodymium isotopes in the Colorado Front Range and crust-mantle evolution in the Proterozoic. *Nature* **291**, 684 – 687.

DePaolo, D.J., 1981b. Trace element and isotopic effects of combined wallrock assimilation and fractional crystallization. *Earth and Planetary Science Letters* **53**, 189 – 202.

DePaolo, D.J., 1988. Neodymium isotope geochemistry: an introduction. *Springer, Berlin*.

DePaolo, D.J., and Wasserburg, G.J., 1976. Nd isotopic variations and petrogenetic models. *Geophysics Research Letters*. **3,** 249 – 252.

DePaolo, D.J., and Wasserburg, G.J., 1979. Petrogenetic mixing models and Nd-Sr isotopic patterns. *Geochemica et Cosmoschimica Acta* **43**, 615 – 627.

Eales, H.V., de Klerk, W.J., Butcher, A.R., and Kruger, F.J., 1990. The cyclic unit beneath the UG1 chromitite (UG1FW unit) at RPM Union Section Platinum Mine – Rosetta stone of the Bushveld Upper Critical Zone. *Mineralogical Magazine* **54**, 23 – 43.

Eales, H.V., and Cawthorn, R.G., 1996. The Bushveld Complex *In:* Cawthorn, R.G., Eds. *Layered Intrusions*

Elliot, D.H., and Fleming, T.H., 2000. Weddell triple junction: The principal focus of Ferrar and Karoo magmatism during initial break-up of Gondwana. *Geology* **28**, 539 – 542.

Ernst, R.E., and Buchan, K.L., 1997. Layered mafic intrusions: a model for their feeder systems and relationships with giant dyke swarms and mantle plume centres. *South African Journal of Geology* **100**, 319 – 334.

Evans, B.W., and Frost, B.R., 1975. Chromian spinel in progressive metamorphism: a preliminary analysis. *Geochimica et Cosmochimica Acta* **39**, 959 – 972.

Faure, G., 1986. Principles of isotope geology. *John Wiley & Sons*

Finnigan, C.S., and Brenan, J.M., 2004. Experimental evidence for the co-precipitation of PGE alloys and chromite as a result of local melt reduction during chromite crystallization. *Geoscience Africa* Johannesburg Abstracts, **201**

Glebovitsky, V.A., Semenov, V.S., Belyatsky, B.V., Koptev-Dvornikov, E.V., Pchelintseva, N.F., Kireev, B.S., and Koltsov, A.B., 2001. The structure of the Lukkulaisvaara intrusion, Oulanka group, northern Karelia: petrological implications. *Canadian Mineralogist* **39**, 607– 637.

Goldschmidt, V.M., 1937. The principles of distribution of chemical elements in minerals and rocks. *Journal of the Chemical Society of London* **140**, 655 – 673.

Green, T.H., 1980. Island arc and continent-building magmatism – A review of petrogenetic models based on experimental petrology and geochemistry. *Tectonophysics* **63**, 367 – 385.

Halkoaho, T.A.A., Alapieti, T.T., and Lahtinen, J.J., 1989. The Sompujärvi PGE mineralization in the Penikat layered intrusion, Northern Finland. *In:* Alapieti, T.T., Eds. *5th International Platinum Symposium. Guide to the post-symposium field trip* Geological Survey of Finland, Guide **29**, pp. 71 – 92.

Halkoaho, T.A.A., Alapieti, T.T., and Lahtinen, J.J., 1990. The Sompujärvi PGE Reef in the Penikat layered intrusion, Northern Finland. *Mineralogy and Petrology* **42**, 39 – 55.

Halkoaho, T.A.A., 1993. The Sompujärvi and Ala-Penikka PGE Reefs in the Penikat layered intrusion, Northern Finland: implications for PGE reef-forming processes. *Acta Universitatis Ouluensis. Series A, Scientiae Rerum Naturalium* **249**, 1 – 122.

Hanski, E., Walker, R.J., Huhma, H., and Suominen, I., 2001. The Os and Nd isotopic systematics of the c. 2.44 Ga Akanvaara and Koitelainen mafic layered intrusions in northern Finland. *Precambrian Research* **109**, 73–102.

Hanson, G.N., 1980. Rare earth elements in petrogenetic studies of igneous systems. *Annual Review of Earth and Planetary Science Letters* **8**, 371 – 406.

Hatton, C. J., and von Gruenewaldt, G., 1987. The geological setting and petrogenesis of the Bushveld chromitite layers. *In*: Stowe, C. W., Eds. *Evolution of chromium ore fields*. Van Nostrand Reinhold Co., New York pp. 109-143.

Haughton, D.R., Roeder, P.L., and Skinner, B.J., 1974. The solubility of sulfur in mafic magmas. *Economic Geology* **69**, 451 – 462.

Heaman, L.M., 1997. Global mafic magmatism at 2.45 Ga: Remnants of an ancient large igneous province. *Geology* **25**, 299–302

Henderson, P., 1975. Geochemical indicator of the efficiency of fractionation of the Skaergaard Intrusion, east Greenland. *Mineralogical Magazine* **40**, 285 – 291.

Hess, P.C., 1989. *Origins of igneous rocks*. Harvard University Press. Pp. 336.

Hiemstra, S.A., 1979. The role of collectors in the formation of the platinum deposits in the Bushveld Complex. *Canadian Mineralogist* **17**, 469 – 482.

Hill, R., and Roeder, P., 1974. The crystallization of spinel from basaltic magma as a function of oxygen fugacity. *Journal of Geology* **82**, 709 – 729.

Huhma, H., Cliff, R.A., Perttunen, V., and Sakko, M., 1990. Sm–Nd and Pb isotopic study of mafic rocks associated with early Proterozoic continental rifting: the Peräpohja schist belt in northern Finland. *Contribution to Mineralogy and Petrology*. **104**, 367–379.

Hulbert, L.J., and von Gruenewaldt, G., 1982. Nickel, Copper and platinum mineralization in the Lower Zone of the Bushveld Complex, south of Potgietersrus. *Economic Geology* **77**, 1296 – 1306.

Huppert, H.E., Sparks, R.S.J., Whitehead, J.A. and Hallworth, M.A. 1986. The replenishment of magma chambers by light inputs. *Journal of Geophysics Research* **91**, 6113 – 6122.

Iljina, M., 1994. The Portimo layered igneous Complex. *Unpublished Ph.D thesis, University of Oulu, Finland* pp 158 and appendices.

Iljina, M., and Hanski, E., 2005. Layered mafic intrusions of the Tornio-Näränkävaara belt. *In*: Lahtinen, P.A., Nurmi, P.A., and Rämö, O.T., Eds. *Precambrian geology of Finland: Key to the evolution of the Fennoscandian Shield,* Developments in Precambrian Geology **14**, pp.118.

Irvine, T.N., 1975. Crystallization sequences in the Muskox intrusion and other layered intrusions – II: Origin of chromitite layers and similar deposits of other magmatic ores. *Geochimica et Cosmochimica Acta* **39**, 991 – 1020.

Irvine, T.N., 1977. Origin of chromitite layers in the Muskox intrusion and other layered intrusions: a new interpretation. *Geology* **2**, 273 – 277.

Irvine, T.N., Keith, N.W., and Todd, S.G., 1983. The J-M platinum-palladium reef of the Stillwater Complex, Montana – II: Origin by double diffusive convective magma mixing and implications for the Bushveld Complex. *Economic Geology* **78**, 1287 – 1334.

Irvine, T.N., and Sharpe, M.R., 1986. Magma mixing and the origin of stratiform oxide ore zones in the Bushveld and Stillwater Complexes. *In*: Gallagher, M.J., Ixer, R.A., Neary, C.R., Prichard, H.M. Eds. *Metallogeny of Basic and Ultrabasic Rocks. Inst. Min. Metall, London*, 183–198.

Jackson, E.D., 1966. Liquid Immiscibility in chromite layer formation – a discussion. *Economic Geology* **61**, 777 – 780.

Jacobsen, S.B., and Wasserburg, G.J., 1984. Sm-Nd isotopic evolution of chondrites and achondrites II. *Earth and Planetary Science Letters* **67**, 137 – 150.

Jahn, B., Vidal, P., and Kröner, A., 1984. Multi-chronometric ages and origin of Archaean tonalitic gneisses in Finnish Lapland: a case for long crustal residence time. *Contributions to Mineralogy and Petrology* **86**, 398–408.

Kennedy, G.C., 1955. Some aspects of the role of water in igneous melts. *Geological Society of America Special Paper* **62**, 489 – 503.

Kruger, F.J., 1994. The Sr-isotopic stratigraphy of the western Bushveld Complex. *South African Journal of Geology* **97**, 393 – 398.

Kojonen, K., Gornostayev, S.S., Pitkajarvi, J. and Knauf, N.N. 2005. The PGE mineralogy of the Kemi chromite deposit: an overview. *In*: Törmänen, T.O., and Alapieti T.T., Eds. *Proceedings of the tenth international platinum symposium abstracts, Platinum-group elements – from genesis to beneficiation and environmental impact.* pp. 412 – 416.

Laajoki, K., 1986. The Precambrian supra-crustal rocks of Finland and their tectono-exogenic evolution. *Precambrian Research* **33**, 67 – 85.

Lambert, D.D., Walker, R.J., Morgan, J.W., Shirey, S.B., Carlson, R.W., Zientek, M.L., Lipin, B.R., Koski, M.S., and Cooper, R.L., 1994. Re–Os and Sm–Nd isotope geochemistry of the Stillwater Complex, Montana; implications for the petrogenesis of the J-M Reef. *Journal of Petrology* **35**, 1717–1753.

Lauri, L.S., Rämö, O.T., Huhma, H., Mänttäri, I., Räsänen, J., 2006. Petrogenesis of silicic magmatism related to the ~2.44 Ga rifting of Archaean crust in Koillismaa, eastern Finland. *Lithos* **86**, 137 – 166.

Lavigne, M.J., and Michaud, M.J., 2001. Geology of North American Palladium Ltd.'s Roby Zone deposit, Lac des Iles. *Exploration and Mining Geology* **10**, 1 – 17.

Levin, E.M., Robbins, C.R., and McMurdie, H.F., 1964. *Phase Diagrams for Ceramists.* Columbus, Ohio: American Ceramic Society.

Li, C., Maier, W.D., and de Waal, S.A., 2001. The role of magma mixing in the genesis of PGE mineralization in the Bushveld Complex: Thermodynamic calculations and new interpretations. *Economic Geology* **96**, 653 – 662.

Li, C., Ripley, E.M., Merino, E., and Maier, W.D., 2004. Replacement of base metal sulfides by actinolite, epidote, calcite, and magnetite in the UG2 and Merensky Reef of the Bushveld Complex, South Africa. *Economic Geology* **99**, 173 – 184.

Lipin, B.R., 1993. Pressure increases, the formation of chromite layers, and the development of the Ultramafic Series in the Stillwater Complex, Montana. *Journal of Petrology* **34**, 955 – 976.

Maier, W.D., 1991. Geochemical and petrological trends in the UG2 – Merensky unit interval of the Upper Critical Zone in the western Bushveld Complex. *PhD Thesis, Rhodes University (unpubl.),* 241pp.

Maier, W.D., and Barnes, S-.J., 1999. Platinum-group elements in silicate rocks of the lower, critical and main zones at Union Section, Bushveld Complex. *Journal of Petrology* **40**, 1647 - 1671.

Maier, W.D., Arndt, N.T., and Curl, E.A., 2000. Progressive crustal contamination of the Bushveld Complex: Evidence from Nd isotopic analyses of the cumulate rocks. *Contributions to Mineralogy and Petrology* **140**, 316 – 327.

Maier, W.D., Barnes, S.-J., Gartz, V., and Andrews, G., 2003.Pt-Pd reefs in magnetites of the Stella layered intrusion, South Africa: A world of new exploration opportunities for platinum-group elements. *Geology* **31**, 885 – 888.

Maier, W.D., and Passaportis, L., 2004. The petrogenesis and magmatic sulphide potential of the Thole Sills and the Usushwana Complex, South Africa - Swaziland. *Geoscience Africa* Wits University, Johannesburg.

Maier, W.D., 2005. Platinum-group element (PGE) deposits and occurrences: Mineralization styles, genetic concepts, and exploration criteria. *Journal of African Earth Sciences* **41,** pp 165 - 191.

Maier, W.D., and Barnes, S-.J., 2010. The petrogenesis of platinum-group element reefs in the Upper Main Zone of the Northern Lobe of the Bushveld Complex on the farm Moorddrift, South Africa. *Economic Geology* **105**, 841 – 854.

Manhes, G., Allègre, C.J., Dupre, B., and Hamelin, B., 1980. Lead isotope study of basic – ultrabasic layered complexes: Speculation about the age of the earth and primitive mantle characteristics. *Earth and Planetary Science Letters* **47**, 370 – 382.

Mathez, E.A., 1999. On factors controlling the concentrations of platinum-group elements in layered intrusions and chromitites. *In:* Keays, R.R., Eds. *Dynamic processes in magmatic ore deposits and their application in mineral exploration. Geological Association of Canada, short course notes* **13**, pp. 251 – 285.

McCandless, T.E., Ruiz, J., Adair, B.I., and Freydier, C., 1999. Re-Os isotope and Pd/Ru variations in chromitites from the Critical Zone, Bushveld Complex, South Africa. *Geochimica et Cosmochimica Acta* **63**, 911 – 923.

McClay, K.R., and Campbell, I.H., 1976. The structure and shape of the Jimberlana intrusion, Western Australia, as indicated by an investigation of the bronzite Complex. *Geological Magazine* **113**, 129 – 139.

McDonald, J.A., 1965. Liquid immiscibility as one factor in chromitite layer formation in the Bushveld igneous Complex. *Economic Geology* **60**, 1674 – 1685.

McDonough, W.F., and Sun, S.S., 1995. The composition of the Earth. *Chemical Geology* **120**, 223 - 253.

McLaren, C.H., and de Villiers, J.P.R., 1982. The platinum-group chemistry and mineralogy of the UG2 chromitite layer of the Bushveld Complex. *Economic Geology* **77**, 1348 – 1366.

Merkle, R.K.W., 1992. Platinum-group minerals in the Middle Group of chromitites layers at Marikana, Bushveld Complex: implications for collection mechanisms and postmagmatic modification. *Canadian Journal of Earth Sciences* **29**, 209 – 221.

Merkle, R.K.W., and McKenzie, A.D., 2002. The mining and beneficiation of South African PGE ores – An overview. *In:* Cabri, L.J., Eds. *The geology, geochemistry, mineralogy and mineral beneficiation of Platinum-Group Elements.* Canadian Institute of mining, metallurgy and petroleum, **54**, 793 – 809.

Mitchell, A.A, 1986. The petrology, mineralogy and geochemistry of the Min Zone of the Bushveld Complex at Rustenburg Platinum Mines, Union Section. *PhD Thesis, Rhodes University (unpubl.),* 119pp.

Mondal, S.K., and Mathez, E.A., 2007. Origin of the UG2 chromitite layer, Bushveld Complex. *Journal of Petrology* **40**, 495 – 510.

Morgan, J.W., Ganapathy, R., Higuchi, H., and Kraehenbuehl, U., 1976. Volatile and siderophile trace elements in anorthositic rocks from Fiskenaesset, West Greenland: Comparison with lunar and meteoric analogues. *Geochemica et Cosmoschimica Acta* **40**, 861 – 887.

Mukasa, S.B., Wilson, A.H., and Carlson, R.W., 1998. A multi-element geochronologic study of the Great Dyke, Zimbabwe: Significance of the robust and reset ages. *Earth and Planetary Science Letters* **164**, 353 – 369.

Mungall, J., 2002. A model for co-precipitation of platinum-group minerals with chromite from silicate melts. *9th International Platinum Symposium, Billings, Montana, Abstracts* 321 – 324.

Murck, B.W., and Campbell, I.H., 1986. The effects of temperature, oxygen fugacity and melt composition on the behaviour of chromium in basic and ultrabasic melts. *Geochemica et Cosmoschimica Acta* **50**, 1871 – 1887.

Naldrett, A.J., and Lehmann, J., 1988. Spinel non-stoichiometry as the explanation for Ni-, Cu-, and PGE-enriched sulphides in chromitites. I*n: 87* Pritchard, H.M., Potts, P.J., Bowles, J.F.W., and Cribb, S.J., Eds. *Geo-Platinum* Elsevier Applied Science, London, pp. 113 – 143.

Naldrett, A.J., and von Gruenewaldt, G., 1989. Association of PGE with chromitite in layered intrusions and ophiolite complexes. *Economic Geology* **84**, 180 – 187.

Naldrett, A.J., Brügmann, G.E., and Wilson, A.H., 1990. Models for the concentration of PGE in layered intrusions. *Canadian Mineralogist* **28**, 389–408.

Naldrett, A.J., Kinnaird, J., Wilson, A., Yudovskaya, M., McQuade, S., Chunnett, G., and Stanley, C., 2009. Chromite composition and PGE content of Bushveld chromitites: Part 1 – the Lower and Middle Groups. *Transaction of the Institution of Mining and Metallurgy Section B* **118**, 131 – 161.

Nicholson, D.M., and Mathez, E.A., 1991. Petrogenesis of the Merensky Reef in the Rustenburg section of the Bushveld Complex. *Contribution to Mineralogy and Petrology* **107**, 293 - 309. *Geochemica et Cosmoschimica Acta* **33,** 431– 453.

Norrish, K., and Hutton, J.T., 1969. An accurate X-ray spectrographic method for the analysis of a wide range of geological samples.

Osborn, E.F., 1959. Role of oxygen pressure in the crystallization and differentiation of basaltic magma. *American Journal of Science* **257**, 609 – 647.

Patchett, P., Kouvo, O., Hedge, C.E., and Tatsumoto, M., 1981. Evolution of continental crust and mantle heterogeneity: Evidence from Hf isotopes. *Contribution to Mineralogy and Petrology* **78**, 279 – 297.

Peach, C.L., and Mathez, E.A., 1996. Constraints on the formation of platinum-element deposits in igneous rocks. *Economic Geology* **91**, 439 – 450.

Peregoedova, A., Barnes, S.-J., and Barker, D.R., 2004. The formation of Pt-Ir alloys and Cu-Pd rich sulphide melts by partial desulphurization of Fe-Ni-Cu sulphide: Results of experiments and implications for natural systems. *Chemical Geology* **208**, 247 – 264.

Perttunen, V., and Vaasjoki, M., 2001. U-Pb lead geochronology of the Peräpohja Schist Belt. In: Vassjoki, M., Eds *Radiometric age determinations from Finnish Lapland and their bearing on the timing of Precambrian volcano-sedimentary sequences.* Geological Survey of Finland special paper **33**, pp 45 – 84.

Prevec, S.A., 2004. Basement tracing using Mid-Proterozoic anorthosites straddling a palaeoterrane boundary, Ontario, Canada. *Precambrian Research* **129**, 169 – 184.

Puchtel, I.S., Haase, K.M., Hofmann, A.W., Chauvel, C., Kulikov, V.S., Garbe-Shönberg, C.-D., and Nemchin, A.A., 1997. Petrology and geochemistry of crustally contaminated komatiitic basalts from the Vetrent Belt, southeastern Baltic Shield: Evidence for an early Proterozoic mantle plume beneath rifted Archaean continental lithosphere. *Geochemica et Cosmoschimica Acta* **61,** 1205 – 1222.

Righter, K., Campbell, A.J., Humayun, M., and Herding, R.L., 2004. Partitioning of Ru, Rh, Pd, Re, Ir and Au between Cr-bearing spinel, olivine, pyroxene and silicate melts. *Geochemica et Cosmoschimica Acta* **68**, 867 – 880.

Rollinson, H.R., 1993. Using geochemical data: Evaluation, presentation, Interpretation. *Longman/Wylie. Harlow/New York.* pp. 108.

Saini-Eidukat, B., Alapieti, T.T., Thalhammer, O.A.R., and Iljina, M.J., 1997. Siliceous, high magnesian parental magma compositions of the PGE-rich early Paleoproterozoic layered intrusion belt of northern Finland. *Proc. 30th Int'l. Geol. Congr*., **vol. 9** 177– 197.

Schoenberg, R., Kruger, F.J., Nägler, T.F., Meisel, T., and Kramers, J.D., 1999. PGE enrichment in chromitite layers and the Merensky Reef of the western Bushveld Complex; a Re–Os and Rb–Sr study. *Earth and Planetary Science Letters* **172**, 49–64.

Scoon, R.J., and Teigler, B., 1994. Platinum-group element mineralization in the Critical Zone of the Western Bushveld Complex: I. sulphide-poor chromitites below the UG2. *Economic Geology* **89**, 1094 – 1121.

Sharpe, M.R., and Irvine, T.N., 1983. Melting relations of two Bushveld chilled margins and implications for the origin of chromitite. *Carnegie Institute Washington Year Book 1982* pp. 295 – 300.

Sigurdsson, H., 2000. Encyclopaedia of volcanoes. *Academic Press, San Diego and London.* pp. 176 +180.

Simonen, A., 1980. The Precambrian of Finland. *Geological survey of Finland bulletin* **304**, pp58.

Sorjonen-Ward, P., and Luukkonen, E.J., 2005. Archaean rocks *In*: Lahtinen, P.A., Nurmi, P.A., and Rämö, O.T., Eds. *Precambrian geology of Finland: Key to the evolution of the Fennoscandian Shield,* Developments in Precambrian Geology **14**,, pp.59.

Talkington, R.W., and Lipin, B.R., 1986. Platinum-group elements in chromite seams of the Stillwater Complex, Montana. *Economic Geology* **81**, 1179 – 1186.

Taylor, S.R., 1982. *Planetary science: A lunar perspective.* Lunar and Planetary Institute. pp. 481.

Taylor, S.R., and McLennan, S.M., 1995. The geochemical evolution of the continental crust. *Reviews of Geophysics* **33**, 241 – 265.

Taylor Jr., H.P., 1980. The effects of assimilation of country rocks by magmas on $^{18}O/^{16}O$ and $^{87}Sr/^{86}Sr$ systematic in igneous rocks. *Earth and Planetary Science Letters* **47**, 243 – 254.

Teigler, B., 1990. Mineralogy, petrology and geochemistry of the Lower and Lower Critical Zones, northwestern Bushveld Complex. *PhD Thesis, Rhodes University (unpubl.),* 247pp.

Tolstikhin, I.N., Dokuchaeva, V.S., Kamensky, I.L., and Amelin, Yu V., 1992. Juvenile helium in ancient rocks; II, U–He, K–Ar, Sm–Nd, and Rb–Sr systematics in the Monche Pluton; 3He/4He ratios frozen in uranium-free ultramafic rocks. *Geochemica et Cosmoschimica Acta* **56**, 987–999.

Tredoux, M., Sellschop, F.J.P., Davies, G., and de Wit, M.J., 1985. The behaviour of the PGE and Au during partial melting and fractional crystallization; evidence from magmas on the Kaapvaal Craton. *Canadian Mineralogist* **23**, 317 – 318.

Turchenko, A.S., Bogomolov, E.S., and Turchenko, S.I., 1998. Petrologic and isotope-geochemical features of PGE-bearing horizons in the Pansky Tundra layered intrusion (2.5 Ga), Fennoscandian Shield. In: Laverov, N.P., and Distler, V.V., Eds. *International Platinum*. *Theophrastus Publishers, Athens*, pp. 71–78.

Ulmer, G.C., 1969. Experimental investigations of chromite spinals. *Economic Geology* **4**, 114 – 131.

Vogel, D.C., Vuollo, J.I., Alapieti, T.T., and James, R.S., 1998. Tectonic, stratigraphic, and geochemical comparisons between ca. 2500 – 2440 Ma mafic igneous events in the Canadian and Fennoscandian Shields. *Precambrian Research* **92**, 89 – 116.

von Gruenewaldt, G., Hatton, C.J., and Merkle, R.K.W., 1986. Platinum-group element-chromitite associations in the Bushveld Complex. *Economic Geology* **81**, 1067 – 1079.

von Gruenewaldt, G., Hulbert, L.J., and Naldrett, A.J., 1989. Contrasting platinum-group element concentration patterns in cumulus of the Bushveld Complex. *Mineralium Deposita* **24**, 219 – 229.

von Gruenewaldt, G. and Merkle, R.K.W. 1995. Platinum group element proportions in chromitites of the Bushveld Complex: implications for the fractionation and magma mixing models. *Journal of African Earth Sciences* **21,** 615 – 632.

Wicks, F.J. and Whittaker, E.J.W., 1977. Serpentine textures and serpentinization. *Canadian Mineralogist* **15**, 459 – 488.

Wicks, F.J., Whittaker, E.J.W., and Zussman, J., 1977. An idealized model for serpentine textures after olivine. *Canadian Mineralogist* **15**, 449 – 458.

Weihed, P., Arndt, N., Billström, K., Duchesne, J.-C., Eilu, P., Martinsson, O., Papunen, H., and Lahtinen, R., 2005. Precambrian geodynamics and ore formation: The Fennoscandian Shield. *Ore Geology Reviews* **27**, 273 – 322.

Wilson, A. and Chunnett, G., 2006. Trace element and platinum group element distributions and the genesis of the Merensky Reef, western Bushveld Complex, South Africa. *Journal of Petrology* **47**, 2369 – 2403.

Wilson, M., 1989. *Igneous petrogenesis: A global tectonic approach.* Unwin Hyman Inc. pp. 466.

Winter, J.D., 2001. *An introduction to Igneous and metamorphic petrology*. Prentice Hall Inc. pp 175 – 176.

## Appendix A

## Determining the stratigraphic height of the samples

The samples were obtained from several bore–holes that were drilled across the stratigraphic profile of the intrusion. The bore-holes were not drilled perpendicular to the basal contact of the intrusion; each bore-hole was drilled with a different angle below the horizontal (below the surface). The only heights or depths that were given for the samples were their depth below the surface in their respective bore-hole. This depth does not correspond with the sample stratigraphic heights within the intrusion.

The cross-section from Alapieti *et al*., (1989), shows the position of the bore-holes within the intrusion. The depth of the bore-holes (and the angles at which each bore-hole was drilled below the surface) was obtained from the bore-hole logs kindly provided by the Outokumpu Chrome Oy Kemi Mine. Table A1 shows the comparison of the bore-hole depths from the bore-hole logs with the measured depths of the bore-holes from the cross-section. The difference between the two depths was divided by the bore-hole log depths to show the accuracy of measurements taken from the cross-section. The largest difference was 3.2 % (Eli 60) with the rest of the measured bore-holes depths having differences below 3 %. These low values for the bore-hole depths gave enough confidence to use the cross-section as the only reference material to measure the distance from the surface outcrop of the basal contact to the surface collars of each bore-hole.

Table A2 shows the distance in millimetres from the surface outcrop of the basal contact of the intrusion to the surface collar of each bore-hole measured from the cross-section of the Kemi Intrusion from Alapieti *et al*. (1989). The measured distances have been converted to meters using the horizontal scale provided on the cross-section. In Table A3 are the angles that the bore-holes were drilled below the surface in degrees and radians. The dip angle of the intrusion is $70^{o}$ (Alapieti *et al*., 1989).

For the samples that were collected above the basal contact method one was used to calculate their stratigraphic heights and for samples collected below the basal contact method two was used to calculate their perpendicular distance below the basal contact of the intrusion.

Figure 39 illustrates the first method which shows the basal contact of the intrusion, one representative bore-hole and the constructed triangles used to calculate the stratigraphic height of a sample taken from that bore-hole. Triangle 1 is constructed via drawing a perpendicular line from the surface down to where the sample is located. DBS represents the depth below the surface of the sample in the bore-hole. Multiplying the DBS by the cosine and sine of angle x (the angle that the bore-hole was drilled below the surface) provides the length of a (the horizontal line from the surface collar to the perpendicular line to the surface of triangle 1) and b (the perpendicular line of triangle 1) respectively.

The horizontal distance between the surface outcrop of the basal contact and the surface collar of the bore-hole is represented by BC-BH in Figure 39 (the values are represented in Table A2). Subtracting the line a from BC-BH will provide c (the distance between the surface outcrop of the basal contact and the perpendicular line of triangle 1). A second line is constructed from the sample location to the surface outcrop of the basal contact to make triangle 2 and 3. Triangle 2 is now bounded on two sides by line b and c. The arctangent of line b over line c provides the angle y in triangle 2. Dividing line b by the sine of angle y will provide the length of d (the hypotenuse of triangle 2 and 3).

The intrusion has a dip angle of $70^{o}$ (Alapieti *et al*., 1989), thus angle z of triangle 3 is obtained via the subtraction of angle y from $70^{o}$. Multiplying the sine of angle z by the d (the hypotenuse of triangle 3) will provide the length of SH in triangle 3. SH represents the stratigraphic height of the sample.

Figure 40 illustrates the second method which shows the basal contact of the intrusion, one representative bore-hole and the constructed triangles used to calculate the perpendicular distance of a sample taken from that bore-hole below the basal contact. The second method was only used three samples and they were all from bore-hole Eli 60. DBS represents the depth below the surface of the sample in the bore-hole and BCD represents the depth of the basal contact in bore-hole Eli 60. Subtracting BCD from DBS provides a (the distance between the basal contact and the sample in bore hole Eli 60). Triangle 2 is constructed by drawing a perpendicular line from the basal contact to the sample and line a is the hypotenuse of triangle 2.

The dip angle of the intrusion is known ($70^o$) and angle x is known (the angle of the bore-hole drilled below the horizontal) in triangle 1. Thus it is easy to calculate the remaining angle (angle y) via $180^o - 70^o$ – angle x. Triangle 1 and 2 shares the same vertex and thus the angle y in triangle 2 and 3 are vertically opposite and equal in magnitude. Multiplying the sine of angle y in triangle 3 by line a (the hypotenuse of triangle 3) will provide the distance of SH, the perpendicular distance of the sample below the basal contact of the intrusion.

Tables A4 and A5 show all the values of these calculations for all the samples. These values and the petrology of the samples can be used to construct a stratigraphic profile of the intrusion. This new stratigraphic profile correlates well with the established stratigraphic profile of the intrusion from literature (e.g., Alapieti *et al*., 1989).

**Table A1:** Measurements in millimetres of the bore-hole depths taken from the cross-section of the Kemi Intrusion (Alapieti *et al*., 1989). The horizontal scale (from the cross-section) of 1 : 9 000 was used to calculate the measured depths of the bore-holes in meters. The actual depths in meters were obtained from the bore-hole logs kindly supplied by the Outokumpu Chrome Oy Kemi Mine. The error (%) represents how inaccurate the measured depths were from the actual depths. The errors were calculated by the difference between the two depths divided by the actual depths.

| Bore Hole | Measured depth (mm) | Measured depth (m) | Actual depth (m) | Error (%) |
|---|---|---|---|---|
| Eli 60 | 23 | 207 | 214.05 | 3.29 |
| Eli 83 | 67 | 603 | 616.77 | 2.23 |
| Eli 259 | 37 | 333 | 336.7 | 1.1 |
| Eli 4 | 23 | 207 | 211.54 | 2.15 |
| Eli 2 | 24 | 216 | 213.84 | 1.01 |
| Eli 260 | 34 | 306 | 309.15 | 1.02 |
| Eli 261 | 36 | 324 | 328.45 | 1.35 |
| Eli 262 | 34 | 306 | 307.45 | 0.47 |
| Eli 263 | 24 | 216 | 222.2 | 2.79 |
| Horizontal Scale | 1 : 9 000 | | | |

**Table A2:** Measurements in millimetres of the distance between the surface outcrops of the basal contact of the intrusion (BC) to the surface collars of the bore-holes (BH) taken from the cross-section of the Kemi Intrusion (Alapieti *et al*., 1989). The horizontal scale (from the cross-section) of 1 : 9 000 was used to calculate the distance between the surface outcrop of the basal contact of the intrusion to the surface collars of the bore-holes in meters.

| Bore Hole | Measured distance BC - BH (mm) | Measured distance BC - BH (m) |
|---|---|---|
| Eli 60 | 13 | 117 |
| Eli 83 | 55 | 495 |
| Eli 259 | 89 | 801 |
| Eli 4 | 104 | 936 |
| Eli 2 | 115 | 1035 |
| Eli 260 | 143 | 1287 |
| Eli 261 | 179 | 1611 |
| Eli 262 | 206 | 1854 |
| Eli 263 | 232 | 2088 |
| Horizontal Scale | 1 : 9 000 | |

**Table A3:** The angle x (in degrees) is the angle at which each bore-hole was drilled below the surface. They were obtained from the bore-hole logs kindly supplied by Outokumpu Chrome Oy Kemi Mine. The angles have been converted to radians.

| Sample | Bore Hole | Angle x | Angle x (radians) | Sample | Bore Hole | Angle x | Angle x (radians) |
|---|---|---|---|---|---|---|---|
| SL 01 | Eli - 60 | 55 | 0.9599311 | SL 24 | Eli-83 | 30 | 0.523599 |
| SL 02 | Eli - 60 | 55 | 0.9599311 | SL 25 | Eli-83 | 30 | 0.523599 |
| SL 03 | Eli - 60 | 55 | 0.9599311 | SL 26 | Eli-83 | 30 | 0.523599 |
| SL 04 | Eli - 60 | 55 | 0.9599311 | SL 27 | Eli-83 | 30 | 0.523599 |
| SL 05 | Eli - 60 | 55 | 0.9599311 | SL 28 | Eli-83 | 30 | 0.523599 |
| SL 06 | Eli - 60 | 55 | 0.9599311 | SL 29 | Eli-83 | 30 | 0.523599 |
| SL 07 | Eli - 83 | 30 | 0.5235988 | SL 30 | Eli-83 | 30 | 0.523599 |
| SL 08 | Eli - 83 | 30 | 0.5235988 | SL 31 | Eli-83 | 30 | 0.523599 |
| SL 09 | Eli - 83 | 30 | 0.5235988 | SL 32 | Eli-83 | 30 | 0.523599 |
| SL 10 | Eli - 83 | 30 | 0.5235988 | SL 33 | Eli-83 | 30 | 0.523599 |
| SL 11 | Eli - 83 | 30 | 0.5235988 | SL 34 | Eli-83 | 30 | 0.523599 |
| SL 12 | Eli - 83 | 30 | 0.5235988 | SL 35 | Eli-83 | 30 | 0.523599 |
| SL 38 | Eli - 259 | 39 | 0.6806784 | SL 36 | Eli-83 | 30 | 0.523599 |
| SL 13 | Eli-4 | 45 | 0.7853982 | SL 37 | Eli-83 | 30 | 0.523599 |
| SL 14 | Eli-4 | 45 | 0.7853982 | SL 39 | Eli - 260 | 45 | 0.7853982 |
| SL 15 | Eli-2 | 45 | 0.7853982 | SL 40 | Eli - 260 | 45 | 0.7853982 |
| SL 16 | Eli-2 | 45 | 0.7853982 | SL 41 | Eli - 261 | 45 | 0.7853982 |
| SL 17 | Eli-83 | 30 | 0.523599 | SL 42 | Eli - 261 | 45 | 0.7853982 |
| SL 18 | Eli-83 | 30 | 0.523599 | SL 43 | Eli - 261 | 45 | 0.7853982 |
| SL 19 | Eli-83 | 30 | 0.523599 | SL 44 | Eli - 262 | 45 | 0.7853982 |
| SL 20 | Eli-83 | 30 | 0.523599 | SL 45 | Eli - 262 | 45 | 0.7853982 |
| SL 21 | Eli-83 | 30 | 0.523599 | SL 46 | Eli - 262 | 45 | 0.785398 |
| SL 22 | Eli-83 | 30 | 0.523599 | SL 47 | Eli - 263 | 45 | 0.785398 |
| SL 23 | Eli-83 | 30 | 0.523599 | SL 48 | Eli - 263 | 45 | 0.785398 |

**Table A4:** The calculations from method one of the stratigraphic heights of all the samples for the Kemi Intrusion. DBS = depth below surface, a = the horizontal length from the surface collar to the perpendicular line to the surface of triangle 1, b = the perpendicular line of triangle 1, c = the distance between the surface outcrop of the basal contact and the perpendicular line of triangle 1 and angle y = found in triangle 2.

| Sample | DBS (m) | a (m) | b (m) | c (m) | Angle y (in radians) | Angle y (in degrees) |
|---|---|---|---|---|---|---|
| SL 04 | 126.9 | 72.8 | 103.9 | 44.2 | 1.2 | 67 |
| SL 05 | 123.1 | 70.6 | 100.9 | 46.4 | 1.1 | 65.3 |
| SL 06 | 24.3 | 14 | 19.9 | 103 | 0.2 | 11 |
| SL 07 | 420.4 | 364.1 | 210.2 | 130.9 | 1 | 58.1 |
| SL 08 | 308.3 | 267 | 154.1 | 228 | 0.6 | 34.1 |
| SL 09 | 312.7 | 270.8 | 156.3 | 224.2 | 0.6 | 34.9 |
| SL 10 | 224.2 | 194.2 | 112.1 | 300.8 | 0.4 | 20.4 |
| SL 11 | 123.2 | 106.7 | 61.6 | 388.3 | 0.2 | 9 |
| SL 12 | 19.8 | 17.1 | 9.9 | 477.9 | 0 | 1.2 |
| SL 13 | 207.3 | 146.6 | 146.6 | 789.4 | 0.2 | 10.5 |
| SL 14 | 97.9 | 69.2 | 69.2 | 866.8 | 0.1 | 4.6 |
| SL 15 | 73.5 | 51.9 | 51.9 | 983.1 | 0.1 | 3 |
| SL 16 | 14.3 | 10.1 | 10.1 | 1024.9 | 0 | 0.6 |
| SL 17 | 329.8 | 285.6 | 164.9 | 209.4 | 0.7 | 38.2 |
| SL 18 | 330.4 | 286.1 | 165.2 | 208.9 | 0.7 | 38.3 |
| SL 19 | 331.1 | 286.7 | 165.5 | 208.3 | 0.7 | 38.5 |
| SL 20 | 331.7 | 287.3 | 165.9 | 207.7 | 0.7 | 38.6 |
| SL 21 | 332.4 | 287.8 | 166.2 | 207.2 | 0.7 | 38.7 |
| SL 22 | 332.8 | 288.2 | 166.4 | 206.8 | 0.7 | 38.8 |
| SL 23 | 333 | 288.4 | 166.5 | 206.6 | 0.7 | 38.9 |
| SL 24 | 333.2 | 288.6 | 166.6 | 206.4 | 0.7 | 38.9 |
| SL 25 | 333.9 | 289.2 | 167 | 205.8 | 0.7 | 39.1 |
| SL 26 | 334.4 | 289.6 | 167.2 | 205.4 | 0.7 | 39.1 |
| SL 27 | 335.1 | 290.2 | 167.5 | 204.8 | 0.7 | 39.3 |
| SL 28 | 335.6 | 290.7 | 167.8 | 204.3 | 0.7 | 39.4 |
| SL 29 | 336.3 | 291.2 | 168.2 | 203.8 | 0.7 | 39.5 |
| SL 30 | 336.9 | 291.8 | 168.5 | 203.2 | 0.7 | 39.7 |
| SL 31 | 337.6 | 292.4 | 168.8 | 202.6 | 0.7 | 39.8 |
| SL 32 | 338.4 | 293 | 169.2 | 202 | 0.7 | 40 |
| SL 38 | 279.3 | 217.1 | 175.8 | 583.9 | 0.3 | 16.8 |
| SL 39 | 208.7 | 147.6 | 147.6 | 1139.4 | 0.1 | 7.4 |
| SL 40 | 101 | 71.4 | 71.4 | 1215.6 | 0.1 | 3.4 |
| SL 41 | 320.4 | 226.5 | 226.5 | 1384.5 | 0.2 | 9.3 |
| SL 42 | 216.2 | 152.8 | 152.8 | 1458.2 | 0.1 | 6 |
| SL 43 | 126.6 | 89.5 | 89.5 | 1521.5 | 0.1 | 3.4 |
| SL 44 | 306.3 | 216.6 | 216.6 | 1637.4 | 0.1 | 7.5 |
| SL 45 | 206.4 | 145.9 | 145.9 | 1708.1 | 0.1 | 4.9 |
| SL 46 | 105.3 | 74.5 | 74.5 | 1779.5 | 0 | 2.4 |
| SL 47 | 221.1 | 156.3 | 156.3 | 1931.7 | 0.1 | 4.6 |
| SL 48 | 123.8 | 87.5 | 87.5 | 2000.5 | 0 | 2.5 |

**Table A4 continued:** The calculations from method one of the stratigraphic heights of all the samples for the Kemi Intrusion. Angle z = found in triangle 3, d = the hypotenuse of triangle 2 and 3 and SH = stratigraphic height of the sample. Samples SL-17 through to SL-32 were taken from a small chromitite layer above the main chromitite layer and surrounding peridotites.

| Sample | Angle z (in degrees) | Angle z (in radians) | d (m) | SH |
|---|---|---|---|---|
| SL 04 | 3 | 0.1 | 113 | 6 |
| SL 05 | 4.7 | 0.1 | 111 | 9.08 |
| SL 06 | 59 | 1 | 105 | 90.01 |
| SL 07 | 11.9 | 0.2 | 247.6 | 51.13 |
| SL 08 | 35.9 | 0.6 | 275.2 | 161.55 |
| SL 09 | 35.1 | 0.6 | 273.3 | 157.24 |
| SL 10 | 49.6 | 0.9 | 321 | 244.31 |
| SL 11 | 61 | 1.1 | 393.1 | 343.79 |
| SL 12 | 68.8 | 1.2 | 478 | 445.68 |
| SL 13 | 59.5 | 1 | 802.9 | 691.65 |
| SL 14 | 65.4 | 1.1 | 869.6 | 790.85 |
| SL 15 | 67 | 1.2 | 984.4 | 906 |
| SL 16 | 69.4 | 1.2 | 1025 | 959.67 |
| SL 17 | 31.8 | 0.6 | 266.5 | 140.36 |
| SL 18 | 31.7 | 0.6 | 266.3 | 139.77 |
| SL 19 | 31.5 | 0.6 | 266 | 139.1 |
| SL 20 | 31.4 | 0.5 | 265.8 | 138.45 |
| SL 21 | 31.3 | 0.5 | 265.6 | 137.84 |
| SL 22 | 31.2 | 0.5 | 265.4 | 137.44 |
| SL 23 | 31.1 | 0.5 | 265.3 | 137.2 |
| SL 24 | 31.1 | 0.5 | 265.3 | 137.01 |
| SL 25 | 30.9 | 0.5 | 265 | 136.28 |
| SL 26 | 30.9 | 0.5 | 264.9 | 135.85 |
| SL 27 | 30.7 | 0.5 | 264.6 | 135.19 |
| SL 28 | 30.6 | 0.5 | 264.4 | 134.61 |
| SL 29 | 30.5 | 0.5 | 264.2 | 133.96 |
| SL 30 | 30.3 | 0.5 | 264 | 133.35 |
| SL 31 | 30.2 | 0.5 | 263.7 | 132.7 |
| SL 32 | 30 | 0.5 | 263.5 | 131.93 |
| SL 38 | 53.2 | 0.9 | 609.8 | 488.61 |
| SL 39 | 62.6 | 1.1 | 1148.9 | 1020.24 |
| SL 40 | 66.6 | 1.2 | 1217.7 | 1117.85 |
| SL 41 | 60.7 | 1.1 | 1402.9 | 1223.51 |
| SL 42 | 64 | 1.1 | 1466.1 | 1317.95 |
| SL 43 | 66.6 | 1.2 | 1524.1 | 1399.15 |
| SL 44 | 62.5 | 1.1 | 1651.7 | 1464.63 |
| SL 45 | 65.1 | 1.1 | 1714.3 | 1555.13 |
| SL 46 | 67.6 | 1.2 | 1781.1 | 1646.76 |
| SL 47 | 65.4 | 1.1 | 1938 | 1761.69 |
| SL 48 | 67.5 | 1.2 | 2002.4 | 1849.9 |

**Table A5:** The calculations from method two of the stratigraphic heights of the three country rock samples. DBS = depth below surface, BCD = the depth below the surface of the basal contact in bore-hole Eli 60, a = the distance from the basal contact to the sample in bore-hole Eli 60 and SH = perpendicular distance of the sample below the basal contact.

| Sample | DBS (m) | BCD (m) | a (m) | angle y (in degrees) | angle y (in radians) | SH (m) |
|---|---|---|---|---|---|---|
| SL 01 | 209.2 | 128.56 | 80.64 | 55 | 0.96 | 66.06 |
| SL 02 | 186.96 | 128.56 | 58.4 | 55 | 0.96 | 47.84 |
| SL 03 | 155.2 | 128.56 | 26.64 | 55 | 0.96 | 21.82 |

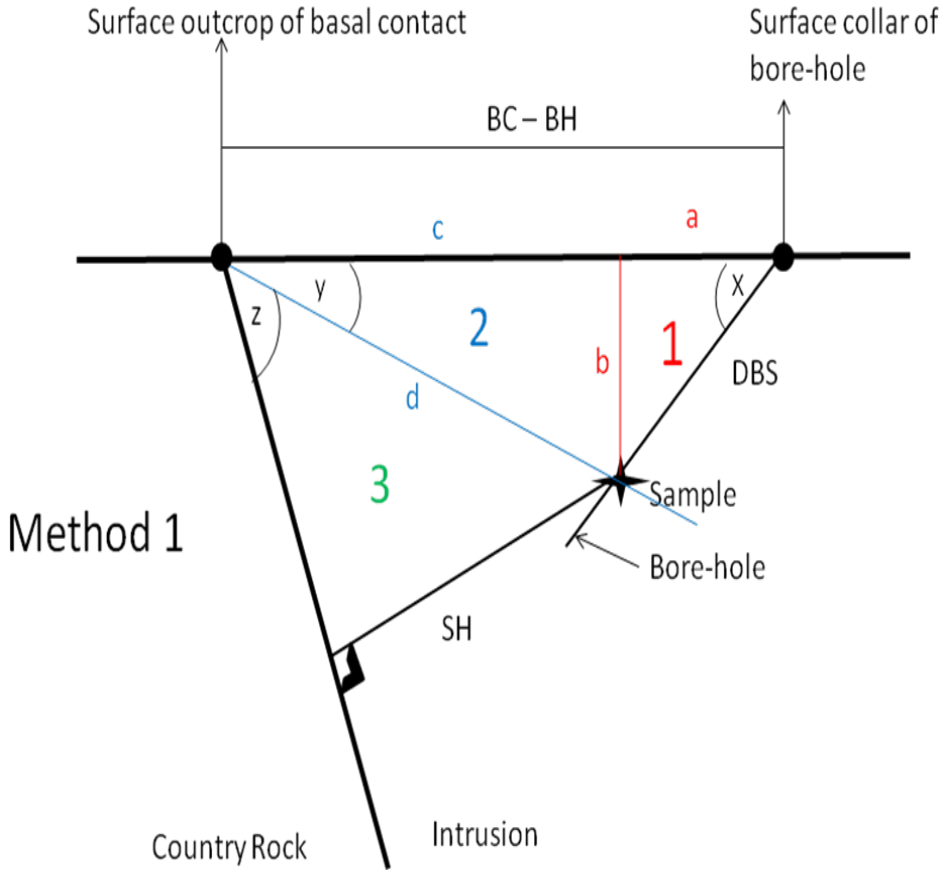


**Figure 39:** Diagram of method 1 showing the basal contact of the Kemi Intrusion with one representative bore-hole. Added are the three constructed triangles used to calculate the stratigraphic heights of the samples for method 1. DBS = depth below surface, a = the horizontal length from the surface collar to the perpendicular line to the surface of triangle 1, b = the perpendicular line of triangle 1, c = the distance between the surface outcrop of the basal contact and the perpendicular line of triangle 1, BC – BH = distance from the surface outcrop of the basal contact to the surface collars of each bore-hole, d = the hypotenuse of triangle 2 and 3 and SH = stratigraphic height of the sample.

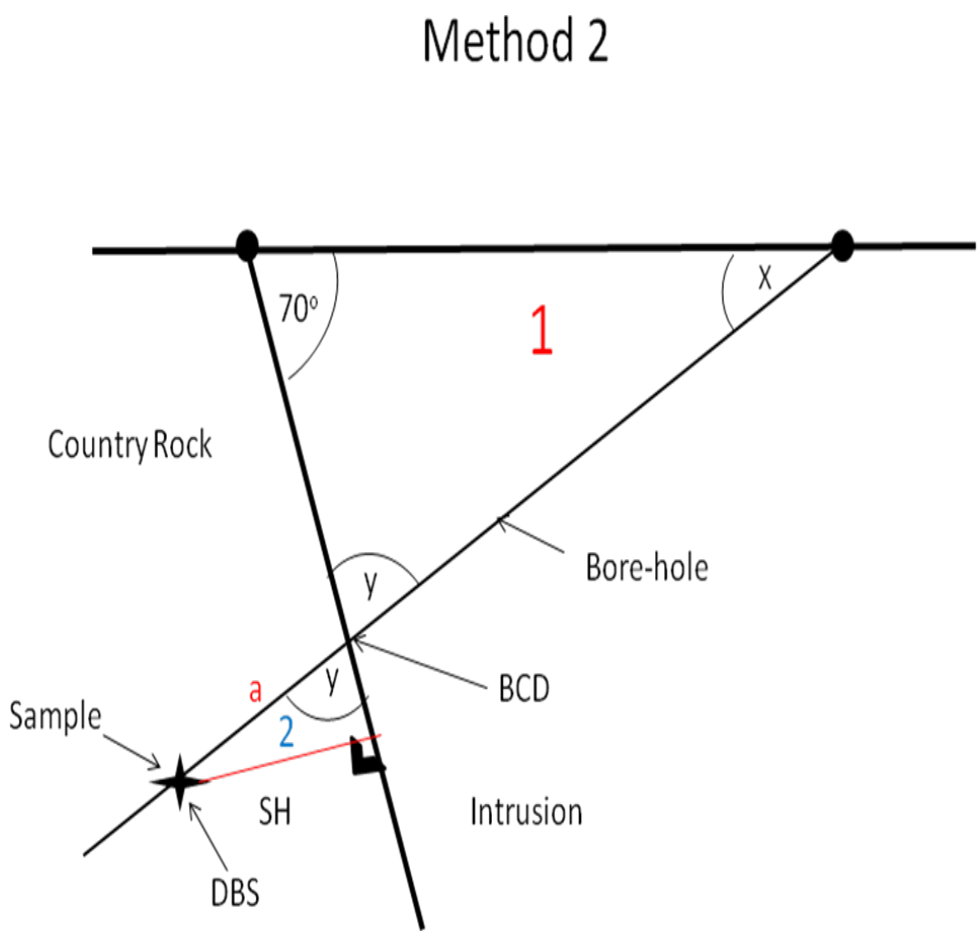


**Figure 40:** Diagram of method 2 showing the basal contact of the Kemi Intrusion with one representative bore-hole. Added is the constructed triangle used to calculate the perpendicular distance of the sample below the basal contact. DBS = depth below surface, BCD = the depth below the surface of the basal contact in bore-hole Eli 60, a = the distance from the basal contact to the sample and SH = perpendicular distance of the sample below the basal contact.

## Appendix B

## Sample preparation

### Crushing and milling of samples into powders

The core samples were crushed into 'chip' size pieces (1 – 2 cm) using the Osborn-Massco 4x6" laboratory jaw crusher. After each sample was crushed the jaw plates were wiped down with paper-towels (dampened by distilled water) until they were clean. The plates were wiped again with paper towels dampened with acetone (to dry the plates). An air-gun (from an air-compressor) was used to dry plates as well. Between the crushing of different rock types (e.g. gabbronorites, chromites, granites, etc), pure quartzite was crushed to get rid of any contamination form the previous sample. The plates were then cleaned as mentioned above.

The chips were placed in a mill (with rings) of a Herzog swing-mill. They were milled for 4 to 6 minutes. The resultant powder was removed (using paper, not metal spatulas to prevent contamination) and placed into glass sample jars, appropriately labelled. After the milling of each sample, the mill and rings were washed with tap water and scrubbed with a nylon scrubber until they were clean. They were then rinsed with tap and distilled water. The mill and rings were then dried with paper towels, acetone and finally the air-gun. If the mill and rings could not be cleaned satisfactory with the water and scrubber, quartz chips were placed into it and milled for 10 minutes. The quartz powder was thrown away and the mill and rings were cleaned as mentioned above.

Two different mills were used in crushing the samples in the Herzog swing-mill. The composition of the first chromium-bearing steel mill (milled samples SL-04; -05; -07; -09 to -18; -20 to -23; -25 to -28 and -38 to -48) is: carbon – 2.1%; silicon – 0.25%; manganese – 0.30%; chromium – 11.5%; vanadium – 0.10% and tungsten – 0.08%. The second chromium-free steel mill (milled samples SL-01 to -03; -06; -08; -19; -24 and -29 to -32) hasthe following composition: carbon – 0.90%; silicon – 0.20%; manganese – 2.10%; phosphorous – 0.03%; vanadium – 0.10% and sulphur – 0.03%.

The powders were placed into a Fritsch agate mill (15 to 20 grams per run) and milled for 45 minutes (or until the powders were milled to roughly 250 to 300 microns). The powders were then placed back into their jars. After each sample was milled, the agate mill was washed with water cleaned with a nylon scrubber. It was rinsed with distilled water. The agate mill was cleaned with paper towels and acetone. If the agate mill could not

be cleaned satisfactory with the water and scrubber, quartzite chips were placed into it and milled for 45 minutes. The quartzite powder was thrown away and the agate mill was cleaned as mentioned above.

A Zeiss Satorius mass balance and an Ohaus triple-beam balance were used for any weighting out of the samples into appropriate bottles or beakers for transport. Paper and the jar lids were used to scoop and move the powders; no metal spatulas were used to limit contamination of the samples.

**Fusion disks preparation and manufacture**

Silica crucibles were cleaned by boiling in dilute HCl acidic solution and dried at 120$^{o}$ C in an oven. Once dry, roughly 2 grams of milled powder was placed into the crucibles (one crucible for each sample). The mass of the crucible was recorded before and after the powder was added, thus the exact mass of each sample used is known (recorded in Table B1).

The crucibles were placed in an oven at 120$^{o}$ C for roughly four hours. They were removed and allowed to cool in a dessicator. Once cool the crucibles were weighed and the difference in mass was recorded (Table B1). The crucibles were then placed in a furnace at 1000$^{o}$ C for roughly eight hours. They were then removed and allowed to cool again in a dessicator. Once cool the crucibles were weighted and the difference in mass of the ashed samples was recorded (Table B1). The ashed samples were transferred to glass vials (appropriately labelled and closed with cling-film) and stored in a dessicator.

Roughly 0.280 grams of each ashed sample was transferred to a new glass vial (appropriately labelled). To these vials roughly 1.50 grams of Flux and 0.020 grams of $NaNO_3$ was also added (see Table B2 for the exact mass measurements). The vials are shaken vigorously to ensure that the added powders are mixed as thoroughly as possible with the ashed samples.

The powdered sample was then poured into a platinum crucible and heated on a bunsen burner until the powder was melted and thoroughly homogenous. Using platinum-tipped tongs, the molten sample was poured onto a heated graphite mould (the fusion disk mould). The graphite mould was heated on a hot-plate in excess of 240$^{o}$ C.

As quickly as possible (before the molten sample could cool and crystallizes) a stamp was lowered onto the graphite-mould and the molten

sample. A fusion disk should be the result. The stamp should be lowered such that it applies constant pressure to the molten sample. If bubbles are formed in the disk (applied pressure is not constant) or the disk is too small (does not fill the entire mould because the stamp was not lowered quickly enough) the disk should be placed back into the platinum crucible and re-melted.

The fusion disk was transferred to a heated asbestos pad and allowed to anneal for a few hours. After this the fusion disk was now allowed to cool. When cooled they were appropriately labelled and were analysed at Rhodes University.

**Powder pellets manufacture**

A clean, metal, hollow cylinder was placed upon a clean piece of paper (a new, clean piece of paper was used for each powder pellet and the metal cylinder was cleaned and dried after each powder pellet was made). Roughly 5 grams of the powdered sample was poured into the hollow metal cylinder. This measurement does not have to be accurate. A plastic rod was used to gently press the powder in the metal cylinder until the top of the powder was flat.

The metal cylinder was carefully placed on top of a thick circular metal base. The centre of the base has a raised circular platform that is the same size as the hollow, metal cylinder. The metal cylinder was placed on top of the raised platform and carefully lifted in such a way that the pressed powder remained behind on the raised platform. A thick metal ring, with a hollow centre the same size as the raised platform, was carefully placed over the raised platform and the powder on top of it. Boric acid crystals were poured on top of the sample powder inside the metal ring (the boric acid crystals act as the outer frame of the powder pellet). A solid metal rod was placed inside the metal ring on top of the powders.

The metal base and the metal ring, with the powders and metal rod enclosed, were placed in a hydraulic press. Roughly ten tons of pressure was applied to the powders within the metal ring. The pressure was slowly released and the metal base removed. Slight pressure was re-applied to the metal rod until the powder pellet was pushed out of the metal ring. The powder pellets were labelled and were analysed at Rhodes University.

**Dissolution process: Stellenbosch University ICP-MS**

The following dissolution process was carried out on the samples before transport to Stellenbosch University for analysis by ICP-MS (to determine the trace, minor and rare earth element concentrations). Roughly 0.50 grams of each sample was weighed out using a Mettler AE 240 scale into labelled 7milli-litre (ml) Teflon beakers. The samples were digested in batches of 16 to 20 samples. Each batch included a TPB sample (Total Procedural Blank) and a standard sample (in this case BHVO-2; United States Geological Survey, Hawaiian Basalt).

4.0 ml of acidic solution (4:1 HF/$HNO_3$) was added into each beaker. Note that all acids used in this procedure are 2-bottled (2B) distilled. The Teflon beakers (with their lids on) are placed onto a heating plate in a drying block for two nights at roughly 90ºC. After two nights the lids are removed and the samples and lids left to dry out.

When the samples are dry, 2.0 ml of $HNO_3$ (2-B distilled) is added to each beaker using a pipette. The beakers are placed back onto the heating plate and left to dry (lids off). Once the samples are dry, the addition of 2.0 ml of $HNO_3$ is repeated and left to dry.

Once dry, 1.5 ml of 5% $HNO_3$ is added to the beakers to dissolve the samples. The solution is then decanted into 1.5 ml centrifuge tubes (appropriately labelled) for transport to Stellenbosch University to be analyzed by ICP-MS (Tables B3 and B4 show all the relevant masses for each sample and other compounds used in the above described process).

Six duplicate analyses were completed for three random samples (SL-11, SL-16 and SL-48, Tables D6 and D7).

**Dissolution process: University of Cape Town MC-ICP-MS**

The following dissolution process was applied to the powdered material as a preparative step prior to the separation of Nd from the matrix by ion exchange column chemistry using resin**.**

Roughly 0.140 to 0.150 g of each sample was weighed out using a Mettler AE 240 scale into labelled 7milli-litre (ml) Teflon beakers. 4.0 ml of acidic solution (4:1 HF/$HNO_3$) was added into each beaker. Note that all acids used in this procedure are 2-bottled (2B) distilled except the 6.2M HCl which is quartz-distilled. The Teflon beakers (with their lids on) are placed onto a heating plate in a drying block for three nights at roughly

90ºC. Afterwards the lids are removed and the samples and lids left to dry out.

When the samples are dry, 4.0 ml of 6.2M HCl is added to each beaker and are placed back onto the heating plate with their lids off to dry. This step is done to ensure that the $HNO_3$ is removed from the sample. When the samples are dry the addition of 6.2M HCl is repeated and left to dry. Once the samples are dry the beakers are removed from the heating plate and left to cool.

Once cool, 1.0 ml of 2.5M HCl (2-B distilled) is added to each beaker using a pipette (Socorex make). When the entire sample is dissolved (or as much as possible) the solution is decanted from the Teflon beakers into labelled 2ml centrifuge tubes. The samples (using a Heraeus sepatech centrifuge) are centrifuged for 20 minutes at 4x1000 rpm (revolutions per minute). A number of samples (SL-05, -06, -07, -09, -14, -46, -17, -20, -22, -23, -24, -25, -26 and -28) still had too much solid material still in solution after the centrifuge process. The liquid from these samples were decanted into other labelled tubes and the centrifuge process was repeated.

**Column chemistry: Cation exchange process (University of Cape Town MC-ICP-MS)**

The primary columns are used first to collect the REE (Rare Earth Element) fraction out of the sample. 0.50 ml of sample is loaded into each column. Each column is calibrated differently, and as such, each has its own sample sheets that prescribe the volumes of acid to be added to the column to extract and isolate certain elements. Labelled 7 ml Teflon beakers are used to collect the REE fraction from the primary columns. The beakers are placed on a heating plate in a drying block and left to dry out (lids off).

Once dry, 0.25 ml of 0.25M HCl is added to each beaker to dissolve the sample. The sample is loaded into the secondary columns (used to collect Neodymium, Nd, out of the REE fraction). Follow the method that has been outlined in the sample sheets for each secondary column. The Nd fraction is collected with small Teflon beakers. The beakers are placed onto a heating plate in a drying block and left to dry out (lids off).

Once dry, 1.50 ml of a 2% $HNO_3$ solution (a 2% concentrated solution was chosen as this best suited the calibration of the collectors in

the MC-ICPMS for the expected strength of signal from the Nd concentrations in the original samples) is added to each sample. The sample is transferred from the small Teflon beakers to labelled 15 ml centrifuge tubes.

The samples were analysed with the MC-ICP-MS (Multiple Collector – Inductively Coupled Plasma-Mass Spectrometry) for its Nd isotope content at the University of Cape Town. Due to financial restrictions not all the samples were analyzed for their Nd isotopic compositions (see Table C7 for which samples were chosen). Roughly every second sample was analyzed for its Nd isotopic composition (twenty samples). The samples chosen are representative of all lithostratigraphic rock units found in the Kemi Intrusion. Half the samples (nine in total) are from the profile across the small chromitite layer and the surrounding peridotites.

## Tables of data used in the methods section

**Table B1:** The original and change in masses of the powdered samples used for the majors analysis in the XRF detector of Rhodes University. Samples from the small chromitite layer and surrounding peridotites are excluded. 4 Hrs is the difference in mass of the powdered samples after 4 hours heating at 120$^{o}$C. $H_2O$% is the percentage of free-water that was evaporated off. 8 Hrs is the difference in mass of the powdered samples after 8 hours heating at 1 000$^{o}$C. LOI% is the percentage of the loss of ignition.

| Sample | Original weight grams | 4 Hrs grams | H2O % % | 8 Hrs grams | LOI % % |
|---|---|---|---|---|---|
| SL 01 | 2.358 | 0.016 | 0.69 | 0.065 | 2.76 |
| SL 02 | 2.146 | 0.013 | 0.62 | 0.037 | 1.70 |
| SL 03 | 2.151 | 0.014 | 0.66 | 0.123 | 5.74 |
| SL 04 | 1.953 | 0.030 | 1.54 | 0.153 | 7.82 |
| SL 05 | 1.969 | 0.005 | 0.25 | 0.220 | 11.18 |
| SL 06 | 1.968 | 0.012 | 0.61 | 0.064 | 3.26 |
| SL 07 | 1.905 | 0.023 | 1.21 | 0.226 | 11.87 |
| SL 08 | 1.999 | 0.025 | 1.25 | 0.185 | 9.23 |
| SL 09 | 1.917 | 0.018 | 0.94 | 0.102 | 5.33 |
| SL 10 | 2.060 | 0.017 | 0.83 | 0.153 | 7.41 |
| SL 11 | 1.985 | 0.022 | 1.11 | 0.172 | 8.64 |
| SL 12 | 2.266 | 0.027 | 1.19 | 0.255 | 11.26 |
| SL 13 | 1.945 | 0.018 | 0.93 | 0.126 | 6.46 |
| SL 14 | 1.949 | 0.013 | 0.68 | 0.059 | 3.03 |
| SL 15 | 1.970 | 0.011 | 0.53 | 0.047 | 2.40 |
| SL 16 | 2.023 | 0.009 | 0.47 | 0.045 | 2.23 |
| SL 17 | 2.063 | 0.029 | 1.41 | 0.143 | 6.95 |
| SL 18 | 2.031 | 0.030 | 1.46 | 0.132 | 6.50 |
| SL 19 | 1.966 | 0.021 | 1.07 | 0.078 | 3.95 |
| SL 20 | 2.000 | 0.023 | 1.14 | 0.098 | 4.90 |
| SL 21 | 2.015 | 0.039 | 1.96 | 0.104 | 5.15 |
| SL 22 | 1.956 | 0.033 | 1.70 | 0.101 | 5.18 |
| SL 23 | 2.082 | 0.048 | 2.31 | 0.123 | 5.91 |
| SL 24 | 1.965 | 0.042 | 2.15 | 0.080 | 4.05 |
| SL 25 | 1.953 | 0.029 | 1.46 | 0.116 | 5.93 |
| SL 26 | 1.963 | 0.030 | 1.52 | 0.101 | 5.17 |
| SL 27 | 1.964 | 0.025 | 1.29 | 0.093 | 4.72 |
| SL 28 | 1.968 | 0.060 | 3.05 | 0.105 | 5.34 |
| SL 29 | 2.087 | 0.076 | 3.67 | 0.101 | 4.82 |
| SL 30 | 1.977 | 0.084 | 4.26 | 0.080 | 4.03 |
| SL 31 | 2.226 | 0.042 | 1.90 | 0.087 | 3.92 |
| SL 32 | 2.653 | 0.074 | 2.77 | 0.126 | 4.75 |
| SL 38 | 1.989 | 0.044 | 2.21 | 0.199 | 10.01 |
| SL 39 | 1.886 | 0.014 | 0.75 | 0.077 | 4.07 |
| SL 40 | 1.977 | 0.019 | 0.96 | 0.101 | 5.09 |
| SL 41 | 1.901 | 0.012 | 0.63 | 0.065 | 3.42 |
| SL 42 | 1.951 | 0.008 | 0.39 | 0.051 | 2.64 |
| SL 43 | 1.955 | 0.021 | 1.05 | 0.154 | 7.88 |
| SL 44 | 1.976 | 0.026 | 1.31 | 0.256 | 12.97 |
| SL 45 | 1.980 | 0.022 | 1.12 | 0.054 | 2.72 |
| SL 46 | 2.028 | 0.024 | 1.19 | 0.106 | 5.23 |
| SL 47 | 2.081 | 0.039 | 1.86 | 0.184 | 8.82 |
| SL 48 | 2.020 | 0.031 | 1.52 | 0.119 | 5.89 |

**Table B2:** The mass of the components used in the creation of the fusion disks analyzed for its majors composition in the XRF detector of Rhodes University. Samples from the small chromitite layer and surrounding peridotites are excluded. Ashed powder is the mass of the powdered sample used; Flux is the mass of the flux used; Total is the total mass of the fusion disk; and S/F Norm is the normalization factor.

| Sample | Ashed powder grams | Flux grams | NaNo3 grams | Total grams | S/F Norm |
|---|---|---|---|---|---|
| SL 01 | 0.286 | 1.491 | 0.024 | 1.800 | 0.287 |
| SL 02 | 0.281 | 1.499 | 0.021 | 1.801 | 0.281 |
| SL 03 | 0.279 | 1.495 | 0.024 | 1.797 | 0.280 |
| SL 04 | 0.272 | 1.515 | 0.021 | 1.808 | 0.269 |
| SL 05 | 0.272 | 1.509 | 0.024 | 1.805 | 0.270 |
| SL 06 | 0.275 | 1.503 | 0.023 | 1.801 | 0.275 |
| SL 07 | 0.278 | 1.501 | 0.024 | 1.803 | 0.277 |
| SL 08 | 0.277 | 1.501 | 0.023 | 1.801 | 0.277 |
| SL 09 | 0.281 | 1.501 | 0.020 | 1.802 | 0.281 |
| SL 10 | 0.279 | 1.490 | 0.022 | 1.791 | 0.281 |
| SL 11 | 0.284 | 1.484 | 0.020 | 1.788 | 0.287 |
| SL 12 | 0.278 | 1.515 | 0.023 | 1.816 | 0.275 |
| SL 13 | 0.285 | 1.489 | 0.020 | 1.793 | 0.287 |
| SL 14 | 0.286 | 1.485 | 0.022 | 1.793 | 0.289 |
| SL 15 | 0.280 | 1.506 | 0.022 | 1.808 | 0.278 |
| SL 16 | 0.272 | 1.485 | 0.023 | 1.780 | 0.274 |
| SL 17 | 0.282 | 1.510 | 0.021 | 1.814 | 0.280 |
| SL 18 | 0.276 | 1.506 | 0.020 | 1.801 | 0.275 |
| SL 19 | 0.279 | 1.484 | 0.023 | 1.786 | 0.282 |
| SL 20 | 0.282 | 1.491 | 0.022 | 1.796 | 0.284 |
| SL 21 | 0.288 | 1.514 | 0.022 | 1.824 | 0.285 |
| SL 22 | 0.279 | 1.492 | 0.020 | 1.791 | 0.280 |
| SL 23 | 0.295 | 1.512 | 0.021 | 1.828 | 0.292 |
| SL 24 | 0.272 | 1.497 | 0.023 | 1.791 | 0.272 |
| SL 25 | 0.272 | 1.507 | 0.020 | 1.799 | 0.271 |
| SL 26 | 0.290 | 1.494 | 0.019 | 1.803 | 0.291 |
| SL 27 | 0.277 | 1.493 | 0.022 | 1.792 | 0.278 |
| SL 28 | 0.275 | 1.486 | 0.023 | 1.784 | 0.278 |
| SL 29 | 0.278 | 1.493 | 0.019 | 1.790 | 0.279 |
| SL 30 | 0.277 | 1.493 | 0.021 | 1.790 | 0.278 |
| SL 31 | 0.278 | 1.492 | 0.021 | 1.791 | 0.279 |
| SL 32 | 0.296 | 1.499 | 0.021 | 1.815 | 0.296 |
| SL 38 | 0.277 | 1.483 | 0.022 | 1.782 | 0.280 |
| SL 39 | 0.278 | 1.486 | 0.022 | 1.786 | 0.281 |
| SL 40 | 0.292 | 1.489 | 0.021 | 1.802 | 0.294 |
| SL 41 | 0.273 | 1.483 | 0.022 | 1.778 | 0.276 |
| SL 42 | 0.272 | 1.487 | 0.023 | 1.782 | 0.275 |
| SL 43 | 0.281 | 1.487 | 0.020 | 1.788 | 0.284 |
| SL 44 | 0.276 | 1.497 | 0.022 | 1.795 | 0.277 |
| SL 45 | 0.276 | 1.510 | 0.021 | 1.807 | 0.274 |
| SL 46 | 0.273 | 1.494 | 0.020 | 1.787 | 0.274 |
| SL 47 | 0.279 | 1.510 | 0.021 | 1.810 | 0.277 |
| SL 48 | 0.274 | 1.497 | 0.020 | 1.791 | 0.274 |

**Table B3:** Masses of powdered sample; 5% $HNO_3$ and dilution factor used in the calculation of the minor and trace element concentrations (obtained from the ICP-MS from Stellenbosch University) from the Kemi Intrusion. Samples from the small chromitite layer and surrounding peridotites are excluded.

| Sample | Sample weight (g) | Mass of 1.5 ml 5% $HNO_3$ (g) | Dilution Factor |
|---|---|---|---|
| SL 01 | 0.0498 | 1.543 | 31.972 |
| SL 02 | 0.0502 | 1.543 | 31.725 |
| SL 03 | 0.0505 | 1.543 | 31.561 |
| SL 04 | 0.0499 | 1.543 | 31.909 |
| SL 05 | 0.0495 | 1.543 | 32.172 |
| SL 06 | 0.0498 | 1.543 | 31.959 |
| SL 07 | 0.0501 | 1.543 | 31.798 |
| SL 08 | 0.0499 | 1.543 | 31.903 |
| SL 09 | 0.0499 | 1.543 | 31.922 |
| SL 10 | 0.0504 | 1.543 | 31.645 |
| SL 11 | 0.0498 | 1.543 | 32.015 |
| SL 12 | 0.0498 | 1.543 | 31.959 |
| SL 13 | 0.0501 | 1.543 | 31.823 |
| SL 14 | 0.0500 | 1.543 | 31.891 |
| SL 15 | 0.0498 | 1.543 | 32.015 |
| SL 16 | 0.0501 | 1.543 | 31.817 |
| SL 17 | 0.0513 | 1.543 | 31.055 |
| SL 18 | 0.0499 | 1.543 | 31.897 |
| SL 19 | 0.0505 | 1.543 | 31.548 |
| SL 20 | 0.0497 | 1.543 | 32.021 |
| SL 21 | 0.0494 | 1.543 | 32.229 |
| SL 22 | 0.0506 | 1.543 | 31.524 |
| SL 23 | 0.0502 | 1.543 | 31.749 |
| SL 24 | 0.0517 | 1.543 | 30.822 |
| SL 25 | 0.0496 | 1.543 | 32.096 |
| SL 26 | 0.0506 | 1.543 | 31.524 |
| SL 27 | 0.0502 | 1.543 | 31.731 |
| SL 28 | 0.0507 | 1.543 | 31.428 |
| SL 29 | 0.0501 | 1.543 | 31.829 |
| SL 30 | 0.0520 | 1.543 | 30.684 |
| SL 31 | 0.0495 | 1.543 | 32.178 |
| SL 32 | 0.0504 | 1.543 | 31.621 |
| SL 38 | 0.0505 | 1.543 | 31.579 |
| SL 39 | 0.0517 | 1.543 | 30.845 |
| SL 40 | 0.0512 | 1.543 | 31.137 |
| SL 41 | 0.0509 | 1.543 | 31.308 |
| SL 42 | 0.0500 | 1.543 | 31.866 |
| SL 43 | 0.0508 | 1.543 | 31.374 |
| SL 44 | 0.0497 | 1.543 | 32.021 |
| SL 45 | 0.0514 | 1.543 | 31.049 |
| SL 46 | 0.0506 | 1.543 | 31.470 |
| SL 47 | 0.0508 | 1.543 | 31.374 |
| SL 48 | 0.0502 | 1.543 | 31.762 |

**Table B4:** Masses of powdered sample; 5% $HNO_3$ and dilution factor used in the calculation of the minor and trace element concentrations (obtained from the ICP-MS from Stellenbosch University) from the small chromitite layer and surrounding peridotites from the Kemi Intrusion and for the standards, duplicates and blanks as well.

| Sample | Sample weight (g) | Mass of 1.5 ml of 5% HNO3 (g) | Dilution Factor |
|---|---|---|---|
| BHVO 2 29/5 | 0.0502 | 1.543 | 31.749 |
| BHVO 2 13/6 | 0.0494 | 1.543 | 32.216 |
| BHVO 2 19/6 | 0.0505 | 1.543 | 31.561 |
| BHVO2 19/6 duplicate | 0.0505 | 1.543 | 31.561 |
| SL 11b | 0.0501 | 1.543 | 31.817 |
| SL 11c | 0.0505 | 1.543 | 31.536 |
| SL 16b | 0.0515 | 1.543 | 30.984 |
| SL 16c | 0.0505 | 1.543 | 31.579 |
| SL 48b | 0.0514 | 1.543 | 31.008 |
| SL 48c | 0.0503 | 1.543 | 31.676 |
| SL Qtz small | 0.0507 | 1.543 | 31.434 |
| SL Qtz big | 0.0503 | 1.543 | 31.706 |
| SL AW3 cont | 0.0504 | 1.543 | 31.645 |

**Table B5:** The various constants used to calculate the initial $^{143}Nd$ / $^{144}Nd$ values of the samples from the Kemi Intrusion and for the epsilon ($\varepsilon_{Nd}$) values of the samples. The first two values are the natural abundance of $^{147}Sm$ in Sm and $^{144}Nd$ in Nd. The age of the Kemi Intrusion (in years) is provided by Alapieti *et al*. (1989) and λ represents the decay constant of the $^{147}Sm$ - $^{144}Nd$ system in years (Faure, 1986; and Winter, 2001). e^(λ*t) – 1 represents the gradient of the isochron equation $^{143}Nd$ / $^{144}Nd$ = $^{143}Nd$ / $^{144}Nd_{initial}$ + $^{147}Sm$ / $^{144}Nd$*( e^(λ*t) – 1). The last two values are the $^{143}Nd$ / $^{144}Nd$ and $^{147}Sm$ / $^{144}Nd$ CHUR values for the present day (DePaolo and Wasserburg, 1976; and Winter, 2001).

| Constanst | |
|---|---|
| Natural abundance of $Sm^{147}$ in Sm | 0.15 |
| Natural abundance of $Nd^{144}$ in Nd | 0.239 |
| Age of Kemi Intrusion | 2.4E+09 |
| λ | 6.5E-12 |
| $e^{\wedge(\lambda*t)} - 1$ | 0.01609 |
| $Nd^{143}/Nd^{144}$ CHUR present day | 0.51264 |
| $Sm^{147}$ / $Nd^{144}$ CHUR present day | 0.1967 |

## APPENDIX C

## Tables of geochemical data

**Table C1:** Whole rock major element data from the Kemi Intrusion (obtained from the Rhodes University XRF detector). All iron oxides reported as FeO*.

| Sample | $SiO_2$ | $TiO_2$ | $Al_2O_3$ | FeO* | MnO | MgO | CaO |
|---|---|---|---|---|---|---|---|
| **SL 01** | 70.05 | 0.16 | 16.79 | 1.59 | 0.03 | 0.79 | 2.32 |
| **SL 02** | 70.62 | 0.14 | 15.98 | 1.68 | 0.02 | 0.83 | 1.05 |
| **SL 03** | 59.57 | 0.32 | 14.78 | 3.89 | 0.10 | 3.09 | 7.02 |
| **SL 04** | 25.68 | 0.23 | 7.66 | 14.31 | 0.34 | 16.70 | 3.10 |
| **SL 05** | 30.86 | 0.26 | 6.47 | 8.48 | 0.10 | 22.87 | 3.95 |
| **SL 06** | 10.60 | 0.25 | 8.64 | 11.88 | 0.21 | 17.41 | 0.02 |
| **SL 07** | 27.07 | 0.15 | 3.22 | 10.02 | 0.13 | 23.54 | 0.97 |
| **SL 08** | 35.55 | 0.23 | 5.14 | 12.01 | 0.21 | 27.96 | 1.38 |
| **SL 09** | 50.06 | 0.40 | 4.28 | 7.71 | 0.18 | 22.56 | 9.17 |
| **SL 10** | 45.55 | 0.13 | 5.16 | 8.99 | 0.19 | 26.13 | 5.24 |
| **SL 11** | 43.33 | 0.08 | 4.82 | 9.95 | 0.16 | 27.76 | 3.90 |
| **SL 12** | 37.58 | 0.11 | 3.22 | 11.05 | 0.18 | 26.62 | 3.04 |
| **SL 13** | 45.20 | 0.08 | 4.30 | 9.90 | 0.19 | 26.02 | 3.63 |
| **SL 14** | 49.68 | 0.23 | 3.32 | 10.16 | 0.21 | 27.78 | 4.71 |
| **SL 15** | 51.30 | 0.17 | 5.79 | 6.57 | 0.17 | 18.25 | 13.62 |
| **SL 16** | 52.20 | 0.19 | 5.18 | 6.18 | 0.15 | 18.45 | 15.23 |
| **SL 17** | 44.90 | 0.27 | 4.00 | 10.32 | 0.17 | 27.66 | 4.01 |
| **SL 18** | 44.99 | 0.14 | 5.68 | 9.15 | 0.17 | 26.49 | 4.80 |
| **SL 19** | 27.83 | 0.41 | 9.31 | 16.53 | 0.31 | 21.18 | 2.02 |
| **SL 20** | 50.01 | 0.39 | 3.99 | 9.66 | 0.17 | 25.59 | 4.09 |
| **SL 21** | 47.33 | 0.12 | 5.68 | 9.32 | 0.21 | 24.24 | 5.48 |
| **SL 22** | 48.71 | 0.24 | 4.93 | 8.93 | 0.19 | 24.72 | 4.93 |
| **SL 23** | 48.84 | 0.13 | 5.12 | 7.20 | 0.16 | 24.87 | 5.69 |
| **SL 24** | 28.29 | 0.30 | 8.56 | 14.38 | 0.34 | 19.25 | 2.91 |
| **SL 25** | 49.16 | 0.12 | 5.34 | 7.77 | 0.15 | 25.59 | 4.79 |
| **SL 26** | 48.90 | 0.20 | 5.47 | 8.82 | 0.24 | 23.91 | 6.36 |
| **SL 27** | 52.31 | 0.22 | 3.20 | 9.83 | 0.19 | 25.02 | 4.30 |
| **SL 28** | 48.30 | 0.11 | 4.82 | 8.28 | 0.18 | 23.58 | 4.88 |
| **SL 29** | 49.13 | 0.10 | 5.64 | 8.04 | 0.18 | 23.84 | 4.72 |
| **SL 30** | 41.10 | 0.14 | 4.39 | 7.76 | 0.18 | 20.78 | 4.47 |
| **SL 31** | 53.16 | 0.40 | 2.90 | 8.21 | 0.20 | 24.22 | 4.46 |
| **SL 32** | 49.79 | 0.14 | 4.66 | 8.66 | 0.22 | 23.40 | 5.73 |
| **SL 38** | 40.09 | 0.11 | 2.18 | 10.38 | 0.18 | 26.90 | 1.93 |
| **SL 39** | 47.98 | 0.11 | 14.18 | 4.80 | 0.12 | 13.37 | 14.99 |
| **SL 40** | 51.68 | 0.15 | 13.05 | 4.66 | 0.11 | 13.62 | 9.00 |
| **SL 41** | 50.45 | 0.12 | 14.13 | 5.12 | 0.13 | 14.20 | 11.87 |
| **SL 42** | 51.52 | 0.14 | 15.05 | 4.40 | 0.11 | 12.07 | 14.80 |
| **SL 43** | 43.98 | 0.07 | 22.66 | 3.30 | 0.05 | 6.33 | 12.56 |
| **SL 44** | 40.40 | 0.04 | 19.01 | 5.18 | 0.09 | 11.87 | 7.23 |
| **SL 45** | 49.62 | 0.10 | 18.02 | 3.58 | 0.09 | 9.91 | 15.45 |
| **SL 46** | 47.38 | 0.10 | 25.90 | 1.78 | 0.04 | 1.44 | 14.94 |
| **SL 47** | 48.15 | 0.24 | 18.56 | 4.19 | 0.07 | 7.76 | 7.49 |
| **SL 48** | 48.66 | 0.20 | 15.79 | 5.07 | 0.08 | 10.71 | 11.38 |

**Table C1 continued:** Whole rock major element data from the Kemi Intrusion (obtained from the Rhodes University XRF detector). Note the set-up of the XRF detector did not allow it to detect any $Cr_2O_3$ and NiO values.

| Sample | $Na_2O$ | $K_2O$ | $P_2O_5$ | $Cr_2O_3$ | NiO | LOI | $H_2O^-$ | Total |
|---|---|---|---|---|---|---|---|---|
| SL 01 | 5.36 | 2.26 | 0.05 | 0.00 | 0.00 | 2.94 | 0.69 | 103.02 |
| SL 02 | 6.62 | 2.33 | 0.04 | 0.00 | 0.00 | 1.89 | 0.62 | 101.81 |
| SL 03 | 4.21 | 1.46 | 0.06 | 0.00 | 0.00 | 6.17 | 0.66 | 101.34 |
| SL 04 | 0.00 | 0.00 | 0.00 | 0.00 | 0.00 | 9.41 | 1.54 | 78.97 |
| SL 05 | 0.00 | 0.00 | 0.01 | 0.00 | 0.00 | 12.13 | 0.25 | 85.39 |
| SL 06 | 0.00 | 0.00 | 0.00 | 0.00 | 0.00 | 4.58 | 0.61 | 54.21 |
| SL 07 | 0.00 | 0.00 | 0.00 | 0.00 | 0.00 | 12.99 | 1.21 | 79.28 |
| SL 08 | 0.05 | 0.01 | 0.00 | 0.00 | 0.00 | 10.57 | 1.25 | 94.36 |
| SL 09 | 0.38 | 0.12 | 0.03 | 0.00 | 0.00 | 6.19 | 0.94 | 102.01 |
| SL 10 | 0.27 | 0.12 | 0.00 | 0.00 | 0.00 | 8.41 | 0.83 | 101.02 |
| SL 11 | 0.19 | 0.07 | 0.00 | 0.00 | 0.00 | 9.75 | 1.11 | 101.11 |
| SL 12 | 0.04 | 0.05 | 0.00 | 0.00 | 0.00 | 12.49 | 1.19 | 95.57 |
| SL 13 | 0.15 | 0.04 | 0.00 | 0.00 | 0.00 | 7.56 | 0.93 | 97.99 |
| SL 14 | 0.16 | 0.12 | 0.02 | 0.00 | 0.00 | 4.16 | 0.68 | 101.22 |
| SL 15 | 0.58 | 0.09 | 0.00 | 0.00 | 0.00 | 3.13 | 0.53 | 100.19 |
| SL 16 | 0.39 | 0.09 | 0.00 | 0.00 | 0.00 | 2.92 | 0.47 | 101.44 |
| SL 17 | 0.18 | 0.06 | 0.04 | 0.00 | 0.00 | 8.10 | 1.41 | 101.11 |
| SL 18 | 0.23 | 0.05 | 0.01 | 0.00 | 0.00 | 7.52 | 1.46 | 100.66 |
| SL 19 | 0.16 | 0.03 | 0.00 | 0.00 | 0.00 | 5.79 | 1.07 | 84.63 |
| SL 20 | 0.47 | 0.07 | 0.07 | 0.00 | 0.00 | 5.97 | 1.14 | 101.61 |
| SL 21 | 0.81 | 0.07 | 0.00 | 0.00 | 0.00 | 6.19 | 1.96 | 101.40 |
| SL 22 | 0.72 | 0.07 | 0.02 | 0.00 | 0.00 | 6.17 | 1.70 | 101.33 |
| SL 23 | 0.95 | 0.08 | 0.00 | 0.00 | 0.00 | 6.71 | 2.31 | 102.05 |
| SL 24 | 0.29 | 0.01 | 0.01 | 0.00 | 0.00 | 5.65 | 2.15 | 82.14 |
| SL 25 | 0.62 | 0.14 | 0.00 | 0.00 | 0.00 | 6.79 | 1.47 | 101.94 |
| SL 26 | 0.72 | 0.18 | 0.01 | 0.00 | 0.00 | 6.15 | 1.52 | 102.48 |
| SL 27 | 0.54 | 0.08 | 0.00 | 0.00 | 0.00 | 5.82 | 1.29 | 102.80 |
| SL 28 | 1.33 | 0.09 | 0.00 | 0.00 | 0.00 | 6.26 | 3.05 | 100.89 |
| SL 29 | 1.48 | 0.48 | 0.00 | 0.00 | 0.00 | 5.72 | 3.67 | 103.01 |
| SL 30 | 1.64 | 0.59 | 0.00 | 0.00 | 0.00 | 4.90 | 4.27 | 90.19 |
| SL 31 | 0.87 | 0.55 | 0.03 | 0.00 | 0.00 | 4.84 | 1.90 | 101.75 |
| SL 32 | 1.26 | 0.26 | 0.01 | 0.00 | 0.00 | 5.72 | 2.77 | 102.62 |
| SL 38 | 0.03 | 0.04 | 0.00 | 0.00 | 0.00 | 11.16 | 2.21 | 95.22 |
| SL 39 | 0.69 | 0.09 | 0.00 | 0.00 | 0.00 | 4.60 | 0.75 | 101.67 |
| SL 40 | 1.96 | 0.05 | 0.00 | 0.00 | 0.00 | 5.61 | 0.96 | 100.87 |
| SL 41 | 0.72 | 0.09 | 0.00 | 0.00 | 0.00 | 3.99 | 0.63 | 101.43 |
| SL 42 | 0.98 | 0.04 | 0.00 | 0.00 | 0.00 | 3.13 | 0.39 | 102.63 |
| SL 43 | 1.30 | 0.15 | 0.00 | 0.00 | 0.00 | 8.25 | 1.05 | 99.69 |
| SL 44 | 0.10 | 2.49 | 0.00 | 0.00 | 0.00 | 13.55 | 1.31 | 101.26 |
| SL 45 | 0.90 | 0.01 | 0.00 | 0.00 | 0.00 | 3.12 | 1.12 | 101.91 |
| SL 46 | 2.66 | 0.13 | 0.00 | 0.00 | 0.00 | 5.42 | 1.19 | 100.99 |
| SL 47 | 1.92 | 0.66 | 0.01 | 0.00 | 0.00 | 9.29 | 1.87 | 100.19 |
| SL 48 | 1.63 | 0.03 | 0.00 | 0.00 | 0.00 | 6.45 | 1.52 | 101.52 |

**Table C2:** Normalized whole rock major element data from the Kemi Intrusion (Cr-, Ni-, LOI- and $H_20$-free). Note the set-up of the XRF detector did not allow it to detect any $Cr_2O_3$ and NiO values.

| Sample | $SiO_2$ wt % | $TiO_2$ wt % | $Al2O_3$ wt % | FeO wt % | MnO wt % | MgO wt % | CaO wt % | $Na_2O$ wt % |
|---|---|---|---|---|---|---|---|---|
| SL 01 | 70.47 | 0.16 | 16.89 | 1.60 | 0.03 | 0.80 | 2.33 | 5.40 |
| SL 02 | 71.11 | 0.14 | 16.09 | 1.69 | 0.02 | 0.83 | 1.05 | 6.67 |
| SL 03 | 63.03 | 0.33 | 15.64 | 4.12 | 0.11 | 3.27 | 7.43 | 4.46 |
| SL 04 | 37.75 | 0.34 | 11.27 | 21.03 | 0.50 | 24.56 | 4.56 | 0 |
| SL 05 | 42.28 | 0.36 | 8.86 | 11.62 | 0.14 | 31.32 | 5.41 | 0 |
| SL06 | 21.63 | 0.52 | 17.63 | 24.25 | 0.43 | 35.52 | 0.04 | 0 |
| SL 07 | 41.59 | 0.22 | 4.95 | 15.40 | 0.19 | 36.17 | 1.48 | 0 |
| SL 08 | 43.07 | 0.28 | 6.23 | 14.56 | 0.25 | 33.88 | 1.68 | 0.06 |
| SL 09 | 52.77 | 0.42 | 4.51 | 8.12 | 0.19 | 23.77 | 9.66 | 0.41 |
| SL 10 | 49.62 | 0.14 | 5.63 | 9.80 | 0.21 | 28.47 | 5.71 | 0.30 |
| SL 11 | 48.01 | 0.09 | 5.34 | 11.02 | 0.18 | 30.75 | 4.32 | 0.21 |
| SL 12 | 45.89 | 0.13 | 3.94 | 13.50 | 0.22 | 32.51 | 3.72 | 0.05 |
| SL 13 | 50.50 | 0.08 | 4.81 | 11.06 | 0.21 | 29.08 | 4.06 | 0.16 |
| SL 14 | 51.54 | 0.24 | 3.44 | 10.54 | 0.22 | 28.83 | 4.88 | 0.17 |
| SL 15 | 53.14 | 0.18 | 6.00 | 6.81 | 0.17 | 18.90 | 14.11 | 0.60 |
| SL 16 | 53.24 | 0.19 | 5.28 | 6.30 | 0.15 | 18.82 | 15.53 | 0.40 |
| SL 17 | 49.01 | 0.30 | 4.36 | 11.27 | 0.18 | 30.20 | 4.38 | 0.20 |
| SL 18 | 49.07 | 0.15 | 6.19 | 9.98 | 0.18 | 28.89 | 5.23 | 0.25 |
| SL 19 | 35.78 | 0.52 | 11.98 | 21.25 | 0.40 | 27.23 | 2.60 | 0.20 |
| SL 20 | 52.92 | 0.41 | 4.22 | 10.22 | 0.18 | 27.08 | 4.33 | 0.50 |
| SL 21 | 50.76 | 0.13 | 6.09 | 10.00 | 0.22 | 26.00 | 5.88 | 0.87 |
| SL 22 | 52.12 | 0.25 | 5.28 | 9.56 | 0.21 | 26.45 | 5.28 | 0.78 |
| SL 23 | 52.50 | 0.14 | 5.50 | 7.74 | 0.17 | 26.74 | 6.12 | 1.02 |
| SL 24 | 38.05 | 0.41 | 11.52 | 19.35 | 0.46 | 25.90 | 3.92 | 0.39 |
| SL 25 | 52.48 | 0.13 | 5.70 | 8.29 | 0.16 | 27.32 | 5.11 | 0.66 |
| SL 26 | 51.57 | 0.21 | 5.77 | 9.31 | 0.25 | 25.22 | 6.71 | 0.76 |
| SL 27 | 54.67 | 0.23 | 3.34 | 10.28 | 0.20 | 26.15 | 4.49 | 0.57 |
| SL 28 | 52.74 | 0.12 | 5.27 | 9.04 | 0.19 | 25.75 | 5.33 | 1.46 |
| SL 29 | 52.48 | 0.11 | 6.03 | 8.59 | 0.19 | 25.46 | 5.04 | 1.58 |
| SL 30 | 50.72 | 0.17 | 5.42 | 9.58 | 0.22 | 25.64 | 5.52 | 2.02 |
| SL 31 | 55.95 | 0.42 | 3.05 | 8.64 | 0.21 | 25.49 | 4.70 | 0.91 |
| SL 32 | 52.90 | 0.15 | 4.95 | 9.20 | 0.23 | 24.86 | 6.09 | 1.34 |
| SL 38 | 48.98 | 0.14 | 2.66 | 12.69 | 0.22 | 32.87 | 2.36 | 0.03 |
| SL 39 | 49.82 | 0.11 | 14.72 | 4.98 | 0.12 | 13.88 | 15.56 | 0.71 |
| SL 40 | 54.81 | 0.16 | 13.84 | 4.95 | 0.12 | 14.44 | 9.55 | 2.07 |
| SL 41 | 52.11 | 0.12 | 14.59 | 5.28 | 0.13 | 14.67 | 12.26 | 0.74 |
| SL 42 | 51.98 | 0.14 | 15.19 | 4.44 | 0.11 | 12.18 | 14.93 | 0.99 |
| SL 43 | 48.66 | 0.07 | 25.07 | 3.65 | 0.06 | 7.00 | 13.90 | 1.44 |
| SL 44 | 46.76 | 0.05 | 22.01 | 6.00 | 0.10 | 13.73 | 8.37 | 0.11 |
| SL 45 | 50.80 | 0.10 | 18.45 | 3.66 | 0.09 | 10.15 | 15.82 | 0.92 |
| SL 46 | 50.20 | 0.11 | 27.44 | 1.89 | 0.05 | 1.52 | 15.83 | 2.82 |
| SL 47 | 54.08 | 0.26 | 20.84 | 4.70 | 0.08 | 8.71 | 8.41 | 2.16 |
| SL 48 | 52.02 | 0.21 | 16.88 | 5.42 | 0.09 | 11.45 | 12.17 | 1.74 |

**Table C2 continued:** Normalized whole rock major element data from the Kemi Intrusion (Cr-, Ni-, LOI- and $H_20$-free). Note the set-up of the XRF detector did not allow it to detect any $Cr_2O_3$ and NiO values.

| Sample | $K_2O$ wt % | $P_2O_5$ wt % | $Cr_2O_3$ wt % | NiO wt % |
|---|---|---|---|---|
| SL 01 | 2.28 | 0.05 | 0 | 0 |
| SL 02 | 2.35 | 0.04 | 0 | 0 |
| SL 03 | 1.55 | 0.07 | 0 | 0 |
| SL 04 | 0 | 0.00 | 0 | 0 |
| SL 05 | 0 | 0.02 | 0 | 0 |
| SL06 | 0 | 0 | 0 | 0 |
| SL 07 | 0 | 0 | 0 | 0 |
| SL 08 | 0.01 | 0 | 0 | 0 |
| SL 09 | 0.13 | 0.03 | 0 | 0 |
| SL 10 | 0.13 | 0 | 0 | 0 |
| SL 11 | 0.08 | 0 | 0 | 0 |
| SL 12 | 0.06 | 0 | 0 | 0 |
| SL 13 | 0.05 | 0 | 0 | 0 |
| SL 14 | 0.13 | 0.02 | 0 | 0 |
| SL 15 | 0.09 | 0 | 0 | 0 |
| SL 16 | 0.09 | 0 | 0 | 0 |
| SL 17 | 0.06 | 0.04 | 0 | 0 |
| SL 18 | 0.06 | 0.01 | 0 | 0 |
| SL 19 | 0.03 | 0 | 0 | 0 |
| SL 20 | 0.07 | 0.08 | 0 | 0 |
| SL 21 | 0.07 | 0 | 0 | 0 |
| SL 22 | 0.07 | 0.02 | 0 | 0 |
| SL 23 | 0.08 | 0 | 0 | 0 |
| SL 24 | 0.01 | 0.01 | 0 | 0 |
| SL 25 | 0.15 | 0 | 0 | 0 |
| SL 26 | 0.19 | 0.02 | 0 | 0 |
| SL 27 | 0.08 | 0 | 0 | 0 |
| SL 28 | 0.10 | 0 | 0 | 0 |
| SL 29 | 0.52 | 0 | 0 | 0 |
| SL 30 | 0.72 | 0 | 0 | 0 |
| SL 31 | 0.58 | 0.04 | 0 | 0 |
| SL 32 | 0.28 | 0.01 | 0 | 0 |
| SL 38 | 0.05 | 0 | 0 | 0 |
| SL 39 | 0.09 | 0 | 0 | 0 |
| SL 40 | 0.06 | 0 | 0 | 0 |
| SL 41 | 0.10 | 0 | 0 | 0 |
| SL 42 | 0.04 | 0 | 0 | 0 |
| SL 43 | 0.16 | 0 | 0 | 0 |
| SL 44 | 2.88 | 0 | 0 | 0 |
| SL 45 | 0.01 | 0 | 0 | 0 |
| SL 46 | 0.14 | 0 | 0 | 0 |
| SL 47 | 0.74 | 0.01 | 0 | 0 |
| SL 48 | 0.03 | 0 | 0 | 0 |

**Table C3:** Whole rock minor and trace element concentrations from the Kemi Intrusion (obtained from the Rhodes University XRF detector). * indicates above detection limits.

| Sample | Zn ppm | Cu ppm | Ni ppm | Co ppm | Cr ppm | V ppm |
|---|---|---|---|---|---|---|
| SL 01 | 33.0 | 8.0 | 4.9 | 3.4 | 20.8 | 12.3 |
| SL 02 | 60.6 | 9.0 | 3.1 | 3.8 | 31.8 | 13.0 |
| SL 03 | 250.4 | 29.2 | 36.4 | 15.2 | 114.2 | 43.0 |
| SL 04 | 245.8 | 20.8 | 1197.7 | 169.3 | * | 684.8 |
| SL 05 | 98.6 | 18.4 | 1501.0 | 103.8 | * | 377.5 |
| SL 06 | 286.1 | 30.3 | 1468.5 | 196.0 | * | 1654.3 |
| SL 07 | 113.9 | 12.3 | 924.3 | 140.0 | * | 313.8 |
| SL 08 | 211.6 | 12.6 | 894.4 | 136.9 | * | 364.8 |
| SL 09 | 32.1 | 29.0 | 391.6 | 76.1 | 2255.3 | 161.0 |
| SL 10 | 59.1 | 33.6 | 567.2 | 101.4 | 4848.8 | 95.9 |
| SL 11 | 56.1 | 19.7 | 646.6 | 109.6 | 2681.4 | 59.4 |
| SL 12 | 60.4 | 22.6 | 909.6 | 133.5 | 5291.4 | 68.0 |
| SL 13 | 61.4 | 18.4 | 698.2 | 113.5 | 2833.0 | 53.3 |
| SL 14 | 72.5 | 36.5 | 528.7 | 99.4 | 3868.3 | 125.9 |
| SL 15 | 42.6 | 15.6 | 234.6 | 54.2 | 3925.0 | 146.7 |
| SL 16 | 34.8 | 24.8 | 240.5 | 52.1 | 4076.3 | 165.4 |
| SL 17 | 32.5 | 33.9 | 624.9 | 95.5 | 6917.0 | 108.6 |
| SL 18 | 38.7 | 30.5 | 554.0 | 96.1 | 9010.8 | 107.4 |
| SL 19 | 344.1 | 21.6 | 739.8 | 168.1 | * | 1011.3 |
| SL 20 | 31.6 | 22.0 | 451.3 | 85.5 | 4253.6 | 138.0 |
| SL 21 | 59.3 | 9.3 | 372.0 | 84.0 | 7681.7 | 116.4 |
| SL 22 | 36.1 | 10.7 | 435.2 | 82.2 | 4199.5 | 108.2 |
| SL 23 | 19.8 | 6.4 | 421.8 | 72.1 | 3505.2 | 91.9 |
| SL 24 | 326.6 | 24.4 | 594.9 | 146.1 | * | 986.1 |
| SL 25 | 17.8 | 5.9 | 404.0 | 79.9 | 2558.9 | 76.4 |
| SL 26 | 33.1 | 11.4 | 345.0 | 77.9 | 2167.8 | 98.8 |
| SL 27 | 45.7 | 61.1 | 376.3 | 82.4 | 2152.5 | 128.5 |
| SL 28 | 53.6 | 7.2 | 349.8 | 77.1 | 2244.7 | 84.2 |
| SL 29 | 53.7 | 7.4 | 378.5 | 75.8 | 2301.1 | 80.7 |
| SL 30 | 112.7 | 9.3 | 320.5 | 78.0 | 9474.1 | 131.0 |
| SL 31 | 66.8 | 21.2 | 369.6 | 78.8 | 2675.2 | 157.4 |
| SL 32 | 56.3 | 8.1 | 337.7 | 74.4 | 2065.2 | 99.6 |
| SL 38 | 69.5 | 24.0 | 838.2 | 123.0 | 932.6 | 59.6 |
| SL 39 | 27.1 | 17.1 | 209.0 | 41.5 | 1951.7 | 97.0 |
| SL 40 | 34.0 | 29.2 | 188.5 | 43.9 | 1207.8 | 99.1 |
| SL 41 | 32.7 | 13.2 | 155.1 | 42.4 | 772.3 | 88.3 |
| SL 42 | 28.2 | 12.4 | 131.6 | 37.5 | 978.6 | 114.8 |
| SL 43 | 24.8 | 5.6 | 118.6 | 27.1 | 156.4 | 40.3 |
| SL 44 | 42.1 | 123.1 | 384.7 | 62.4 | 24.1 | 17.2 |
| SL 45 | 19.9 | 27.8 | 118.7 | 29.5 | 400.5 | 90.5 |
| SL 46 | 9.8 | 15.5 | 17.3 | 18.8 | 53.8 | 31.4 |
| SL 47 | 35.4 | 143.5 | 160.9 | 31.6 | 683.1 | 92.8 |
| SL 48 | 39.4 | 8.6 | 183.5 | 36.6 | 911.4 | 113.0 |

**Table C3 continued:** Whole rock minor and trace element concentrations from the Kemi Intrusion (obtained from the Rhodes University XRF detector).

| Sample | Sr ppm | Rb ppm | Zr ppm | Nb ppm | Y ppm |
|---|---|---|---|---|---|
| SL 01 | 387.0 | 32.9 | 109.1 | 0.8 | 0.4 |
| SL 02 | 343.8 | 27.8 | 129.3 | 0.8 | 1.3 |
| SL 03 | 400.7 | 27.1 | 55.4 | 2.9 | 7.2 |
| SL 04 | 89.2 | -0.2 | 10.7 | 0.3 | 3.0 |
| SL 05 | 212.0 | -0.9 | 20.0 | 1.4 | 4.3 |
| SL 06 | 0.2 | 0.6 | 2.3 | 0.2 | 1.0 |
| SL 07 | 9.6 | 0.9 | 5.1 | 0.5 | 2.5 |
| SL 08 | 9.6 | 0.9 | 5.1 | 0.5 | 2.5 |
| SL 09 | 63.0 | 3.5 | 33.0 | 2.0 | 9.9 |
| SL 10 | 59.3 | 4.3 | 5.3 | 0.9 | 3.0 |
| SL 11 | 38.5 | 1.3 | 4.1 | 0.4 | 1.6 |
| SL 12 | 11.1 | 1.8 | 6.4 | 0.3 | 2.9 |
| SL 13 | 39.6 | 1.4 | 3.2 | 0.8 | 1.8 |
| SL 14 | 28.3 | 4.2 | 16.7 | 0.6 | 5.2 |
| SL 15 | 49.9 | 1.0 | 13.3 | 1.9 | 6.2 |
| SL 16 | 35.7 | 1.3 | 9.3 | 0.8 | 5.4 |
| SL 17 | 47.9 | 3.2 | 28.7 | 1.6 | 6.8 |
| SL 18 | 55 | 2.8 | 8.5 | 0.6 | 3.1 |
| SL 19 | 24.3 | 2.4 | 8.7 | 0.4 | 3.2 |
| SL 20 | 51 | 1.3 | 35.8 | 1.7 | 8.6 |
| SL 21 | 85.5 | 2 | 4 | 0.8 | 2.4 |
| SL 22 | 78 | 2.8 | 18.1 | 1.2 | 5.2 |
| SL 23 | 79.9 | 2 | 5.2 | 0.2 | 2.9 |
| SL 24 | 34.1 | 0.7 | 7.7 | 1.5 | 3.1 |
| SL 25 | 60.6 | 5.3 | 4.3 | 0.1 | 2.6 |
| SL 26 | 70.1 | 4.8 | 13.5 | 0.7 | 6 |
| SL 27 | 44.3 | 2.1 | 13.4 | 0.6 | 5.7 |
| SL 28 | 73.3 | 3.2 | 4.5 | 0.2 | 3.2 |
| SL 29 | 85.2 | 17.2 | 5.9 | 0.2 | 2.2 |
| SL 30 | 98.5 | 21.4 | 5.6 | 0.7 | 2.5 |
| SL 31 | 71.8 | 19.2 | 31.7 | 1.8 | 8.5 |
| SL 32 | 96 | 9.2 | 6.5 | 1 | 3.7 |
| SL 38 | 20.1 | 1.2 | 6.8 | 0.3 | 3.3 |
| SL 39 | 170.8 | 1.5 | 4.3 | 0.4 | 3.6 |
| SL 40 | 111.7 | -0.2 | 8.5 | 0.8 | 2.9 |
| SL 41 | 121.2 | 1.8 | 6.6 | 0.9 | 3.0 |
| SL 42 | 169.4 | -0.1 | 6.4 | 0.4 | 4.3 |
| SL 43 | 235.0 | 1.9 | 3.4 | 0.6 | 1.3 |
| SL 44 | 33.6 | 39.3 | 3.7 | 0.7 | 0.6 |
| SL 45 | 189.1 | 0.4 | 3.5 | 0.8 | 2.8 |
| SL 46 | 333.8 | 1.5 | 6.8 | 0.4 | 2.3 |
| SL 47 | 233.9 | 11.1 | 16.0 | 0.8 | 4.9 |
| SL 48 | 274.1 | 0.8 | 9.0 | 0.1 | 5.4 |

**Table C4:** The C1 chondrite and primitive mantle normalization values (McDonough and Sun, 1995).

| Element | Units | C1 Chrondrite | Mantle | Element | Units | C1 Chrondrite | Mantle |
|---|---|---|---|---|---|---|---|
| Li | ppb | 1500 | 1600 | Rh | ppb | 130 | 0.9 |
| Be | ppb | 25 | 68 | Pd | ppb | 550 | 3.9 |
| B | ppb | 900 | 300 | Ag | ppb | 200 | 8 |
| C | ppb | 35000000 | 120000 | Cd | ppb | 710 | 40 |
| N | ppb | 3180000 | 2000 | In | ppb | 80 | 11 |
| F | ppb | 60000 | 25000 | Sn | ppb | 1650 | 130 |
| Na | ppb | 5100000 | 2670000 | Sb | ppb | 140 | 5.5 |
| Na | ppm | 5100 | 2670 | Te | ppb | 2330 | 12 |
| Mg | ppm | 96500 | 228000 | I | ppb | 450 | 10 |
| Al | ppm | 8600 | 23500 | Cs | ppb | 190 | 21 |
| Si | ppb | 1.07E+08 | 2.10E+08 | Ba | ppb | 2410 | 6600 |
| P | ppb | 1080000 | 90000 | La | ppb | 237 | 648 |
| S | ppb | 54000000 | 250000 | Ce | ppb | 613 | 1675 |
| Cl | ppb | 680000 | 17000 | Pr | ppb | 92.8 | 254 |
| K | ppb | 550000 | 240000 | Nd | ppb | 457 | 1250 |
| K | ppm | 550 | 240 | Sm | ppb | 148 | 406 |
| Ca | ppm | 9250000 | 25300000 | Eu | ppb | 56.3 | 154 |
| Sc | ppb | 5920 | 16200 | Gd | ppb | 199 | 544 |
| Ti | ppb | 440000 | 1205000 | Tb | ppb | 36.1 | 99 |
| V | ppb | 56000 | 82000 | Dy | ppb | 246 | 674 |
| Cr | ppm | 2650 | 2625 | Ho | ppb | 54.6 | 149 |
| Cr | ppb | 2650000 | 2625000 | Er | ppb | 160 | 438 |
| Mn | ppb | 1920000 | 1045000 | Tm | ppb | 24.7 | 68 |
| Fe | ppm | 1.81E+08 | 62600000 | Yb | ppb | 161 | 441 |
| Co | ppb | 500000 | 105000 | Lu | ppb | 24.6 | 67.5 |
| Ni | ppb | 10500000 | 1960000 | Hf | ppb | 103 | 283 |
| Cu | ppb | 120000 | 30000 | Ta | ppb | 13.6 | 37 |
| Zn | ppb | 310000 | 55000 | W | ppb | 93 | 29 |
| Ga | ppb | 9200 | 4000 | Re | ppb | 40 | 0.28 |
| Ge | ppb | 31000 | 1100 | Os | ppb | 490 | 3.4 |
| As | ppb | 1850 | 50 | Ir | ppb | 455 | 3.2 |
| Se | ppb | 21000 | 75 | Pt | ppb | 1010 | 7.1 |
| Br | ppb | 3570 | 50 | Au | ppb | 140 | 1 |
| Rb | ppb | 2300 | 600 | Hg | ppb | 300 | 10 |
| Sr | ppb | 7250 | 19900 | Tl | ppb | 140 | 3.5 |
| Y | ppb | 1570 | 4300 | Pb | ppb | 2470 | 150 |
| Zr | ppb | 3820 | 10500 | Bi | ppb | 110 | 2.5 |
| Nb | ppm | 0.24 | 0.658 | Th | ppb | 29 | 79.5 |
| Mo | ppb | 900 | 50 | U | ppb | 7.4 | 20.3 |
| Ru | ppb | 710 | 5 | | | | |

**Table C5:** Whole rock minor and trace element concentrations from the Kemi Intrusion (obtained from the Stellenbosch University ICP-MS). Note the units are in PPB. * indicates values below the detection limits.

| Sample (PPB) | Li | Be | B | Si | Ti | V | Mn | Co |
|---|---|---|---|---|---|---|---|---|
| SL 01 | 11871 | 952 | 5729 | 2220101 | 1233460 | 19525 | 202699 | 3913 |
| SL 02 | 6992 | 510 | 836 | 7636162 | 1015194 | 20786 | 193299 | 4121 |
| SL 03 | 14051 | 555 | 281 | 2835712 | 2553245 | 55231 | 897581 | 16677 |
| SL 04 | 11653 | 112 | * | 482790 | 714772 | 103897 | 1033547 | 49938 |
| SL 05 | 7863 | 43 | * | 475498 | 1065206 | 123379 | 477107 | 51861 |
| SL 06 | 1706 | 19 | * | 225120 | 295430 | 64302 | 285842 | 19795 |
| SL 07 | 81 | 25 | * | 444860 | 526900 | 105475 | 685256 | 68844 |
| SL 08 | 661 | 76 | 4486 | 701872 | 893610 | 168800 | 1051532 | 87160 |
| SL 09 | 243 | 135 | 1667 | 766124 | 2530125 | 136147 | 1216541 | 60843 |
| SL 10 | 420 | 43 | 2676 | 563290 | 760441 | 89209 | 1343034 | 81107 |
| SL 11 | 58 | 21 | 6009 | 369774 | 441488 | 49847 | 999511 | 76100 |
| SL 12 | 464 | 23 | 9693 | 505912 | 545861 | 54075 | 1098753 | 96484 |
| SL 13 | 434 | 16 | * | 409880 | 399061 | 47957 | 965828 | 72429 |
| SL 14 | 101 | 38 | 446 | 433716 | 1157639 | 90474 | 1045383 | 64420 |
| SL 15 | 661 | 52 | * | 942204 | 921714 | 109812 | 910189 | 39218 |
| SL 16 | 227 | 18 | * | 974550 | 947188 | 123990 | 833602 | 36685 |
| SL 17 | 252 | 55 | 663 | 346258 | 1308017 | 73320 | 859279 | 68817 |
| SL 18 | 559 | 45 | * | 417214 | 594881 | 67271 | 876532 | 66792 |
| SL 19 | 1944 | 47 | * | 229389 | 703530 | 126478 | 746120 | 48837 |
| SL 20 | 897 | 89 | * | 393542 | 2234447 | 127285 | 1093208 | 67821 |
| SL 21 | 1381 | 75 | 428 | 437663 | 555619 | 84471 | 1246598 | 62749 |
| SL 22 | 738 | 91 | * | 486104 | 1310147 | 95361 | 1239533 | 65823 |
| SL 23 | 1946 | 82 | 407 | 504496 | 769921 | 86136 | 1040107 | 59752 |
| SL 24 | 3791 | 78 | * | 367401 | 936378 | 229595 | 1146277 | 59209 |
| SL 25 | 1445 | 63 | 236 | 536972 | 730513 | 77063 | 1019059 | 67370 |
| SL 26 | 1027 | 132 | * | 585405 | 1264437 | 98860 | 1672991 | 69542 |
| SL 27 | 474 | 91 | * | 526733 | 1532921 | 130192 | 1399334 | 72283 |
| SL 28 | 1531 | 78 | 197 | 675072 | 773756 | 89224 | 1412371 | 72064 |
| SL 29 | 6773 | 101 | 1160 | 1076463 | 784271 | 83965 | 1309134 | 71902 |
| SL 30 | 6591 | 147 | 2022 | 1366687 | 1108324 | 109912 | 1510291 | 74103 |
| SL 31 | 645 | 207 | 100 | 1141354 | 3269286 | 170608 | 1457021 | 73559 |
| SL 32 | 2070 | 119 | 1589 | 1126662 | 1152591 | 107512 | 1784698 | 74594 |
| SL 38 | 794 | 69 | 13134 | 941360 | 1071780 | 87410 | 1623776 | 138883 |
| SL 39 | 4022 | 79 | * | 1676440 | 1042570 | 131894 | 989516 | 74275 |
| SL 40 | 8370 | 105 | * | 1597625 | 1433535 | 140022 | 1094456 | 70680 |
| SL 41 | 2206 | 82 | * | 1365359 | 1195041 | 117782 | 1082018 | 64245 |
| SL 42 | 911 | 62 | * | 1231946 | 1240869 | 143334 | 917427 | 53854 |
| SL 43 | 5638 | 73 | * | 425118 | 557830 | 48881 | 487552 | 49791 |
| SL 44 | 13314 | 228 | 8716 | 395783 | 430687 | 25495 | 765309 | 80502 |
| SL 45 | 1441 | 45 | * | 582473 | 863154 | 114477 | 705737 | 53590 |
| SL 46 | 4717 | 47 | * | 494079 | 760630 | 43523 | 336414 | 57968 |
| SL 47 | 15562 | 266 | * | 363939 | 1197232 | 112131 | 639716 | 49791 |
| SL 48 | 8544 | 137 | * | 406230 | 1705596 | 142133 | 722893 | 55138 |

**Table C5 continued:** Whole rock minor and trace element concentrations from the Kemi Intrusion (obtained from the Stellenbosch University ICP-MS). Note the units are in PPB.

| Sample (PPB) | Ni | Cu | Zn | As | Se | Mo | Cd | Ba |
|---|---|---|---|---|---|---|---|---|
| SL 01 | 6260 | 6989 | 25427 | 332 | 173 | 1585 | 67 | 1347279 |
| SL 02 | 4302 | 7236 | 59294 | 588 | 310 | 819 | 88 | 2106845 |
| SL 03 | 38851 | 26725 | 181568 | 676 | 826 | 832 | 1838 | 712005 |
| SL 04 | 789121 | 517252 | 47290 | 137 | 202 | 309 | 69 | 3465 |
| SL 05 | 877001 | 2186 | 41823 | 186 | 177 | 188 | 115 | 3100 |
| SL 06 | 558964 | 3388 | 24500 | 261 | 175 | 454 | 5 | 16654 |
| SL 07 | 567602 | 949 | 37236 | 207 | 164 | 122 | 10 | 376 |
| SL 08 | 604567 | 1304 | 99921 | 3940 | 180 | 221 | 14 | 1559 |
| SL 09 | 310217 | 21171 | 18796 | 559 | 222 | 91 | 100 | 10742 |
| SL 10 | 456644 | 24978 | 47532 | 112 | 187 | 41 | 51 | 7032 |
| SL 11 | 442448 | 10376 | 35953 | 129 | 197 | 52 | 34 | 4024 |
| SL 12 | 634707 | 13324 | 35538 | 133 | 280 | 82 | 45 | 4500 |
| SL 13 | 445204 | 9155 | 35292 | 140 | 388 | 91 | 45 | 14050 |
| SL 14 | 340914 | 21686 | 37280 | 135 | 352 | 163 | 67 | 18624 |
| SL 15 | 168976 | 7155 | 25205 | 170 | 305 | 66 | 64 | 20214 |
| SL 16 | 165320 | 13516 | 17989 | 99 | 196 | 106 | 57 | 5902 |
| SL 17 | 423584 | 20741 | 14077 | 244 | 273 | 154 | 70 | 4500 |
| SL 18 | 381808 | 20637 | 15942 | 311 | 136 | 74 | 65 | 4159 |
| SL 19 | 324002 | 2030 | 51392 | 237 | 179 | 417 | 24 | 4246 |
| SL 20 | 326617 | 20385 | 25098 | 339 | 396 | 135 | 84 | 5332 |
| SL 21 | 270655 | 2575 | 30150 | 243 | 148 | 97 | 81 | 6346 |
| SL 22 | 326591 | 4902 | 29270 | 349 | 290 | 88 | 105 | 6251 |
| SL 23 | 348607 | 2045 | 11735 | 372 | 240 | 82 | 60 | 7591 |
| SL 24 | 347366 | 4802 | 82388 | 659 | 356 | 1285 | 30 | 3150 |
| SL 25 | 339579 | 2287 | 11673 | 505 | 358 | 39 | 54 | 6220 |
| SL 26 | 292829 | 6935 | 22360 | 707 | 507 | 114 | 81 | 19703 |
| SL 27 | 313978 | 66825 | 27625 | 980 | 677 | 119 | 73 | 4277 |
| SL 28 | 321193 | 4991 | 35891 | 1204 | 602 | 42 | 44 | 6804 |
| SL 29 | 344073 | 4790 | 31355 | 967 | 634 | 74 | 53 | 13976 |
| SL 30 | 305679 | 4759 | 50077 | 3035 | 1618 | 54 | 61 | 31881 |
| SL 31 | 350097 | 24436 | 47591 | 1191 | 1300 | 196 | 118 | 5428 |
| SL 32 | 326647 | 4740 | 38515 | 1536 | 1355 | 39 | 493 | 10214 |
| SL 38 | 933150 | 28105 | 50621 | 5204 | 3085 | 102 | 79 | 6619 |
| SL 39 | 271994 | 19577 | 27912 | 3902 | 3313 | 187 | 80 | 29019 |
| SL 40 | 237822 | 45709 | 37240 | 3923 | 3898 | 279 | 82 | 25591 |
| SL 41 | 205070 | 18344 | 32749 | 3125 | 3095 | 170 | 65 | 30294 |
| SL 42 | 175487 | 15242 | 28074 | 2124 | 2659 | 321 | 68 | 12393 |
| SL 43 | 150125 | 5770 | 18260 | 2399 | 1257 | 176 | 21 | 38057 |
| SL 44 | 473595 | 184187 | 31944 | 6158 | 972 | 112 | 54 | 415957 |
| SL 45 | 169712 | 38128 | 22697 | 2683 | 1830 | 534 | 110 | 7123 |
| SL 46 | 53940 | 21195 | 12623 | 2047 | 1397 | 263 | 67 | 27250 |
| SL 47 | 205657 | 219901 | 37868 | 4427 | 3344 | 162 | 196 | 74796 |
| SL 48 | 243198 | 19254 | 52121 | 4008 | 4917 | 148 | 103 | 8430 |

**Table C5 continued:** Whole rock minor and trace element concentrations from the Kemi Intrusion (obtained from the Stellenbosch University ICP-MS). Note the units are in PPB.

| Sample (PPB) | La | Ce | Pr | Nd | Sm | Eu | Gd | Dy |
|---|---|---|---|---|---|---|---|---|
| SL 01 | 13150 | 21351 | 2112 | 7082 | 998 | 1091 | 976 | 212 |
| SL 02 | 48158 | 70461 | 6247 | 18220 | 1506 | 1797 | 1860 | 271 |
| SL 03 | 24876 | 43774 | 4832 | 18873 | 2637 | 1245 | 2436 | 1139 |
| SL 04 | 2101 | 4129 | 466 | 1868 | 385 | 155 | 428 | 402 |
| SL 05 | 2671 | 5495 | 662 | 2773 | 567 | 171 | 584 | 468 |
| SL 06 | 162 | 342 | 45 | 211 | 66 | 32 | 84 | 101 |
| SL 07 | 991 | 1904 | 270 | 1194 | 271 | 52 | 305 | 298 |
| SL 08 | 1094 | 2080 | 258 | 1075 | 248 | 56 | 300 | 318 |
| SL 09 | 5127 | 10480 | 1276 | 5366 | 1250 | 252 | 1388 | 1308 |
| SL 10 | 702 | 1593 | 226 | 1014 | 248 | 134 | 288 | 311 |
| SL 11 | 541 | 1115 | 152 | 669 | 159 | 84 | 197 | 216 |
| SL 12 | 733 | 1582 | 248 | 1165 | 282 | 101 | 332 | 328 |
| SL 13 | 364 | 730 | 109 | 511 | 127 | 66 | 159 | 171 |
| SL 14 | 2499 | 4203 | 583 | 2620 | 601 | 179 | 735 | 698 |
| SL 15 | 3304 | 7395 | 895 | 3618 | 824 | 269 | 952 | 859 |
| SL 16 | 1112 | 2804 | 417 | 2107 | 617 | 213 | 792 | 863 |
| SL 17 | 4900 | 9456 | 1236 | 5382 | 1162 | 260 | 1479 | 1222 |
| SL 18 | 1395 | 2497 | 350 | 1607 | 391 | 176 | 523 | 513 |
| SL 19 | 1290 | 2605 | 340 | 1543 | 397 | 119 | 543 | 537 |
| SL 20 | 7464 | 12069 | 1536 | 6555 | 1360 | 291 | 1906 | 1344 |
| SL 21 | 1580 | 1598 | 233 | 1059 | 263 | 213 | 375 | 365 |
| SL 22 | 2736 | 5545 | 687 | 2955 | 665 | 217 | 960 | 718 |
| SL 23 | 902 | 2034 | 292 | 1386 | 347 | 182 | 516 | 432 |
| SL 24 | 743 | 1964 | 276 | 1312 | 349 | 111 | 546 | 421 |
| SL 25 | 734 | 1716 | 247 | 1103 | 263 | 156 | 439 | 333 |
| SL 26 | 2847 | 5510 | 676 | 2990 | 693 | 362 | 1292 | 800 |
| SL 27 | 1388 | 3054 | 432 | 2143 | 630 | 141 | 1131 | 856 |
| SL 28 | 828 | 1612 | 215 | 1020 | 250 | 152 | 533 | 303 |
| SL 29 | 538 | 1362 | 189 | 859 | 221 | 198 | 463 | 269 |
| SL 30 | 944 | 1687 | 227 | 1009 | 261 | 372 | 797 | 361 |
| SL 31 | 4386 | 8585 | 1035 | 4325 | 974 | 211 | 2294 | 1021 |
| SL 32 | 721 | 1757 | 261 | 1221 | 321 | 230 | 739 | 399 |
| SL 38 | 521 | 1088 | 155 | 723 | 203 | 129 | 679 | 269 |
| SL 39 | 755 | 1353 | 192 | 941 | 301 | 489 | 1027 | 381 |
| SL 40 | 869 | 1732 | 225 | 1041 | 293 | 387 | 1258 | 350 |
| SL 41 | 663 | 1361 | 173 | 805 | 223 | 461 | 918 | 255 |
| SL 42 | 712 | 1541 | 213 | 978 | 301 | 277 | 1007 | 397 |
| SL 43 | 592 | 1089 | 138 | 616 | 170 | 570 | 825 | 195 |
| SL 44 | 303 | 440 | 51 | 309 | 127 | 4649 | 2319 | 73 |
| SL 45 | 444 | 895 | 122 | 610 | 190 | 200 | 730 | 267 |
| SL 46 | 576 | 1078 | 140 | 642 | 164 | 552 | 1008 | 205 |
| SL 47 | 2007 | 3636 | 430 | 1898 | 476 | 1563 | 3523 | 390 |
| SL 48 | 1073 | 2179 | 288 | 1364 | 380 | 356 | 2111 | 417 |

**Table C5 continued:** Whole rock minor and trace element concentrations from the Kemi Intrusion (obtained from the Stellenbosch University ICP-MS). Note the units are in PPB.

| Sample (PPB) | Ho | Er | Tm | Yb | Lu | Pb |
|---|---|---|---|---|---|---|
| SL 01 | 36 | 116 | 15 | 107 | 21 | 37375 |
| SL 02 | 44 | 160 | 16 | 111 | 20 | 15355 |
| SL 03 | 212 | 629 | 81 | 535 | 83 | 468989 |
| SL 04 | 84 | 253 | 36 | 251 | 40 | 2664 |
| SL 05 | 94 | 279 | 39 | 255 | 44 | 4411 |
| SL 06 | 21 | 66 | 10 | 66 | 14 | 311 |
| SL 07 | 62 | 187 | 26 | 168 | 35 | 352 |
| SL 08 | 69 | 208 | 29 | 192 | 40 | 264 |
| SL 09 | 264 | 757 | 103 | 663 | 105 | 1177 |
| SL 10 | 66 | 200 | 29 | 194 | 40 | 704 |
| SL 11 | 46 | 146 | 22 | 152 | 49 | 303 |
| SL 12 | 69 | 203 | 27 | 173 | 47 | 726 |
| SL 13 | 36 | 114 | 17 | 115 | 50 | 744 |
| SL 14 | 148 | 437 | 61 | 404 | 100 | 570 |
| SL 15 | 170 | 486 | 66 | 430 | 96 | 379 |
| SL 16 | 178 | 513 | 70 | 462 | 103 | 652 |
| SL 17 | 248 | 714 | 93 | 576 | 133 | 843 |
| SL 18 | 111 | 341 | 51 | 351 | 112 | 376 |
| SL 19 | 117 | 361 | 54 | 377 | 116 | 434 |
| SL 20 | 268 | 796 | 101 | 667 | 170 | 541 |
| SL 21 | 80 | 263 | 40 | 286 | 131 | 447 |
| SL 22 | 148 | 443 | 60 | 411 | 149 | 516 |
| SL 23 | 90 | 282 | 40 | 282 | 151 | 569 |
| SL 24 | 86 | 265 | 37 | 269 | 155 | 916 |
| SL 25 | 73 | 231 | 34 | 235 | 189 | 343 |
| SL 26 | 165 | 542 | 71 | 516 | 256 | 503 |
| SL 27 | 178 | 565 | 80 | 597 | 310 | 357 |
| SL 28 | 64 | 210 | 30 | 228 | 285 | 302 |
| SL 29 | 55 | 195 | 27 | 196 | 273 | 425 |
| SL 30 | 73 | 260 | 34 | 266 | 378 | 283 |
| SL 31 | 206 | 688 | 85 | 624 | 417 | 408 |
| SL 32 | 86 | 279 | 37 | 286 | 342 | 560 |
| SL 38 | 56 | 209 | 26 | 215 | 509 | 2036 |
| SL 39 | 72 | 266 | 33 | 269 | 473 | 525 |
| SL 40 | 74 | 274 | 33 | 266 | 578 | 356 |
| SL 41 | 50 | 201 | 22 | 179 | 520 | 251 |
| SL 42 | 81 | 274 | 32 | 290 | 484 | 742 |
| SL 43 | 39 | 151 | 17 | 145 | 460 | 1590 |
| SL 44 | 18 | 62 | 7 | 68 | 588 | 780 |
| SL 45 | 52 | 205 | 23 | 199 | 586 | 1035 |
| SL 46 | 40 | 177 | 22 | 156 | 576 | 4384 |
| SL 47 | 79 | 429 | 34 | 380 | 669 | 6231 |
| SL 48 | 80 | 386 | 36 | 358 | 720 | 2942 |

**Table C6:** Whole rock major element concentrations from the Kemi Intrusion (obtained from the Stellenbosch University ICP-AES). Note the units are in PPM. * indicate values below the detection limits.

| Sample (PPM) | Al | Ca | Fe | K | Mg | Na | Cr |
|---|---|---|---|---|---|---|---|
| SL 01 | 89201 | 16773 | 12099 | 17327 | 3822 | 40495 | 23 |
| SL 02 | 84544 | 7630 | 12868 | 18513 | 3867 | 48218 | 40 |
| SL 03 | 67419 | 45362 | 27899 | 11052 | 7558 | 31639 | 121 |
| SL 04 | 16518 | 21907 | 42199 | 2499 | 97360 | 129 | 25323 |
| SL 05 | 3786 | 26268 | 43398 | 1297 | 111309 | 12 | 32366 |
| SL 06 | 9940 | 223 | 18019 | 1216 | 76823 | 26 | 24597 |
| SL 07 | 1312 | 8005 | 66306 | 1229 | 140572 | 8 | 18942 |
| SL 08 | 1684 | 9680 | 75572 | 1085 | 138292 | 276 | 28871 |
| SL 09 | 11752 | 52764 | 51234 | * | 94427 | 787 | 2159 |
| SL 10 | 3413 | 30995 | 66108 | 373 | 115475 | 813 | 4831 |
| SL 11 | 2039 | 26458 | 77527 | 91 | 134206 | 1134 | 2684 |
| SL 12 | 1071 | 21560 | 81390 | 38 | 165404 | 225 | 4077 |
| SL 13 | 1484 | 23791 | 70828 | 53 | 139735 | 371 | 2782 |
| SL 14 | 2533 | 30630 | 71377 | 215 | 118760 | 654 | 3627 |
| SL 15 | 16362 | 76576 | 40978 | 406 | 72532 | 465 | 4013 |
| SL 16 | 13852 | 87238 | 37885 | 375 | 73584 | 277 | 4171 |
| SL 17 | 1683 | 28479 | 74532 | 105 | 136923 | 1291 | 4451 |
| SL 18 | 3309 | 34072 | 65072 | 136 | 128778 | 1612 | 5100 |
| SL 19 | 6400 | 14507 | 57202 | 81 | 102887 | 990 | 21671 |
| SL 20 | 2878 | 27796 | 74954 | 188 | 126375 | 2307 | 4329 |
| SL 21 | 4523 | 34667 | 66263 | 234 | 118112 | 3439 | 4898 |
| SL 22 | 3498 | 29629 | 65627 | 292 | 116751 | 2376 | 3909 |
| SL 23 | 5821 | 35222 | 53355 | 438 | 124338 | 2737 | 3198 |
| SL 24 | 6499 | 20051 | 64097 | 559 | 87882 | 1593 | 41808 |
| SL 25 | 2838 | 29905 | 58478 | 628 | 121205 | 2428 | 2582 |
| SL 26 | 4580 | 41422 | 68536 | 858 | 118419 | 3232 | 2176 |
| SL 27 | 3926 | 30315 | 77019 | 617 | 125296 | 3148 | 2128 |
| SL 28 | 4340 | 27365 | 62638 | 792 | 115602 | 2812 | 2191 |
| SL 29 | 16740 | 30628 | 59489 | 4426 | 128686 | 6706 | 3537 |
| SL 30 | 4761 | 24442 | 60326 | 3338 | 117079 | 2138 | 2077 |
| SL 31 | 6291 | 29492 | 61862 | 4292 | 117279 | 3006 | 2470 |
| SL 32 | 4833 | 34155 | 67133 | 2004 | 120751 | 2038 | 1938 |
| SL 38 | 1312 | 14120 | 83022 | 263 | 173191 | 358 | 955 |
| SL 39 | 61470 | 94584 | 34080 | 679 | 61940 | 3202 | 1972 |
| SL 40 | 64498 | 60410 | 36594 | 456 | 77261 | 14359 | 1307 |
| SL 41 | 45156 | 59070 | 33545 | 524 | 53621 | 2211 | 842 |
| SL 42 | 46276 | 77264 | 28180 | 305 | 33545 | 1913 | 1003 |
| SL 43 | 107667 | 82213 | 24604 | 1023 | 24015 | 7934 | 159 |
| SL 44 | 73313 | 32560 | 38033 | 15564 | 42217 | 271 | 23 |
| SL 45 | 61146 | 87213 | 23728 | 197 | 23440 | 2444 | 422 |
| SL 46 | 129832 | 97854 | 14129 | 1257 | 1084 | 18731 | 53 |
| SL 47 | 86141 | 47370 | 31936 | 5119 | 33917 | 14659 | 691 |
| SL 48 | 51817 | 60410 | 34668 | 288 | 29470 | 6283 | 958 |

**Table C7:** The $^{143}Nd$ / $^{144}Nd$ isotopic values from the Kemi Intrusion (obtained from the AEON EarthLAB MC-ICP-MS housed at the University of Cape Town). The table on the left excludes any samples from the small chromitite layer and surrounding peridotites and the table on the right is samples from the small chromitite layer and surrounding peridotites.

| Sample | $^{143}Nd$ /$^{144}Nd$ |
|---|---|
| SL 05 | 0.511459 |
| SL 07 | 0.511689 |
| SL 06 | 0.512288 |
| SL 09 | 0.511734 |
| SL 38 | 0.511906 |
| SL 14 | 0.511732 |
| SL 16 | 0.512377 |
| SL 39 | 0.512253 |
| SL 42 | 0.512193 |
| SL 46 | 0.511781 |
| SL 47 | 0.511491 |

| Sample | $^{143}Nd$ / $^{144}Nd$ |
|---|---|
| SL 17 | 0.511837 |
| SL 20 | 0.511773 |
| SL 22 | 0.511830 |
| SL 23 | 0.511992 |
| SL 24 | 0.511967 |
| SL 25 | 0.511956 |
| SL 26 | 0.511753 |
| SL 28 | 0.512029 |
| SL 31 | 0.511916 |

**Table C8:** The initial $^{143}Nd$ /$^{144}Nd$ and $\varepsilon_{Nd}^{2.44}$ values obtained for the Kemi Intrusion. The table on the left excludes any samples from the small chromitite layer and surrounding peridotites and the table on the right is samples from the small chromitite layer and surrounding peridotites. The $\varepsilon_{Nd}^{2.44}$ values were calculated as described in DePaolo and Wasserburg (1976).

| Sample | Initial $^{143}Nd$ /$^{144}Nd$ | $\varepsilon_{Nd}^{2.44}$ |
|---|---|---|
| SL 05 | 0.509394 | -1.6 |
| SL 07 | 0.509398 | -1.5 |
| SL 06 | 0.509108 | -7.2 |
| SL 09 | 0.509382 | -1.8 |
| SL 38 | 0.509065 | -8 |
| SL 14 | 0.509415 | -1.2 |
| SL 16 | 0.509423 | -1 |
| SL 39 | 0.509026 | -8.8 |
| SL 42 | 0.509084 | -7.7 |
| SL 46 | 0.509202 | -5.3 |
| SL 47 | 0.508958 | -10.1 |

| Sample | Initial $^{143}Nd$ /$^{144}Nd$ | $\varepsilon_{Nd}^{2.44}$ |
|---|---|---|
| SL 17 | 0.509658 | 3.6 |
| SL 20 | 0.509678 | 4 |
| SL 22 | 0.509558 | 1.7 |
| SL 23 | 0.509466 | -0.2 |
| SL 24 | 0.509284 | -3.7 |
| SL 25 | 0.509551 | 1.5 |
| SL 26 | 0.509413 | -1.2 |
| SL 28 | 0.509551 | 1.5 |
| SL 31 | 0.509642 | 3.3 |

**Table C9:** Whole rock PGE and chalcophile element concentrations from the Kemi Intrusion (PGE data obtained from the University of Quebec ICP-MS and the chalcophile element data obtained from the University of Quebec AAS thermo elemental analyser). * indicate values below the detection limits. The PGE and Au concentrations are in ppb and the Ni, Cu and S concentrations are in ppm.

| Sample | Os | Ir | Ru | Rh | Pd | Pt | Au |
|---|---|---|---|---|---|---|---|
| SL 05 | 12.3 | 7.6 | 34.8 | 4.6 | 11.7 | 11.6 | 25.4 |
| SL 06 | 202.7 | 94.1 | 162.9 | 11.9 | 33.4 | 9.5 | 6.8 |
| SL 07 | 18.2 | 9.9 | 51.7 | 4.4 | 2.5 | 2 | * |
| SL 09 | 0.4 | 3.8 | 0.7 | 15.2 | 25.9 | 106.8 | 3.4 |
| SL 11 | * | 0.7 | 0.8 | 1.5 | 26.3 | 6 | 1.9 |
| SL 14 | * | 1.4 | 0.5 | 2.9 | 8.3 | 14 | 1.1 |
| SL 16 | * | 0.9 | 0.2 | 2.1 | 11.2 | 15.9 | 0.6 |
| SL 17 | 1.7 | 9.7 | 4.4 | 18.5 | 8.4 | 14.2 | * |
| SL 20 | 0.6 | 3.3 | 1.7 | 7.2 | 2.6 | 8.2 | * |
| SL 22 | 0.4 | 3 | 1.2 | 6.9 | 4.5 | 9.3 | * |
| SL 23 | 0.5 | 2.4 | 1.2 | 5.7 | 2.1 | 6.8 | * |
| SL 25 | * | 2.2 | 0.7 | 3.9 | 11.2 | 7.2 | * |
| SL 26 | 0.6 | 4.4 | 1.5 | 9.6 | 5.8 | 14.8 | * |
| SL 28 | 8 | 2.2 | 0.8 | 4.7 | 7.5 | 8.8 | * |
| SL 31 | 0.7 | 5.5 | 1.9 | 13.6 | 3.8 | 16.1 | * |
| SL 38 | 0.4 | 1.7 | 1 | 2.3 | 3.3 | 6.2 | * |
| SL 39 | * | 0.5 | 0.2 | 1.2 | 3.8 | 3.6 | * |
| SL 42 | * | 0.3 | 0.1 | 0.6 | 2.8 | 4.5 | * |
| SL 45 | * | 0.3 | 0.2 | 0.5 | 2.7 | 1.6 | 1.1 |
| SL 47 | * | 0.2 | 0.2 | 0.2 | 2 | 5.6 | 8.3 |

**Table C9 continued:** Whole rock PGE and chalcophile element concentrations from the Kemi Intrusion (PGE data obtained from the University of Quebec ICP-MS and the chalcophile element data obtained from the University of Quebec AAS thermo elemental analyser). * indicate values below the detection limits. The PGE and Au concentrations are in ppb and the Ni, Cu and S concentrations are in ppm.

| Sample | Ni | Cu | S |
|---|---|---|---|
| **SL 05** | 328.8 | * | * |
| **SL 06** | 527.3 | * | 60 |
| **SL 07** | 534.9 | * | * |
| **SL 09** | 190.9 | 26.4 | 33 |
| **SL 11** | 480 | 17.4 | 294 |
| **SL 14** | 298.2 | 31.9 | 92 |
| **SL 16** | 70.3 | 20.9 | 28 |
| **SL 17** | 472.5 | 32.1 | 481 |
| **SL 20** | 199.7 | 22.2 | 163 |
| **SL 22** | 227.8 | * | 52 |
| **SL 23** | 243.6 | * | * |
| **SL 25** | 219.2 | * | 115 |
| **SL 26** | 190 | * | 22 |
| **SL 28** | 188.1 | * | 46 |
| **SL 31** | 117.9 | 19.7 | 21 |
| **SL 38** | 735.2 | 20.5 | 164 |
| **SL 39** | 90.1 | 14.4 | 46 |
| **SL 42** | 38.7 | 10.4 | 53 |
| **SL 45** | 57.6 | 27.4 | 232 |
| **SL 47** | 150.3 | 161.2 | 244 |

## Appendix D

### Tables of errors, uncertainties, standards, blanks and duplicates

**Table D1:** Errors for the whole rock minor and trace element concentrations from the Kemi Intrusion (obtained from the Rhodes University XRF detector). Included are the errors and the LLD – Lower Limits of Detection.

| Sample | Zn | | | Cu | | | Ni | | |
|---|---|---|---|---|---|---|---|---|---|
| | ppm | Error | LLD | ppm | Error | LLD | ppm | Error | LLD |
| SL 01 | 33.0 | 0.5 | 1.4 | 8.0 | 0.5 | 1.5 | 4.9 | 0.5 | 1.6 |
| SL 02 | 60.6 | 0.6 | 1.4 | 9.0 | 0.5 | 1.6 | 3.1 | 0.5 | 1.6 |
| SL 03 | 250.4 | 0.9 | 1.6 | 29.2 | 0.6 | 1.7 | 36.4 | 0.7 | 1.8 |
| SL 04 | 245.8 | 1.4 | 2.9 | 20.8 | 1.0 | 2.9 | 1197.7 | 2.7 | 3.4 |
| SL 05 | 98.6 | 0.9 | 2.2 | 18.4 | 0.8 | 2.3 | 1501.0 | 2.5 | 2.6 |
| SL 06 | 286.1 | 1.7 | 3.7 | 30.3 | 1.2 | 3.6 | 1468.5 | 3.3 | 4.3 |
| SL 07 | 113.9 | 0.9 | 2.2 | 12.3 | 0.8 | 2.3 | 924.3 | 2.0 | 2.5 |
| SL 08 | 211.6 | 1.0 | 2.1 | 12.6 | 0.8 | 2.2 | 894.4 | 1.9 | 2.5 |
| SL 09 | 32.1 | 0.7 | 1.8 | 29.0 | 0.7 | 1.9 | 391.6 | 1.3 | 2.1 |
| SL 10 | 59.1 | 0.7 | 1.8 | 33.6 | 0.7 | 1.9 | 567.2 | 1.4 | 2.1 |
| SL 11 | 56.1 | 0.7 | 1.8 | 19.7 | 0.7 | 1.9 | 646.6 | 1.5 | 2.1 |
| SL 12 | 60.4 | 0.7 | 1.9 | 22.6 | 0.7 | 2.0 | 909.6 | 1.8 | 2.1 |
| SL 13 | 61.4 | 0.7 | 1.8 | 18.4 | 0.7 | 1.9 | 698.2 | 1.6 | 2.1 |
| SL 14 | 72.5 | 0.7 | 1.9 | 36.5 | 0.7 | 2.0 | 528.7 | 1.4 | 2.2 |
| SL 15 | 42.6 | 0.7 | 1.8 | 15.6 | 0.7 | 2.0 | 234.6 | 1.1 | 2.1 |
| SL 16 | 34.8 | 0.7 | 1.9 | 24.8 | 0.7 | 2.0 | 240.5 | 1.1 | 2.1 |
| SL 17 | 32.5 | 0.7 | 1.8 | 33.9 | 0.7 | 2.0 | 624.9 | 1.5 | 2.1 |
| SL 18 | 38.7 | 0.7 | 1.8 | 30.5 | 0.7 | 1.9 | 554.0 | 1.4 | 2.1 |
| SL 19 | 344.1 | 1.5 | 2.9 | 21.6 | 1.0 | 2.9 | 739.8 | 2.2 | 3.4 |
| SL 20 | 31.6 | 0.7 | 1.8 | 22.0 | 0.7 | 1.9 | 451.3 | 1.3 | 2.1 |
| SL 21 | 59.3 | 0.7 | 1.8 | 9.3 | 0.7 | 1.9 | 372.0 | 1.3 | 2.1 |
| SL 22 | 36.1 | 0.7 | 1.8 | 10.7 | 0.7 | 1.9 | 435.2 | 1.3 | 2.1 |
| SL 23 | 19.8 | 0.6 | 1.7 | 6.4 | 0.6 | 1.8 | 421.8 | 1.2 | 1.9 |
| SL 24 | 326.6 | 1.4 | 2.8 | 24.4 | 1.0 | 2.8 | 594.9 | 2.0 | 3.2 |
| SL 25 | 17.8 | 0.6 | 1.7 | 5.9 | 0.6 | 1.8 | 404.0 | 1.2 | 1.9 |
| SL 26 | 33.1 | 0.7 | 1.8 | 11.4 | 0.7 | 1.9 | 345.0 | 1.2 | 2.1 |
| SL 27 | 45.7 | 0.7 | 1.8 | 61.1 | 0.7 | 1.9 | 376.3 | 1.2 | 2.1 |
| SL 28 | 53.6 | 0.7 | 1.7 | 7.2 | 0.6 | 1.9 | 349.8 | 1.2 | 2.0 |
| SL 29 | 53.7 | 0.7 | 1.7 | 7.4 | 0.6 | 1.9 | 378.5 | 1.2 | 2.0 |
| SL 30 | 112.7 | 0.8 | 1.8 | 9.3 | 0.7 | 1.9 | 320.5 | 1.2 | 2.1 |
| SL 31 | 66.8 | 0.7 | 1.7 | 21.2 | 0.7 | 1.9 | 369.6 | 1.2 | 2.0 |
| SL 32 | 56.3 | 0.7 | 1.8 | 8.1 | 0.6 | 1.9 | 337.7 | 1.2 | 2.0 |
| SL 38 | 69.5 | 0.7 | 1.8 | 24.0 | 0.7 | 1.9 | 838.2 | 1.6 | 2.0 |
| SL 39 | 27.1 | 0.6 | 1.7 | 17.1 | 0.6 | 1.9 | 209.0 | 1.0 | 2.0 |
| SL 40 | 34.0 | 0.6 | 1.6 | 29.2 | 0.6 | 1.7 | 188.5 | 0.9 | 1.8 |
| SL 41 | 32.7 | 0.6 | 1.7 | 13.2 | 0.6 | 1.8 | 155.1 | 0.9 | 1.9 |
| SL 42 | 28.2 | 0.6 | 1.7 | 12.4 | 0.6 | 1.8 | 131.6 | 0.9 | 2.0 |
| SL 43 | 24.8 | 0.6 | 1.6 | 5.6 | 0.6 | 1.7 | 118.6 | 0.8 | 1.8 |
| SL 44 | 42.1 | 0.6 | 1.6 | 123.1 | 0.7 | 1.7 | 384.7 | 1.1 | 1.8 |
| SL 45 | 19.9 | 0.6 | 1.7 | 27.8 | 0.6 | 1.8 | 118.7 | 0.8 | 1.9 |
| SL 46 | 9.8 | 0.5 | 1.6 | 15.5 | 0.6 | 1.7 | 17.3 | 0.6 | 1.8 |
| SL 47 | 35.4 | 0.6 | 1.5 | 143.5 | 0.7 | 1.7 | 160.9 | 0.8 | 1.7 |
| SL 48 | 39.4 | 0.6 | 1.7 | 8.6 | 0.6 | 1.8 | 183.5 | 0.9 | 1.9 |

**Table D1 continued:** Whole rock minor and trace element concentrations from the Kemi Intrusion (obtained from the Rhodes University XRF detector). Included are the errors and the LLD – Lower Limits of Detection. * indicates below detection limits.

| Sample | Co | | | Cr | | | V | | |
|---|---|---|---|---|---|---|---|---|---|
| | ppm | Error | LLD | ppm | Error | LLD | ppm | Error | LLD |
| SL 01 | 3.4 | 0.9 | 4.3 | 20.8 | 0.7 | 2.7 | 12.3 | 0.9 | 4.0 |
| SL 02 | 3.8 | 0.9 | 4.3 | 31.8 | 0.7 | 2.7 | 13.0 | 0.9 | 4.1 |
| SL 03 | 15.2 | 1.0 | 4.8 | 114.2 | 1.0 | 3.1 | 43.0 | 1.0 | 4.5 |
| SL 04 | 169.3 | 2.0 | 8.7 | * | 34.5 | 11.4 | 684.8 | 3.3 | 11.1 |
| SL 05 | 103.8 | 1.6 | 6.8 | * | 21.3 | 7.6 | 377.5 | 2.3 | 7.9 |
| SL 06 | 196.0 | 2.5 | 10.9 | * | 64.2 | 19.5 | 1654.3 | 5.5 | 16.6 |
| SL 07 | 140.0 | 1.5 | 6.3 | * | 14.9 | 6.0 | 313.8 | 2.0 | 6.9 |
| SL 08 | 136.9 | 1.4 | 6.1 | * | 14.9 | 5.8 | 364.8 | 2.0 | 6.6 |
| SL 09 | 76.1 | 1.2 | 5.2 | 2255.3 | 3.3 | 3.5 | 161.0 | 1.4 | 5.1 |
| SL 10 | 101.4 | 1.2 | 5.1 | 4848.8 | 4.6 | 3.5 | 95.9 | 1.2 | 4.9 |
| SL 11 | 109.6 | 1.2 | 5.0 | 2681.4 | 3.3 | 3.4 | 59.4 | 1.1 | 4.8 |
| SL 12 | 133.5 | 1.2 | 5.0 | 5291.4 | 4.6 | 3.5 | 68.0 | 1.1 | 4.9 |
| SL 13 | 113.5 | 1.2 | 5.0 | 2833.0 | 3.5 | 3.4 | 53.3 | 1.1 | 4.8 |
| SL 14 | 99.4 | 1.2 | 5.3 | 3868.3 | 4.2 | 3.6 | 125.9 | 1.3 | 5.1 |
| SL 15 | 54.2 | 1.2 | 5.4 | 3925.0 | 4.6 | 3.7 | 146.7 | 1.4 | 5.3 |
| SL 16 | 52.1 | 1.2 | 5.4 | 4076.3 | 4.7 | 3.8 | 165.4 | 1.5 | 5.3 |
| SL 17 | 95.5 | 1.2 | 5.0 | 6917.0 | 5.4 | 3.6 | 108.6 | 1.2 | 4.9 |
| SL 18 | 96.1 | 1.2 | 5.1 | 9010.8 | 6.3 | 3.7 | 107.4 | 1.2 | 5.0 |
| SL 19 | 168.1 | 1.9 | 8.3 | * | 29.7 | 10.1 | 1011.3 | 3.5 | 10.2 |
| SL 20 | 85.5 | 1.2 | 5.1 | 4253.6 | 4.3 | 3.5 | 138.0 | 1.3 | 5.0 |
| SL 21 | 84.0 | 1.2 | 5.2 | 7681.7 | 5.8 | 3.7 | 116.4 | 1.3 | 5.0 |
| SL 22 | 82.2 | 1.1 | 5.0 | 4199.5 | 4.3 | 3.5 | 108.2 | 1.2 | 4.9 |
| SL 23 | 72.1 | 1.1 | 4.8 | 3505.2 | 3.9 | 3.3 | 91.9 | 1.1 | 4.6 |
| SL 24 | 146.1 | 1.8 | 7.9 | * | 30.2 | 10.1 | 986.1 | 3.4 | 10.0 |
| SL 25 | 79.9 | 1.1 | 4.8 | 2558.9 | 3.3 | 3.2 | 76.4 | 1.1 | 4.6 |
| SL 26 | 77.9 | 1.1 | 5.1 | 2167.8 | 3.1 | 3.4 | 98.8 | 1.2 | 4.9 |
| SL 27 | 82.4 | 1.2 | 5.1 | 2152.5 | 3.1 | 3.4 | 128.5 | 1.3 | 4.8 |
| SL 28 | 77.1 | 1.1 | 4.9 | 2244.7 | 3.1 | 3.3 | 84.2 | 1.1 | 4.7 |
| SL 29 | 75.8 | 1.1 | 4.9 | 2301.1 | 3.2 | 3.3 | 80.7 | 1.1 | 4.7 |
| SL 30 | 78.0 | 1.2 | 5.1 | 9474.1 | 6.5 | 3.7 | 131.0 | 1.3 | 5.1 |
| SL 31 | 78.8 | 1.1 | 5.0 | 2675.2 | 3.4 | 3.4 | 157.4 | 1.3 | 4.8 |
| SL 32 | 74.4 | 1.1 | 5.0 | 2065.2 | 3.1 | 3.4 | 99.6 | 1.2 | 4.8 |
| SL 38 | 123.0 | 1.1 | 4.8 | 932.6 | 2.0 | 3.2 | 59.6 | 1.1 | 4.6 |
| SL 39 | 41.5 | 1.1 | 5.2 | 1951.7 | 3.2 | 3.5 | 97.0 | 1.2 | 4.9 |
| SL 40 | 43.9 | 1.0 | 4.8 | 1207.8 | 2.4 | 3.1 | 99.1 | 1.2 | 4.5 |
| SL 41 | 42.4 | 1.1 | 5.1 | 772.3 | 2.1 | 3.3 | 88.3 | 1.2 | 4.8 |
| SL 42 | 37.5 | 1.1 | 5.1 | 978.6 | 2.4 | 3.4 | 114.8 | 1.3 | 4.9 |
| SL 43 | 27.1 | 1.0 | 4.7 | 156.4 | 1.1 | 3.0 | 40.3 | 1.0 | 4.4 |
| SL 44 | 62.4 | 1.1 | 4.7 | 24.1 | 0.8 | 3.0 | 17.2 | 1.0 | 4.4 |
| SL 45 | 29.5 | 1.1 | 5.0 | 400.5 | 1.6 | 3.3 | 90.5 | 1.2 | 4.8 |
| SL 46 | 18.8 | 1.0 | 4.8 | 53.8 | 0.9 | 3.1 | 31.4 | 1.0 | 4.5 |
| SL 47 | 31.6 | 1.0 | 4.6 | 683.1 | 1.8 | 3.0 | 92.8 | 1.1 | 4.3 |
| SL 48 | 36.6 | 1.1 | 4.9 | 911.4 | 2.2 | 3.3 | 113.0 | 1.2 | 4.7 |

**Table D1 continued:** Whole rock minor and trace element concentrations from the Kemi Intrusion (obtained from the Rhodes University XRF detector). Included are the errors and the LLD – Lower Limits of Detection.

| Sample | Sr | | | Rb | | | Zr | | |
|---|---|---|---|---|---|---|---|---|---|
| | ppm | Error | LLD | ppm | Error | LLD | ppm | Error | LLD |
| SL 01 | 387.0 | 0.7 | 0.7 | 32.9 | 0.3 | 0.7 | 109.1 | 0.4 | 0.7 |
| SL 02 | 343.8 | 0.6 | 0.7 | 27.8 | 0.3 | 0.7 | 129.3 | 0.4 | 0.7 |
| SL 03 | 400.7 | 0.7 | 0.8 | 27.1 | 0.4 | 0.8 | 55.4 | 0.3 | 0.8 |
| SL 04 | 89.2 | 0.7 | 1.3 | -0.2 | 0.5 | 1.3 | 10.7 | 0.5 | 1.3 |
| SL 05 | 212.0 | 0.7 | 1.1 | -0.9 | 0.4 | 1.1 | 20.0 | 0.4 | 1.0 |
| SL 06 | 0.2 | 0.5 | 1.5 | 0.6 | 0.6 | 1.5 | 2.3 | 0.5 | 1.5 |
| SL 07 | 9.6 | 0.4 | 1.0 | 0.9 | 0.4 | 1.0 | 5.1 | 0.4 | 1.0 |
| SL 08 | 9.6 | 0.4 | 1.0 | 0.9 | 0.4 | 1.0 | 5.1 | 0.4 | 1.0 |
| SL 09 | 63.0 | 0.4 | 0.9 | 3.5 | 0.3 | 0.9 | 33.0 | 0.3 | 0.9 |
| SL 10 | 59.3 | 0.4 | 0.9 | 4.3 | 0.3 | 0.9 | 5.3 | 0.3 | 0.9 |
| SL 11 | 38.5 | 0.4 | 0.9 | 1.3 | 0.3 | 0.9 | 4.1 | 0.3 | 0.9 |
| SL 12 | 11.1 | 0.3 | 0.9 | 1.8 | 0.3 | 0.9 | 6.4 | 0.3 | 0.9 |
| SL 13 | 39.6 | 0.4 | 0.9 | 1.4 | 0.3 | 0.9 | 3.2 | 0.3 | 0.9 |
| SL 14 | 28.3 | 0.4 | 0.9 | 4.2 | 0.4 | 0.9 | 16.7 | 0.3 | 0.9 |
| SL 15 | 49.9 | 0.4 | 0.9 | 1.0 | 0.4 | 0.9 | 13.3 | 0.3 | 0.9 |
| SL 16 | 35.7 | 0.4 | 0.9 | 1.3 | 0.4 | 0.9 | 9.3 | 0.3 | 0.9 |
| SL 17 | 47.9 | 0.4 | 0.9 | 3.2 | 0.3 | 0.9 | 28.7 | 0.3 | 0.9 |
| SL 18 | 55.0 | 0.4 | 0.9 | 2.8 | 0.3 | 0.9 | 8.5 | 0.3 | 0.9 |
| SL 19 | 24.3 | 0.5 | 1.3 | 2.4 | 0.5 | 1.3 | 8.7 | 0.4 | 1.3 |
| SL 20 | 51.0 | 0.4 | 0.9 | 1.3 | 0.3 | 0.9 | 35.8 | 0.3 | 0.9 |
| SL 21 | 85.5 | 0.5 | 0.9 | 2.0 | 0.3 | 0.9 | 4.0 | 0.3 | 0.9 |
| SL 22 | 78.0 | 0.4 | 0.9 | 2.8 | 0.3 | 0.9 | 18.1 | 0.3 | 0.9 |
| SL 23 | 79.9 | 0.4 | 0.8 | 2.0 | 0.3 | 0.8 | 5.2 | 0.3 | 0.8 |
| SL 24 | 34.1 | 0.5 | 1.2 | 0.7 | 0.5 | 1.3 | 7.7 | 0.4 | 1.2 |
| SL 25 | 60.6 | 0.4 | 0.8 | 5.3 | 0.3 | 0.8 | 4.3 | 0.3 | 0.8 |
| SL 26 | 70.1 | 0.4 | 0.9 | 4.8 | 0.3 | 0.9 | 13.5 | 0.3 | 0.9 |
| SL 27 | 44.3 | 0.4 | 0.9 | 2.1 | 0.3 | 0.9 | 13.4 | 0.3 | 0.9 |
| SL 28 | 73.3 | 0.4 | 0.8 | 3.2 | 0.3 | 0.9 | 4.5 | 0.3 | 0.8 |
| SL 29 | 85.2 | 0.4 | 0.8 | 17.2 | 0.4 | 0.9 | 5.9 | 0.3 | 0.8 |
| SL 30 | 98.5 | 0.5 | 0.9 | 21.4 | 0.4 | 0.9 | 5.6 | 0.3 | 0.9 |
| SL 31 | 71.8 | 0.4 | 0.9 | 19.2 | 0.4 | 0.9 | 31.7 | 0.3 | 0.8 |
| SL 32 | 96.0 | 0.5 | 0.9 | 9.2 | 0.3 | 0.9 | 6.5 | 0.3 | 0.9 |
| SL 38 | 20.1 | 0.3 | 0.8 | 1.2 | 0.3 | 0.9 | 6.8 | 0.3 | 0.8 |
| SL 39 | 170.8 | 0.6 | 0.9 | 1.5 | 0.3 | 0.9 | 4.3 | 0.3 | 0.9 |
| SL 40 | 111.7 | 0.5 | 0.8 | -0.2 | 0.3 | 0.8 | 8.5 | 0.3 | 0.8 |
| SL 41 | 121.2 | 0.5 | 0.9 | 1.8 | 0.3 | 0.9 | 6.6 | 0.3 | 0.8 |
| SL 42 | 169.4 | 0.6 | 0.9 | -0.1 | 0.3 | 0.9 | 6.4 | 0.3 | 0.9 |
| SL 43 | 235.0 | 0.6 | 0.8 | 1.9 | 0.3 | 0.8 | 3.4 | 0.3 | 0.8 |
| SL 44 | 33.6 | 0.3 | 0.8 | 39.3 | 0.4 | 0.8 | 3.7 | 0.3 | 0.8 |
| SL 45 | 189.1 | 0.6 | 0.9 | 0.4 | 0.3 | 0.9 | 3.5 | 0.3 | 0.8 |
| SL 46 | 333.8 | 0.7 | 0.8 | 1.5 | 0.3 | 0.8 | 6.8 | 0.3 | 0.8 |
| SL 47 | 233.9 | 0.6 | 0.8 | 11.1 | 0.3 | 0.8 | 16.0 | 0.3 | 0.8 |
| SL 48 | 274.1 | 0.7 | 0.8 | 0.8 | 0.3 | 0.9 | 9.0 | 0.3 | 0.8 |

**Table D1 continued:** Whole rock minor and trace element concentrations from the Kemi Intrusion (obtained from the Rhodes University XRF detector). Included are the errors and the LLD – Lower Limits of Detection.

| Sample | Nb | | | Y | | |
|---|---|---|---|---|---|---|
| | ppm | Error | LLD | ppm | Error | LLD |
| SL 01 | 0.8 | 0.2 | 0.7 | 0.4 | 0.2 | 0.7 |
| SL 02 | 0.8 | 0.2 | 0.7 | 1.3 | 0.2 | 0.7 |
| SL 03 | 2.9 | 0.2 | 0.8 | 7.2 | 0.2 | 0.8 |
| SL 04 | 0.3 | 0.4 | 1.2 | 3.0 | 0.4 | 1.3 |
| SL 05 | 1.4 | 0.3 | 1.0 | 4.3 | 0.3 | 1.0 |
| SL 06 | 0.2 | 0.4 | 1.4 | 1.0 | 0.4 | 1.5 |
| SL 07 | 0.5 | 0.3 | 1.0 | 2.5 | 0.3 | 1.0 |
| SL 08 | 0.5 | 0.3 | 1.0 | 2.5 | 0.3 | 1.0 |
| SL 09 | 2.0 | 0.2 | 0.8 | 9.9 | 0.3 | 0.9 |
| SL 10 | 0.9 | 0.2 | 0.8 | 3.0 | 0.3 | 0.8 |
| SL 11 | 0.4 | 0.2 | 0.8 | 1.6 | 0.2 | 0.8 |
| SL 12 | 0.3 | 0.2 | 0.8 | 2.9 | 0.3 | 0.8 |
| SL 13 | 0.8 | 0.2 | 0.8 | 1.8 | 0.2 | 0.8 |
| SL 14 | 0.6 | 0.2 | 0.9 | 5.2 | 0.3 | 0.9 |
| SL 15 | 1.9 | 0.3 | 0.9 | 6.2 | 0.3 | 0.9 |
| SL 16 | 0.8 | 0.3 | 0.9 | 5.4 | 0.3 | 0.9 |
| SL 17 | 1.6 | 0.2 | 0.8 | 6.8 | 0.3 | 0.9 |
| SL 18 | 0.6 | 0.2 | 0.8 | 3.1 | 0.3 | 0.8 |
| SL 19 | 0.4 | 0.3 | 1.2 | 3.2 | 0.4 | 1.2 |
| SL 20 | 1.7 | 0.2 | 0.8 | 8.6 | 0.3 | 0.8 |
| SL 21 | 0.8 | 0.2 | 0.8 | 2.4 | 0.3 | 0.9 |
| SL 22 | 1.2 | 0.2 | 0.8 | 5.2 | 0.3 | 0.8 |
| SL 23 | 0.2 | 0.2 | 0.8 | 2.9 | 0.2 | 0.8 |
| SL 24 | 1.5 | 0.3 | 1.2 | 3.1 | 0.4 | 1.2 |
| SL 25 | 0.1 | 0.2 | 0.8 | 2.6 | 0.2 | 0.8 |
| SL 26 | 0.7 | 0.2 | 0.8 | 6.0 | 0.3 | 0.8 |
| SL 27 | 0.6 | 0.2 | 0.8 | 5.7 | 0.3 | 0.9 |
| SL 28 | 0.2 | 0.2 | 0.8 | 3.2 | 0.2 | 0.8 |
| SL 29 | 0.2 | 0.2 | 0.8 | 2.2 | 0.2 | 0.8 |
| SL 30 | 0.7 | 0.2 | 0.8 | 2.5 | 0.3 | 0.8 |
| SL 31 | 1.8 | 0.2 | 0.8 | 8.5 | 0.3 | 0.8 |
| SL 32 | 1.0 | 0.2 | 0.8 | 3.7 | 0.3 | 0.8 |
| SL 38 | 0.3 | 0.2 | 0.8 | 3.3 | 0.2 | 0.8 |
| SL 39 | 0.4 | 0.2 | 0.8 | 3.6 | 0.3 | 0.8 |
| SL 40 | 0.8 | 0.2 | 0.8 | 2.9 | 0.2 | 0.8 |
| SL 41 | 0.9 | 0.2 | 0.8 | 3.0 | 0.2 | 0.8 |
| SL 42 | 0.4 | 0.2 | 0.8 | 4.3 | 0.3 | 0.8 |
| SL 43 | 0.6 | 0.2 | 0.8 | 1.3 | 0.2 | 0.8 |
| SL 44 | 0.7 | 0.2 | 0.8 | 0.6 | 0.2 | 0.8 |
| SL 45 | 0.8 | 0.2 | 0.8 | 2.8 | 0.2 | 0.8 |
| SL 46 | 0.4 | 0.2 | 0.8 | 2.3 | 0.2 | 0.8 |
| SL 47 | 0.8 | 0.2 | 0.7 | 4.9 | 0.2 | 0.8 |
| SL 48 | 0.1 | | 0.8 | 5.4 | 0.2 | 0.8 |

**Table D2:** Standards used in the calculations of the minor and trace element concentrations from the Kemi Intrusion (obtained from the Rhodes University XRF detector). Units are in PPM.

| Calculation of Standards | | | | | | | | | |
|---|---|---|---|---|---|---|---|---|---|
| **Sample** | **Zinc** | | | **Copper** | | | **Nickel** | | |
| | **Std** | **Calc** | **Diff** | **Std** | **Calc** | **Diff** | **Std** | **Calc** | **Diff** |
| BHVO-1 | 105.0 | 105.1 | -0.1 | 136.0 | 127.7 | 8.3 | 121.0 | 112.7 | 8.3 |
| G-2 | 86.0 | 88.2 | -2.2 | 11.0 | 15.9 | -4.9 | 5.0 | 2.9 | 2.1 |
| KRF-13 | 82.0 | 82.0 | 0.0 | 66.0 | 74.6 | -8.6 | 51.0 | 42.9 | 8.1 |
| INS-79 | 101.0 | 104.1 | -3.1 | 126.0 | 127.8 | -1.8 | 1335.0 | 1329.6 | 5.4 |
| INS-33 | 44.0 | 40.1 | 3.9 | 15.0 | 18.9 | -3.9 | 80.0 | 75.2 | 4.8 |
| BCR-1 | 130.0 | 129.3 | 0.7 | 19.0 | 29.6 | -10.6 | 13.0 | 10.4 | 2.6 |
| AGV-1 | 88.0 | 90.0 | -2.0 | 60.0 | 60.9 | -0.9 | 16.0 | 13.6 | 2.4 |
| NIM-N | 68.0 | 61.1 | 6.9 | 14.0 | 19.4 | -5.4 | 120.0 | 108.5 | 11.5 |
| JB-1 | 83.0 | 81.9 | 1.1 | 56.0 | 52.8 | 3.2 | 139.0 | 123.3 | 15.7 |
| DTS-1 | 46.0 | 48.7 | -2.7 | 7.1 | 17.5 | -10.4 | 2360.0 | 2365.4 | -5.4 |
| **Sample** | **Cobalt** | | | **Chromium** | | | **Vanadium** | | |
| | **Std** | **Calc** | **Diff** | **Std** | **Calc** | **Diff** | **Std** | **Calc** | **Diff** |
| BHVO-1 | 45.0 | 42.8 | 2.2 | 289.0 | 277.3 | 11.7 | 317.0 | 325.5 | -8.5 |
| G-2 | 4.6 | 3.6 | 1.0 | 8.7 | 6.9 | 1.8 | 36.0 | 28.0 | 8.0 |
| NIM-N | 58.0 | 60.0 | -2.0 | 30.0 | 28.5 | 1.5 | 220.0 | 215.4 | 4.6 |
| KRF-13 | 39.0 | 38.1 | 0.9 | 268.0 | 267.0 | 1.0 | 254.0 | 254.6 | -0.6 |
| INS-33 | 26.4 | 25.2 | 1.2 | 672.0 | 659.3 | 12.7 | 150.0 | 147.8 | 2.2 |
| GSN-005 | 0.1 | 0.5 | -0.4 | 190.0 | 190.0 | -0.2 | 12.0 | 11.0 | 1.0 |
| KL-11 | 44.0 | 39.0 | 5.0 | 250.0 | 249.5 | 0.5 | 231.0 | 237.0 | -6.0 |
| INS-79 | 148.0 | 148.5 | -0.5 | 3200.0 | 3304.9 | **** | 108.0 | 109.7 | -1.7 |
| JB-1 | 38.7 | 36.3 | 2.4 | 401.0 | 408.7 | -7.7 | 212.0 | 199.2 | 12.8 |
| DTS-1 | 147.0 | 148.9 | -1.9 | 3700.0 | 3611.8 | 88.2 | 11.0 | 7.7 | 3.3 |
| **Sample** | **Niobium** | | | **Zirconium** | | | **Yttrium** | | |
| | **Std** | **Calc 1** | **Calc 2** | **Std** | **Calc 1** | **Calc 2** | **Std** | **Calc 1** | **Calc 2** |
| BHVO-1 | 20.0 | 20.8 | 20.5 | 170.0 | 174.1 | 174.1 | 27.6 | 27.2 | 27.2 |
| G-2 | 13.5 | 12.8 | 13.3 | 309.0 | 324.9 | 325.3 | 11.0 | 9.1 | 8.6 |
| KRF-13 | 6.5 | 7.3 | 7.3 | 107.0 | 111.6 | 111.6 | 28.5 | 28.6 | 28.9 |
| KL-11 | 6.3 | 6.9 | 7.0 | 93.0 | 93.9 | 94.0 | 24.3 | 24.4 | 24.8 |
| GSN-005 | 42.5 | 42.3 | 41.9 | 616.0 | 616.0 | 615.0 | 99.0 | 99.9 | 99.8 |
| INS-79 | 0.9 | 0.5 | 0.6 | 14.0 | 13.9 | 14.2 | 5.1 | 5.0 | 5.4 |
| INS-33 | 2.2 | 2.6 | 2.8 | 45.0 | 46.0 | 46.6 | 12.0 | 11.7 | 11.9 |
| BCR-1 | 14.0 | 14.3 | 14.4 | 186.0 | 192.3 | 192.4 | 38.0 | 38.1 | 38.2 |
| AGV-1 | 15.0 | 15.8 | 16.1 | 227.0 | 235.9 | 236.6 | 20.0 | 20.0 | 19.6 |
| GSP-1 | 30.0 | 29.2 | 29.6 | 525.0 | 507.1 | 507.5 | 26.8 | 24.7 | 24.2 |
| **Sample** | **Strontium** | | **Rubidium** | | | | | | |
| | **Std** | **Calc** | **Std** | **Calc** | | | | | |
| BHVO-1 | 403.0 | 396.6 | 11.0 | 9.0 | | | | | |
| G-2 | 478.0 | 476.5 | 170.0 | 168.7 | | | | | |
| KRF-13 | 208.0 | 207.5 | 10.0 | 9.8 | | | | | |
| KL-11 | 205.0 | 205.3 | 15.0 | 15.5 | | | | | |
| GSN-005 | 59.8 | 60.5 | 149.0 | 149.5 | | | | | |
| INS-79 | 63.1 | 62.4 | 2.1 | 3.4 | | | | | |
| INS-33 | 292.0 | 293.3 | 12.8 | 12.9 | | | | | |
| BCR-1 | 333.0 | 336.5 | 47.8 | 47.6 | | | | | |
| AGV-1 | 662.0 | 664.2 | 67.3 | 67.3 | | | | | |
| GSP-1 | 234.0 | 235.5 | 254.0 | 254.6 | | | | | |

**Table D3:** The %RSD values used in the calculation of the minor and trace element concentrations (obtained from the ICP-MS from Stellenbosch University) using the BHVO2 standard sample and a dilution factor of 31.7493.

| Element | ICP values (ppb) | Dilution corrected (ppb) | Final (ppm) | Certified value (ppm) | % RSD |
|---|---|---|---|---|---|
| Li | 141.7 | 4498.88 | 4.50 | 4.80 | 6.69 |
| Be | 26.09 | 828.34 | 0.83 | 1.00 | 20.72 |
| B | * | | | | |
| Si | 7939 | 252057.70 | 252.06 | 233265.30 | |
| Ti | 729800 | 23170641.00 | 23170.64 | 16300.00 | 29.65 |
| V | 13530 | 429568.10 | 429.57 | 317.00 | 26.20 |
| Mn | 49380 | 1567781.00 | 1567.78 | 1316.58 | 16.02 |
| Co | 1529 | 48544.68 | 48.54 | 45.00 | 7.30 |
| Ni | 3780 | 120012.40 | 120.01 | 119.00 | 0.84 |
| Cu | 3664 | 116329.40 | 116.33 | 127.00 | 9.17 |
| Zn | 3083 | 97883.10 | 97.88 | 103.00 | 5.23 |
| As | 34.44 | 1093.45 | 1.09 | | |
| Se | 42.92 | 1362.68 | 1.36 | | |
| Mo | 134.5 | 4270.28 | 4.27 | 4.00 | 6.33 |
| Cd | 7.024 | 223.01 | 0.22 | 0.06 | 73.10 |
| Ba | 4566 | 144967.30 | 144.97 | 131.00 | 9.63 |
| La | 501.3 | 15915.93 | 15.92 | 15.20 | 4.50 |
| Ce | 1264 | 40131.12 | 40.13 | 37.50 | 6.56 |
| Pr | 177.9 | 5648.20 | 5.65 | 5.35 | 5.28 |
| Nd | 824 | 26161.43 | 26.16 | 24.50 | 6.35 |
| Sm | 200.4 | 6362.56 | 6.36 | 6.07 | 4.60 |
| Eu | 67.6 | 2146.25 | 2.15 | 2.07 | 3.55 |
| Gd | 202 | 6413.36 | 6.41 | 6.24 | 2.70 |
| Dy | 164 | 5206.89 | 5.21 | 5.31 | 1.98 |
| Ho | 29.65 | 941.37 | 0.94 | 0.98 | 4.10 |
| Er | 78.08 | 2478.99 | 2.48 | 2.54 | 2.46 |
| Tm | 9.708 | 308.22 | 0.31 | 0.33 | 7.07 |
| Yb | 58.03 | 1842.41 | 1.84 | 2.00 | 8.55 |
| Lu | 8.001 | 254.03 | 0.25 | 0.27 | 7.86 |
| Pb | 39.21 | 1244.89 | 1.24 | 1.60 | 28.53 |

**Table D4:** Quality Control values (in ppb) obtained from the concentration values of the minor and trace elements from the Kemi Intrusion (obtained from the ICP-MS at Stellenbosch University).

| Element | Certified | Analysed | % RSD | Unspiked | Spike Value | Analysed Spike | % Recovery |
|---|---|---|---|---|---|---|---|
| Li | 92 | 94.05 | 2.2 | 49.4 | 97 | 149.7 | 103.4 |
| Be | 13.64 | 14.61 | 7.1 | 4.2 | 938 | 874.8 | 92.8 |
| B | | 92.71 | | 23.9 | 1086 | 1178 | 106.3 |
| Si | | | | 9246.0 | | 8,581 | |
| Ti | | | | 5137.0 | | 4,686 | |
| V | | | | 85.5 | 195 | 308.4 | 114 |
| Mn | 92 | 89 | 3.2 | 855.2 | | 896.3 | |
| Co | 92 | 89.9 | 2.3 | 16.3 | 97 | 115.4 | 102 |
| Ni | 92 | 92.5 | 0.5 | 25.8 | 97 | 121.6 | 99 |
| Cu | 92 | 93.38 | 1.5 | 29.1 | 97 | 116.1 | 89.7 |
| Zn | 92 | 87 | 5 | 106.0 | 986 | 1,011 | 92 |
| As | 58.98 | 57.75 | 2.1 | 1.4 | 957 | 1004 | 104.8 |
| Se | 11.68 | 12.65 | 8.3 | 0.7 | 986 | 1224 | 124.1 |
| Mo | 118.5 | 120 | 1.3 | 6.6 | 195 | 226.7 | 112.9 |
| Cd | 92 | 92.95 | 1 | 0.3 | 97 | 94.37 | 97 |
| Ba | 92 | 91.32 | 0.7 | 5611.0 | 97 | 5694 | 85.6 |
| La | | | | 54.8 | 98 | 160.3 | 107.7 |
| Ce | | | | 88.9 | 98 | 195.8 | 109.1 |
| Pr | | | | 8.8 | 98 | 114.9 | 108.3 |
| Nd | | | | 29.5 | 98 | 138.5 | 111.2 |
| Sm | | | | 4.2 | 98 | 113.5 | 111.6 |
| Eu | | | | 4.5 | 98 | 110.4 | 108 |
| Gd | | | | 4.1 | 98 | 111.2 | 109.3 |
| Dy | | | | 0.9 | 98 | 106.7 | 108 |
| Ho | | | | 0.2 | 98 | 103.8 | 105.8 |
| Er | | | | 0.5 | 98 | 105.2 | 106.9 |
| Tm | | | | 0.1 | 98 | 102.4 | 104.4 |
| Yb | | | | 0.4 | 98 | 105.4 | 107.1 |
| Lu | | | | 0.1 | 98 | 104.8 | 106.8 |
| Pb | 92 | 91.14 | 0.9 | 155.6 | 97 | 251.2 | 98.6 |

**Table D5:** Quality Control values (in ppb) obtained from the concentration values of the minor and trace elements from the Kemi Intrusion (obtained from the ICP-AES at Stellenbosch University).

| Element | Certified | Analysed | % RSD | Unspiked sample | Sample + 9.2 ppm spike | % Recovery |
|---|---|---|---|---|---|---|
| Al | 1.3 | 1.5 | 13.5 | 26.1 | 35.76 | 104.6 |
| Ca | 97 | 103.9 | 7.1 | 34.7 | 43.59 | 96.7 |
| Fe | 9.7 | 9.8 | 1.2 | 3.9 | 12.81 | 97 |
| K | 0.97 | 1 | 7.6 | 1.8 | 11.28 | 103.2 |
| Mg | 0.97 | 1.1 | 10.2 | 12.6 | 22.47 | 107.4 |
| Na | 0.97 | 1 | 4.5 | 5.6 | 15.1 | 103 |
| Cr | 0.97 | 0.9 | 3.1 | 0.1 | 9.28 | 99.4 |

**Table D6:** Concentrations of the minor and trace elements from standards (BHVO 2 and TPB), duplicates Kemi Intrusions samples and blank samples (obtained from the Stellenbosch University ICP-MS). Note the units are in PPB. * indicates values below the detection limits.

| Sample (PPB) | Li | Be | B | Si | Ti | V | Mn | Co |
|---|---|---|---|---|---|---|---|---|
| BHVO 2 29/5 | 4498.9 | 828.3 | * | 252057.7 | 23170641.0 | 429568.1 | 1567781.0 | 48544.7 |
| BHVO 2 13/6 | 2108.2 | 542.8 | * | 207244.6 | 13968797.0 | 267617.2 | 1026075.0 | 35179.7 |
| BHVO 2 19/6 | 2783.6 | 1181.6 | * | 364839.5 | 20675288.0 | 376516.8 | 1295874.0 | 49202.8 |
| BHVO2 19/6 dupl | 3085.7 | 1087.3 | * | 312796.2 | 19857871.0 | 363261.4 | 1236856.0 | 45983.7 |
| TPB 29/5 | 12870.0 | 1017.0 | * | 4119000.0 | 31140.0 | 11710.0 | 116100.0 | 6637.0 |
| TPB 13/6 | 5749.0 | 1675.0 | * | 3756000.0 | 13350.0 | 10270.0 | 83370.0 | 4289.0 |
| TPB 19/6 | 3455.0 | 1075.0 | * | 4582000.0 | 11930.0 | 9819.0 | 68690.0 | 3030.0 |
| SL 11b | 131.8 | 24.9 | 9036.0 | 575885.1 | 502706.3 | 58193.0 | 1144770.0 | 86860.0 |
| SL 11c | 206.5 | 25.4 | 9328.4 | 490389.7 | 500481.3 | 55440.8 | 1097464.0 | 83508.2 |
| SL 16b | 276.8 | 20.5 | * | 1090033.0 | 989643.5 | 123101.2 | 824186.5 | 37770.0 |
| SL 16c | 169.4 | 21.9 | * | 1108727.0 | 999149.3 | 135283.0 | 837782.3 | 37610.2 |
| SL 48b | 8570.6 | 173.8 | * | 400620.5 | 1687753.0 | 141643.5 | 722481.3 | 57550.4 |
| SL 48c | 8704.5 | 115.2 | * | 363956.6 | 1620225.0 | 140419.5 | 715876.3 | 58157.0 |
| SL Qtz small | 1876.9 | 236.5 | 10329.2 | 171377.8 | 5456929.0 | 24069.0 | 23311.4 | 1167.5 |
| SL Qtz big | 1771.4 | 269.3 | 2917.0 | 210340.7 | 3030187.0 | 20590.2 | 161924.9 | 1618.9 |
| SL AW3 cont | 14430.3 | 125.8 | * | 1021833.0 | 1179427.0 | 125885.7 | 1883856.0 | 92563.0 |

| Sample (PPB) | Ni | Cu | Zn | As | Se | Mo | Cd | Ba |
|---|---|---|---|---|---|---|---|---|
| BHVO 2 29/5 | 120012.4 | 116329.4 | 97883.1 | 1093.4 | 1362.7 | 4270.3 | 223.0 | 144967.3 |
| BHVO 2 13/6 | 84792.2 | 86402.9 | 66783.5 | 818.0 | 859.5 | 4619.8 | 245.4 | 191458.9 |
| BHVO 2 19/6 | 119866.8 | 153889.0 | 123717.2 | 3433.8 | 4636.2 | 3629.5 | 762.2 | 159159.6 |
| BHVO2 19/6 dupl | 112166.0 | 138582.2 | 109767.4 | 2824.4 | 3156.1 | 3739.9 | 647.0 | 159790.8 |
| TPB 29/5 | 25310.0 | 37440.0 | 78790.0 | 5090.0 | 6319.0 | 886.7 | 357.6 | 2765.0 |
| TPB 13/6 | 21800.0 | 31690.0 | 115500.0 | 3723.0 | 5773.0 | 823.4 | 4514.0 | 1388.0 |
| TPB 19/6 | 18070.0 | 22040.0 | 72650.0 | 3716.0 | 5287.0 | 1748.0 | 318.9 | 1272.0 |
| SL 11b | 503979.0 | 11683.2 | 37989.3 | 128.3 | 207.1 | 48.4 | 26.9 | 3223.0 |
| SL 11c | 487236.1 | 11460.3 | 39199.6 | 127.7 | 224.7 | 60.0 | 32.3 | 3405.9 |
| SL 16b | 171034.2 | 13763.3 | 19523.3 | 104.4 | 166.7 | 109.0 | 59.7 | 6407.6 |
| SL 16c | 169261.7 | 13878.8 | 18647.2 | 102.3 | 149.4 | 99.8 | 57.7 | 6315.7 |
| SL 48b | 249116.5 | 19569.0 | 48062.1 | 3835.7 | 4914.7 | 212.4 | 56.2 | 8195.4 |
| SL 48c | 247927.6 | 19160.8 | 51346.7 | 4064.0 | 5346.9 | 241.3 | 84.3 | 7957.0 |
| SL Qtz small | 7808.2 | 49854.2 | 92887.3 | 1277.2 | 19303.6 | 1466.4 | 568.0 | 50231.4 |
| SL Qtz big | 9759.3 | 36145.4 | 57737.5 | 1622.1 | 10723.1 | 1169.3 | 370.0 | 48796.3 |
| SL AW3 cont | 312182.7 | 105031.4 | 76898.5 | 5920.9 | 6882.9 | 217.6 | 131.8 | 173702.0 |

**Table D6 continued:** Concentrations of the minor and trace elements from standards (BHVO 2 and TPB), duplicates Kemi Intrusions samples and blank samples (obtained from the Stellenbosch University ICP-MS). Note the units are in PPB. * indicates values below the detection limits.

| Sample (PPB) | La | Ce | Pr | Nd | Sm | Eu | Gd | Dy |
|---|---|---|---|---|---|---|---|---|
| BHVO 2 29/5 | 15915.9 | 40131.1 | 5648.2 | 26161.4 | 6362.6 | 2146.3 | 6413.4 | 5206.9 |
| BHVO 2 13/6 | 21297.9 | 52318.6 | 7155.1 | 33826.7 | 8366.5 | 2921.0 | 9291.1 | 7245.3 |
| BHVO 2 19/6 | 16629.2 | 38472.3 | 5112.8 | 23926.0 | 6028.1 | 2679.8 | 11510.1 | 5087.6 |
| BHVO2 19/6 dupl | 16802.8 | 38882.5 | 5166.5 | 24295.3 | 6163.8 | 2693.4 | 11424.9 | 5157 |
| TPB 29/5 | * | * | -3.4 | 33.2 | 9.0 | 145.0 | 77.6 | 14.7 |
| TPB 13/6 | * | * | 0.2 | * | 22.4 | 130.4 | 54.9 | 5.8 |
| TPB 19/6 | * | * | 0.2 | 7.6 | 35.4 | 91.0 | 48.3 | 5.7 |
| SL 11b | 509.1 | 1016.2 | 139.2 | 616.0 | 145.7 | 75.1 | 175.0 | 193.4 |
| SL 11c | 589.4 | 1090.8 | 146.0 | 638.6 | 150.9 | 78.5 | 180.2 | 194.7 |
| SL 16b | 1240.3 | 2774.3 | 414.3 | 2081.5 | 616.3 | 205.8 | 757.6 | 808.7 |
| SL 16c | 1109.4 | 2746.1 | 401.0 | 2050.1 | 591.2 | 204.2 | 758.2 | 823.6 |
| SL 48b | 1033.5 | 2123.4 | 281.6 | 1331.5 | 363.1 | 353.2 | 2130.5 | 418.3 |
| SL 48c | 966.1 | 1929.7 | 256.5 | 1229.3 | 357.3 | 355.1 | 2128.6 | 393.1 |
| SL Qtz small | 5843.6 | 9804.2 | 1005.3 | 3677.8 | 826.7 | 1231.3 | 7915.1 | 571.5 |
| SL Qtz big | 4277.2 | 7073.7 | 721.6 | 2737.5 | 660.8 | 1184.6 | 5916.4 | 377.0 |
| SL AW3 cont | 920.9 | 1639.6 | 200.5 | 955.1 | 317.4 | 4439.9 | 2940.5 | 278.5 |

| Sample (PPB) | Ho | Er | Tm | Yb | Lu | Pb |
|---|---|---|---|---|---|---|
| BHVO 2 29/5 | 941.4 | 2479 | 308.2 | 1842.4 | 254.0 | 1244.9 |
| BHVO 2 13/6 | 1318.6 | 3527.6 | 439.7 | 2716.8 | 411.7 | 2112.7 |
| BHVO 2 19/6 | 910.5 | 2865.4 | 311.4 | 2242.4 | 515.7 | 1507.6 |
| BHVO2 19/6 dupl | 928.2 | 2905.1 | 313.5 | 2240.2 | 499.9 | 1563.2 |
| TPB 29/5 | 2.3 | 5.8 | -0.5 | 87.1 | 26250 | 3069 |
| TPB 13/6 | 0.2 | 2.6 | 2.4 | 67.6 | 25780 | 2325 |
| TPB 19/6 | 3.1 | -0.4 | 2.4 | 41.7 | 25110 | 1994 |
| SL 11b | 42.9 | 135.4 | 20.0 | 140.2 | 34.6 | 258.2 |
| SL 11c | 43.0 | 131.7 | 19.8 | 136.8 | 37.8 | 339.3 |
| SL 16b | 164.5 | 472.8 | 65.0 | 420.1 | 99.9 | 647.3 |
| SL 16c | 167.9 | 481.9 | 66.1 | 441.8 | 102.3 | 648.3 |
| SL 48b | 84.5 | 385.4 | 34.9 | 389.1 | 739.2 | 2984.5 |
| SL 48c | 73.6 | 378.5 | 32.5 | 363.6 | 740.3 | 2846.4 |
| SL Qtz small | 96.7 | 770.8 | 38.0 | 578.7 | 873.5 | 3473.4 |
| SL Qtz big | 68.3 | 569.1 | 23.0 | 398.9 | 886.5 | 3230.9 |
| SL AW3 cont | 55.7 | 314.4 | 29.3 | 336.4 | 934.8 | 11879.7 |

**Table D7:** Concentrations of the major elements from standards (BHVO 2 and TPB), duplicates Kemi Intrusions samples and blank samples (obtained from the Stellenbosch University ICP-AES). Note the units are in PPM. * indicates values below the detection limits.

| Sample (PPM) | Al | Ca | Fe | K | Mg | Na | Cr |
|---|---|---|---|---|---|---|---|
| BHVO 2 29/5 | 55275.7 | 73349.1 | 87848.3 | 3777.9 | 26608.1 | 11899.1 | 298.1 |
| BHVO 2 13/6 | 59882.0 | 78466.3 | 90176.5 | 3992.9 | 31846.8 | 12653.5 | 348.0 |
| BHVO 2 19/6 | 54559.4 | 71455.0 | 86240.0 | 4785.1 | 25662.8 | 11491.0 | 307.7 |
| TPB 29/5 | 0.8 | 1.8 | 5.5 | 1.6 | 2.1 | 0.3 | 0.1 |
| TPB 13/6 | 1.2 | 3.3 | 1.5 | 1.5 | 0.3 | 0.3 | 0.1 |
| TPB 19/6 | 0.5 | 3.8 | * | * | 0.2 | 0.1 | 0.0 |
| SL 11b | 1786.2 | 26955.2 | 77845.0 | 85.0 | 130989.3 | 1377.3 | 2619.5 |
| SL 11c | 2609.5 | 24241.2 | 75982.9 | 85.9 | 128528.1 | 899.0 | 2613.6 |
| SL 16b | 13835.4 | 87038.8 | 36257.8 | 381.1 | 69916.5 | 162.3 | 4303.3 |
| SL 16c | 14378.1 | 87579.3 | 37144.2 | 171.2 | 73096.1 | 149.8 | 4279.4 |
| SL 48b | 54985.3 | 61910.8 | 35216.3 | 317.1 | 32963.2 | 7371.8 | 916.1 |
| SL 48c | 54775.6 | 62467.4 | 35037.7 | 226.7 | 32225.4 | 7066.5 | 946.5 |
| SL Qtz small | 7105.6 | 69.1 | 3787.8 | 1485.1 | 122.9 | 146.0 | 511.7 |
| SL Qtz big | 6846.1 | 132.0 | 6968.8 | 1427.1 | 93.5 | 135.8 | 6.6 |
| SL AW3 cont | 4334.0 | 34820.3 | 74651.4 | 3221.3 | 96062.8 | 3499.2 | 1750.4 |

**Table D8:** The calculations of the averages, standard deviations and 95% confidence levels (± 2s) from the duplicate analyses from three samples from the Kemi Intrusion (obtained from the Stellenbosch University ICP-MS). The average ± 2s values were used as the errors on the Nd and Sm abundances to calculate the epsilon Nd values.

| a) Concentration | | | b) Errors | | | | | |
|---|---|---|---|---|---|---|---|---|
| Sample (PPB) | Nd | Sm | Nd (PPB) | | | Sm (PPB) | | |
| SL 11 | 669 | 159 | Average | Stan Dev | ± 2s | Average | Stan Dev | ± 2s |
| SL 11b | 616 | 146 | 641 | 27 | 30 | 152 | 6 | 7 |
| SL 11c | 639 | 151 | | | | | | |
| SL 16 | 2107 | 617 | | | | | | |
| SL 16b | 2082 | 616 | 2080 | 29 | 32 | 608 | 15 | 17 |
| SL 16c | 2050 | 591 | | | | | | |
| SL 48 | 1364 | 380 | | | | | | |
| SL 48b | 1331 | 363 | 1308 | 70 | 80 | 367 | 12 | 13 |
| SL 48c | 1229 | 357 | Average ±2 | | 47 | Average ±2 | | 12 |

**Table D9:** The $^{143}Nd$ / $^{144}Nd$ isotopic values of the standards analyzed alongside the samples from the Kemi Intrusion (obtained from the AEON EarthLAB MC-ICP-MS housed at the University of Cape Town).

| UCT Standard errors | Nd143/Nd144 |
|---|---|
| Jndi 1 | 0.512059 |
| Jndi 1 | 0.512071 |
| Jndi 1 | 0.512076 |
| Jndi 1 | 0.512086 |
| Jndi 1 | 0.512088 |
| Jndi 1 | 0.512089 |
| Jndi 1 | 0.512082 |
| Jndi 1 | 0.512085 |
| Jndi 1 | 0.512085 |
| Sample mean | 0.51208 |
| Standard deviation | 9.98E-06 |
| ± 2s | 6.52E-06 |

**Table D10:** The $\varepsilon_{Nd}^{2.44}$ and 2 sigma error values obtained for the Kemi Intrusion. The table on the left excludes any samples from the small chromitite layer and surrounding peridotites and the table on the right is samples from the small chromitite layer and surrounding peridotites. The $\varepsilon_{Nd}^{2.44}$ values were calculated as described in DePaolo and Wasserburg (1976). The errors were calculated using standard error propagation equations.

| Sample | $\varepsilon^{2.44}_{Nd}$ | ± 2s |
|---|---|---|
| SL 05 | -1.6 | 0.3 |
| SL 07 | -1.5 | 0.7 |
| SL 06 | -7.2 | 4.7 |
| SL 09 | -1.8 | 0.2 |
| SL 38 | -8.0 | 1.3 |
| SL 14 | -1.2 | 0.3 |
| SL 16 | -1.0 | 0.5 |
| SL 39 | -8.8 | 1.1 |
| SL 42 | -7.7 | 1.0 |
| SL 46 | -5.3 | 1.4 |
| SL 47 | -10.1 | 0.5 |

| Sample | $\varepsilon^{2.44}_{Nd}$ | ± 2s |
|---|---|---|
| SL 17 | 3.6 | 0.2 |
| SL 20 | 4.0 | 0.1 |
| SL 22 | 1.7 | 0.3 |
| SL 23 | -0.2 | 0.6 |
| SL 24 | -3.7 | 0.7 |
| SL 25 | 1.5 | 0.8 |
| SL 26 | -1.2 | 0.3 |
| SL 28 | 1.5 | 0.9 |
| SL 31 | 3.3 | 0.2 |

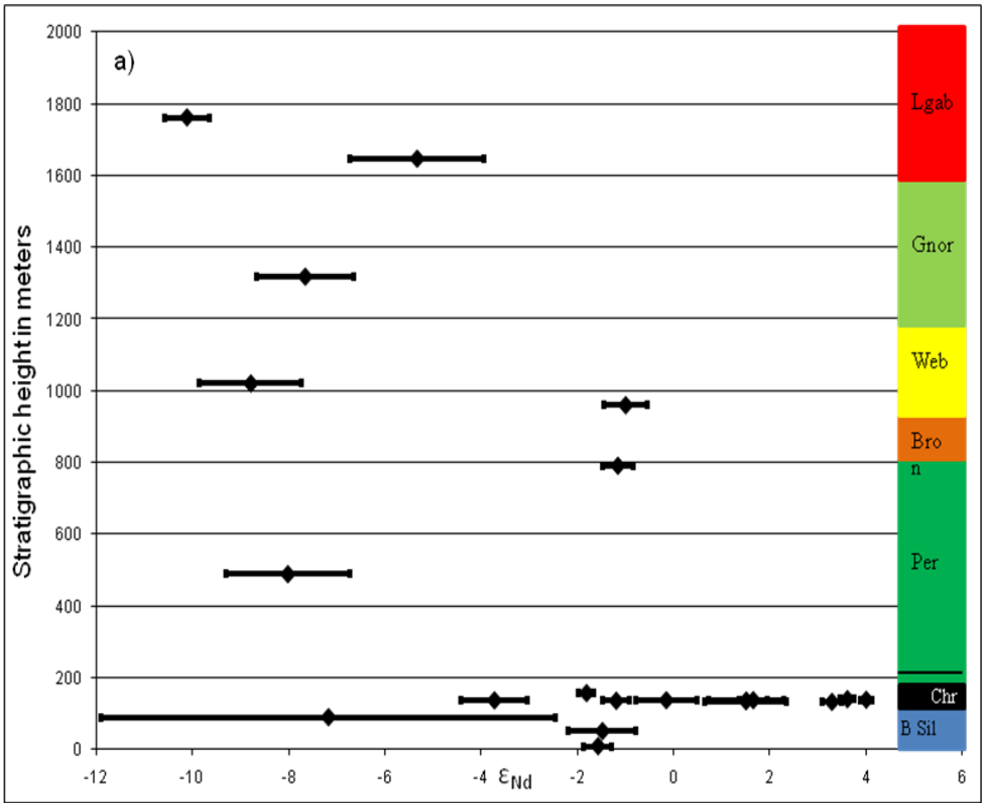


**Figure 41:** (a) Plot of the $\varepsilon_{Nd}$ values and error bars of all the samples versus the stratigraphic profile of the Kemi Intrusion. Diamonds represent silicate cumulates and squares chromitite samples.

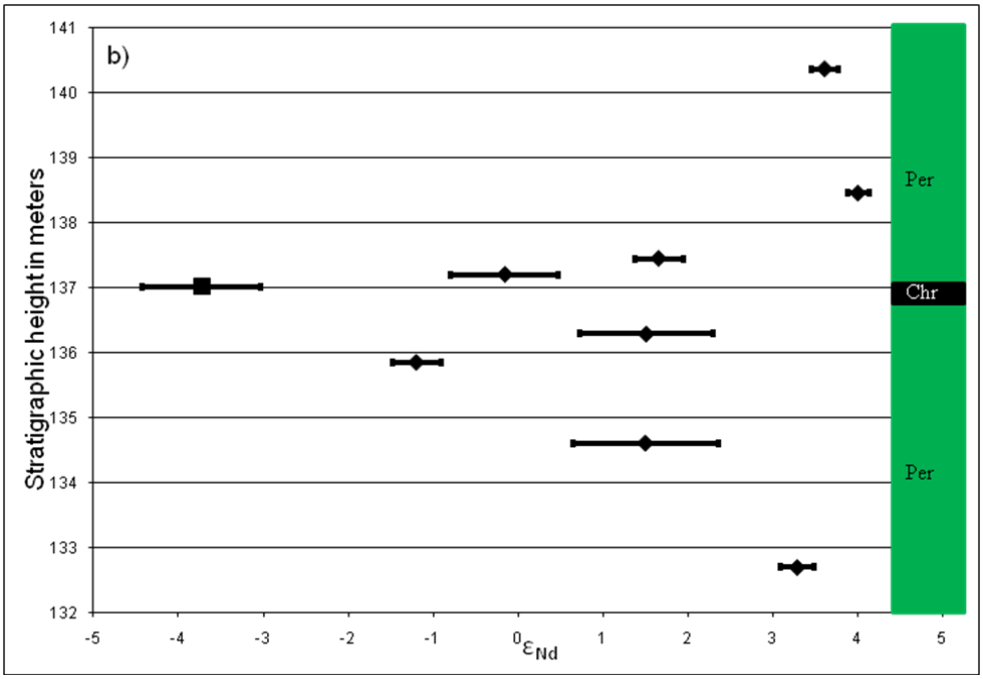


**Figure 41:** (b) plot of the $\varepsilon_{Nd}$ values and errors of the detailed profile across the small chromitite layer above the main Kemi chromitite layer. Diamonds represent silicate cumulates and squares chromitite samples.

**Table D11:** Whole rock PGE concentrations from the Kemi Intrusion (PGE data obtained from the University of Quebec ICP-MS and the minor element data obtained from the University of Quebec AAS thermo elemental analyser). Error values are included as well. * indicate values below the detection limits. Samples SL-11 and -14 through to -47 have osmium concentrations that are below the detection limits (0.31 ppm). For these samples the osmium concentrations was assumed to be at most 0.31 ppm for the sake of the primitive mantle-normalized PGE diagrams. Au has LLD of 0.43 ppb.

| Sample | Ru | | Rh | | Pd | | Os | |
|---|---|---|---|---|---|---|---|---|
| | ppb | Error | ppb | Error | ppb | Error | ppb | Error |
| SL 05 | 34.75 | 1.09 | 4.64 | 0.16 | 11.73 | 0.32 | 12.26 | 0.28 |
| SL 06 | 162.9 | 4.91 | 11.91 | 0.28 | 33.44 | 1.27 | 202.7 | 6.05 |
| SL 07 | 51.68 | 1.04 | 4.36 | 0.15 | 2.47 | 0.14 | 18.15 | 0.38 |
| SL 09 | 0.72 | 0.12 | 15.2 | 0.31 | 25.87 | 0.43 | 0.41 | 0.07 |
| SL 11 | 0.75 | 0.05 | 1.46 | 0.05 | 26.31 | 0.63 | * | |
| SL 14 | 0.51 | 0.06 | 2.9 | 0.13 | 8.3 | 0.13 | * | |
| SL 16 | 0.16 | 0.02 | 2.14 | 0.08 | 11.15 | 0.39 | * | |
| SL 17 | 4.40 | 0.19 | 18.50 | 0.26 | 8.42 | 0.27 | 1.72 | 0.12 |
| SL 20 | 1.69 | 0.06 | 7.20 | 0.09 | 2.60 | 0.15 | 0.57 | 0.07 |
| SL 22 | 1.19 | 0.12 | 6.92 | 0.32 | 4.49 | 0.24 | 0.44 | 0.04 |
| SL 23 | 1.15 | 0.15 | 5.72 | 0.11 | 2.12 | 0.11 | 0.49 | 0.06 |
| SL 25 | 0.74 | 0.15 | 3.91 | 0.09 | 11.19 | 0.50 | * | |
| SL 26 | 1.45 | 0.12 | 9.61 | 0.19 | 5.82 | 0.30 | 0.56 | 0.08 |
| SL 28 | 0.79 | 0.08 | 4.73 | 0.06 | 7.51 | 0.16 | * | |
| SL 31 | 1.85 | 0.08 | 13.63 | 0.21 | 3.75 | 0.18 | 0.66 | 0.05 |
| SL 38 | 0.99 | 0.1 | 2.25 | 0.05 | 3.3 | 0.1 | 0.42 | 0.09 |
| SL 39 | 0.18 | 0.04 | 1.16 | 0.05 | 3.84 | 0.16 | * | |
| SL 42 | 0.14 | 0.05 | 0.62 | 0.01 | 2.79 | 0.16 | * | |
| SL 45 | 0.18 | 0.02 | 0.48 | 0.01 | 2.74 | 0.28 | * | |
| SL 47 | 0.16 | 0.05 | 0.16 | 0.02 | 2.02 | 0.11 | * | |

| Sample | Ir | | Pt | | Au | | Ni | |
|---|---|---|---|---|---|---|---|---|
| | ppb | Error | ppb | Error | ppb | Error | ppm | Error |
| SL 05 | 7.64 | 0.16 | 11.6 | 0.13 | 25.37 | 0.19 | 328.79 | 0.99 |
| SL 06 | 94.11 | 0.55 | 9.52 | 0.31 | 6.78 | 0.26 | 527.34 | 2.64 |
| SL 07 | 9.92 | 0.15 | 1.96 | 0.03 | * | | 534.89 | 1.6 |
| SL 09 | 3.75 | 0.14 | 106.8 | 1.76 | 3.41 | 0.07 | 190.94 | 0.95 |
| SL 11 | 0.69 | 0.03 | 5.98 | 0.16 | 1.94 | 0.08 | 479.99 | 0.48 |
| SL 14 | 1.39 | 0.03 | 13.96 | 0.49 | 1.07 | 0.06 | 298.19 | 0.6 |
| SL 16 | 0.89 | 0.03 | 15.94 | 0.36 | 0.61 | 0.03 | 70.32 | 0.42 |
| SL 17 | 9.69 | 0.24 | 14.18 | 0.28 | * | | 472.47 | 0.94 |
| SL 20 | 3.31 | 0.11 | 8.22 | 0.38 | * | | 199.73 | 0.60 |
| SL 22 | 2.98 | 0.08 | 9.31 | 0.24 | * | | 227.77 | 0.46 |
| SL 23 | 2.41 | 0.04 | 6.80 | 0.21 | * | | 243.56 | 0.97 |
| SL 25 | 2.21 | 0.02 | 7.15 | 0.19 | * | | 219.19 | 1.53 |
| SL 26 | 4.37 | 0.10 | 14.78 | 0.16 | * | | 189.96 | 1.52 |
| SL 28 | 2.23 | 0.07 | 8.84 | 0.12 | * | | 188.13 | 2.07 |
| SL 31 | 5.52 | 0.10 | 16.13 | 0.36 | * | | 117.91 | 1.41 |
| SL 38 | 1.67 | 0.06 | 6.17 | 0.17 | * | | 735.2 | 2.21 |
| SL 39 | 0.54 | 0.05 | 3.62 | 0.15 | * | | 90.09 | 2.34 |
| SL 42 | 0.3 | 0.02 | 4.47 | 0.16 | * | | 38.71 | 0.62 |
| SL 45 | 0.25 | 0.01 | 1.64 | 0.04 | 1.09 | 0.06 | 57.64 | 0.81 |
| SL 47 | 0.19 | 0.01 | 5.63 | 0.27 | 8.3 | 0.15 | 150.29 | 0.45 |

**Table D11 continued:** Whole rock PGE concentrations from the Kemi Intrusion (PGE data obtained from the University of Quebec ICP-MS and the minor element data obtained from the University of Quebec AAS thermo elemental analyser). Samples from the small chromitite layer and surrounding peridotites are excluded. Error values are included as well. * indicate values below the detection limits. Samples SL-05 and -07 have sulphur concentrations that are below the detection limits (15 ppm). For these two samples the sulphur concentrations was assumed to be at most 15 ppm for the sake of the PGE / S ratios. The Cu LLD is 10 ppm.

| Sample | Cu | | S | |
|---|---|---|---|---|
| | ppm | Error | ppm | ppb |
| SL 05 | * | | * | |
| SL 06 | * | | 60 | 60,000 |
| SL 07 | * | | * | |
| SL 09 | 26.44 | 0.56 | 33 | 33,000 |
| SL 11 | 17.38 | 0.52 | 294 | 294,000 |
| SL 14 | 31.89 | 0.80 | 92 | 92,000 |
| SL 16 | 20.90 | 0.82 | 28 | 28,000 |
| SL 17 | 32.13 | 0.26 | 481 | 481,000 |
| SL 20 | 22.18 | 1.57 | 163 | 163,000 |
| SL 22 | * | | 52 | 52,000 |
| SL 23 | * | | * | |
| SL 25 | * | | 115 | 115,000 |
| SL 26 | * | | 22 | 22,000 |
| SL 28 | * | | 46 | 46,000 |
| SL 31 | 19.73 | 0.91 | 21 | 21,000 |
| SL 38 | 20.51 | 0.51 | 164 | 164,000 |
| SL 39 | 14.44 | 1.18 | 46 | 46,000 |
| SL 42 | 10.39 | 1.21 | 53 | 53,000 |
| SL 45 | 27.36 | 1.09 | 232 | 232,000 |
| SL 47 | 161.19 | 0.48 | 244 | 244,000 |

**Table D12:** Concentrations of the PGE from standards (BB-235 and AMIS-5) and blank samples (obtained from the University of Quebec ICP-AES). * indicates values below the detection limits.

| Standard | Ru | | Rh | | Pd | |
|---|---|---|---|---|---|---|
| | ppb | Error | ppb | Error | ppb | Error |
| Measured BB-235 values. | 1.77 | 0.19 | 1.45 | 0.03 | 13.7 | 0.33 |
| BB-235 international standard values. | 1.7 | 0.3 | 1.5 | 0.2 | 15 | 1.3 |
| First measured AMIS0005 values. | 1125 | 24.33 | 649 | 13.41 | 2199 | 44.42 |
| Second measured AMIS0005 values. | 1173 | 7.38 | 682.7 | 9.17 | 2267 | 40.26 |
| Chromitite AMIS-0005 standard values. | 1240 | 90 | 660 | 80 | 2230 | 180 |
| First blank values | <0.09 | | <0.05 | | 0.65 | 0.03 |
| Second blank values | <0.09 | | <0.05 | | 0.6 | 0.05 |
| Third blank values | <0.09 | | <0.05 | | 0.56 | 0.06 |
| Fourth blank values | <0.09 | | <0.05 | | <0.53 | |
| Fifth blank values | <0.09 | | <0.05 | | <0.53 | |
| Limit of detection | 0.09 | | 0.05 | | 0.53 | |

| Standard | Os | | Ir | | Pt | |
|---|---|---|---|---|---|---|
| | ppb | Error | ppb | Error | ppb | Error |
| Measured BB-235 values | 0.33 | 0.05 | 0.17 | 0.01 | 14.14 | 0.2 |
| BB-235 international standard values | 0.16 | 0.07 | 0.14 | 0.05 | 15.3 | 1.3 |
| First measured AMIS0005 values | 214.9 | 4.77 | 258.8 | 2.32 | 3207 | 55.97 |
| Second measured AMIS0005 values | 201.8 | 2.23 | 265.6 | 3.57 | 3234 | 19.14 |
| Chromitite AMIS-0005 standard values | * | | 290 | 80 | 3380 | 330 |
| First blank values | <0.31 | | <0.08 | | <0.26 | |
| Second blank values | <0.31 | | <0.08 | | <0.26 | |
| Third blank values | <0.31 | | <0.08 | | <0.26 | |
| Fourth blank values | <0.31 | | <0.08 | | <0.26 | |
| Fifth blank values | <0.31 | | <0.08 | | <0.26 | |
| Limit of detection | 0.31 | | 0.08 | | 0.26 | |

**Table D12 continued:** Concentrations of the PGE from standards (BB-235 and AMIS-5) and blank samples (obtained from the University of Quebec ICP-MS).

| Standard | Au | | Ni | |
|---|---|---|---|---|
| | ppb | Error | ppm | Error |
| Measured BB-235 values | 1.62 | 0.03 | | |
| BB-235 international standard values | 1.25 | 0.4 | | |
| First measured AMIS0005 values | 27.67 | 0.22 | 159.58 | 1.4 |
| Second measured AMIS0005 values | 26.52 | 0.23 | | |
| Chromitite AMIS-0005 standard values | 20 | | 160 | 18 |
| First blank values | 0.61 | 0.02 | | |
| Second blank values | 0.7 | 0.03 | | |
| Third blank values | 0.66 | 0.04 | | |
| Fourth blank values | 0.65 | 0.05 | | |
| Fifth blank values | <0.43 | | | |
| Limit of detection | 0.43 | | | |

| Standard | Cu | | S | |
|---|---|---|---|---|
| | ppm | Error | ppm | Error |
| Measured BB-235 values | | | | |
| BB-235 international standard values | | | | |
| First measured AMIS0005 values | 57.40422 | 3.1 | 211 | 6 |
| Second measured AMIS0005 values | | | | |
| Chromitite AMIS-0005 standard values | 60 | 6 | 200 | |
| First blank values | | | | |
| Second blank values | | | | |
| Third blank values | | | | |
| Fourth blank values | | | | |
| Fifth blank values | | | | |
| Limit of detection | | | | |

**Table D12 continued:** Concentrations of the Ni, Cu and S from standards (BB-235 and AMIS-5) and blank samples (obtained from the University of Quebec ICP-MS).

| Standard | Ni | | Cu | | S | |
|---|---|---|---|---|---|---|
| | ppm | Error | ppm | Error | ppm | Error |
| Measured AMIS0007 values | 1677.22 | 1.68 | 1171.85 | 3.52 | | |
| AMIS007 standard values | 1669 | 200 | 1296 | 150 | | |
| | | | | | | |
| Measured Ni-Cu-S KPT values | 1197.13 | 2.39 | 1172.14 | 8.2 | 10300 | 143 |
| Standard KPT values | 1169 | 185 | 1116 | 330 | 10600 | |
| Measured Ni-Cu-S SARM-7 values | | | | | 4173 | 50 |
| Standard SARM-7 values | | | | | 4000 | |
| Measured Ni-Cu-S TDB-1 values | | | | | 304 | 18 |
| Standard TDB-1 values | | | | | 300 | |
| Measured Ni-Cu-S JSD-2 values | | | | | 12758 | |
| Standard JSD-2 values | | | | | 13000 | |

## Appendix E

## Starting parameters used and results of the mixing calculations

The mixing equation used for the trace and REE calculations:

$C_{mag} = X_{pm} \times C_{pm} + X_{cr} \times C_{cr}$

where C = concentration in ppm

X = weight fraction

pm = parent magma

cr = country rock

mag = resultant magma

$X_{pm} = 1 - X_{cr}$

The mixing equation used for the isotopic calculations:

$$\frac{\varepsilon^{2.44}_{mag} = (X_{pm} \times C_{pm} \times \varepsilon^{2.44}_{pm}) + (X_{cr} \times C_{cr} \times \varepsilon^{2.44}_{Cr})}{(X_{pm} \times C_{pm}) + (X_{cr} \times C_{cr})}$$

where $\varepsilon^{2.44}$ = initial Nd epsilon value of Nd at 2.44 Ga

The equations were obtained from Talyor Jr (1980) and DePaolo (1988).

**Table E1:** Summary of the starting isotopic parameters used in the mixing calculations.

| Parent magma / Contaminants | Sm (ppm) | Nd (ppm) | $^{147}Sm/^{144}Nd$ | $^{143}Nd/^{144}Nd$ | $\varepsilon^{2.44}_{Nd}$ | La (ppm) | Y (ppm) |
|---|---|---|---|---|---|---|---|
| Komatiite (DM) [a,b,c] | 0.5 | 2 | | | 5 | 1.5 | 0.3 |
| Basaltic (DM) [d,c] | 2.5 | 10 | | | 5 | 11 | 1.3 |
| Komatiite (EM) [a,b,e] | 0.5 | 2 | | | 0 | 1.5 | 0.3 |
| Basaltic (eM) [d,e] | 2.5 | 10 | | | 0 | 11 | 1.3 |
| Neoarchaean 2.8 Ga [f,g] | 1.71 | 14 | 0.1079 | 0.511049 | -3.2 | 28.73 | 0.25 |
| Mesoarchaean 3.1 Ga [f,g,h] | 1.71 | 14 | 0.1058 | 0.510442 | -11 | 28.73 | 0.25 |
| Eoarchaean 3.7 Ga [h,i] | 3.4 | 16 | 0.1058 | 0.507424 | -15 | 15 | 2.2 |

a - Sigurdsson, 2000.
b - Komatiite samples 94174 and 94175, Puchtel et al., 1997.
c - DePaolo and Wasserburg, 1979.
d - Iljina and Hanski, 2005.
e - Jacobsen and Wasserburg, 1984.
f - REE results of this study
g - Hanski et al., 2001
h - Granite samples F20 to F25, Jahn et al., 1984.
i - Taylor and McLennan, 1995.

**Table E2:** Mixing results for $\varepsilon^{2.44}_{Nd}$ of the four parent magmas with the Neoarchaean (2.8 Ga) and Mesoarchaean (3.1 Ga) crust contaminant.

| εNd | | | | | | | | | |
|---|---|---|---|---|---|---|---|---|---|
| **2.8 AC** | **Kom(DM)** | **Bas(DM)** | **Kom(EM)** | **Bas(EM)** | **3.1 AC** | **Kom(DM)** | **Bas(DM)** | **Kom(EM)** | **Bas(EM)** |
| **Xcr** | | | | | **Xcr** | | | | |
| **0.01** | 4.5 | 4.9 | -0.2 | 0.0 | **0.01** | 3.9 | 4.8 | -0.7 | -0.2 |
| **0.02** | 4.0 | 4.8 | -0.4 | -0.1 | **0.02** | 3.0 | 4.6 | -1.4 | -0.3 |
| **0.03** | 3.5 | 4.7 | -0.6 | -0.1 | **0.03** | 2.2 | 4.3 | -2.0 | -0.5 |
| **0.04** | 3.1 | 4.5 | -0.7 | -0.2 | **0.04** | 1.4 | 4.1 | -2.5 | -0.6 |
| **0.05** | 2.8 | 4.4 | -0.9 | -0.2 | **0.05** | 0.7 | 3.9 | -3.0 | -0.8 |
| **0.06** | 2.5 | 4.3 | -1.0 | -0.3 | **0.06** | 0.1 | 3.7 | -3.4 | -0.9 |
| **0.07** | 2.2 | 4.2 | -1.1 | -0.3 | **0.07** | -0.5 | 3.5 | -3.8 | -1.0 |
| **0.08** | 1.9 | 4.1 | -1.2 | -0.3 | **0.08** | -1.1 | 3.3 | -4.2 | -1.2 |
| **0.09** | 1.6 | 4.0 | -1.3 | -0.4 | **0.09** | -1.5 | 3.1 | -4.5 | -1.3 |
| **0.1** | 1.4 | 3.9 | -1.4 | -0.4 | **0.1** | -2.0 | 2.8 | -4.8 | -1.5 |
| **0.11** | 1.2 | 3.8 | -1.5 | -0.5 | **0.11** | -2.4 | 2.6 | -5.1 | -1.6 |
| **0.12** | 1.0 | 3.7 | -1.6 | -0.5 | **0.12** | -2.8 | 2.4 | -5.4 | -1.8 |
| **0.13** | 0.8 | 3.6 | -1.6 | -0.6 | **0.13** | -3.2 | 2.2 | -5.6 | -1.9 |
| **0.14** | 0.6 | 3.5 | -1.7 | -0.6 | **0.14** | -3.5 | 2.0 | -5.9 | -2.0 |
| **0.15** | 0.5 | 3.4 | -1.8 | -0.6 | **0.15** | -3.8 | 1.8 | -6.1 | -2.2 |
| **0.16** | 0.3 | 3.3 | -1.8 | -0.7 | **0.16** | -4.1 | 1.6 | -6.3 | -2.3 |
| **0.17** | 0.2 | 3.2 | -1.9 | -0.7 | **0.17** | -4.4 | 1.4 | -6.5 | -2.5 |
| **0.18** | 0.0 | 3.1 | -1.9 | -0.8 | **0.18** | -4.7 | 1.2 | -6.7 | -2.6 |
| **0.19** | -0.1 | 3.0 | -2.0 | -0.8 | **0.19** | -4.9 | 1.0 | -6.8 | -2.7 |
| **0.2** | -0.2 | 2.9 | -2.0 | -0.8 | **0.2** | -5.2 | 0.9 | -7.0 | -2.9 |
| **0.3** | -1.2 | 1.9 | -2.4 | -1.2 | **0.3** | -7.0 | -1.0 | -8.3 | -4.1 |
| **0.4** | -1.8 | 1.0 | -2.6 | -1.5 | **0.4** | -8.2 | -2.7 | -9.1 | -5.3 |
| **0.5** | -2.2 | 0.2 | -2.8 | -1.9 | **0.5** | -9.0 | -4.3 | -9.6 | -6.4 |
| **0.6** | -2.5 | -0.6 | -2.9 | -2.2 | **0.6** | -9.6 | -5.8 | -10.0 | -7.5 |
| **0.7** | -2.7 | -1.3 | -3.0 | -2.5 | **0.7** | -10.1 | -7.3 | -10.4 | -8.4 |
| **0.8** | -2.9 | -2.0 | -3.1 | -2.7 | **0.8** | -10.4 | -8.6 | -10.6 | -9.3 |
| **0.9** | -3.1 | -2.6 | -3.2 | -3.0 | **0.9** | -10.8 | -9.8 | -10.8 | -10.2 |

**Table E3:** Mixing results for Sm, La and Yb in ppm and $\varepsilon^{2.44}_{Nd}$ with the upper crustal contaminant.

| | Sm | | La | | Yb | |
|---|---|---|---|---|---|---|
| **U crust Xcr** | **Kom** | **Bas** | **Kom** | **Bas** | **Kom** | **Bas** |
| **0.01** | 3.46 | 16.84 | 7.48 | 47.16 | 1.86 | 8.01 |
| **0.02** | 3.54 | 16.79 | 8.63 | 47.91 | 1.86 | 7.94 |
| **0.03** | 3.62 | 16.73 | 9.78 | 48.66 | 1.85 | 7.88 |
| **0.04** | 3.71 | 16.68 | 10.92 | 49.41 | 1.85 | 7.81 |
| **0.05** | 3.79 | 16.63 | 12.07 | 50.15 | 1.85 | 7.75 |
| **0.06** | 3.87 | 16.57 | 13.22 | 50.90 | 1.84 | 7.68 |
| **0.07** | 3.95 | 16.52 | 14.37 | 51.65 | 1.84 | 7.62 |
| **0.08** | 4.03 | 16.46 | 15.52 | 52.40 | 1.84 | 7.55 |
| **0.09** | 4.11 | 16.41 | 16.67 | 53.15 | 1.84 | 7.49 |
| **0.1** | 4.20 | 16.36 | 17.82 | 53.89 | 1.83 | 7.42 |
| **0.11** | 4.28 | 16.30 | 18.97 | 54.64 | 1.83 | 7.36 |
| **0.12** | 4.36 | 16.25 | 20.12 | 55.39 | 1.83 | 7.29 |
| **0.13** | 4.44 | 16.20 | 21.27 | 56.14 | 1.82 | 7.23 |
| **0.14** | 4.52 | 16.14 | 22.41 | 56.89 | 1.82 | 7.16 |
| **0.15** | 4.60 | 16.09 | 23.56 | 57.64 | 1.82 | 7.10 |
| **0.16** | 4.69 | 16.04 | 24.71 | 58.38 | 1.81 | 7.03 |
| **0.17** | 4.77 | 15.98 | 25.86 | 59.13 | 1.81 | 6.97 |
| **0.18** | 4.85 | 15.93 | 27.01 | 59.88 | 1.81 | 6.90 |
| **0.19** | 4.93 | 15.88 | 28.16 | 60.63 | 1.80 | 6.84 |
| **0.2** | 5.01 | 15.82 | 29.31 | 61.38 | 1.80 | 6.77 |
| **0.3** | 5.83 | 15.29 | 40.80 | 68.86 | 1.77 | 6.12 |
| **0.4** | 6.65 | 14.76 | 52.29 | 76.34 | 1.74 | 5.47 |
| **0.5** | 7.47 | 14.22 | 63.78 | 83.82 | 1.71 | 4.81 |
| **0.6** | 8.28 | 13.69 | 75.27 | 91.30 | 1.68 | 4.16 |
| **0.7** | 9.10 | 13.16 | 86.76 | 98.78 | 1.65 | 3.51 |
| **0.8** | 9.92 | 12.62 | 98.24 | 106.26 | 1.61 | 2.86 |
| **0.9** | 10.74 | 12.09 | 109.73 | 113.74 | 1.58 | 2.20 |

**Table E4:** Mixing results for Sm, La and Yb in ppm and $\varepsilon^{2.44}_{Nd}$ with the Eoarchaean (3.7 Ga) crust contaminant.

| εNd | | | Sm | | La | | Yb | |
|---|---|---|---|---|---|---|---|---|
| 3.7 AC Xcr | Kom(DM) | Bas(DM) | Kom | Bas | Kom | Bas | Kom | Bas |
| **0.01** | 3.5 | 4.7 | 3.57 | 16.95 | 6.90 | 46.58 | 1.98 | 8.13 |
| **0.02** | 2.2 | 4.4 | 3.77 | 17.01 | 7.47 | 46.75 | 2.10 | 8.19 |
| **0.03** | 1.0 | 4.1 | 3.97 | 17.07 | 8.04 | 46.92 | 2.22 | 8.24 |
| **0.04** | 0.0 | 3.8 | 4.16 | 17.14 | 8.61 | 47.09 | 2.34 | 8.30 |
| **0.05** | -0.9 | 3.4 | 4.36 | 17.20 | 9.18 | 47.26 | 2.45 | 8.35 |
| **0.06** | -1.8 | 3.1 | 4.55 | 17.26 | 9.75 | 47.43 | 2.57 | 8.41 |
| **0.07** | -2.5 | 2.9 | 4.75 | 17.32 | 10.32 | 47.59 | 2.69 | 8.47 |
| **0.08** | -3.2 | 2.6 | 4.95 | 17.38 | 10.89 | 47.76 | 2.81 | 8.52 |
| **0.09** | -3.8 | 2.3 | 5.14 | 17.44 | 11.46 | 47.93 | 2.93 | 8.58 |
| **0.1** | -4.4 | 2.0 | 5.34 | 17.50 | 12.03 | 48.10 | 3.04 | 8.63 |
| **0.11** | -4.9 | 1.7 | 5.53 | 17.56 | 12.59 | 48.27 | 3.16 | 8.69 |
| **0.12** | -5.4 | 1.4 | 5.73 | 17.62 | 13.16 | 48.44 | 3.28 | 8.75 |
| **0.13** | -5.9 | 1.1 | 5.93 | 17.68 | 13.73 | 48.61 | 3.40 | 8.80 |
| **0.14** | -6.3 | 0.9 | 6.12 | 17.74 | 14.30 | 48.78 | 3.52 | 8.86 |
| **0.15** | -6.7 | 0.6 | 6.32 | 17.80 | 14.87 | 48.95 | 3.63 | 8.91 |
| **0.16** | -7.1 | 0.3 | 6.51 | 17.86 | 15.44 | 49.11 | 3.75 | 8.97 |
| **0.17** | -7.4 | 0.1 | 6.71 | 17.93 | 16.01 | 49.28 | 3.87 | 9.02 |
| **0.18** | -7.7 | -0.2 | 6.91 | 17.99 | 16.58 | 49.45 | 3.99 | 9.08 |
| **0.19** | -8.0 | -0.5 | 7.10 | 18.05 | 17.15 | 49.62 | 4.11 | 9.14 |
| **0.2** | -8.3 | -0.7 | 7.30 | 18.11 | 17.72 | 49.79 | 4.22 | 9.19 |
| **0.3** | -10.5 | -3.1 | 9.26 | 18.72 | 23.42 | 51.48 | 5.40 | 9.75 |
| **0.4** | -11.8 | -5.3 | 11.22 | 19.32 | 29.11 | 53.16 | 6.58 | 10.31 |
| **0.5** | -12.8 | -7.3 | 13.18 | 19.93 | 34.81 | 54.85 | 7.76 | 10.87 |
| **0.6** | -13.5 | -9.1 | 15.14 | 20.54 | 40.51 | 56.54 | 8.94 | 11.43 |
| **0.7** | -14.0 | -10.8 | 17.09 | 21.15 | 46.20 | 58.23 | 10.12 | 11.99 |
| **0.8** | -14.4 | -12.3 | 19.05 | 21.76 | 51.90 | 59.92 | 11.30 | 12.55 |
| **0.9** | -14.7 | -13.7 | 21.01 | 22.36 | 57.59 | 61.60 | 12.48 | 13.11 |

**Table E5:** Summary of the various heat capacities and enthalpy of fusion constants used to calculate the maximum ratio of country rock assimilated to crystallized cumulates. Values obtained from Sigurdsson (2000).

| Mineral | Enthal | Mineral | Enthalpy |
|---|---|---|---|
| **Orthopyroxene** | 729 | **Anorthite** | 478 |
| **Forsterite** | 1010 | **Albite** | 14 |
| **Fayalite** | 438 | **Country Rock** | **Heat Capacity (cal/g C)** |
| **Clinopyroxene** | 636 | **Granite** | 0.3284 |